

WATER FLOW THROUGH UNSATURATED MINE WASTE ROCK  
IN A REGION OF PERMAFROST

by

MATTHEW NEUNER

B.Sc. James Madison University, 2000

A THESIS SUBMITTED IN PARTIAL FULFILLMENT OF  
THE REQUIREMENTS FOR THE DEGREE OF

MASTER OF SCIENCE

in

THE FACULTY OF GRADUATE STUDIES

(Geological Sciences)

THE UNIVERSITY OF BRITISH COLUMBIA

(Vancouver)

February 2009

© Matthew Neuner, 2009

## ABSTRACT

A field experiment was constructed at the Diavik Diamond Mine in northern Canada to investigate water flow through unsaturated piles of mine waste rock in a region of permafrost. Two test piles 15 m-high were built on collection systems 60 m by 50 m, each consisting of lysimeters and a large impermeable HDPE liner, and instrumentation was installed within the piles to measure moisture content, temperature, and tension head. Upper collection lysimeters were installed near the test piles to investigate infiltration, evaporation, and the effect of the thermal regime in the upper 2 m of the waste rock. Hydrogeological characterization was performed at a range of scales to relate hydraulic properties of the fine-grained matrix to the test piles, of which, roughly half is estimated to be boulders. After the initial 1.5 year of monitoring, under drier than average conditions, net infiltration did not reach a depth of 2 m. Applied rainfall events raised the rainfall to the annual mean at one of the test piles, where a wetting front propagated to a depth of about 7 m during the summer and autumn of 2007. Infiltration into frozen waste rock froze and was then remobilized with thaw propagation, and thermal controls on flow were significant throughout the year. Rapid flow with high spatial variability was detected in response to a high-intensity applied rainfall event. Rainfall with recurrence intervals less than 10 years produced flow with less spatial variability and lower flow rates. A calibrated numerical model was developed using VS2D to aid in the description of the flow system at the upper collection lysimeters and the test piles. Solute mass loading estimates were dictated primarily by the flow behaviour, rather than by changes in solute concentrations. Loading from one of the test piles during July 2007 was twice the average rate of approximately  $0.8 \text{ g SO}_4^{2-}/\text{d}/\text{m}^2$ .

# TABLE OF CONTENTS

ABSTRACT.....	ii
TABLE OF CONTENTS.....	iii
LIST OF TABLES.....	vi
LIST OF FIGURES.....	vii
LIST OF ABBREVIATIONS.....	xii
ACKNOWLEDGEMENTS.....	xiii
<b>CHAPTER 1 INTRODUCTION.....</b>	<b>1</b>
1.1    BACKGROUND: THE HYDROGEOLOGY OF MINE WASTE ROCK .....	1
1.2    PERMAFROST CONDITIONS.....	4
1.3    RESEARCH OBJECTIVES .....	6
<b>CHAPTER 2 METHODS.....</b>	<b>9</b>
2.1    STUDY SITE: THE DIAVIK DIAMOND MINE .....	9
2.2    FIELD EXPERIMENT CONSTRUCTION .....	9
2.2.1 <i>Test pile construction</i> .....	9
2.2.2 <i>Upper collection lysimeter construction</i> .....	10
2.3    INSTRUMENTATION .....	11
2.3.1 <i>Outflow instrumentation</i> .....	11
2.3.2 <i>Instrumentation within the test piles</i> .....	11
2.3.3 <i>Meteorological instrumentation</i> .....	13
2.3.4 <i>Applied rainfall</i> .....	13
2.3.5 <i>Problems with instrumentation</i> .....	14
2.4    HYDROGEOLOGICAL CHARACTERIZATION OF THE WASTE ROCK .....	15
2.4.1 <i>Particle and clast size</i> .....	15
2.4.2 <i>Porosity</i> .....	16
2.4.3 <i>Infiltration capacity</i> .....	16
2.4.4 <i>Saturated hydraulic conductivity</i> .....	17
2.4.5 <i>Water retention curves</i> .....	18
2.4.6 <i>Field capacity and initial moisture content</i> .....	18
2.4.7 <i>Unsaturated hydraulic conductivity</i> .....	19
2.4.8 <i>Porewater freezing and thawing</i> .....	20
2.4.9 <i>Upscaling from the matrix-scale to the large-scale</i> .....	21
2.5    MODELING .....	22
2.5.1 <i>Evaporation</i> .....	22
2.5.2 <i>2D flow modeling using VS2D</i> .....	25
<b>CHAPTER 3 RESULTS.....</b>	<b>30</b>
3.1    WASTE ROCK HYDROGEOLOGICAL CHARACTERIZATION.....	30
3.1.1 <i>Particle and clast size</i> .....	30
3.1.2 <i>Porosity</i> .....	31
3.1.3 <i>Infiltration capacity</i> .....	32
3.1.4 <i>Saturated hydraulic conductivity</i> .....	33
3.1.5 <i>Water retention curves</i> .....	34
3.1.6 <i>Field capacity and initial moisture content</i> .....	35
3.1.7 <i>Unsaturated hydraulic conductivity</i> .....	38

3.1.8	<i>Pore water freezing and thawing</i> .....	38
3.1.9	<i>Upscaling from the matrix-scale to the large-scale</i> .....	39
3.2	RAINFALL.....	41
3.3	SNOWMELT.....	42
3.4	EVAPORATION AND INFILTRATION.....	43
3.4.1	<i>Type 3 upper collection lysimeters: wet conditions</i> .....	44
3.4.2	<i>Type 1 upper collection lysimeters: dry conditions</i> .....	44
3.4.3	<i>Test piles: top surface</i> .....	45
3.4.4	<i>Test piles: batters</i> .....	47
3.5	HYDROLOGIC AND THERMAL INTERACTION IN THE PERMAFROST ACTIVE LAYER.....	47
3.5.1	<i>Depth of the active layer</i> .....	47
3.5.2	<i>Pore water redistribution toward a frost layer</i> .....	49
3.5.3	<i>Infiltration into frozen waste rock</i> .....	51
3.5.4	<i>Temperature-dependent outflow</i> .....	54
3.6	INFILTRATION THROUGH BATTERS AND THE POTENTIAL FOR NON-VERTICAL FLOW.....	56
3.6.1	<i>Portion of the test pile contributing to outflow</i> .....	57
3.6.2	<i>Water balance approach</i> .....	59
3.7	FLOW MECHANISMS: UPPER 1.7 M.....	61
3.7.1	<i>Unsaturated groundwater flux</i> .....	62
3.7.2	<i>Wetting front propagation</i> .....	63
3.7.3	<i>Flow velocity</i> .....	65
3.7.4	<i>Modeling</i> .....	66
3.7.5	<i>Effects of freeze-thaw conditions at the ground surface</i> .....	68
3.8	FLOW MECHANISMS: 14 M-HIGH TEST PILES.....	70
3.8.1	<i>Response to high- and moderate-intensity rainfall</i> .....	70
3.8.2	<i>Flow on a seasonal time scale</i> .....	75
3.9	SOLUTE MASS LOADING ESTIMATES.....	78
<b>CHAPTER 4 DISCUSSION.....</b>		<b>112</b>
4.1	PERMAFROST CONSIDERATIONS: A LONG-TERM CONCEPTUAL MODEL.....	112
4.1.1	<i>Period 1: unlimited infiltration</i> .....	113
4.1.2	<i>Period 2: formation of an impermeable layer</i> .....	114
4.1.3	<i>Period 3: steady state</i> .....	116
4.2	NON-VERTICAL FLOW.....	117
4.3	WASTE ROCK HYDROGEOLOGICAL CHARACTERIZATION.....	120
4.4	FLOW MECHANISMS.....	122
<b>CHAPTER 5 CONCLUSIONS.....</b>		<b>126</b>
<b>RECOMMENDATIONS.....</b>		<b>128</b>
<b>REFERENCES.....</b>		<b>129</b>
<b>APPENDIX A CONSTRUCTION DETAILS.....</b>		<b>137</b>
A.1	CONSTRUCTION OF THE TEST PILES.....	137
A.2	CONSTRUCTION OF THE UPPER COLLECTION LYSIMETERS.....	141
<b>APPENDIX B INSTRUMENTATION DETAILS.....</b>		<b>167</b>
B.1	MOISTURE CONTENT SENSORS.....	167
B.1.1	<i>Time Domain Reflectometry (TDR)</i> .....	167
B.1.2	<i>Capacitance sensors</i> .....	175
B.2	TENSIOMETERS.....	180
B.2.1	<i>Standpipe tensiometers</i> .....	180
B.2.2	<i>Using suction samplers as tensiometers</i> .....	182
B.3	INSTRUMENT POSITIONS.....	185
B.4	CONTINUALLY-LOGGING SPECIFIC CONDUCTANCE.....	188

B.5	CONTINUALLY-LOGGING PH.....	192
B.6	FLOW GAUGES .....	192
B.6.1	<i>Gauge requirements</i> .....	192
B.6.2	<i>Flow-through drainage monitoring system</i> .....	196
B.6.3	<i>Gauging problems in 2007</i> .....	199
B.6.4	<i>Low flow tipping bucket gauges</i> .....	200
B.6.5	<i>High flow tipping bucket gauges</i> .....	202
B.6.6	<i>Paddlewheel gauges</i> .....	205
<b>APPENDIX C   DETAILS OF CHARACTERIZATION OF THE WASTE ROCK.....</b>		<b>207</b>
C.1	GRAIN SIZE DISTRIBUTION .....	207
C.1.1	<i>Boulder fraction of 100 m<sup>3</sup> samples</i> .....	207
C.1.2	<i>Grain size distribution of a 40 m<sup>3</sup> sample</i> .....	210
C.1.3	<i>Grain size distribution of hand samples</i> .....	210
C.2	HYDRAULIC TESTING OF A 16 M <sup>3</sup> SAMPLE .....	221
C.3	LABORATORY PERMEAMETER TESTS .....	236
C.4	RING INFILTRMETER TESTS .....	239
C.5	WATER RETENTION CURVES.....	247
C.5.1	<i>Tempe cell tests</i> .....	247
C.5.2	<i>Field water retention curves</i> .....	249
C.6	UNSATURATED HYDRAULIC CONDUCTIVITY .....	250
C.6.1	<i>Estimation from the water retention curve</i> .....	250
C.6.2	<i>Field calibration of the unsaturated hydraulic conductivity</i> .....	250
<b>APPENDIX D   DATA LOGGING DETAILS.....</b>		<b>270</b>
D.1	DATA LOGGER WIRING DIAGRAMS .....	271
D.2	DATA LOGGER PROGRAMS.....	280
D.2.1	<i>Station 3Ba</i> .....	281
D.2.2	<i>Station 3Da</i> .....	291
D.2.3	<i>Station 3Db</i> .....	300
D.2.4	<i>Station 3Ta</i> .....	302
D.2.5	<i>Station 1Ta</i> .....	312
D.2.6	<i>Station ULa</i> .....	321
<b>APPENDIX E   DATA SET FOR SEPTEMBER 2006 TO MARCH 2008 .....</b>		<b>332</b>
E.1	RAIN.....	332
E.1.1	<i>Natural rainfall</i> .....	332
E.1.2	<i>Applied Rainfall Events</i> .....	333
E.2	SNOW .....	333
E.3	EVAPORATION.....	334
E.4	TYPE 3 TEST PILE.....	335
E.5	TYPE 1 TEST PILE.....	337
E.6	UPPER COLLECTION LYSIMETERS .....	337
<b>REFERENCES CITED IN THE APPENDICES.....</b>		<b>368</b>

## LIST OF TABLES

TABLE 3.1 WASTE ROCK HYDRAULIC PARAMETERS.....	81
TABLE 3.2 MODELING RESULTS FOR THE UPPER COLLECTION LYSIMETERS.....	82
TABLE 3.3 INFILTRATION PERIODS AND THE FLUX SPECIFIED IN THE VS2D MODELS.....	83
TABLE 3.4 THE PARAMETERS USED IN THE CALIBRATED VS2D MODEL.....	84
TABLE 3.5 RESULTS OF THE CALIBRATION OF THE VS2D MODEL.....	85
TABLE 3.6 SUMMARY OF THE FLOW BEHAVIOUR IN 2006 AND 2007.....	86
TABLE A.1 A LIST OF THE TDR PROBES THAT SURVIVED CONSTRUCTION OF THE TEST PILES.....	144
TABLE B.1 SURVEYED POSITIONS OF TDR PROBES AND TENSIO METERS AT THE TYPE 3 TEST PILE....	186
TABLE B.2 SURVEYED POSITIONS OF TDR PROBES AT THE TYPE 1 TEST PILE AND ECH <sub>2</sub> O PROBES AND TENSIO METERS AT THE UPPER COLLECTION LYSIMETERS.....	187
TABLE B.3 ESTIMATIONS OF FLOW GAUGE REQUIREMENTS.....	195
TABLE B.4 RISE IN HEAD IN THE DRAIN PIPE DUE TO RESISTANCE IN THE FLOW-THROUGH SYSTEM.....	199
TABLE C. 1 THE FRACTION OF 100 M <sup>3</sup> SAMPLES WITH PARTICLE SIZE FINER THAN 300MM.....	208
TABLE C. 2 A SUMMARY OF THE GRAIN SIZE DISTRIBUTION OF THE WASTE ROCK.....	214
TABLE C. 3 LIST OF HAND SAMPLES ANALYZED.....	220
TABLE C.4 RESULTS FROM PERMEAMETER TESTS WITH A 16.0 M <sup>3</sup> SAMPLE.....	226
TABLE C. 5 RESULTS FROM CONSTANT HEAD PERMEAMETER TESTS CONDUCTED ON WASTE ROCK HAND SAMPLES IN THE LABORATORY.....	238
TABLE C. 6 RESULTS FROM SINGLE RING INFILTROMETER TESTS CONDUCTED AT THE TOP OF THE TYPE 3 TEST PILE.....	241
TABLE C. 7 WATER RETENTION CURVE FITTING PARAMETERS.....	256
TABLE C. 8 VALUES USED IN THE GREEN-AMPT APPROACH TAKEN IN CALIBRATION OF THE K( $\phi$ ) FUNCTION USED AT THE UPPER COLLECTION LYSIMETERS.....	263
TABLE C. 9 VALUES USED IN THE GREEN-AMPT APPROACH TAKEN IN CALIBRATION OF THE K( $\phi$ ) FUNCTION USED AT THE TYPE 3 TEST PILE.....	268
TABLE E.1 A SUMMARY OF HISTORIC PRECIPITATION AND MONTHLY DATA DURING 2006 AND '07. ...	340
TABLE E.2 SUMMARY OF APPLIED RAINFALL EVENTS CONDUCTED AT THE TEST PILES AND COLLECTION LYSIMETERS IN 2006 AND 2007.....	341

## LIST OF FIGURES

FIGURE 1. 1 TWO OPEN-PIT MINES AND THE MAIN WASTE ROCK PILE AT DIAVIK .....	8
FIGURE 2.1 LOCATION AND OVERVIEW OF THE STUDY AREA.....	26
FIGURE 2. 2 A DRAWING OF THE TYPE 3 TEST PILE AND PHOTOGRAPHS OF THE CONSTRUCTION .....	27
FIGURE 2. 3 THE UPPER COLLECTION LYSIMETERS.....	28
FIGURE 2. 4 HYDRAULIC TESTING CONDUCTED ON A 16 M <sup>3</sup> WASTE ROCK SAMPLE. ....	29
FIGURE 3.1 GRAIN SIZE DISTRIBUTION .....	87
FIGURE 3.2 INFILTRATION CAPACITY AT THE TOP OF THE TYPE 3 TEST PILE. ....	88
FIGURE 3.3 THE VOLUME THAT DRAINED RAPIDLY FROM THE 16 M <sup>3</sup> SAMPLE. ....	88
FIGURE 3.4 WATER RETENTION CURVES, HYDRAULIC CONDUCTIVITY CURVES, AND THE PORTION OF MOISTURE REMAINING LIQUID AS THE MATRIX FREEZES OR THAWS. ....	89
FIGURE 3.5 RAINFALL IN 2006 AND 2007. ....	91
FIGURE 3.6 SNOW DISTRIBUTION AND ABLATION.....	90
FIGURE 3.7 EVAPORATION AND INFILTRATION.....	92
FIGURE 3.8 INFILTRATION AND WETTING FRONT PROPAGATION MEASURED BY TDR.....	93
FIGURE 3.9 TEMPERATURE WITHIN THE TEST PILES.....	94
FIGURE 3.10 VAPOR TRANSPORT .....	95
FIGURE 3.11 HYDRAULIC GRADIENT TOWARD A FROST SURFACE.....	95
FIGURE 3.12 INFILTRATION INTO FROZEN WASTE ROCK.....	96
FIGURE 3.13 WETTING FRONT PROPAGATION WITH THE THAW PROPAGATION.....	97
FIGURE 3.14 HYDROLOGIC AND THERMAL INTERACTION AT THE TYPE 3 TEST PILE BATTERS.....	98
FIGURE 3.15 CONCEPTUAL MODEL FOR THE PORTION OF THE TEST PILE THAT CONTRIBUTES TO OUTFLOW DURING THE INITIAL WET-UP PERIOD.....	99
FIGURE 3.16 PORE ICE MELTING OBSERVED IN TEST PILE OUTFLOW .....	100
FIGURE 3.17 SURFACE FREEZE AND THAW EFFECTS ON LYSIMETER OUTFLOW.....	101
FIGURE 3.18 NON-VERTICAL FLOW ON A LARGE-SCALE? A WATER BALANCE APPROACH.....	102
FIGURE 3.19 OUTFLOW FROM THE BASE OF THE TYPE 3 TEST PILE. ....	103
FIGURE 3.20 FLOW RESPONSE FROM A HIGH-INTENSITY APPLIED RAINFALL EVENT AT THE UPPER COLLECTION LYSIMETERS: OBSERVATIONS AND MODELING.....	104
FIGURE 3.21 MODELING FLOW IN THE UPPER COLLECTION LYSIMETERS. ....	105
FIGURE 3.22 FLOW RESPONSE FROM RAINFALL EVENTS AT THE TYPE 3 TEST PILE: TDR.....	106
FIGURE 3.23 TENSIO METER MEASUREMENTS AND AN ESTIMATION OF GROUNDWATER FLUX.....	107
FIGURE 3.24 MODELING THE HYDROLOGIC BEHAVIOUR IN THE TYPE 3 TEST PILE. ....	108
FIGURE 3.25 MODELING RESULTS: OUTFLOW AND EVAPORATION FROM THE TYPE 3 TEST PILE .....	109

FIGURE 3.26	SOLUTE MASS LOADING ESTIMATE AT THE UPPER COLLECTION LYSIMETERS. ....	110
FIGURE 3.27	SULFATE MASS LOADING ESTIMATED AT THE TYPE 3 TEST PILE.....	111
FIGURE A.1	AS-BUILT DRAWINGS OF THE TYPE 1 TEST PILE BASAL DRAIN AND BASAL LYSIMETERS. ..	145
FIGURE A.2	AS-BUILT DRAWINGS OF THE TYPE 3 TEST PILE BASAL DRAIN AND BASAL LYSIMETERS. ..	146
FIGURE A.3	TDR PROBES IN THE TYPE 1 TEST PILE. ....	147
FIGURE A.4	TDR PROBES AND STANDPIPE TENSIMETERS IN THE T3 PILE.....	148
FIGURE A.5	THERMISTORS IN THE T1 TEST PILE. ....	149
FIGURE A.7	CONSTRUCTION OF THE BASAL DRAIN OF A TEST PILE. ....	151
FIGURE A.8	INSTRUMENT HUTS BUILT TO MONITOR THE OUTFLOW OF THE TYPE 3 BASAL DRAIN. ....	152
FIGURE A.9	BASAL LYSIMETER PLUMBING AND INSULATION. ....	153
FIGURE A.10	BASAL LYSIMETERS: OVERVIEW AND CROSS SECTION. ....	154
FIGURE A.11	BASAL LYSIMETER CONSTRUCTION. ....	155
FIGURE A.12	THE T1 AND T3 INSTRUMENT BUILDING: HEAT TRACE THERMOSTATS AND FLOW-THROUGH MONITORING SYSTEMS. ....	156
FIGURE A.13	FILLING THE BASAL LYSIMETERS WITH WASTE ROCK.....	157
FIGURE A.14	END-DUMPING AND PUSH-DUMPING. ....	158
FIGURE A.15	TIP FACE INSTRUMENTATION.....	159
FIGURE A.16	COVERING THE INSTRUMENTS WITH WASTE ROCK BEFORE DUMPING AND EXCAVATING THE INSTRUMENT LEADS AFTER COMPLETION OF TEST PILE CONSTRUCTION. ....	160
FIGURE A.17	THE TOP SURFACES AND AN AERIAL VIEW OF THE TEST PILES.....	161
FIGURE A.18	THE TYPE 3 TEST PILE. ....	162
FIGURE A.19	AS-BUILT DRAWINGS OF THE UPPER COLLECTION LYSIMETERS.....	163
FIGURE A.20	CONSTRUCTION OF THE UPPER COLLECTION LYSIMETERS. ....	164
FIGURE A.21	THE UPPER COLLECTION LYSIMETERS FILLED WITH WASTE ROCK.....	165
FIGURE A.22	SHALLOW BOREHOLE NEAR THE UPPER COLLECTION LYSIMETERS FOR ECH <sub>2</sub> O PROBES AND TENSIMETERS. ....	166
FIGURE A.23	TENSIMETERS AND ECH <sub>2</sub> O PROBES AT THE UPPER COLLECTION LYSIMETERS. ....	166
FIGURE B. 1	CUSTOM-BUILT TDR PROBES. ....	174
FIGURE B. 2	SOIL CALIBRATION OF A TDR PROBE. ....	174
FIGURE B.3	THE SOIL CALIBRATION CURVE FOR TDR PROBES IN DIAVIK WASTE ROCK.....	175
FIGURE B.4	ECH <sub>2</sub> O-TE PROBES. ....	178
FIGURE B.5	SOIL CALIBRATION OF ECH <sub>2</sub> O PROBES. ....	179

FIGURE B.6	THE SOIL CALIBRATION CURVE FOR ECH <sub>2</sub> O PROBES IN DIAVIK WASTE ROCK.....	179
FIGURE B.7	WIRING DIAGRAM FOR A TENSIO METER PRESSURE TRANSDUCER. ....	182
FIGURE B.8	PROCEDURE FOR MEASURING MATRIC SUCTION IN A SOIL WATER SAMPLER.....	184
FIGURE B.9	CUSTOM-BUILT ELECTRICAL CONDUCTIVITY PROBE INSIDE A FLOW-THROUGH CELL. ....	190
FIGURE B.10	WIRING DIAGRAM FOR THERMISTOR MEASUREMENT. ....	191
FIGURE B.11	DRAINAGE MONITORING SYSTEM AT ONE OF THE UPPER COLLECTION LYSIMETERS.....	196
FIGURE B.12	DRAINAGE MONITORING SYSTEM FOR THE TYPE 3 TEST PILE BASAL LYSIMETERS. ....	197
FIGURE B.13	THE TYPE 3 TEST PILE NORTH BASAL DRAIN.....	198
FIGURE B.14	CALIBRATION CURVE FOR THE LOW FLOW TIPPING BUCKET GAUGES. ....	202
FIGURE B.15	DESIGN FOR THE HIGH FLOW TIPPING BUCKET FLOW GAUGES. ....	203
FIGURE B.16	CALIBRATION OF THE HIGH FLOW TIPPING BUCKET FLOW GAUGES. ....	204
FIGURE B.17	CALIBRATION CURVE FOR THE PADDLEWHEEL FLOW GAUGES. ....	205
FIGURE B.18	A RAIN GAUGE AT THE TOP OF ONE OF THE TEST PILES.....	206
FIGURE C. 1	BOULDER FRACTION OF 100 M <sup>3</sup> SAMPLES OF WASTE ROCK.....	209
FIGURE C. 2	WASTE ROCK HAND SAMPLES .....	215
FIGURE C. 3	LOCATION OF THE SAMPLING REGIONS .....	215
FIGURE C. 4	GRAIN SIZE DISTRIBUTION SUMMARY CURVE S .....	216
FIGURE C. 5	GRAIN SIZE DISTRIBUTION OF THE FRACTION FINER THAN 5MM.....	217
FIGURE C. 6	GRAIN SIZE DISTRIBUTION OF T3 HAND SAMPLES .....	218
FIGURE C. 7	GRAIN SIZE DISTRIBUTION OF T1 HAND SAMPLES .....	219
FIGURE C. 8	A 16.0 M <sup>3</sup> PERMEAMETER USED TO ESTIMATE REV-SCALE HYDRAULIC PARAMETERS.....	231
FIGURE C. 9	CONSTRUCTION OF THE 16.0 M <sup>3</sup> PERMEAMETER.....	232
FIGURE C. 10	POROSITY AND SATURATED HYDRAULIC CONDUCTIVITY MEASUREMENTS OF A 16M <sup>3</sup> WASTE ROCK SAMPLE.....	233
FIGURE C. 11	A DRAIN-DOWN TEST CONDUCTED WITH THE 16 M <sup>3</sup> SAMPLE.....	234
FIGURE C. 12	A DRAIN-DOWN TEST CONDUCTED WITH THE 16 M <sup>3</sup> SAMPLE (2).....	235
FIGURE C. 13	LABORATORY CONSTANT HEAD PERMEAMETER TESTS .....	237
FIGURE C. 14	INFILTRATION CAPACITY AT THE TYPE 3 TEST PILE.....	242
FIGURE C. 15	RING INFILTROMETRY TESTS.....	243
FIGURE C. 16	RING INFILTROMETRY PROCEDURE.....	245
FIGURE C. 17	TEMPE CELL TESTS.....	257
FIGURE C. 18	TEMPE CELL TESTS.(2) .....	258
FIGURE C. 19	WATER RETENTION CURVES .....	259
FIGURE C. 20	WASTE ROCK MATRIX HYDRAULIC CONDUCTIVITY (K <sub>φ</sub> ) CURVES.....	260
FIGURE C. 21	GROUNDWATER FLUX SENSITIVITY TO A RANGE IN K <sub>φ</sub> .....	261

FIGURE C. 22 TENSIO METER DATA FROM THE UPPER COLLECTION LYSIMETERS .....	262
FIGURE C. 23 FIELD CALIBRATION OF THE HYDRAULIC CONDUCTIVITY FUNCTION FOR THE UPPER COLLECTION LYSIMETERS AND THE IMPROVED GROUNDWATER FLUX ESTIMATE .....	264
FIGURE C. 24 MODELING VERIFICATION OF THE METHOD USED FOR FIELD CALIBRATION OF $K_{\phi}$ .....	265
FIGURE C. 25 PONDING AT THE TYPE 3 TEST PILE .....	266
FIGURE C. 26 TENSIO METER DATA FROM THE TYPE 3 TEST PILE .....	267
FIGURE C. 27 FIELD CALIBRATION OF THE HYDRAULIC CONDUCTIVITY FUNCTION FOR THE TYPE 3 TEST PILE AND AN ESTIMATE OF GROUNDWATER FLUX AND CUMULATIVE INFILTRATION .....	269
FIGURE D.1 A MAP OF THE STUDY SITE.....	270
FIGURE D.2 WIRING DIAGRAM FOR THE 3BA DATA LOGGER STATION.. .....	271
FIGURE D.3 PHOTOGRAPHS OF THE 3BA DATA LOGGER STATION. ....	272
FIGURE D.4 WIRING DIAGRAMS FOR THE T3 BASAL DRAIN. ....	273
FIGURE D.5 PHOTOGRAPHS OF THE 3DA DATA LOGGER STATIONS. ....	274
FIGURE D.6 WIRING DIAGRAM FOR THE 1TA DATA LOGGER STATION.....	275
FIGURE D.7 PHOTOGRAPHS OF THE 3TA DATA LOGGER STATION. ....	276
FIGURE D.8 WIRING DIAGRAM FOR THE 3TA DATA LOGGER STATION.....	277
FIGURE D.9 WIRING DIAGRAM FOR THE ULA DATA LOGGER STATION. ....	278
FIGURE D.10 PHOTOGRAPH OF THE ULA DATA LOGGER STATION. ....	279
FIGURE E.1 METEOROLOGICAL STATIONS AT DIAVIK. ....	339
FIGURE E.2 RAINFALL MEASURED AT DIAVIK. ....	342
FIGURE E.3 HISTOGRAM COMPARISON OF RAINFALL MEASURED AT GAUGES AT DIAVIK. ....	343
FIGURE E.4 RELATIONSHIPS BETWEEN RAINFALL MEASURED AT GAUGES AT DIAVIK.....	344
FIGURE E.5 AN APPLIED RAINFALL EVENT. ....	347
FIGURE E.6 RAIN AND SNOWFALL DURING THE INITIAL 1.5YR OF THE EXPERIMENT. ....	348
FIGURE E.7 DISTRIBUTION OF SNOW ON THE TEST PILES.....	349
FIGURE E.8 SNOWPACK CHANGES AT THE TYPE 3 TEST PILE DUE TO SUBLIMATION.....	345
FIGURE E.9 EVAPORATION RATE AND CUMULATIVE EVAPORATION. ....	350
FIGURE E.10 VAPOR TRANSPORT FROM VENTS AND EVIDENCE FOR ZONATION OF HEAT TRANSFER.. .	351
FIGURE E.11 MOISTURE CONTENT MEASURED BY TDR IN THE TYPE 3 TEST PILE: 2006-2007.....	352
FIGURE E.12 MOISTURE CONTENT MEASURED BY TDR IN THE TYPE 3 TEST PILE: 2007.....	353
FIGURE E.13 TENSION HEAD AT TENSIO METER PROFILES IN THE TYPE 3 TEST PILE.....	354
FIGURE E.14 TENSION HEAD AT SUCTION SAMPLERS IN THE TYPE 3 TEST PILE.....	355
FIGURE E.15 THE OUTFLOW RATE AT THE T3 BASAL DRAIN IN 2006.. ..	356

FIGURE E.16	RESOLUTION OF THE OUTFLOW RATE MEASURED AT THE T3 BASAL DRAIN.....	357
FIGURE E.17	THE SUM OF THE OUTFLOW RATE AT THE T3 NORTH AND SOUTH BASAL DRAIN. ....	358
FIGURE E.18	CUMULATIVE OUTFLOW OF THE NORTH AND SOUTH BASAL DRAIN. ....	359
FIGURE E.19	THE PH OF THE OUTFLOW AT THE T3 SOUTH BASAL DRAIN. ....	360
FIGURE E.20	MOISTURE CONTENT MEASURED BY TDR IN THE TYPE 1 TEST PILE. ....	361
FIGURE E.21	OUTFLOW AT THE TYPE 1 BASAL DRAIN.....	362
FIGURE E.22	MOISTURE CONTENT MEASURED BY ECH <sub>2</sub> O PROBES BETWEEN THE TYPE 3 UPPER COLLECTION LYSIMETERS.....	363
FIGURE E.23	TENSION HEAD MEASURED AT A TENSIO METER PROFILE BETWEEN THE TYPE 3 UPPER COLLECTION LYSIMETERS.....	364
FIGURE E.24	TEMPERATURE MEASURED BY ECH <sub>2</sub> O PROBES BETWEEN THE TYPE 3 UPPER COLLECTION LYSIMETERS. ....	365
FIGURE E.25	OUTFLOW AT THE WEST TYPE 3 UPPER COLLECTION LYSIMETER. ....	366
FIGURE E.26	OUTFLOW AT THE EAST TYPE 3 UPPER COLLECTION LYSIMETER. ....	367

## LIST OF ABBREVIATIONS

$\alpha$	a water retention curve fitting parameter of the van Genuchten-Mualem model that is inversely related to the air entry pressure and typically has units $\text{kPa}^{-1}$ or $\text{m}^{-1}$
ARD	acid rock drainage
DDMI	Diavik Diamond Mines, Incorporated; a subsidiary of Rio Tinto, plc
EC	electrical conductivity; units typically $\mu\text{S}/\text{cm}$ or $\text{mS}/\text{cm} = \text{dS}/\text{m}$
$\phi$	matric potential, the suction component of the unsaturated hydraulic potential; units typically $\text{kPa}$ (positive) or $\text{m}$ of head (negative)
HDPE	high-density polyethylene, a common plastic
$K_{\text{sat}}$	saturated hydraulic conductivity
$n$	a water retention curve fitting parameter of the van Genuchten-Mualem model that is directly related to the slope of the curve; it is unitless
NAG	non-acid generating
PAG	potentially acid generating
PVC	polyvinyl chloride, a common plastic pipe material
REV	representative elemental volume, the scale at which pore-scale properties may be replaced by parameters applied equally at any point within an approximate volume
SC	specific conductance is electrical conductivity at $25^{\circ}\text{C}$
SD	standard deviation
T1	the Type 1 test pile, or Type 1 waste rock
T3	the Type 3 test pile, or Type 3 waste rock
$\theta$ or VMC	volumetric moisture content; $\text{m}^3$ water/ $\text{m}^3$ bulk volume (unitless)
WRC	water retention curve, also known as the soil water characteristic curve

## **ACKNOWLEDGEMENTS**

I would like to thank Leslie Smith for decisive, thorough, and expert research supervision amidst the good humour.

I would also like to thank Dave Blowes and Dave Sego for their support and leadership.

I am grateful to those who have helped with technical instruction and patient support during the instrumentation, construction, and analysis of this experiment:

Craig Nichol, Joe Marcoline, Judy Andrina, Cindy Starzyk

Lianna Smith, Mike Gupton, Mike Moncur, Blair Gibson, Brenda Bailey, Ashley Stanton, Rich Amos, Corina MacDonald, Adam McRae, Andrea Mosher, Hector Ruiz, Scott Cousins, Jordan, Kevin, Dave Barci, Brian Greenwood, Olalekan Magbade, Mandy Moore, Richard So, David Jones, Juan Carlos Corazao, Danny Bay, the Diavik Environment Dept., Geology Dept., Geotechnical Engineering Dept., Mining Operations, and Site Services.

This research was part of the Diavik Mine Waste Rock Project, a research project with participation and funding from the University of British Columbia, the University of Waterloo, the University of Alberta, Diavik Diamond Mines, Inc., the International Network for Acid Prevention (INAP), the Mine Environment Neutral Drainage Program (MEND), and the Natural Sciences and Engineering Research Council of Canada (NSERC).

Smiling is very important.

*Thich Nhat Hanh*

## **CHAPTER 1 INTRODUCTION**

The magnitude and timing of metal loading to the environment from mine waste rock piles depends upon the flow of water through this heterogeneous unsaturated material. Flow in waste rock may be dominated by permeability and gradients in fluid potential or by gravity-driven macropore or film flow. Each type of flow may follow pathways that are vertical at a large scale or may follow pathways within structures in the waste rock created by gradation of the material during its deposition. Rapid gravity-driven flow occurs in coarse-grained material only under certain conditions. In cold climates flow is dependent upon changes in temperature about the water-ice phase boundary, and is complicated by contrasts in permeability as a function of both moisture content and ice content. Few locations have provided comprehensive data sets characterizing hydrogeology in mine waste rock, despite the complex behaviour and significant environmental risk (Blowes *et al.*, 2003). No comprehensive studies have been carried out to characterize the hydrogeological behaviour in waste rock deposited onto permafrost. This thesis presents results from experiments constructed at multiple scales to examine flow through unsaturated mine waste rock deposited onto permafrost.

### **1.1 Background: the hydrogeology of mine waste rock**

Overburden and mineralized rock with sub-economic grades is blasted, hauled, and dumped to form piles of unconsolidated material (Figure 1.1) with particles and clasts ranging in size from clay to boulders. Waste rock piles are constructed by repeatedly dumping material down slopes that form at the angle of repose, a process which is often done in a series of lifts. Matrix material, which consists of particles finer than about

1 cm, fills in some of the pore space between cobbles and boulders. Both the matrix and larger void spaces create pathways for fluid flow around the cobbles and boulders. Regions of connected large pore spaces, called macropores, may be randomly orientated, isolated, or continuous in an orientation parallel to deposition (Stockwell *et al.*, 2006).

Challenges in characterizing flow through waste rock lie primarily in determining hydraulic parameters of the extremely heterogeneous media, accounting for preferential flow, and then specifying preferential flowpaths in a site-specific context. Hydraulic properties of the matrix may be measured with standard methods, but much uncertainty exists in the application of the parameters to large-scale waste rock piles. Flow through soil-like waste rock piles dominated by matrix material may be reasonably characterized by the Richards equation, but flow through piles with significant cobble and boulder fractions is typically complicated by preferential flow through macropores (Smith *et al.*, 1995; Smith and Beckie, 2003). In a relatively dry climate, the majority of the water travels at low rates through the matrix, because the matrix has the highest hydraulic conductivity at low flux rates (Nichol *et al.*, 2005). The matrix is also where weathering is greatest due to the high surface area of the fine-grained material (Stockwell *et al.*, 2006). At high flux rates, a significant proportion of the water may flow rapidly through preferential pathways in coarse material, resulting in low rock-water contact times, less interaction with fine-grained material, and drainage with lower solute concentrations (Tran *et al.*, 2003; Wagner, 2004). Long-term solute mass loading is therefore dominated by the contribution from matrix flow, but peak mass loading may occur during outflow maxima (Earman, 2004; Wagner *et al.*, 2006).

Mines are required to take precautions to prevent excessive mass loading across all time scales so that mine discharge at its compliance point meets the regulatory standard (Mackenzie Valley Land and Water Board, 2002). Mass loading is calculated as the concentration of a chemical species multiplied by the flow rate. A typical average flow velocity through matrix material is on the order of 1 m/yr to 5 m/yr (Ritchie, 1994; Nichol *et al.*, 2005; Marcoline, 2008). Rapid increases in the rate of drainage from waste rock piles pose a particular risk to exceedance of mass loading standards on a short-term basis. A previous study found that, for waste rock with matrix moisture content above field capacity, about 5% of the net infiltration may flow through preferential pathways at velocities up to several meters per day (Nichol *et al.*, 2005).

In Nichol's study, macropores activated as fluid pathways when matrix moisture content and infiltration rate were high. The activation of macropores as fluid pathways occurs as the hydraulic conductivity of coarse-grained material becomes greater than that of the matrix material: a transition that results from introduction of moisture to the coarse-grained material at infiltration or flux rates higher than the saturated hydraulic conductivity of the matrix material. Different pathways activate under particular moisture contents and infiltration rates, and may evolve over time. High spatial variability in flow response is typical of macropore flow, while lower spatial variability and a greater proportion of porewater displacement are typical of wetting fronts traveling through the matrix. A wetting front is a wave of high moisture content that propagates downward through the unsaturated zone in response to infiltration. It may consist of particles of water traveling at the speed of the wave, as is the case with macropore flow, but wetting fronts more often consist of porewater displaced by a propagating pressure

wave initiated by the application of the infiltrating water. Considerable difficulty exists in distinguishing between bypassing flow and displaced flow, but this distinction is critical in understanding the relation with dissolved loads. Due to these uncertainties, a need persists to better understand flow in large piles of unsaturated waste rock (Blowes *et al.*, 2003).

## **1.2 Permafrost conditions**

In regions of permafrost, water flow and the potential for acid rock drainage (ARD) occur during summer months in the active layer. The active layer is the near-surface ground layer that thaws in the summer. In regions of continuous permafrost the depth of the active layer ranges from 0.1 m to 5 m in natural ground. Due to a large fraction of air-filled porosity, the active layer is expected to extend deeper in waste rock than in surrounding soils. Infiltration rates calculated during the summer season must be multiplied by the proportion of days the ground was thawed during the year to extend the rates to a longer time period.

ARD has been observed in various locations in the Arctic: in natural settings and at mine tailings and waste rock piles in the presence of metal sulfide deposits (Kelly and Taylor, 1996; Dawson and Morin, 1997; Kyhn and Elberling, 2001; Meldrum *et al.*, 2001). Sulfide oxidation may continue in the winter and 10 to 20% of pore water with high dissolved solids (10 to 25 g/L sulfate) may remain liquid at temperatures to about -5 °C (Elberling, 2001). In northern Canada, seepage from the toe of large waste rock piles with low sulfur content at the EKATI Diamond Mine typically has an acidic pH similar to natural tundra drainage (pH 5 to 6) but with sulfate and metal concentrations elevated

above natural conditions (Morin, 2003; SRK, 2007). Seepage and collection ponds near the toe of the main waste rock pile at the Diavik Diamond Mine (Diavik), have pH and specific conductance similar to that of runoff from tundra (author's review of data collected by Diavik, 2000 to 2007), and the source of these acidic conditions has yet to be declared.

Current mine closure strategies in regions of permafrost typically seek to deposit waste rock or tailings so that permafrost develops within those materials potentially capable of generating ARD. Strategies include segregation of potentially acid generating (PAG) rock and covering the PAG rock with less permeable material and non-acid generating (NAG) rock so that the extent of the summer thaw (the active layer depth) will be limited to the NAG rock only (Diavik Diamond Mines, Inc., 2005; DDMI, 2006). However, segregation may promote heat production by sulfide oxidation in concentrated zones of PAG rock (see Appendix C in SRK, 2007), whereas the mixing of PAG and NAG rock may better promote permafrost development. The permafrost active layer depth in large waste rock piles at EKATI with compositional and environmental conditions similar to the research field site was typically 3 to 5 m several years after deposition, but was as deep as 11 m where concentrated PAG rock existed (SRK, 2003; SRK, 2007).

Permafrost conditions are changing throughout the Arctic due to current trends in climate change. Active layer depths are expected to increase by as much as 100% by the year 2100 throughout the Arctic (Lawrence and Slater, 2005; Walvoord and Striegl, 2007). Permafrost thickness near the study site increases from the shore of Lac de Gras, where permafrost is absent, to a thickness of at least 150 m (DDMI, 2006). The study

site is about 1 km from the shore of Lac de Gras on East Island, but it has not been studied in detail whether permafrost under the waste rock piles is thick enough to remain frozen by 2100.

### **1.3 Research objectives**

This research is intended to advance the understanding of unsaturated flow through uncovered mine waste rock deposited onto permafrost using instrumented field experiments carried out at multiple scales. The development of conceptual models for flow through highly heterogeneous coarse porous media is extended from previous results of field experiments in a subarctic zone (*i.e.* Nichol *et al.*, 2005; Stockwell *et al.*, 2006; and Marcoline, 2008) and modeling studies (*i.e.* Fala *et al.*, 2003) to a field experiment in a region of continuous permafrost. Another goal is to improve estimates of mass loading from waste rock piles at a large-scale. The principal method for improving understanding of large-scale processes in waste rock involves the monitoring of instrumented test piles. Contemporary test pile studies are being carried out in humid climates in Peru (Corazao Gallegos, 2007) and Indonesia (Andrina *et al.*, 2006). The analysis presented here focuses on the water accumulation phase of the early portion of the life of the test piles, rather than the phases of hydrogeological dynamic equilibrium and thermal equilibrium that will follow. Advances in the quantification of this complex flow system focus on waste rock characterization at multiple scales, and on the collection of a detailed data set to potentially improve predictive modeling. The primary objective in this study is to develop a conceptual model for water flow in unsaturated waste rock

piles deposited onto permafrost. This task is divided into the following research objectives:

1. Characterize the particle size, porosity, and hydraulic properties of coarse waste rock on a range of spatial scales.
2. Investigate the interaction between unsaturated flow and thermal conditions near the freezing point.
3. Determine whether a significant amount of infiltration may flow along bedding structures.
4. Determine the conditions of rainfall intensity, permeability, and waste rock characteristics that lead to rapid preferential flow.



*DDMI*

**Figure 1.1** Two open-pit mines and the main waste rock pile in August 2008, at the Diavik Diamond Mine, Lac de Gras, Northwest Territories, Canada.

## **CHAPTER 2    METHODS**

### **2.1 Study site: The Diavik Diamond Mine**

The experimental methods explained here in the main text are a summary of the details included in the appendices. Unsaturated flow in waste rock was investigated with constructed experiments at the Diavik Diamond Mine located in the Northwest Territories of Canada (64°29' N, 110°18' W, el. 440 m). With a mean annual temperature of -12 °C and total precipitation of 373 mm, of which 148 mm comes as rainfall (Golder Associates, 1997), Diavik resides in a region of continuous permafrost with a semi-arid polar climate and a tundra environment. The permafrost in the area has an average temperature of -3°C. The topography in the region is relatively flat. As a result, the surface area of the top of large waste rock pile is greater than the area of the outer slopes of the pile, which are referred to as the batters.

### **2.2 Field experiment construction**

#### *2.2.1 Test pile construction*

A summary of the construction details in Appendix A is presented here. Two waste rock test piles were built 14 m-high with run-of-mine waste rock using haul truck end-dumping and bulldozer push-dumping methods, from June to August 2006. Diavik classifies and segregates waste rock by sulfur content into Type 1, Type 2, and Type 3 waste rock (Mackenzie Valley Land and Water Board, 2002; DDMI, 2005; DDMI, 2006). Diavik refers to waste rock as country rock. The Type 1 test pile consists of rock that is not likely to generate acid rock drainage (ARD), and has sulfur content less than 0.04 wt% S. The Type 3 test pile consists of rock classified as having the potential to

generate ARD, and has a higher proportion of biotite-schist and a sulfur content greater than 0.05 wt% S. The location and overview of the site is shown in Figure 2.1. Smith (in progress) describes the test pile construction and instrumentation and Gupton (in progress) describes flow in a test pile constructed with a cover composed of glacial till and non-acid generating rock (Type 1) in further detail.

Each test pile was built atop a 50 m by 60 m basal collection system of zero-tension pan lysimeters and a basal drain. The basal collection systems were built from June to September, 2005, and from May to June, 2006. The 50 m by 60 m basal drain consists of a perforated drainpipe on a sloped impermeable HDPE geomembrane that collects all of the discharge from the pile except the discharge collected by the basal lysimeters. A schematic drawing and photographs of the Type 3 test pile are shown in Figure 2.2. Six lysimeters, each with a 4 m by 4 m collection area, and four lysimeters, each with a 2 m by 2 m collection area are located near the base of the pile, beneath the flat top of each pile. Two lysimeters, each with a collection area of 2 m by 2 m, are located below one of the batters of each pile. These basal lysimeters were constructed with walls at least 60cm high to avoid flow bypass, following the guidance in O’Kane (2003), and were filled with waste rock by an excavator. The basal drain and the basal lysimeters introduce a condition of zero tension ( $h=0$ ) at each drain location, such that drainage to a flow-through monitoring system occurs when saturation is reached at the drain.

### 2.2.2 *Upper collection lysimeter construction*

Four upper collection lysimeters were constructed at the elevation of the top of the test piles, about 100 m from the test piles (Figure 2.3). The upper collection lysimeters were constructed from 1000 gal HDPE water tanks and were filled with waste rock by an

excavator. The walls of the lysimeters extend from the surface to a depth of between 1.4 m and 1.7 m. Two upper collection lysimeters were filled with Type 1 waste rock and have a collection diameter of 2.2 m and a zero-tension drain at a depth of 1.45 m. Two upper collection lysimeters were filled with Type 3 waste rock and have a collection diameter of 1.6 m and a zero-tension drain at a depth of 1.70 m.

## **2.3 Instrumentation**

A summary of the instrumentation details in Appendix B is presented here.

### *2.3.1 Outflow instrumentation*

Outflow from each of the basal lysimeters, basal drain, and upper collection lysimeters is directed through heat-traced conduit to a flow-through monitoring system. This system consists of a sampling cell, cells with continuously logging pH and electrical conductivity sensors, and a flow gauge. Lysimeter outflow is measured with tipping bucket rain gauges, and basal drain outflow is measured with larger tipping bucket gauges custom-built for the anticipated range in flow rate. Tipping bucket gauges were calibrated to relate the time between tips to flow rate. Paddlewheel flow gauges are also incorporated in the flow-through systems for the basal drains to measure any extreme outflow that may overwhelm the tipping bucket.

### *2.3.2 Instrumentation within the test piles*

Instrumentation was installed in the test piles to monitor wetting front advance, the propagation of frost and thaw fronts, and to characterize matrix water retention. The test piles were each constructed in five stages, or tip face advances. After each stage, time domain reflectometry (TDR) moisture content sensors, thermistors, and other

instrumentation were installed on the tip face advance of the pile. TDR sensors were located approximately above the basal lysimeters, and were placed on the tip face. All instrumentation was covered with waste rock, first by an excavator to a thickness of about 50 cm, and then by end-dumping as pile construction was resumed. After completion of construction, four tensiometers were installed in the Type 3 test pile at depths of 60 cm and 120 cm, and three ECH<sub>2</sub>O soil moisture probes (Decagon Devices, Inc.) and three tensiometers were installed adjacent to the upper collection lysimeters at depths of 30, 60, and 90 cm using a jack-hammer drill.

The moisture content of the matrix material is measured with time domain reflectometry by relating the impedance of a radio frequency pulse along a conductor in contact with the matrix material. Water has a dielectric permittivity twenty times higher than dry soil components, causing the pulse to travel measurably slower in moist soil. TDR sensors were built using a three-rod design with diodes in the probe head and probe end to enhance pulse reflection transitions (Zegelin *et al.*, 1989, Hook *et al.*, 1992). The central rod of each probe was coated with polyolefin following the design of Nichol *et al.* (2002) to minimize signal loss inaccuracies caused by highly conductive pore waters typical of mine waste. ECH<sub>2</sub>O capacitance sensors (Decagon Devices, Inc., [www.decagon.com](http://www.decagon.com)) measure the rate of change of charge in the soil between the cathode and anode of the sensor, which relates directly to dielectric permittivity and hence moisture content. Calibrations were conducted at various moisture contents with waste rock samples taken during test pile construction for both TDR and ECH<sub>2</sub>O sensors. Matric potential is measured during summer months with pressure transducers installed in tensiometers whose body was maintained water-filled with a jet valve. The water in

the tensiometers and the pressure transducers were removed for the winter with the onset of sub-zero air temperatures.

### 2.3.3 *Meteorological instrumentation*

Rainfall is measured at the top of each test pile and at the Diavik meteorological station, located 1 km from the research site. Measurements of solar (shortwave) radiation, air temperature, wind speed, and relative humidity are made at the Diavik station, at 2 m above a waste rock surface, an elevation within 10 m of the elevation of the test piles. Measurements from the Diavik station are used as the primary air temperature measurement, as a quality control for rainfall measurements made at the test piles, and in estimation of evaporation. Diavik also measures snowfall. Due to the high degree of wind redistribution, however, this measurement is used only as an indicator of how the snow depth observed at the test piles might compare to an average year.

Weather data are also available from the Ekati meteorological station at the EKATI Diamond Mine (64°42' N, 110°37' W, el. 470 m), which is located 30 km north of Diavik (Environment Canada, 2008). Weather data is available from 1959 at the Contwoyto (65°28' N, 110°22' W, el. 451 m) and Lupin (65°45' N, 111°15' W, el. 490 m) Environment Canada weather stations, which are located about 130 km north of Diavik in a similar environment.

### 2.3.4 *Applied rainfall*

Several applied rainfall events were conducted at the Type 3 test pile and upper collection lysimeters to investigate the response to high-intensity rainfall events and to allow the application of tracers. Applied rainfall events and tracer tests at the top of the Type 3 test pile are discussed in more detail by Gupton (in progress). The events were

conducted using a number of lawn sprinklers. A grid of cups was placed at the ground surface to gauge the applied rainfall. At the Type 3 test pile, three rainfall events were applied in each of 2006 and 2007, corresponding to recurrence intervals of five to thirty-five years. Recurrence intervals are based on rainfall statistics for the region, and specifically for Diavik, reported by Golder Associates (2008). The events in 2007 were applied during a time when natural rainfall was about half of the mean annual precipitation and the events amounted to 40% of mean annual precipitation.

At the Type 3 upper collection lysimeters three high-intensity rainfall events were applied to raise the moisture content in the lysimeters to field capacity before applying a rainfall event corresponding to an eight-year recurrence interval. The events at the Type 3 upper collection lysimeters increased the annual rainfall there to 115% of the annual mean rainfall, or less than half of the total for the rainiest year on record.

### *2.3.5 Problems with instrumentation*

Three significant failures occurred during construction and monitoring of the experiment. (1) Only 45% of the 38 TDR probes installed in the Type 1 and Type 3 test pile survived burial. Instrumentation was covered with waste rock by track-mounted excavator, prior to burial by end-dumping and push-dumping (Appendix A). This method of instrument installation favored the creation of measurement conditions representative of large waste rock piles and was chosen over a method relying more on manual labour due to practical and safety considerations.

(2) The drain pipes for the basal drain and several of the basal lysimeters in the Type 1 test pile became disconnected by the thermal displacement of insulating pipe around the drainpipes. The failures were not discovered until the end of the 2007 summer season,

but appeared to have occurred in late May 2007. It should be noted that during the time when the pipes were disconnected, no flow reported to any of the basal lysimeters that remained connected. However, it seems likely that flow in the basal drain was not recorded. Repairs were completed in May 2008.

(3) The custom-built tipping bucket gauges were incorporated into the monitoring systems Aug. 1, 2007, after paddlewheel flow gauges failed to measure flow rates at the low end of the range specified in the gauge manual (Appendix B). Manual flow measurements were made with a graduated cylinder and stopwatch from May to the end of July, 2007.

## **2.4 Hydrogeological characterization of the waste rock**

A summary of the details of characterizing the physical and hydrogeological properties of the waste rock, discussed in Appendix C, is presented here. Waste rock hydrogeological characterization was carried out in the laboratory and in the field on samples ranging in volume from 250 cm<sup>3</sup> to 100 m<sup>3</sup> so that measured flow behaviour may be related to material properties. A method for relating characterization at the matrix scale to characterization at the large-scale is presented at the end of this section.

### *2.4.1 Particle and clast size*

The boulder fraction of two 100 m<sup>3</sup> samples of Type 3 waste rock was estimated by separating boulders from the finer fraction with an excavator and weighing each fraction with the payload meter of a calibrated haul truck. A large-scale particle and clast size distribution was also determined from a 90 t (about 40 m<sup>3</sup>) sample of Type 1 waste rock. The sample was sieved by hand by following the procedure described in ASTM standard

method D 5519 (ASTM, 2001). These particle and clast size distributions are considered to be representative of the waste rock distribution on the scale of a representative elemental volume (REV). An REV is the scale at which small-scale properties may be replaced by parameters applied equally at any point within an approximate volume (Bear, 1972). To characterize the grain size distribution of the matrix material, nearly two hundred samples of material finer than 10 cm were collected during construction of the test piles and upper collection lysimeters and were sieved following the ASTM standard method D422 (ASTM 2002).

#### 2.4.2 *Porosity*

Several hydraulic parameters of the waste rock at the large-scale were estimated from a 16 m<sup>3</sup> sample of material finer-than 0.5 m placed in a tank by an excavator (Figure 2.4). This tank is referred to as the field permeameter. Porosity at the large-scale was estimated by direct measurement of the volume of water required to saturate the 16 m<sup>3</sup> sample from the bottom. The estimation of porosity at the large-scale accounted for the initial moisture content in the matrix material, based upon the average moisture content of fifteen hand samples collected during construction of the test piles (discussed in Section 2.4.6). At the matrix-scale, porosity was estimated gravimetrically by saturating samples with a spray bottle, packing each into a container to a bulk density of 1.6 to 1.8 g/cm<sup>3</sup>, and decanting excess water. This method was used for six samples of material finer-than 5 mm and for one sample of material finer-than 15 mm.

#### 2.4.3 *Infiltration capacity*

Rainfall at a rate that exceeds the infiltration capacity of the matrix material at the surface of the test pile creates small-scale runoff that activates macropores as rapid

flowpaths. Infiltration capacity was measured under thawed conditions using single ring infiltrometers, with a diameter of 90 cm, at seven locations at the top of the Type 3 test pile, following the technique described by Bellehumeur (2001) and Dingman (pp. 242-243, 2002). Large (90 cm diameter) single ring infiltrometers were used minimize the effect of lateral flow below the edge of the ring (Bellehumeur, 2001). The tests were conducted to achieve a constant infiltration rate, so that the infiltration capacity approximates the saturated hydraulic conductivity.

#### 2.4.4 *Saturated hydraulic conductivity*

Saturated hydraulic conductivity at the large-scale was estimated with a constant head test by pumping water upwards through the 16 m<sup>3</sup> sample. During the tests, head was measured at three manometers and outflow at the spillway. For the matrix, the saturated hydraulic conductivity of 18 samples, taken from various locations at each test pile and the upper collection lysimeters, was estimated with constant head permeameter tests. The tests followed the method described by Freeze and Cherry (1979). The matrix material was sieved to the finer-than 5 mm fraction to be consistent with the grain size of the samples used to determine water retention curves in Tempe cells.

A qualitative evaluation of the degree of interaction between rapid pathways and matrix material was inferred from dispersion at the leading front of a tracer test conducted during a drain-down test on the 16 m<sup>3</sup> sample. As the 16 m<sup>3</sup> sample was drained, the outflow rate and water level were measured continuously, and 39 samples were taken to investigate the transport of the rhodamine dye tracer.

#### 2.4.5 *Water retention curves*

Water retention curves (WRC's) were measured with five samples of matrix material placed in Tempe cells using the technique described by Fredlund and Rahardjo (1993). Only particles finer-than 5 mm were included in the Tempe cell tests, based on observations that little retention and capillary flow occurs within pore spaces in the waste rock fraction coarser than 5mm (Yazdani *et al.*, 2000; Tokunaga *et al.*, 2002). WRC's were also estimated in the field at a profile of co-located ECH<sub>2</sub>O soil moisture probes and tensiometers with pressure transducers, which are located between the upper collection lysimeters filled with Type 3 material. Water retention curve parameters were determined by fitting the van Genuchten (1980) and Mualem (1976) model to the results from the Tempe cell tests and the field instrumentation using the SoilVision software (Fredlund *et al.*, 1996).

#### 2.4.6 *Field capacity and initial moisture content*

Field capacity is defined as the moisture content at which gravity drainage ceases (Bear, 1972), and was suggested by Richards (1950, in Bear, 1972) to be the moisture content at a suction of 10 to 50 kPa. It may also be thought of as the moisture content at which any additional moisture will generate drainage. Field capacity of the matrix material was determined from moisture content measurement at the time when the hydraulic gradient was zero at an adjacent tensiometer profile after the passing of a wetting front. At a hydraulic gradient of zero after the passing of a wetting front, drainage ceases and the moisture content is equal to the field capacity.

At the large-scale, field capacity was estimated by lysimetry as the moisture required for drainage to initiate. This moisture requirement was the sum of the initial moisture

content and rainfall by natural and sprinkler application. The average initial moisture content of waste rock finer-than 40 mm, at the time the waste rock was delivered from the open pit to the test site, was determined gravimetrically from 15 hand samples. Large-scale initial moisture content was determined by multiplying the initial moisture content of the hand samples by the portion of the large-scale grain size distribution that was finer-than 40 mm.

#### 2.4.7 *Unsaturated hydraulic conductivity*

Hydraulic conductivity curves were estimated for the waste rock matrix material from the water retention curves using the relationship of Fredlund *et al.* (1994) with the SoilVision software. Field calibration of the hydraulic conductivity curve was conducted using a Green-Ampt analysis of infiltration events at the Type 3 test pile and the Type 3 upper collection lysimeters. The Green-Ampt model for infiltration was used to relate rainfall rate to infiltration rate, and Darcy's law was used to relate the infiltration rate to the unsaturated hydraulic conductivity. The method is described in more detail in Appendix C, Section 6.

In this approach, the assumption is made that the maximum possible hydraulic conductivity at a particular point as a wetting front passes ( $K_w(\phi)_M$ ) is equal to the rainfall rate. This assumption is based on an extension of the Green-Ampt model to time after the rainfall event and to depths greater than the near-surface. This assumption was subsequently confirmed to be reasonable by comparison of cumulative flux estimated using the resulting  $K(\phi)$  function and cumulative rainfall observed, and by a VS2D modeling exercise. The actual hydraulic conductivity at a particular point as a wetting front passes ( $K_w(\phi)$ ) must be equal to or less than  $K_w(\phi)_M$ . Using soil tension maxima

during infiltration, unsaturated hydraulic gradient maxima during infiltration, and the rainfall rate (assumed to be equal to  $K_w(\phi)_M$ ), points were plotted in  $K-\phi$  space by applying Darcy's Law for the unsaturated condition. If the above assumptions are true, the actual  $K(\phi)$  curve must fall below the  $K_w(\phi)_M$  points.

#### 2.4.8 *Porewater freezing and thawing*

Soil moisture held in retention by capillary forces may remain liquid at temperatures below the ambient freezing point. The portion of the matrix moisture content remaining liquid during freezing or thawing was related to the temperature below the freezing point by the mean water retention curve using the method of Black and Tice (1989) with the SoilVision software. The strength of the capillary forces determine the dynamics of freezing and thawing in porous media (Black and Tice, 1989). The method reasons that soil freezing occurs in a similar fashion as soil drying. Soil moisture held by a relatively low soil tension drains with the greatest ease as the soil tension increases. Similarly, soil moisture held by a relatively low soil tension will freeze with the greatest ease as the temperature decreases. The relationship between soil tension and freezing is dependent upon pore-scale processes involving particle surface charge and the dipole of water molecules. The method of Black and Tice (1989) utilizes a relationship between pressure in the liquid and solid phase of water and liquid moisture content, along with the dependence of both freezing and drying upon the pore size distribution, in deriving theoretically and empirically a power relationship between temperature and moisture content. The method does not account for the depression of the freezing point due to inclusion of solutes, and therefore underestimates unfrozen moisture content at any temperature below  $0^\circ\text{C}$  for soil moisture with high dissolved solids.

#### 2.4.9 Upscaling from the matrix-scale to the large-scale

Several methods were used to relate hydraulic properties of the waste rock matrix material to hydraulic properties of the large-scale waste rock:

1. Porosity at the matrix-scale and at the large-scale was estimated by direct measurements. A drain-down test is used to relate porosity at the matrix-scale to porosity at the large-scale. At the large-scale, the porosity is the sum of the volume of large pores, which are often entirely air-filled under unsaturated conditions, and the volume of the pores in the matrix. The volume of the matrix pores as a proportion of the large-scale porosity was estimated by measuring the volume of water that drained from the 16 m<sup>3</sup> sample, up to the time when the full depth of the sample had drained to unsaturated conditions. Assuming that large pores drained before any drainage occurred from the matrix pores, the volume of water remaining in the 16 m<sup>3</sup> sample at the onset of unsaturated conditions approximates the volume of the pores in the matrix. This estimate of matrix porosity is a somewhat larger proportion of the bulk waste rock volume at the large-scale than both the specific yield and the field capacity.

The matrix porosity as a proportion of the volume of the waste rock at the large-scale was also estimated by multiplying the porosity of the matrix material at the matrix-scale (*i.e.* 0.25) by the proportion of the waste rock at the large-scale that consists of matrix material (*i.e.* 20%), using the grain size distribution. In this method, the matrix material was considered to be the size fraction finer-than 5 to 20 mm.

2. Field capacity measured at the matrix-scale was related to the large-scale by a comparison of a lysimetry method to the evaluation of water retention curves for matrix material at measured tension values. Field capacity of the matrix as a portion of the

volume of the waste rock at the large-scale was also estimated by multiplying the field capacity of the matrix material by the proportion of the waste rock at the large-scale that consists of matrix material, using the grain size distribution.

3. Hydraulic conductivity at the matrix-scale was related to the large-scale by infiltration analysis (as described in Section 2.4.7).

These upscaling techniques are discussed in further detail in Chapter 3.

## **2.5 Modeling**

Two processes were modeled in this study: evaporation from a partially-saturated surface and flow through unsaturated porous media. Evaporation was modeled for two reasons: (1) to estimate evaporation beyond the time when it was measured directly by lysimetry to the full period of the study (from pile construction in 2006 to the end of 2007), and (2) to estimate net infiltration into the test piles and upper lysimeters. Flow through the upper lysimeters and the Type 3 test pile was modeled to gain an understanding of the conditions under which the flow system may be approximated with the groundwater flow equation for a homogenous unsaturated porous medium (the Richards equation).

### *2.5.1 Evaporation*

Evaporation was modeled separately from flow (described in Section 2.5.2) as 1D calculations using meteorological measurements made at the study site. In this study, evaporation modeling was not calibrated, due to insufficient lysimetry data, and the results were not coupled with the flow modeling. Evaporation (E) was estimated using

the FAO-56 Penman-Monteith formulation (Allen *et al.*, 1998) for reference evapotranspiration ( $ET_0$ ):

$$ET_0 = \frac{0.408\Delta(R_n - G) + \gamma \frac{37}{T_{hr} + 273} u_2 \left[ e^0(T_{hr}) - e^0(T_{hr}) \frac{RH_{hr}}{100} \right]}{\Delta + \gamma(1.0.34u_2)}, \quad (1)$$

and a soil moisture-dependent coefficient for bare soil ( $K_{bs}$ ) (modified from Allen *et al.* (1998) to limit evaporation during frozen conditions ( $K_f$ ):

$$E = K_f \cdot K_{bs} \cdot ET_0. \quad (2)$$

Evaporation from a partially-saturated surface occurs over two stages: an energy-balance-limiting stage and a moisture-transfer-limiting stage (Dingman, 2002; Smith and Beckie, 2003). The energy balance formulation in Equation (1) estimates the evaporation during the energy-balance-limiting stage, and may be considered approximately equal to the potential evaporation (PE).  $ET_0$  was calculated on an hourly basis using measurements made at the Diavik meteorological station. Equation (2) determines E on a daily basis by using  $K_f$  to either allow evaporation or limit evaporation based on the presence of frozen conditions, and by using  $K_{bs}$  to either allow E to equal  $ET_0$  or to limit E based on the time since the last rainfall and the magnitude of the previous rainfall.  $K_f$  was set to 1 for above-freezing surface conditions and set to 0 on days when the average of the daily mean and daily maximum temperature was below 0 °C.  $K_{bs}$  was determined to be a number between 0 and 1.25 as an estimate of soil moisture at the surface that was available for evaporation, using a type curve method that is described below.

Values for albedo of 0.48 and for the ratio of net heat flux to the ground to net radiation ( $G/R_n$ ) of 0.3 determined by Carey, *et al.* (2005) for a waste rock pile surface in northern Saskatchewan, Canada, were adopted in the calculation. The hourly reference

evapotranspiration estimates were summed to daily totals for application of the bare soil coefficient ( $K_{bs}$ ). The bare soil coefficient was determined with a minor modification to the method described in Allen, *et al.* (pp. 117-118, 1998) by evaluating type curves for the actual number of days after a rainfall, rather than for an average time between rainfall.

Type curves for  $K_{bs}$  were evaluated by classifying each day as having high, moderate, or low soil moisture supply for evaporation based upon the infiltration depth of the previous rainfall. Infiltration depth resulting from each rainfall (mm below the ground surface) was estimated to be 2.4 times greater than the rainfall (mm rain), based on Green-Ampt analysis of four rainfall events in 2007 that generated surface ponding. The reference evapotranspiration estimated for each day was classified as high, moderate, or low. These classifications yielded nine possible relationships from which the soil coefficient was evaluated, using days since last rainfall as the independent variable. In addition to these nine possible type curve solutions, on rainy days (days with rainfall greater than 0.1 mm)  $K_{bs}$  was set to a value between 0.25 and 0.75 based on the magnitude of the rainfall.

The approach based on the Penman-Monteith formulation is less comprehensive than the method of Wilson *et al.* (1994), which was utilized in a previous study by Marcoline (2008) to describe infiltration into waste rock. The method of Wilson *et al.* (1994) that is utilized by the SoilCover modeling software (SoilCover, 1997) calculates evaporative flux using both meteorological and soil moisture measurements. The Penman-Monteith method is considered suitable given the lack of detailed soil moisture measurements within the upper 30 cm of the waste rock at the Diavik test piles.

### 2.5.2 2D flow modeling using VS2D

Flow through the Type 3 test pile and the Type 3 upper collection lysimeters is modeled using the 2D finite difference code VS2D (Lapalla *et al.*, 1987). Boundary conditions of specified flux, in the form of either precipitation or evaporation, and seepage that transmits water from the domain only under certain calculated flow conditions, are applied in the VS2D models. Flow calculations with VS2D are based on finite difference solutions of the two-dimensional form of the Richards (1931) equation:

$$\frac{\partial}{\partial x} K(\theta) \left( \frac{\partial \phi(\theta)}{\partial x} \right) + \frac{\partial}{\partial z} K(\theta) \left( \frac{\partial \phi(\theta)}{\partial z} \right) + \frac{\partial K(\theta)}{\partial z} = \frac{\partial \theta}{\partial t} \quad (3)$$

The model is used to explore the potential for the application of a Richards equation approach for a simplified homogenous domain to the complex flow system found in mine waste rock. The dynamics of heat and fluid transport for systems near the water-ice phase equilibrium (*e.g.* Harlan 1974) are accounted for using a simplification that adjusts the value for the saturated hydraulic conductivity during the thawing period.

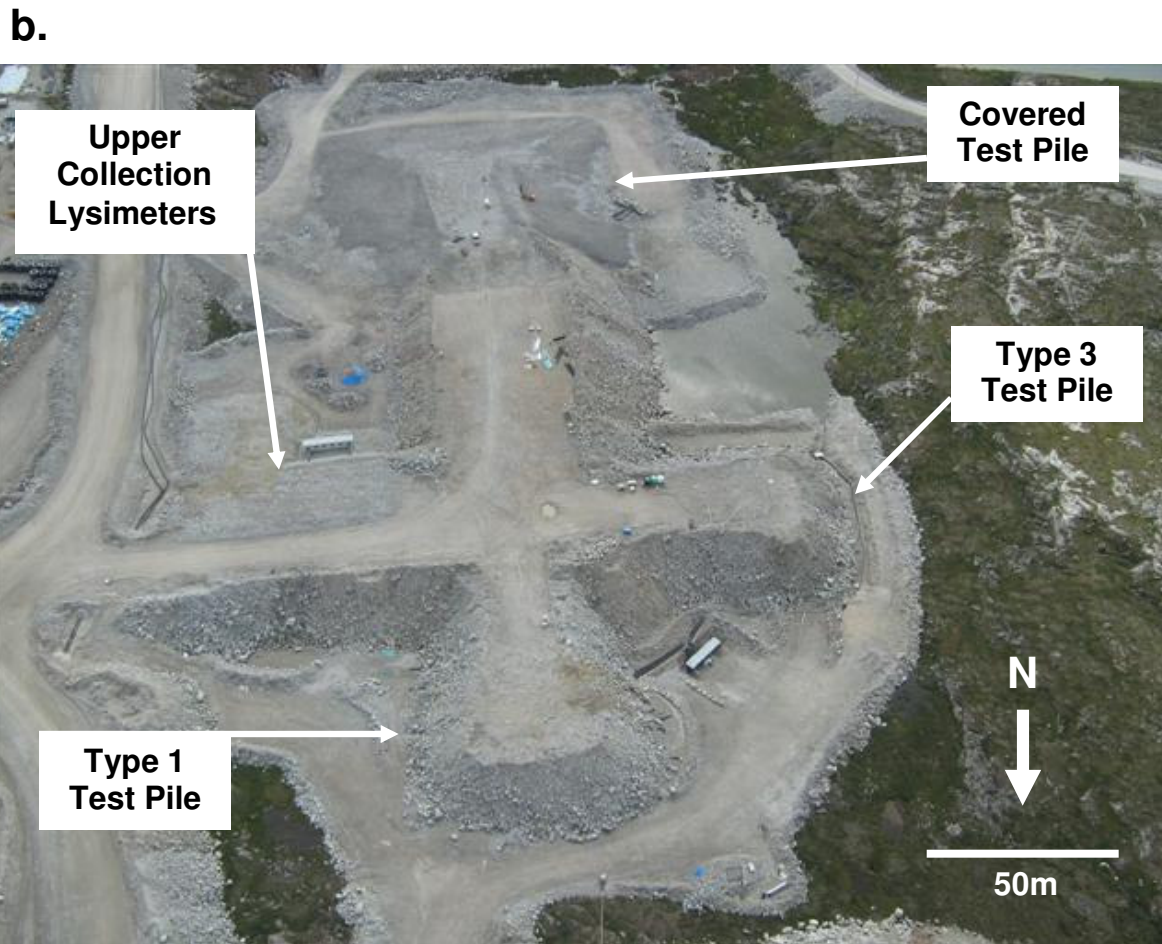
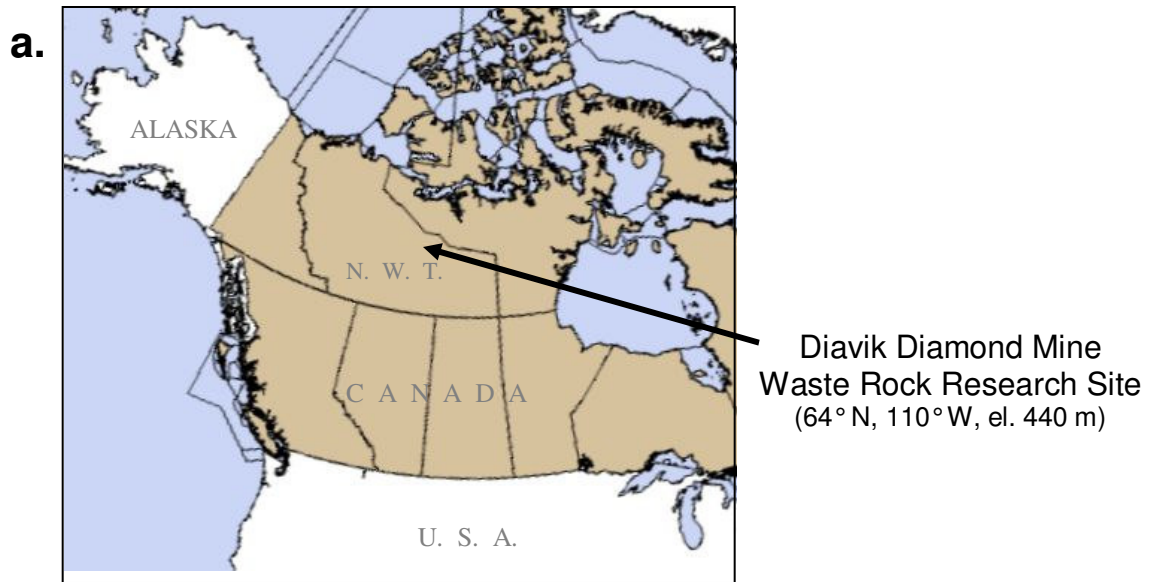
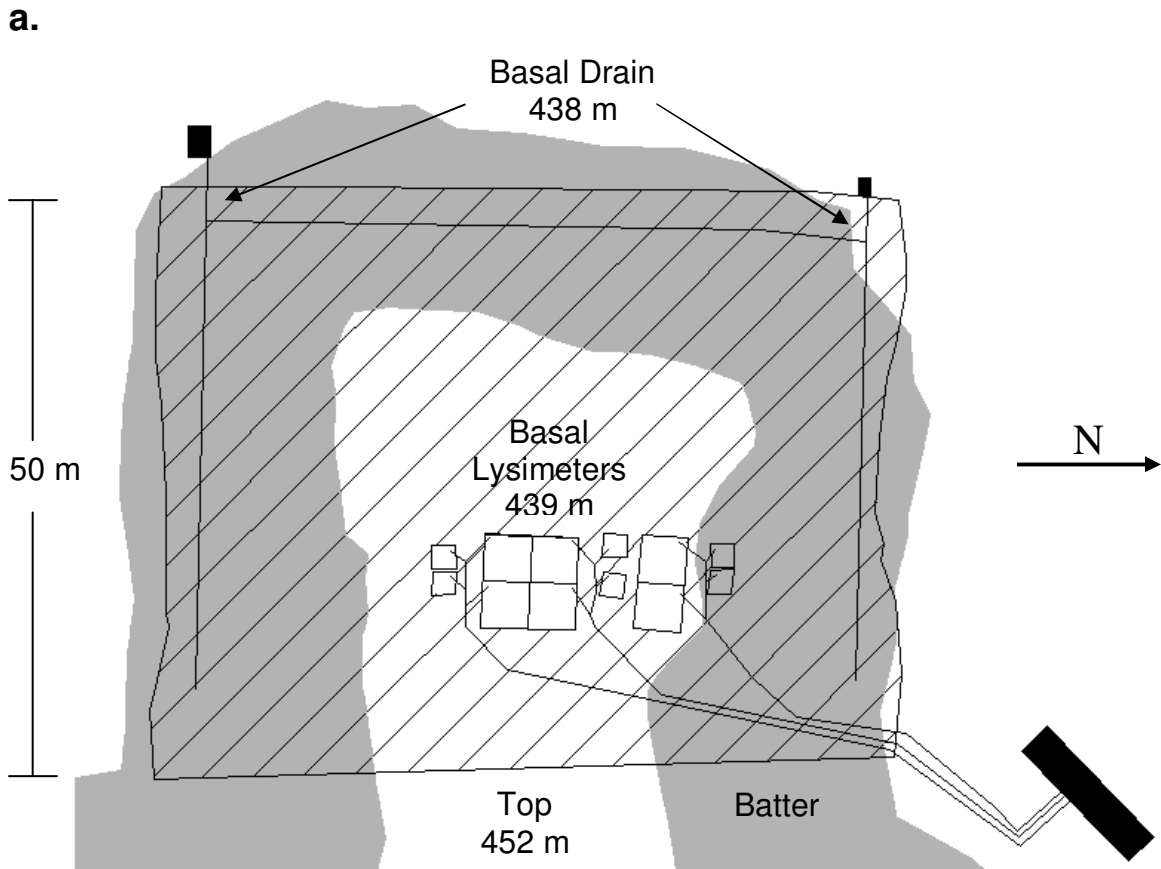


**Figure 2.1** (a) Location of the Diavik Diamond Mines and (b) an aerial photograph of the waste rock research area.



**b.**



**c.**



**Figure 2.2** (a) A transparent plan view of the Type 3 test pile and (b) photographs of the construction of the basal collection system and (c) covering of internal instruments.

a.



b.



**Figure 2.3** Upper collection lysimeters (a) during construction and (b) during an applied rainfall event. Moisture content sensors and tensiometers are between the lysimeters.

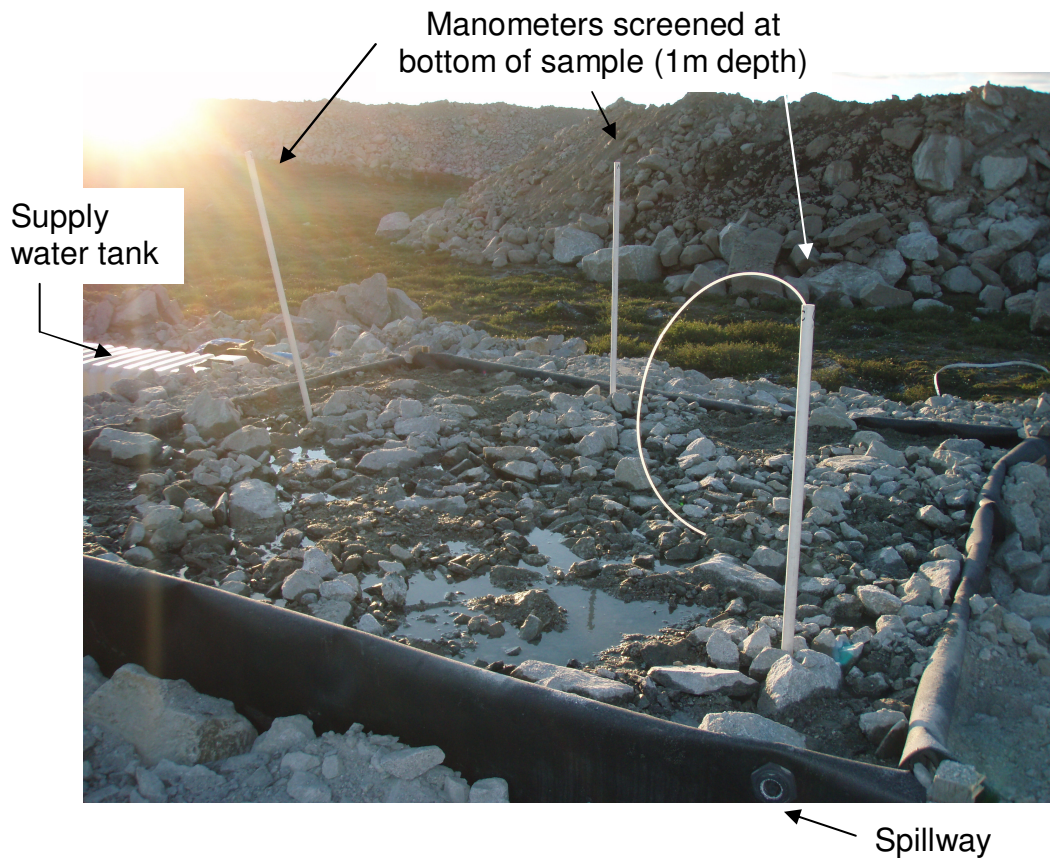


**Figure 2.4** A 16 m<sup>3</sup> waste rock sample inside the field permeameter. The sample was saturated from the bottom through a 10cm thick layer of clean gravel.

## CHAPTER 3 RESULTS

The field results presented in this thesis reflect the first 20 months of the waste rock project conducted at the Diavik Diamond Mine. This period of the data set begins with the completion of the construction of the uncovered test piles and upper collection lysimeters in August to September, 2006, and ends with the end of winter in March 2008. During this period, the test piles existed in a stage of water accumulation, evolving toward an expected state of dynamic equilibrium with respect to both the hydrologic and thermal regime. This thesis focuses on water flow through uncovered waste rock, while Gupton (in progress) focuses on tracer tests conducted at the Type 3 test pile and the hydrologic behaviour of a test pile with an engineered cover; Smith (in progress), Bailey (in progress), and Stanton (in progress) focus on geochemistry and microbiology; Moore (in progress) focuses on geochemical and microbiological characterization in the laboratory; Pham (in progress) and Klassen (in progress) focus on the thermal regime; and Amos (in progress) focuses on air composition and gas flow in the test piles.

### 3.1 Waste rock hydrogeological characterization

A summary of the details described in Appendix C is presented here.

#### 3.1.1 *Particle and clast size*

Tonalite, granite, pegmatite, and biotite-schist country rock around diamondiferous kimberlite intrusions (Roscoe and Postle, 2005) are mined from open pits and underground workings at Diavik and placed in coarse-grained waste rock piles. Half of a 90 t sample sieved from 90 cm to 2.5 mm was cobbles and boulders, and about half of the two 260 t samples taken during construction of the test piles were boulders (Figure 3.1a). The hand samples of Type 1 waste rock had a grain size distribution slightly coarser than

Type 3 waste rock (Figure 3.1b). Of the nearly 200 hand samples taken during construction of the test piles and the collection lysimeters, the particle size distribution was dominated by sand and gravel. The uniformity coefficient ( $C_U = D_{60}/D_{10}$ ) of the mean hand sample was 50. This value is 25% of the uniformity coefficient of the 90 t sample. Samples taken from the top surface of the test piles had a mean grain size distribution finer than about 70% of the 200 samples. The <5 mm fraction accounted for 18% of the waste rock and consisted of, on average, 92% sand and 8% silt and clay.

### 3.1.2 Porosity

Results from hydraulic testing of a 16 m<sup>3</sup> waste rock sample (Figure 2.4) are summarized in Table 3.1. Practical considerations in the construction of the field permeameter limited the sample size to about one fifth of the representative elemental volume (REV) for waste rock. An approximate volume of 80 m<sup>3</sup> for the REV of the waste rock at Diavik was estimated by calculating the volume at which the addition or removal of the largest clast would make no significant change to hydraulic properties of that volume (see Appendix C for more details). The measured large-scale porosity of 0.25 is lower than a suggested typical value (Ritchie 1994) but similar to other measured values (e.g. Martin *et al.*, 2005). Waste rock with a high proportion of boulders is likely to have lower porosity than a more soil-like waste rock, assuming each boulder has essentially no porosity.

A summary of the hydraulic properties of the waste rock matrix material is also presented in Table 3.1. Porosity of six samples of matrix material finer-than 5 mm and one sample finer-than 15 mm was 0.25 +/- 0.02.

### 3.1.3 *Infiltration capacity*

#### 3.1.3.a Surface ponding

Rainfall at a rate in excess of the infiltration capacity creates surface ponding. Under thawed conditions, ponding at the top of the Type 3 test pile was observed after rainfall rates of 7 mm/h or greater. Surface ponding was not observed at the upper collection lysimeters, indicating that the infiltration capacity of the surface was greater than 12 mm/h (the highest rainfall rate applied). Surface runoff was never observed on the test piles. Ponding generated small-scale runoff from low infiltration areas that infiltrated at adjacent high infiltration areas. During the initial days of thawing of the test piles, ponding was observed in regions where the surface was dominated by silt and sand, but some ponding was also observed where the surface was dominated by cobbles and boulders. Partially-frozen conditions are considered in more detail in Section 3.5.

#### 3.1.3.b Ring infiltrometer tests

Infiltration capacity at steady-state infiltration, measured at seven locations on the top of the Type 3 test pile with single ring infiltrometer tests, ranges from 2 to 74 mm/h ( $6 \cdot 10^{-7}$  to  $2 \cdot 10^{-5}$  m/s) with a geometric mean of 19 mm/h ( $5 \cdot 10^{-6}$  m/s) (Figure 3.2). Lower infiltration capacity was measured at the center of the pile where haul truck and bulldozer traffic had been the greatest. Nearly the entire surface of the test pile was excavated in the final step of the test pile construction (to extend instrument leads to the surface of the pile), so no direct relationship may be made between traffic patterns and infiltration capacity. No effort was made to measure infiltration capacity at zones with very little visible fine-grained material. Such regions compose perhaps 20 to 50% of the surface

and are assumed to have an infiltration capacity in excess of the most extreme rainfall rate.

The mean and maximum infiltration capacity at the Type 3 test pile are about two times greater than the results from 30 tests conducted at a compacted waste rock surface with a grain size distribution (for the material finer than 30 mm) similar to the Diavik waste rock (Bellehumeur, 2001). Infiltration capacity is two orders of magnitude lower than four tests conducted at a free-dumped waste rock surface that had very little fine-grained material and had not been subjected to truck and bulldozer traffic (Bellehumeur, 2001).

The significance of the infiltration capacity measurements may be seen in comparison to rainfall statistics for the region. A rainfall rate of 2 mm/h sustained over 8 hours has a recurrence interval of less than 2 years, and a rainfall rate of 78 mm/h over 20 minutes has a recurrence interval of 100 years (Golder Associates, 1997; Golder Associates, 2008). Therefore the tests revealed infiltration capacities that span the range of surface conditions under which ponding is generated during storms ranging from common to the most extreme.

#### 3.1.4 Saturated hydraulic conductivity

At the large-scale, a saturated hydraulic conductivity ( $K_{\text{sat}}$ ) of  $1 \cdot 10^{-2}$  m/s (permeability  $1 \cdot 10^{-9}$  m<sup>2</sup>) was measured with a constant head test on the 16 m<sup>3</sup> waste rock sample. This value is similar to the values measured *in situ* with air permeability tests in the Type 1 and Type 3 waste rock (Amos, in progress) and is similar to values reported for coarse waste rock (Morin *et al.*, 1991, in Fala *et al.*, 2005).

The mean  $K_{\text{sat}}$  of the finer-than 5mm fraction of 18 hand samples was  $2 \cdot 10^{-5}$  m/s, and the standard deviation was  $1 \cdot 10^{-5}$  m/s. There were no discernible spatial trends in  $K_{\text{sat}}$  for samples taken from material that was push-dumped to form the interior of the test piles. But samples taken from the top of the piles after construction was completed have a mean  $K_{\text{sat}}$  of  $3 \cdot 10^{-6}$  m/s; nearly an order of magnitude lower than the matrix samples representing the interior of the test piles. A lower  $K_{\text{sat}}$  in the matrix samples taken from the top of the test piles is consistent with a finer grain size distribution measured in the same samples.

A dye tracer applied to the top of the  $16 \text{ m}^3$  permeameter at the beginning of the drain-down test (Figure 3.3) provides an indication of a relation between the fastest flow paths and slower flow paths under saturated conditions. The maximum tracer concentration passed through the sample after 0.8 h while only the upper 0.18 m of the sample had drained to unsaturated conditions. The tracer first reached the bottom of the large permeameter at a velocity 10 times greater than the velocity experienced by the maximum tracer concentration. The resulting  $v_{\text{max}}/v_{\text{avg}}$  term, measured to be 10, is a value five times greater than that of the  $v_{\text{max}}/v_{\text{avg}}$  in sand and gravel at the detailed study of dispersion at Cape Cod, Massachusetts (LeBlanc, *et al.*, 1991), and is four times less than the  $v_{\text{max}}/v_{\text{avg}}$  in a highly heterogeneous aquifer with a non-uniform flow field (Adams and Gelhar, 1992). This measure of dispersion indicates that water followed flow paths through both large pores and matrix pores.

### 3.1.5 Water retention curves

The range of matrix water retention curves (Figure 3.4a), determined with Tempe cell tests conducted on the finer-than 5mm fraction of five hand samples, is similar to

those reported for sand and loamy sand, but with somewhat steeper slopes and lower air-entry pressures. Porous media with a steep water retention curve experience large changes in moisture content over relatively small changes in tension: a characteristic that promotes relatively rapid drainage. The drying WRC measured in the field at the 0.6 m depth at the upper collection lysimeters has a slope as steep as the steepest of the WRC's from the Tempe cell tests. The wetting WRC measured at the 0.6 m depth at the upper collection lysimeters has a significantly steeper slope. The observed field conditions at this location required extrapolation to estimate the air-entry pressure and the residual saturation, but the drying curve is similar to the WRC's estimated with Tempe cell tests. WRC parameters are presented in terms of the van Genuchten model with the Mualem assumption applied, as recommended for coarse sediment (Mace *et al.*, 1998). The mean WRC for the matrix material under both laboratory and field conditions yields van-Genuchten-Mualem parameters of  $\alpha$  of  $0.2 \text{ kPa}^{-1}$ ,  $n$  of 3, and an air-entry pressure ( $\phi_e$ ) of 2 kPa. The residual moisture content ( $\theta_r$ ) was estimated to be 0.01 by curve fitting, but the mean moisture content in the tempe cells at the highest tension observed under field conditions in 2007 was 0.05.

### 3.1.6 *Field capacity and initial moisture content*

Field capacity of the matrix material, which has porosity of about 0.25, was estimated to be 0.1 to 0.15, based on the range of moisture content in the water retention curves (Figure 3.4a) at the highest observed matric potential (about 35 kPa). Field capacity of waste rock at the 2-m-scale and the test-pile-scale was estimated by measuring the infiltration required to generate drainage at the upper collection lysimeters and the Type 3 test pile. This method requires an estimate of evaporation, which is

discussed in detail in Sections 2.5.1 and 3.4, and an estimate of the initial moisture content.

To estimate the field capacity of the waste rock at the large-scale based on measurements made at the upper lysimeters and test piles, the initial moisture content must first be estimated. The initial moisture content is considered to be equal to the average of 15 hand samples taken during construction of the test piles, which was 0.025 +/- 0.01 for the samples which consisted of material finer than 40 mm. To upscale this estimation of initial moisture content to the large-scale, it is multiplied by the fraction of the waste rock finer than 40 mm: 0.35 (Figure 3.1a). This method of upscaling assumes that the material larger than 40 mm did not contribute to the initial moisture content, an assumption that also applies to upscaling of the field capacity using the grain size distribution. This assumption is based on observations of very little retention of moisture by particles and clasts larger than 5 mm (Yazdani *et al.*, 2000; Tokunaga *et al.*, 2002). By multiplying the mean initial moisture content of the hand samples (0.025) by the fraction of the waste rock finer than 40 mm (0.35), the average initial moisture content at the large-scale is estimated to be 0.01 m<sup>3</sup> water/m<sup>3</sup> bulk volume.

Drainage from both of the Type 3 upper collection lysimeters was first observed several days after the rainfall of August 21, 2007. The Type 3 upper collection lysimeters were filled with waste rock in one day (July 28, 2006) and were not subsequently disturbed. Total rainfall, including applied events, before the initiation of drainage was 213 mm, and evaporation over the period is estimated to be 122 mm +/- 20%, based on the estimation discussed in Section 3.4.1. About 10 mm of rainfall was required to saturate the bottom of the lysimeters to the level of the drain. The remaining

81 mm +/- 25 mm can be attributed to the moisture content required for the lysimeters to reach field capacity over the depth of 1.70 m. An increase in volumetric moisture content of 0.047 +/- 0.008 is calculated by dividing the height of the infiltration required to reach field capacity (81 mm) by the depth of to the lysimeter drain (1.70 m). By adding this moisture content (0.047) to the estimated initial moisture content of the waste rock, the field capacity at the large-scale is estimated to be 0.057 +/- 0.008.

At the Type 3 test pile, significant percolation to the 3 m +/- 1 m depth in the Type 3 test pile was measured by a rapid increase in moisture content at TDR probes after an estimated 65 +/- 15 mm of infiltration in 2006. Field capacity is therefore estimated to be 0.02 to 0.07 at the Type 3 test pile, using the method described above. Error in this estimate results from uncertainty in how to deal with infiltration at the test pile prior to excavation of the top surface to extend instrument leads to the surface and uncertainty as to whether this infiltration would have generated percolation to a depth greater than 3 m without additional rainfall that came in 2007.

The difference between the estimate of the initial average moisture content in the matrix material (0.025) and the estimate of field capacity of the matrix material (0.1 to 0.15) indicates that the test piles were constructed with relatively dry waste rock. The test piles therefore require infiltration to wet up to field capacity or greater before the test piles reach an expected long-term state of dynamic equilibrium. By the end of 2007, the initial wetting front had reached the bottom of the test pile only under the batters. At the test-pile scale, then, this thesis pertains to the initial wet-up period. In the upper several meters of the piles, however, infiltration was measured after the initial wetting front had passed through the waste rock. In these regions, some observations were made of the

behaviour of water flow through waste rock that may be indicative of the long-term period of dynamic equilibrium.

### 3.1.7 *Unsaturated hydraulic conductivity*

A range of hydraulic conductivity curves (Figure 3.4b) has been determined for the waste rock matrix material, based on the water retention curves and the relationship of Fredlund *et al.* (1994) provided in the SoilVision software (Fredlund *et al.*, 1996). The range reflects the uncertainty involved in assigning a single  $K(\phi)$  curve to the matrix material, due to the range of estimated WRC's. At any value of soil tension, hydraulic conductivity estimated from these curves may vary by as much as three orders of magnitude, for the matrix material alone. A field calibration was performed to better estimate the hydraulic conductivity curve at the large-scale at the Type 3 test pile and at the upper collection lysimeters. The field calibration was applied using the Green-Ampt infiltration analysis described in Section 2.4.7. At both the Type 3 test pile and the upper collection lysimeters the best solution for the hydraulic conductivity function is the curve estimated using the relationship of Fredlund *et al.* (1994), from a water retention curve with van-Genuchten-Mualem parameters of  $\alpha$  of  $0.7 \text{ kPa}^{-1}$ ,  $n$  of 1.5, air-entry pressure ( $\phi_e$ ) of 0.6 kPa, residual moisture content ( $\theta_r$ ) of 0.01, and moisture content of 0.07 at the highest tension measured under the field conditions in 2007 (33 kPa).

### 3.1.8 *Pore water freezing and thawing*

The unfrozen moisture content of the matrix at temperatures below the freezing point, determined from the average WRC, is shown in Figure 3.4c. Due to the relatively small amount of very fine particles and the relatively steep water retention curves, the predicted freezing and thawing curves are steep. Freezing and thawing are therefore

expected to proceed as rapid transitions, relative to the transition for a fine-grained soil, during seasonal change in temperature. The relationship presented in Figure 3.4c does not account for inclusion of solutes during the freezing process, and therefore underestimates the unfrozen moisture content at any temperature less than 0°C. The analysis presented in Figure 3.4c indicates that moisture content remains above approximately 0.01 for all temperature measured at the study site.

### *3.1.9 Upscaling from the matrix-scale to the large-scale*

The methods used to relate hydraulic properties of the waste rock matrix material to hydraulic properties of the large-scale waste rock yield the following results:

1. Porosity of the matrix material is related by a drain-down test conducted with a 16 m<sup>3</sup> waste rock sample. The drain-down test (Figure 3.3) indicates that the volume of the pores of the matrix material is about 25% of the volume of the pores of the large-scale waste rock (which has a porosity of 0.25), or 0.06 to 0.08 of the volume of the waste rock at the large scale. In Figure 3.3, the line of best fit to the water level measurements is estimated to enable estimation of the time when the water level reached the base of the waste rock sample (5.6 hours), which could not be measured directly. Considering the large-scale grain size distribution (Figure 3.1a), it is not surprising that the porosity of the matrix as a fraction of the large-scale bulk volume is estimated to be about 25% of the value at the matrix scale. The matrix material, defined previously as the material finer-than 10 to 20 mm constitutes 19% to 24% of the waste rock. The volume of the pores of the matrix material as a fraction of the large-scale waste rock is estimated using the grain size distribution with the following method:

$$0.25 \quad * \quad 19\% \text{ to } 24\% \quad = \quad 0.05 \text{ to } 0.06 \quad (4)$$

porosity of matrix \* % finer-than 10 to 20 mm = matrix porosity at the large-scale

$$[\text{m}^3 \text{ pores/m}^3 \text{ matrix}] * [\text{m}^3 \text{ matrix/m}^3 \text{ large-scale bulk}] = [\text{m}^3 \text{ matrix pores/ m}^3 \text{ large-scale bulk}]$$

It should be noted that this volumetric analysis of the grain size distribution assumes that the *in situ* bulk density of the large-scale waste rock equals that of the matrix.

2. Field capacity is related by lysimetry at the 2 m-scale and by monitoring of wetting fronts at the test pile-scale. These analyses indicate that the field capacity of the waste rock is between 0.02 and 0.07. Incorporation of the results of the drain-down test for the porosity of the matrix as a fraction of the large-scale waste rock into the estimate of field capacity yields a field capacity of 0.04 to 0.05 of the total volume. These values are 20% to 45% of the estimates of field capacity of the matrix material (0.1 to 0.15). This ratio of the matrix-scale to large-scale field capacity is also similar to that of the matrix fraction of the large-scale grain size distribution.

3. Unsaturated hydraulic conductivity at the matrix-scale is related to the  $K(\phi)$  at the large scale by an infiltration analysis. This analysis found that the hydraulic conductivity curve at the large-scale is within the range of hydraulic conductivity curves determined for the matrix material. The unsaturated hydraulic conductivity of the waste rock analyzed in this study shows no apparent scale-dependency.

It should also be noted that net infiltration in response to a high-intensity applied rainfall, measured at the at the upper lysimeters to be 6 mm, was about 20% of net infiltration estimated with the ECH<sub>2</sub>O sensor at the 0.9 m depth. The estimation of net infiltration made by lysimetry (6 mm) represents net infiltration for that event at the 2 m scale. The 2 m scale includes clasts finer-than about 1 m. At the ECH<sub>2</sub>O sensor, net infiltration of 30 mm is estimated as a 0.03 increase in moisture content divided by the

depth of the sensor ( $0.03 \text{ m}^3 \text{ moisture/m}^3 \text{ waste rock} / 0.9 \text{ m depth} = 30 \text{ mm}$ ). Net infiltration estimated by the increase in moisture content at the ECH<sub>2</sub>O sensor represents net infiltration into the matrix material. Therefore net infiltration at the matrix-scale was 20% greater than net infiltration at the 2 m scale. This factor is similar to those discussed above regarding upscaling volumetric measurements at the matrix scale to the large-scale.

### **3.2 Rainfall**

A summary of the details described and listed in Appendix E are presented here. Mean annual rainfall at Diavik is estimated to be 148 mm from 45 years of measurements at the Contwoyto and Lupin weather stations (Golder Associates 1997, Golder Associates 2005). At upland areas such as the top of a waste rock pile, where snow accumulation is scant, this mean annual rainfall is typical of desert conditions (McKnight 2002). During the construction of the test piles, from late May to early September 2006, approximately 130 mm of rain fell (Figure 3.5a). Several storms in August 2006 dropped a total of 58 mm of rain when the test pile construction was near completion and the construction of the upper lysimeters was complete (Figure 3.5b). These storms are included as rainfall in water balance calculations carried out for the upper lysimeters and the test piles, but the rainfall in May to July 2006 is instead considered to have contributed to the initial moisture content of a portion of the test piles. In 2007, total rainfall measured in rain gauges on the instrument huts on the tops of the test piles was 93 mm, only 63% of the mean annual rainfall for the region.

Details of the applied rainfall events are listed in Appendix E. With three applied rainfall events, rainfall at the top of the Type 3 test pile in 2007 was 153 mm, 102% of

the mean annual value. At the Type 3 upper collection lysimeters, rainfall in 2007 with five applied rainfall events was 184 mm, 124% of the mean annual and 41% of the maximum annual rainfall for the region on record.

### **3.3 Snowmelt**

During the 2006 to 2007 winter (October to May), snowfall at Diavik was 212 cm (91% of mean annual snowfall). The hydrological contribution of snowmelt in the Arctic is controlled by the distribution of snow deposition, which is dominated by wind transport of snow both as it falls and subsequently by scouring and re-deposition (Woo *et al.*, 2000; Golder Associates 2005). Snow is transported and re-distributed for approximately six months of the year. Air temperature, recorded on an hourly basis, remained below the freezing point from October 13 until May 5, with minor exceptions in late October and late April. Wind speed during this period averaged 17 km/h with gusts to 60 km/h. Snow depth at the tops of the test piles and upper collection lysimeters at the beginning of the melt period in 2007 was less than 10 cm, but deposition onto the batters of the piles was about 100 to 200 cm (Figure 3.6a). Due to the irregular surface of the boulder-dominated pile batters, no attempt could be made to measure snowpack depth on the batters of the test piles, due to safety considerations.

Sublimation accounts for about 30% of snow ablation on average in the Arctic (Pomeroy *et al.*, 1997). Snowpack ablation while air temperature was below 0 °C, from the time of maximum snowpack at the Ekati meteorological station, was about 15 cm (Figure 3.6b). Snowmelt in the Arctic is controlled primarily by convective heat transfer and solar radiation (Kane *et al.*, 1997), and therefore may occur on sunny days when the

temperature remains slightly below the freezing point. Snow sublimated and melted at the highest rates on southern and western aspects of the test piles, as observed visually. In this study, an average snow depth on the batters of the test piles immediately prior to ablation is estimated to have been 1.5 m, based on visual assessment. The air temperature has been used as a simplified estimation of the time when either sublimation or snowmelt occurred. This simplified approach is applicable in the estimation of snowmelt, due to the uncertainty in the estimations of snow depth and snow density at the test piles. Snow density is estimated to have been between approximately 270 kg/m<sup>3</sup> (*i.e.*, 27% water), based on 3 years of measurements at Diavik (Golder Associates, 2008) and studies that included as many as 1100 measurements in Arctic tundra environments (Weller and Holmgren, 1974; Woo and Marsh, 1978; Liston and Sturm, 2002). Snowmelt on the batters of the test piles in 2007 began on about May 5 but was interrupted from May 7 to May 14 by cold temperatures and snowfall. All snow at the test piles had melted by May 26, 2007. After that time, some amount of the snowmelt evaporated. Evaporation from the batters is discussed below. Based on these estimations and assumptions, average snowmelt into the batters of the test piles is estimated to have been approximately 345 mm in 2007.

### **3.4 Evaporation and infiltration**

Mean annual lake evaporation for the region around Diavik has been estimated to be 271 mm (Golder Associates, 2008) from meteorological data. The mean annual evapotranspiration from upland areas of tundra and exposed bedrock is estimated to be 138 mm (Golder Associates 1997), based on a water balance calculated at the regional

scale, and 110 mm (Golder Associates, 2008), based on the application of a correction factor to the lake evaporation. Evaporation from waste rock was estimated at the upper collection lysimeters by lysimetry and by the FAO-PM method. At the test piles, evaporation was estimated by the FAO-PM method and was compared to net infiltration monitored by TDR.

#### *3.4.1 Type 3 upper collection lysimeters: wet conditions*

Evaporation is estimated for a ten-day period, from 11:30 on September 1 to 22:30 on September 11, 2008, following an applied rainfall of 15 mm. Evaporation is estimated by lysimetry and by meteorological-based modeling using the FAO-56 Penman-Monteith (FAO-PM) method described in Section 2.5.1. This ten-day period was chosen because the change in storage in the lysimeter, estimated as the change in moisture content midway between the ground surface and the lysimeter drain (the location of the ECH<sub>2</sub>O sensor at a depth of 0.9 m), was zero at 22:30 on September 11 (Figure 3.7a). Evaporation is estimated to be 12.1 mm, based on a water balance calculated with measured rainfall, lysimeter outflow, and change in storage. Based on FAO-PM modeling, an estimate of 9.4 mm of water evaporated over the same period. Evaporation over this period, during which the average temperature was 4°C, is thus estimated to have been 10.8 +/- 1.4 mm, with an average evaporation rate of 1.0 +/- 0.1 mm/d. The context of this rate on the annual cycle is discussed below in Section 3.4.3.

#### *3.4.2 Type 1 upper collection lysimeters: dry conditions*

Evaporation was also estimated for the period from the date the lysimeters were filled with waste rock (July 28, 2006), to the end of 2007 for the Type 1 upper collection

lysimeters. The Type 1 upper collection lysimeters received only natural precipitation, which totaled 161.6 mm (72% of average rainfall) (Figure 3.7b). No drainage reported to the base of the lysimeters, so all infiltration contributed to an increase in the moisture content of the matrix material, except that which evaporated. Using the FAO-PM method, the estimated evaporation totaled 142 mm (88% of rainfall), yielding an increase in storage equivalent to only 19 mm of infiltration. By comparison, about 100 mm of infiltration was required to produce drainage at the Type 3 upper collection lysimeters.

#### 3.4.3 *Test piles: top surface*

An estimation of the daily evaporation rate ( $E$ ) from the top surface of the Type 3 test pile for 2007 is presented in Figure 3.7c. Reference evaporation ( $E_0$ ) is also plotted in the figure to illustrate how the estimation of moisture available for evaporation (the  $K_{bs}$  term) and frozen conditions (the  $K_f$  term) affect the estimate of evaporation. The average evaporation rate for the period including all of the days when the average daily temperature was above freezing (May 5 to October 14, 2007) is estimated to have been 0.6 mm/d. The average evaporation rate for the period when the average daily temperature remained above freezing every day (June 9 to September 13, 2007) is estimated to have been 0.9 mm/d. Recall that the evaporation rate estimated for the 10-day period during which an estimate of evaporation was made by both water balance and the FAO-PM method was 1.0 +/-0.1 mm/d.

Total rainfall at the top of the Type 3 test pile, from the time of completion of construction to the end of 2007 including six applied rainfall events, was 279.6 mm (124% of average). Evaporation over this period is estimated to have been 143 mm (51% of rainfall) using the FAO-PM method (Figure 3.7d), and the remaining 137 mm of water

is the estimated net infiltration. Net infiltration is also estimated by calculating the cumulative groundwater flux past two tensiometer profiles in the Type 3 test pile (discussed further in Section 3.7.1). Net infiltration estimated in this way supports the estimate made by modeling the evaporation from meteorological data (Figure 3.7d).

Net infiltration in the Type 3 test pile created wetting fronts that were detected by TDR as increases in moisture content of the matrix material that propagated to a depth of about 7 m by the end of 2007 (Figure 3.8). The moisture content in the test piles is shown in Figure 3.8 as profiles of average measurements made at several horizontal positions at each depth. Estimated error bars on moisture content, which are the same for all sensors but omitted from the Type 3 test pile profile for clarity, reflect the error in the sensor calibration, the potential effect of void spaces within the field of measurement, and variability between probes at the same depth (Appendix B). The error bars imply that in the Type 1 test pile, net infiltration to a depth of 2 m may have been zero.

For the year 2007, at the top of the Type 3 test pile, the total rainfall including applied events was 153 mm (103% of mean annual), evaporation is estimated to be 93 mm (61% of rainfall) by the FAO-PM method, and net infiltration is estimated to be 60 mm. This ratio of evaporation to rainfall is similar to the values reported by Carey *et al.*, 2005, Nichol *et al.*, 2005, and Marcoline 2008, where evaporation was measured by eddy covariance or lysimetry at waste rock piles in northern Saskatchewan, Canada. For the year 2007, at the top of the Type 1 test pile, the total rainfall was 93 mm (63% of mean annual), evaporation is estimated to be 95 mm (102% of rainfall), and net infiltration is estimated to be negligible. Based on TDR measurements and evaporation estimates from

lysimetry and modeling using meteorological measurements, net infiltration to the top surface of the Type 1 test pile is estimated to be zero.

#### *3.4.4 Test piles: batters*

Evaporation from the batters of the test piles was likely to have been less than evaporation from the tops of the piles. Less fine-grained material was present on the surface of the batters of the test piles than at the top of the piles. This condition could be expected to allow for less water retention at the surface and lower upward water supply to the evaporative surface. Evaporation from the batters of a test pile in a humid climate could be inferred to have been low, based on measurement of lysimeter outflow from the batters that was higher than outflow from the core of the test pile (Corazao Gallegos, 2007; Bay, in progress).

### **3.5 Hydrologic and thermal interaction in the permafrost active layer**

#### *3.5.1 Depth of the active layer*

Both test piles froze throughout the 14 m depth during the first winter (2006-2007). The piles froze over a period of approximately 50 days, from October 17 to December 5, 2006, and thawed to a depth of at least 11 m over a period of approximately 50 days, from June 1 to July 20, 2007 (Figure 3.9). Within the upper 5 m, the time frozen and the time thawed began and ended at times that varied with distance from the pile surface above or the permafrost below the piles. The upper 5 m is highlighted here because it is within this region that any groundwater flow occurred prior to freezing in the winter of 2006-2007. The upper 5 m remained frozen about 220 days before fully thawing and

remaining unfrozen for about 145 days during 2007. The total time frozen or thawed varied no more than 10 days at any depth, except for the regions at the core of the piles at depths greater than 11 m. For example, the time of freezing at the 3 to 5 m depth occurred last, but this depth also thawed late. The region of the piles slowest to freeze and thaw was somewhat higher in the piles than expected, particularly in the Type 3 test pile. A relatively slow freezing and thawing rate at the 3 to 5 m depth may have been controlled by the distribution of moisture content in the piles (Figure 3.8), due to the heat required for the phase change from water to ice.

Between the depths of 5 to 7 m, the test piles were thawed for between approximately 100 and 145 days in 2007. At depths greater than 7 m in the test piles, the waste rock was thawed for less time than the regions nearer the surface during the 2007 summer. At a depth of 11 m, the test piles were thawed for a period of about 100 days during 2007. At a depth of about 14 m, 0.3 m below the basal drain HDPE liner, the temperature remained within about 1° of the freezing point throughout the 2007 summer season, with regions that remained frozen interspersed with regions that thawed for some period of time. This implies that portions of the HDPE liner of the basal drain collection system may have remained frozen throughout the year 2007. Heat trace in the plumbing of the collection system, however, ensured that any water that flowed to the piping of the basal drain would also flow to the instrumentation huts to be recorded. Based on more detailed analysis of the regions of the pile where water flow occurred (see Sections 3.5.3, 3.5.4, and 3.6), little water flow is thought to have reached the partially-frozen regions at the core of the pile at the 14 m depth in 2007. Therefore, after the first winter, the depth of the active layer was approximately 14 m.

The long-term depth of the active layer within the test piles remains uncertain. Thermistor strings at several locations in large waste rock piles at the EKATI Diamond Mine have measured temperature in climatic and waste rock conditions similar to those at Diavik. Measurements indicate that the active layer depth typically decreased from about 8 m to about 4 m several years after waste rock deposition, but the active layer was as deep as 11 m in a location where primarily biotite schist waste rock was concentrated (SRK, 2003; SRK, 2007). The 50 m by 60 m by 15 m high test piles may be too small to accurately represent the active layer depth in large-scale waste rock piles.

### 3.5.2 *Pore water redistribution toward a frost layer*

Upward pore water flow towards a frozen ground surface is known to increase the ice content in soil near the ground surface, which in turn leads to lower infiltration during the subsequent spring thaw (Dirksen and Miller, 1966; Kane and Stein, 1983). This process thereby contributes to the conditions that cause overland flow. Redistribution of pore water toward a frost layer occurs by two processes: (1) the development of a gradient in soil suction by effectively drying the porous media at the frost layer by freezing (Black and Tice, 1989), and (2) to a lesser extent (Dirksen and Miller, 1966), the transport of moisture in both the liquid and vapor phase associated with heat transfer toward the frost layer (Cary, 1964). The physical basis for these processes is the Clapeyron equation, which relates pressure and temperature about the ice-water phase change, and enables coupling of soil moisture flow and heat transport in mathematical models (*i.e.* Hansson *et al.*, 2004).

Vapor transport associated with heat transfer was observed as steam vents at a waste rock pile adjacent to the test piles (Figure 3.10), but was not measured. Flux of vapor

associated with a thermal gradient of approximately  $5^{\circ}\text{C}/\text{cm}$  has been estimated to be 0.3 to 0.6 mm/d (Cary, 1964). Vapor transport could be expected to be greater in waste rock than in soil due to a high air-filled porosity (Section 3.1) and the process of convective heat transport (Pham, in progress).

At the upper lysimeters, frost penetration caused a hydraulic gradient greater than any measured during evaporation, forcing pore water upward towards the pile surface (Figure 3.11). A gradient of as much as 2.0 was measured between two tensiometers with porous cups at depths of 0.3 and 0.6 m in a profile, at a time on October 6, 2007, when the waste rock above the porous cups was beginning to freeze (Figure 3.11a). By multiplying this gradient by the estimated  $K(\phi)$  at the average  $\phi$  measured at the two tensiometers, the upward groundwater flux toward the penetrating frost layer on October 6 is estimated to have been approximately 0.4 mm/d. The thermal gradient at that time was approximately  $0.01$  to  $0.08^{\circ}\text{C}/\text{cm}$ , indicating that the estimated upward redistribution was caused primarily by capillarity due to the penetrating frost, rather than by a thermal gradient.

Two weeks later at the same location, the seasonal frost propagated downward past ECH<sub>2</sub>O moisture content sensors at depths of 0.3 and 0.6 m. The tensiometers were no longer recording soil tension as the frost passed, from approximately October 21 to October 27, 2007, due to the requirement for liquid water inside the instruments. Soil tension is therefore estimated, and a gradient as high as 230 is estimated to have been present at the instrument profile as the frost horizon passed, using measurements of moisture content and the drying water retention curve estimated at the same location. By multiplying this gradient by the estimated  $K(\phi)$  at the average  $\phi$  estimated at the two

ECH<sub>2</sub>O sensors, the upward groundwater flux toward the penetrating frost layer is estimated to have been as high as 10 mm/d. Net upward redistribution during these 6 days is therefore estimated to have been approximately 50 mm (Figure 3.11b). The thermal gradient at this time is estimated to have been from 0.1 to 0.4°C/cm, indicating that the estimated upward redistribution during the frost penetration was caused primarily by capillarity due to the penetrating frost, rather than by a thermal gradient.

At the test piles, frozen conditions existed in October at the top surface of the piles and in the permafrost directly below the piles. From October to December, 2007, heat in the test piles transferred outward in all directions from the center of the piles, specifically from the 3 to 5 m depth, enabling frozen conditions to propagate inward. Since a frost layer propagated into the waste rock from the atmosphere and from the permafrost, redistribution of pore water toward frost surfaces may have flowed in an upward, outward, or downward direction.

### 3.5.3 *Infiltration into frozen waste rock*

During the thaw period at the waste rock surface in May 2007, infiltration into the frozen waste rock during moderate rainfall events was restricted in some regions by ice-filled pores (Figure 3.12a, b). Surface ponding at some locations at the top of the test piles created small-scale runoff that infiltrated into air-filled pores of the adjacent waste rock. Thus, the large-scale response was “unlimited infiltration” (with respect to the effect of ice saturation) into frozen waste rock, as would be expected of coarse material with a high air-filled porosity (Gray *et al.*, 2001). While the waste rock was frozen, moisture content sensors surrounded by matrix material remained frozen so that infiltration could not be directly observed. Infiltration was instead estimated by

subtracting the estimated evaporation for this time period from the measured rainfall (Figure 3.12c). The frost depth was determined by the average time when thermistor measurements at various depths rose to 0°C and the time when TDR measurements rose to the antecedent moisture content (the moisture content at the time of freezing in 2006). On this basis, approximately 15 mm of rainfall is estimated to have infiltrated into frozen waste rock below the top of the test piles in early May 2007. This estimate implies that this process has the potential to be one of the major mechanisms for recharge.

The depth of penetration of this water into the frozen test pile is unknown. As the waste rock thawed, this infiltration created a wetting front that propagated into the Type 3 test pile in addition to the thawing wetting front that was created by applied rainfall events in September 2006. The additional wetting front that propagated with the thaw front is inferred from measurements of moisture content during the thaw that were greater than the antecedent moisture content (Figure 3.13). The estimation of cumulative infiltration plotted in Figure 3.12c trends downward after the 15 mm of infiltration into frozen waste rock, due to a period of little rainfall and a high evaporation potential. During this period, the wetting front inferred from the data presented in Figure 3.13 appears to have propagated through waste rock with moisture content in the matrix material between 0.14 and 0.18 to a depth of 3 m or greater before the strong evaporation potential of June 2007 could significantly affect it.

At the Type 1 test pile, however, infiltration into the frozen test pile in May 2007 may have created a wetting front that remained near the surface of the test pile. The antecedent moisture content of the matrix material in the Type 1 test pile is estimated to have been approximately 0.03 to 0.08. Due to the low moisture content, the hydraulic

conductivity of the matrix material in the upper several meters of the Type 1 test pile is estimated to have been as low as  $1 \cdot 10^{-12}$  m/s. This conductivity is up to 4 orders of magnitude lower than the estimated hydraulic conductivity of the upper several meters of the Type 3 test pile during the propagation of the wetting front in June 2007. This estimated difference in hydraulic conductivity may have caused the water from the same May rainfall to remain near the surface of the Type 1 test pile, where it was subject to evaporation. While the net infiltration of this event is estimated to have been approximately 15 mm at the Type 3 test pile, net infiltration at the Type 1 test pile is estimated to have been approximately zero.

The snow that was deposited onto the batters of the Type 3 test pile melted during a time when very little of the test pile was thawed (Figure 3.14). A snowpack with a depth of approximately 1.5 m sublimated from and melted into the batters of the test piles by May 26, 2007. Based on snowpack ablation, air temperature measurements (Figure 3.5b), and reported sublimation estimates in the Arctic (Golder Associates, 1997), 0.2 m of snow is estimated to have sublimated. Assuming a snow density of  $270 \text{ kg/m}^3$ , an average of 310 mm snowmelt either created surface runoff or infiltrated into the pile batters before May 26. No surface runoff was observed at the batters of the test piles. Due to the large air-filled porosity of the waste rock, all of the estimated 310 mm snowmelt was assumed to have infiltrated into the pile batters where it was likely to have frozen. No temperature measurements were made in the upper several meters under the batters. The depth of the thaw front at the batters was assumed to be the same as at the top of the pile, which was essentially zero on May 26 (Figure 3.12c).

As the batters thawed, the snowmelt that infiltrated and re-froze was remobilized. Approximately 10% of the snowmelt is estimated to have subsequently evaporated, based on the discussion in Section 3.4.4, so that the net infiltration due to snowmelt in 2007 is estimated to have been 280 mm. As the depth to the frost horizon increased in June and July 2007, the basal area of the Type 3 test pile contributing to the outflow from the pile increased (Figure 3.14b). Figure 3.15 presents a conceptual model for the changing area of the base of the test pile that contributes to outflow during the initial wet-up period, based on the seasonal movement of the frost horizon, propagation of the initial wetting front into the initially dry waste rock, and the presence of permafrost below the pile. The outflow from the Type 3 test pile (Figure 3.14) was at the yearly maximum on July 23, when the cumulative rainfall was just 29 mm. The outflow maximum of 1800 L/d occurred 3 days after the maximum daily air temperature in 2007, indicating that the major mechanism for outflow in 2007 was flow occurring during the thaw of the snowmelt that had infiltrated into the frozen waste rock in the batters of the test pile.

#### *3.5.4 Temperature-dependent outflow*

Changes in temperature within the waste rock had the greatest impact on outflow from the test piles during the seasonal thaw, which propagated into the piles during June and July, 2007, and the seasonal freeze, which occurred mostly during October and November, 2007 (Figure 3.9 a,b). During the period of snowmelt at the batters of the test piles in May 2007, a total of about 0.5 m<sup>3</sup> of the snowmelt reported to the basal drain of each test pile. It should be noted that this assessment assumes that the infiltrating snowmelt did not displace any moisture that was present in the waste rock from rain in 2006; an assumption that is consistent with the low specific conductance of the outflow.

During this time in May, outflow generally occurred only during the afternoons while the air temperature was above freezing. Most of the snowmelt, however, froze after entering the batters of the piles and later created a wetting front that propagated through the pile and reported to the basal drain at a rate determined by the propagation of the thaw front (Figure 3.14) and to a depth limited by the moisture deficit of the matrix material.

Outflow from the test piles was assumed to have flowed only through portions of the piles that were above the area of the basal collection system that had both wetted up and thawed (Figure 3.15). The depth of the thaw front limited the area of the basal collection system that contributed to outflow at the beginning of the summer, based upon temperature measurements made at the top of the pile and an estimate of snowmelt infiltration depth. From about July 20 to September 13, 2007, the outer 10 to 14 m of the test pile top and presumably the batters were thawed, and wetting front advance under the batters of the piles was limited primarily by the supply of water by infiltration and the deficit in moisture content of the matrix material between the field capacity and the initial value.

Changes in air temperature on a daily basis affected the outflow from the Type 3 test pile and the upper collection lysimeters in two different ways in 2007:

1. Temperature increases caused increases in outflow by melting pore ice. Temperature measurements made just beneath the basal collection system below the western batter of the Type 1 test pile (Figure 3.9c) indicate that portions of the base of each test pile may have remained frozen throughout the summer. Contribution of pore ice melt to outflow from the Type 3 test pile was observed distinctly on two occasions in 2007 (Figure 3.16). On October 11, an increase in air temperature re-mobilized flow

associated with the rainfall of October 7 that had frozen, leading to an increase in outflow on October 12. From August 18 to 20, outflow increased from 500 to 700 L/d, despite there having been only 2.4 mm of rainfall in the 10 days prior to the increase in outflow. Melting pore ice at the interior of the pile in response to rising air temperatures might be explained by wind advective heat transport through the permeable waste rock (Amos *in progress*). Melting pore ice may also have been simply the result of further penetration of the seasonal frost isotherm into the test pile, which was occurring at a depth of about 13 m at that time (Figure 3.9b).

2. Temperature fluctuations about the freezing point at the onset of the autumn freeze caused stoppages in outflow. On September 12, the same conditions caused outflow to stop at the east Type 3 upper lysimeter while causing macropore flow at the west Type 3 upper lysimeter (Figure 3.17). Stoppages in outflow from the upper collection lysimeters occurred on several occasions when saturation at the surface was relatively high and the air temperature increased from below-freezing to above-freezing. The effect of surface freezing and thawing during the autumn freeze is discussed in more detail in Section 3.7.5.

### **3.6 Infiltration through batters and the potential for non-vertical flow**

Infiltration through batters formed at the angle of repose (about 40° from horizontal) may be higher than infiltration through flat waste rock surfaces typical of the top of a pile. Cumulative outflow flux (volume divided by collection area) from lysimeters beneath the batter of test piles in humid climates has been measured higher than rainfall over periods of several months (inspection of Figure 5.5 in Corazao Gallegas 2007;

Andrina, personal communication, April 2008; Bay, personal communication, 2008). Outflow greater than precipitation suggests that the outflow includes flow from an area of the pile larger than the collection area at the base of the pile. This condition could occur by preferential flow directed through a non-vertical channel (Nichol *et al.*, 2005) or by the addition of both vertical and non-vertical flow at a large scale (Figure 3.18). Water balance calculations made over the full duration of the Type 3 test pile experiment through the 2007 summer season indicate potential for a significant component of large-scale non-vertical flow (discussed below).

Non-vertical flow should not be confused with preferential flow. Preferential flow refers to focused rapid flow that may follow a macropore pathway. Non-vertical flow refers to flow that may occur within a dipping stratigraphic unit or along a capillary or permeability boundary. Fala *et al.* (2005) simulated both preferential flow, which was vertical through homogenous media, and non-vertical flow through alternating sand and gravel layers inclined at the angle of repose in a waste rock pile. In their simulation, flow followed non-vertical pathways through coarse material at a permeability boundary and through fine material at a capillary boundary (see Figure 13 in Fala *et al.*, 2005).

### *3.6.1 Portion of the test pile contributing to outflow during water accumulation stage*

The area of the base of the test pile that contributes to outflow changes during the year (Figure 3.14). The fraction of the basal drain contributing to the outflow from the Type 3 test pile in 2007 increased from zero to a maximum of approximately 1000 m<sup>2</sup> as the thaw front propagated inward and the initial wetting front propagated downward (Figure 3.15). The maximum area of the basal drain contributing to outflow in 2007 was estimated by calculating the maximum depth of net infiltration of the total rainfall and

snowmelt. An estimated 350 +/- 50 mm of net infiltration by rainfall and snowmelt in 2006 and 2007 percolated into the pile batters to a maximum depth of 7 +/- 2 m ( $INF_{max}$  in Figure 3.18).  $INF_{max}$  was estimated as the depth over which the moisture content would have risen from the initial condition (0.01 at the large-scale) to field capacity (approximately 0.06, as discussed in Section 3.1.6). The area of the basal drain contributing to flow at that time was then estimated by evaluating the length from the berm of the HDPE liner to the location under the maximum depth of infiltration ( $L_{max}$  in Figure 3.18). Evaluation of the cumulative outflow during 2006 and 2007 required that the average area contributing to the outflow be considered, rather than the maximum area. The average area of the basal drain contributing to outflow during the period from May 5 to November 11, 2007, is estimated to be 550 m<sup>2</sup>.

This method of determining the area of the base of the test pile contributing to the outflow is supported by moisture content measurements and by the absence of outflow from the basal lysimeters. The wetting front under the batters, generated primarily by re-melted snowmelt, propagated into initially dry waste rock. Moisture content of the matrix at the core of the Type 3 test pile remained about 0.03 (+/- 0.05) throughout 2006 and 2007, based on initial moisture content estimates (Section 3.5.1) and TDR measurements at probes located at depths of 8 m and 9 m (Figure 3.8b). No flow reported to the two lysimeters located at a depth of about 10 m beneath the north batter (and at least one of these was confirmed to be capable of draining to the instrument shack without problems). Therefore the outflow observed is thought to have come from the outer portion of the pile, where the depth of the waste rock was less than 10 m over the HDPE liner of the basal drain.

It should be noted however, that water that originated as precipitation onto the test pile during construction may have continued to drain from the base of the pile in 2007. This portion of the outflow is thought to have drained at a rate of approximately 80 L/d (as high as that observed in 2006) or less. Based on these analyses, an estimated 99% of the outflow from the Type 3 test pile in 2007 is thought to have flowed through the batters. Approximately 80% of the outflow from the test pile originated as snowmelt.

### 3.6.2 *Water balance approach*

The potential for non-vertical flow is investigated by calculating the water balance across the average area of the basal drain contributing to outflow, with the hypothesis that the large-scale flow direction is vertical. The time period considered in this calculation is the period from the end of the construction of the Type 3 test pile until the end of October, 2007, when outflow ceased for the year. As discussed in the previous section, the average area of the base of the Type 3 test pile contributing to outflow is estimated to be 550 m<sup>2</sup>. If outflow calculated over that area is in significant deficit of the observed outflow, a component of non-vertical flow could be inferred to have added to the observed outflow (Figure 3.18). The following water balance equation is used to evaluate the potential for non-vertical flow at the Type 3 test pile:

$$Q = P - E - \Delta S, \quad (5)$$

where Q is outflow, P is precipitation as snowmelt and rainfall, E is evaporation, and  $\Delta S$  is the change in storage (moisture content).

Precipitation as snowmelt and rainfall onto the 550 m<sup>2</sup> area of the batters of the test piles is estimated to have been 240 +/- 80 m<sup>3</sup> for 2006 through 2007. Evaporation is estimated to have been approximately 40 +/- 20 m<sup>3</sup> by assuming that 20% of the snowmelt and rainfall evaporated: approximately half of the proportion of the precipitation estimated to have evaporated from the top of the Type 3 pile. Change in storage is estimated to have been 40 +/- 20 m<sup>3</sup> by calculating the change in moisture content of the waste rock at the large scale over an average depth of the area contributing to outflow. The estimation of the change in storage was made by estimating an average change in matrix moisture content of +0.15, estimating the matrix as 20% of the large-scale waste rock, estimating the average depth of the region contributing to outflow to be 3 m based on the discussion in Section 3.6.1, and multiplying all of these factors by the average contributing area (550 m<sup>2</sup>). Uncertainty in this calculation was large due to the lack of measurement of snow depth and limited knowledge regarding application of evaporation and change in storage estimates for waste rock to the boulder-dominated region near the toe of the pile (referred to as the rubble zone by *e.g.* Andrina *et al.*, 2006 and Stockwell *et al.*, 2006).

Estimated outflow if it is assumed the large-scale flow direction was vertical was 160 +/- 80 m<sup>3</sup>. The cumulative observed outflow from the Type 3 test pile by the end of 2007 is estimated to be from 100 to 200 m<sup>3</sup> (Figure 3.19a). The cumulative observed outflow, if a linear interpolation between manual flow measurements is made, from the Type 3 test pile during 2006 and 2007 was 135 m<sup>3</sup> (the heavy line in Figure 3.19a). Due to the large uncertainties in this estimate, it cannot be concluded whether non-vertical flow occurred within the test piles in significant proportion at the large scale.

### **3.7 Flow mechanisms: upper 1.7 m**

Flow mechanisms were analyzed for the response to a high-intensity applied rainfall event conducted at the upper collection lysimeters. In this study, a high-intensity rainfall refers to rainfall with a recurrence interval of approximately 2 years or greater. In the region around Diavik, examples of such storms are rainfall of 6 mm/h for one hour or rainfall of 1.5 mm/h for twelve hours, based on rainfall statistics reported by Golder Associates (2008). The following questions are addressed:

- Under what conditions did macropore flow occur, if it was observed?
- Under what conditions did matrix flow occur?
- Did the outflow response to rainfall reflect by-passing flow or porewater displaced by a wetting front?
- How did changes in temperature about the freezing point affect the flow?

After applying rainfall to bring the moisture content in the two lysimeters containing Type 3 waste rock up to field capacity, 14.8 mm of rain was applied on Sep. 1, 2007, at a rate of 9.7 mm/h: an event with approximately an 8 year recurrence interval. No ponding or runoff was observed during the event. The response to the event was detected as a pressure wave by a tensiometer profile, as increases in moisture content (a wetting front) at an ECH<sub>2</sub>O probe profile, and as lysimeter outflow (Figure 3.20). A summary of the flow response is listed at the end of the chapter in Table 3.4, with comparison to the flow behaviour at the Type 3 test pile. The mechanisms of the flow response are discussed below.

### 3.7.1 *Groundwater flux through unsaturated waste rock*

#### 3.7.1.a Lysimeter outflow

The groundwater flux through the unsaturated waste rock was calculated at the two lysimeters as the outflow rate divided by the lysimeter collection area (2.09 m<sup>2</sup>). The flux at the peak outflow, which corresponded with the arrival of a wetting front at the 1.7 m-deep drain of each lysimeter, was 0.78 +/- 0.07 mm/d ( $9 \cdot 10^{-9}$  +/-  $1.5 \cdot 10^{-9}$  m/s) (Figure 3.20). Cumulative net infiltration was determined at a time 10 days after the applied rainfall, when the change in moisture content at an ECH<sub>2</sub>O probe at a depth of 0.9 m was zero. Of the 14.8 mm of applied rain, 6 +/- 1 mm reported to the drain of the lysimeters as net infiltration. The rest of the applied rainfall was assumed to have evaporated (Section 3.4). The average groundwater flux during the response to the applied rainfall event was 0.6 +/- 0.1 mm/d.

Subsequent to the applied rainfall event, on September 14, an extremely high outflow flux of 96 mm/d ( $1 \cdot 10^{-6}$  m/s) was measured at the west lysimeter after a rainfall of only 1 mm. This small rainfall event came after the surface had been frozen for approximately two nights and then thawed for one day (Figure 3.17). This short-duration extreme event may be inappropriately discussed in terms of a groundwater flux (due to doubt that the entire area of the lysimeter contributed to the flow), and is further discussed below in Section 3.7.5.

#### 3.7.1.b Estimation from tensiometer profile

The flux past the tensiometer profile is calculated at the tensiometer profile by applying Darcy's Law and the hydraulic gradient between two tensiometers and the hydraulic conductivity at the measured value of tension (using the  $K(\phi)$  curve determined

appropriate in Section 3.1.7). An assumption of matrix flow is justified by the following observations. The response to the Sep. 1, 2007, applied event at the tensiometers, ECH<sub>2</sub>O probes, and lysimeter drain was rapid (Figure 3.20), but did not show indications of preferential macropore flow: the pressure gradient immediately behind the wetting front did not oppose flow (Philip 1975), the wetting front velocity decreased with depth (Raats 1973), the moisture content at the wetting front was less than saturation (Birkholzer and Tsang 1997), and the outflow hydrograph lacks an abrupt change in the flow rate after peak discharge. The term matrix flow is used here to describe flow that may be characterized by the Richards equation. Further evidence of Darcian flow is discussed below in the interpretation of flow velocity from observations of the wetting front and the specific conductance of the outflow.

The flux past the tensiometer profile (which was observed as tension minima that propagated slightly faster than the wetting front) is estimated to have been 12 mm/d ( $1.4 \cdot 10^{-7}$  m/s) between tensiometers at 0.3 m and 0.6 m depths and 3.6 mm/d ( $4.1 \cdot 10^{-8}$  m/s) between the tensiometers at 0.6 m and 0.9 m depth. The average flux during the 10 days after the applied rainfall was 1.3 +/- 0.15 mm/d (0.05 +/- 0.002 mm/h) at the tensiometer profile. This flux was approximately twice the flux derived from the lysimeter outflow (0.6 mm/d), indicating a decrease in flux with an increase in depth.

### 3.7.2 *Wetting Front Propagation*

A distinct wetting front was measured after each of five rainfall events at the profile of ECH<sub>2</sub>O sensors at the upper lysimeters in 2007. Two of these wetting fronts reached the drains of the lysimeters. The wetting front generated by the applied rainfall event of September 1 propagated at a velocity that decreased from 1.9 m/d (80 mm/h) at the 0.3 m

depth to 0.7 +/- 0.1 m/d (25 mm/h) at the 1.7 m depth. These wetting front velocities were calculated as the depth to the moisture content sensor or lysimeter drain divided by the average time of wetting front arrival. The average time of wetting front arrival is defined here as the average of 1. the elapsed time from the rainfall to the initial increase in moisture content or outflow, and 2. the elapsed time from the rainfall to the peak in moisture content or outflow. This method follows a simplified application of the kinematic wave model (Germann *et al.*, 1997). The uncertainty in the velocity of the wetting front at the 1.7 m depth reflects the 28% difference in the wetting front arrivals observed at the two lysimeters.

A wetting front may propagate by the displacement of resident porewater in response to propagation of a pressure wave, by by-passing flow through large pores, or by a combination of both of these processes. Non-preferential by-passing flow is considered conceptually here as water that travels through larger pores that are mostly air-filled ahead of the wetting front. This type of flow is essentially the same as macropore flow, with the distinction that the large pores are relatively ubiquitous in the porous medium and therefore enable rapid flow to by-pass resident porewater without following a preferential pathway. Outflow from macropore flow or non-preferential by-passing flow would be expected to have relatively low concentrations of dissolved solids (Tran *et al.*, 2003; Wagner *et al.*, 2006). However, the drainage from both lysimeters had a specific conductance that remained high throughout the outflow response to the applied rainfall event (Figure 3.20). In addition, the estimates of wetting front velocity are approximately 1,000 times greater than the values of groundwater flux discussed above, indicating that the wetting front represents a wave of kinematic energy rather than the velocity of the

flow of molecules of water. Flow by displacement of porewater rather than by-passing flow, therefore, appears to have dominated the flow mechanisms at the upper collection lysimeters under thawed conditions.

### 3.7.3 *Flow velocity*

Flow velocity, the velocity at which water molecules travel through porous media, was not measured directly at the upper lysimeters. No tracer was applied at the upper collection lysimeters. Because the flow was apparently dominated by the displacement of porewater, the flow velocity is understood to have been significantly slower than the wetting front velocity. The flow velocity was calculated by two methods: 1) by dividing the groundwater flux by the moisture content of the matrix material as a fraction of the total waste rock volume, and 2) by simulating particle transport with a numerical model calibrated by the observed lysimeter outflow (see Section 3.7.4 for the modeling details). The moisture content of the matrix material at the upper lysimeters, as a fraction of the large-scale waste rock, is estimated to be between 0.036 and 0.046  $\text{m}^3/\text{m}^3$  by assuming that the moisture content recorded by the ECH<sub>2</sub>O probes represents the moisture content of the matrix material, which has an average porosity as a fraction of the large-scale waste rock of 0.06  $\text{m}^3/\text{m}^3$  (Section 3.1.9). The average flow velocity during the response to the event is therefore estimated to be approximately 30 mm/d at the tensiometer profile and approximately 15 mm/d at the base of the lysimeters. In a simulation of the event using the VS2D model, particles applied to the top of the lysimeter with the applied rainfall traveled to a depth of about 0.3 m at a velocity of about 30 mm/d.

Therefore, flow in response to the high-intensity applied rainfall was Darcian and moved by displacement of porewater.

#### 3.7.4 Modeling

The transient flow behaviour following the 14.8 mm applied rainfall was modeled in two-dimensional space using VS2D. Simulations were carried out for three types of model domain (Figure 3.21): Simulation 1. a homogenous domain consisting entirely of the hydraulic properties measured in the matrix material, Simulation 2. a domain consisting of a lattice zone of the hydraulic properties of the matrix, making up a proportion (20%) of the domain area equivalent to the finer-than-10 mm proportion of the waste rock, around zones of no flow, and Simulation 3. a homogenous domain consisting of estimates of the hydraulic properties of the waste rock at the large-scale. In simulation 2, the zones of no flow represent boulders, cobbles, and large voids that remain unsaturated. Boundary conditions in the models are: 1. specified flux at the top (either rain or evaporation), 2. no flow at the sides, and 3. possible seepage at the bottom (which establishes a condition of  $h=0$ ). Simulations were carried out in 2D to allow for lateral flow, particularly under the sloped section of the top of the lysimeter walls and through the lattice of Simulation 2. Initial conditions in the models are the moisture content measured by the ECH<sub>2</sub>O probes prior to the applied rainfall, which, in the case of Simulation 3, was multiplied by the matrix proportion (approximately 20%) to estimate the initial moisture content of the large-scale waste rock.

Simulations were run on a trial-and-error basis to identify parameters from the range of measured values that produced the best fit of the lysimeter outflow. The model parameters are given in Table 3.2. Simulation 1 underestimated the wetting front velocity by 13% and underestimated the cumulative outflow by 6%. Simulation 2 overestimated the wetting front velocity by 190% and underestimated the cumulative

outflow by 141%. Simulation 3 was surprisingly unsuccessful given the success of back-of-the-envelope calculations utilizing the particle-size-distribution-based, multiplicative scale-up technique. This effort, however, was not exhaustive, and further research involving estimation of the WRC at the large-scale and parameter optimization may yield a better fit to the measured flow behaviour.

This modeling exercise was undertaken to illustrate that a simplified representation of the flow system is capable of characterizing flow under thawed conditions over a depth range of 1.7 m. However, the modeled flow behaviour is highly sensitive to the hydraulic parameters used in the model, relative to the uncertainty in those parameters. For example, a 0.01 change in porosity or a 25% change to the WRC  $\alpha$  value can cause the simulated flow behaviour to change from one with overestimated outflow rate and cumulative outflow to a simulation with no outflow at all. This high level of sensitivity results in a very unique set of parameters, when only one of the parameters is allowed to vary in the trial-and-error process of multiple simulations. Since each of the parameters may be adjusted during calibration, however, the set of parameters listed in Table 3.2 is not a unique solution: several others may exist. The degree of sensitivity relative to uncertainty in the accuracy of the estimated hydraulic parameters limit the potential for application of these simplified model simulations for predictions of flow in waste rock, even where preferential flow is insignificant.

The model described as Simulation 1 is considered to be applicable to flow at the Type 3 upper collection lysimeters. Despite having a poor physical representation of the actual flow system, the model was calibrated to the observed wetting front propagation and lysimeter outflow. It is understood that the hydraulic properties of the waste rock at

the large-scale are different than that of the matrix material, but a model that neglects this difference is nonetheless capable of simulating the flow behaviour over a depth range of 1.7 m. Attempts at modeling flow through waste rock were less successful for a model domain that accounts for an assumption that water is channeled around boulders and large voids. More research is required to further explore treatment of the flow system as a homogenous domain characterized by hydraulic parameters that are estimated for the large-scale waste rock using the up-scaling factors suggested in Section 3.1.9.

### 3.7.5 *Effects of freeze-thaw conditions at the ground surface*

Changing thermal conditions near the waste rock surface were associated with a reduction in the flow rate at both lysimeters (Sep. 12, Figure 3.17) that was followed by extremely rapid flow at the west lysimeter. Outflow at the west lysimeter increased by a factor of 300 in less than 1 minute, to a peak outflow of approximately 100 L/d (or 4 mm/h, if the event may be described as having a flux through the full area of the lysimeter), and then returned to the antecedent flow rate after 8 hours. This event had a cumulative outflow per unit area of 0.7 mm (volumetric flow of 1.4 L): 9% of the total outflow from Sep. 1 to Sep. 20. In terms of the increase in flow rate and the steepness of the recession, this event was at the extreme of macropore flow observed under thawed conditions in waste rock (Nichol *et al.*, 2005; Marcoline, 2008).

The peak outflow may represent macropore flow caused by the following process: (1) an increase in saturation near the surface from the 2.4 mm rainfall on Sep. 8; that (2) froze in the upper several centimeters on September 10 and 11 (minimum air temperature -2.9° C) to limit the infiltration capacity; (3) infiltration from the 1 mm rainfall Sep. 12 and 13 focused through coarse material at the surface in locations where ice saturation

was not reached; and (4) macropore flow (or film flow along the lysimeter wall) to the 1.7 m depth. The cumulative outflow associated with this event represented 70% of the rain that fell on September 12 and 13, or 20% of the rain that fell between September 8 and 13.

During this apparent macropore flow event, the specific conductance of the outflow remained elevated (Figure 3.20). The significance that an event such as this may have on solute mass loading is discussed below in Section 3.9.

While rapid flow was observed at the west lysimeter, outflow was abruptly reduced at the east lysimeter. The cause for the rapid reduction of flow at the east lysimeter from Sep. 12 to Sep. 13 is unknown. Immediate stoppage or significant reduction of lysimeter outflow was observed on at least three other occasions during the time when air temperatures changed about the freezing point in September and October (Figure 3.17). On a shorter (hourly) time-scale the outflow depression was associated with an increase in temperature from freezing to above freezing conditions.

It should be noted that the apparent macropore flow was not due to the release of an air lock in the outflow plumbing. The establishment of an air lock requires a meniscus to form that completely stops the flow until pressure is sufficient to break the meniscus. Prior to the rapid increase in outflow rate observed on September 12, the outflow rate was abruptly reduced, but the flow did not stop. Similarly, the abrupt reductions in the flow rate were not due to freezing of the waste rock at the base of the lysimeter, freezing of water in the drain pipe, or freezing of the tipping bucket flow gauge. Thermistors in the vicinity of each of these locations indicate that freezing at this time occurred only in the upper several centimeters of the waste rock.

In summary, abrupt changes in flow through waste rock may occur in association with the onset of freezing conditions in September and October at the study site. The indications of macropore flow and abrupt decreases in flow rate presented here are preliminary, and more measurements during this time period of subsequent years are required to verify these measurements and to provide evidence of causation. The uncertainty in whether these events represent hydrologic phenomena, as opposed to some unexplained problem with flow gauging, results in just a 3% uncertainty in the estimate of cumulative outflow in 2007. However, these events indicate that even in very coarse material, a hydraulic connection through the vadose zone may enable the onset of freezing conditions at the surface to have immediate and drastic effects on the outflow rate.

### **3.8 Flow mechanisms: 14 m-high test piles**

#### *3.8.1 Response to high- and moderate-intensity rainfall*

Flow in the Type 3 test pile in response to high-intensity rainfall events was observed under two conditions: (1) initial matrix moisture content at or below residual moisture content and (2) initial matrix moisture content greater than field capacity (0.1 to 0.15). The first condition was measured throughout the test piles in 2006 and at depths greater than approximately 7 m in 2007. The second condition was measured in the upper 5 to 7 m of the Type 3 test pile in 2007.

Wetting fronts were detected by TDR as distinct increases in moisture content in response to rainfall events. For each rainfall event, the velocity of a wetting front was estimated at each TDR probe that measured a distinct rise in moisture content, using the

method described in Section 3.7.2. In Figure 3.22a, the wetting front velocity is reported as the average of the velocities calculated at each of the TDR probes that detected the wetting front. A general direct relationship was observed between the average wetting front velocity and both the magnitude of the rainfall and the initial moisture content of the matrix (Figure 3.22a). The magnitude of the rainfall is best measured by the intensity (mm/h) and duration, and it was expressed as a recurrence interval relative to the forty-eight year climate record for the region using statistics reported by Golder Associates (2008). Only the event with about a 35 yr recurrence interval (7.7 mm/h rainfall intensity for a duration of 3.8 h on September 13, 2007), which infiltrated into waste rock with matrix moisture content above field capacity, generated rapid, spatially variable flow indicative of macropore flow.

Soon after completion of test pile construction in 2006, three applied rainfall events, of 24 mm, 19 mm, and 15 mm, were conducted at the top of the pile over seven days when the average matrix moisture content over the full height of the test pile was just 0.03 (12% saturation) (Figure 3.22b). The wetting front generated by these events propagated into the upper 2 m at an approximate velocity of 0.2 m/d (Figure 3.22b), froze during the winter, was remobilized with the thaw propagation, and propagated to a depth of about 5 +/- 1 m by the end of July, 2007, with an estimated average velocity for the entire event of 0.01 m/d (5 m/yr). The wetting front was relatively uniform, with an average relative standard deviation of 0.29 m/d between TDR observations at approximately the same depth, and the front slowed as it propagated into the dry waste rock. No flow reported to the base of the pile and there was no evidence of significant macropore flow. Since the waste rock was near residual saturation prior to the applied

rainfall events, flow by displacement of porewater was likely insignificant. The applied water from these events contributed solely to an increase in storage. Therefore the wetting front velocity for these initial events was approximately equal to the flow velocity (the velocity of an average water particle).

Moderate-intensity rainfall events in 2007 produced hydraulic responses that differed from one another despite the presence of similar conditions prior to each event. A 15.5 mm natural rainfall (1.3 mm/hr, < 2yr recurrence interval) generated no discernable response in the TDR sensors at a time when the moisture content of the matrix in the upper 4 to 5 m of the Type 3 test pile was approximately 14%. However, subsequent natural rainfall of 10.7 mm and 4.1 mm (0.9 mm/hr and 0.6 mm/hr) at a time when the moisture content of the matrix in the upper 4 to 5 m of the Type 3 test pile averaged 15% and 18%, respectively, generated similar wetting fronts to a depth of 2 m with average velocities of 0.3 m/d and 0.2 m/d (Figure 3.22c). The groundwater flux at the wetting front generated by the 10.7 mm rainfall, at a depth of 0.9 m, is estimated to be approximately 2 mm/d and 5 mm/d at the tensiometer profiles, using Darcy's Law and the hydraulic conductivity curve determined by the method described in Section 2.4.1. These moderate-intensity natural rainfall events did not generate macropore flow that could be detected by the TDR sensors below the horizontal top of the pile, but they caused a rapid increase in the pile outflow measured at the basal drain (Figure 3.19). At the pile toe, where the flow path to the basal drain is the shortest, the average depth of the HDPE liner is 3 to 4m, and boulders dominate the waste rock. The significance of rapid flow through batters is discussed below in Section 3.9 (*Solute mass loading estimates*).

An applied rainfall event of 29 mm (8 mm/h, 35 yr recurrence interval) on September 13, 2007, created a significantly different hydraulic behaviour at a time when the moisture content of the matrix in the upper 4 to 5 m of the Type 3 test pile was approximately 14% (55% saturation). The response in volumetric moisture content to this event is shown in Figure 3.22d. The event was conducted as the application of a LiCl and LiBr tracer 27 days after a deuterium ( $D_2O$ ) tracer was applied with 16 mm of rain. The tracer tests are discussed in more detail by Gupton (in progress). Preliminary results from the tracer tests indicate that flow did not reach the base of the test pile (14 m depth) from the top of the pile in 2007. The detection of an initial increase in both  $Cl^-$  and  $Br^-$  in samples taken from soil water suction samplers indicates a maximum flow velocity, which is calculated as the depth to the sampler divided by the time from the application of the tracer to the approximate time of the initial increase in tracer concentration. A maximum flow velocity at four locations in the upper 5 m of the Type 3 test pile was less than 50 to 140 mm/d (0.05 to 0.1 m/d). However, maximum flow velocity at samplers located at depths of 3.4 m, 4.5 m, and 6.8 m was 120 to 720 mm/d (0.1 to 0.7 m/d), and with higher velocity calculated at greater depth. This overall range in flow velocity of 50 to 720 mm/d shows a highly heterogeneous flow response to this high-intensity applied rainfall event. The following observations indicate that macropore flow occurred at various locations to a depth of at least 6.8 m in response to the applied rainfall: (1) highly heterogeneous flow response, (2) higher flow velocity at greater depth, and (3) flow velocities were on the order of the rainfall rate or greater.

Flow detected at two tensiometer profiles in response to the 29 mm applied rainfall event (Figure 3.23), however, appeared to be Darcian: the pressure gradient immediately

behind the wetting front did not oppose flow (Philip 1975) and the wetting front velocity decreased with depth (Raats 1973). A groundwater flux at the wetting front at an approximate depth of 0.9 m was calculated as 10 mm/d and 17 mm/d at the tensiometer profiles, using Darcy's Law and the hydraulic conductivity curve determined by the method described in Section 2.4.1. An estimate of the average groundwater flux past the tensiometer profiles in the Type 3 test pile was 0.8 +/- 0.2 mm/d downward for the duration of tensiometer deployment in 2007: from Aug. 2 to Sep. 16. The upper 5 to 7 m of the test pile was thawed for about 145 days of 2007, so this flux may be expanded to make an average annual flux estimate of 120 +/- 30 mm/yr (0.8 +/- 0.2 mm per day times 145 days). However, this period of 2007 included three applied rainfall events that each had recurrence intervals greater than five years. The infiltration estimate of 60 mm/yr, obtained by estimating evaporation and neglecting any long-term change in storage, may provide a better estimate of average annual flux through the top of the waste rock pile.

The wetting front in response to this rainfall event was detected by TDR to a depth of about 7 m with an average velocity of 1.1 m/d. The wetting front did not propagate uniformly, with observed velocities from the different TDR probes ranging from 0.09 m/d to 5 m/d and an average relative standard deviation of 0.77 m/d between observations at approximately the same depth. The fastest response and slowest response was observed at TDR probes located in the same depositional layer only about 2 m apart from one another. The outflow at the base of the pile did not respond to this applied rainfall event (Figure 3.19), indicating that no significant amount of flow and no pressure wave response reached the 14 m depth.

### 3.8.2 Modeling

Unsaturated flow through the Type 3 test pile is simulated using VS2D. The purpose of modeling the flow behaviour is to determine whether the flow can be described using the measured hydraulic parameters and to explore the conditions under which predictive modeling may potentially be most useful in future studies.

A 2D model was defined with the dimensions of a cross-sectional area of the pile: 50 m at the base, 35 m at the flat top 14 m above the basal drain, and with an angle-of-repose batter representing the west aspect of the pile (Figure 3.24). The boundary condition is a specified flux at the flat top surface and the sloping surface of the batter, which was either an infiltration flux or an evaporative flux. A boundary condition of no flow is set at the 14 m vertical eastern boundary, and the condition of possible seepage, which established a condition of  $h = 0$ , is set at the base of the pile.

The sum of the natural and applied rainfall rate and the snowmelt rate are applied to the top boundary of the model as the infiltration flux. The measured rainfall rate for 2007 was specified at the top boundary of the model over periods ranging in time from 1.7 h to 28 d. The rainfall rates specified in the model are listed in Table 3.3. Snowmelt occurs primarily on the pile batters, where wind deposition is greatest. Snow depths at the onset of the 2007 spring melt were estimated from visual inspection to be less than 10 cm at the top of the piles and between approximately 100 and 200 cm on the pile batters. The following estimates were used to assign a snowmelt infiltration flux to the model batter of 11.4 mm/d from May 5 to May 12, 2007, and 26.0 mm/d from May 20 to May 30, 2007: average snow depth on the batters of the pile of 1.4 m, 20 cm of snow sublimated (based on measurements presented in Figure 3.5 and estimates made by Golder Associates,

2005), and 30% snow moisture content (based on measurements at Diavik presented in Golder Associates, 2008). The snowmelt periods were assigned based on visual observations and air temperature measurements made at the study site. The snowmelt rates specified in the model are listed in Table 3.3.

The evaporative flux is modeled in VS2D by specifying the potential evaporation, surface resistance, and the pressure potential of the atmosphere over a period of time. In the model, these parameters are used together with the unsaturated hydraulic potential in the uppermost model cells, which is related to the moisture content by the water retention curve parameters, to calculate the evaporative flux across the boundary (Lappala, *et al.*, 1987). Since the flux through the boundary can proceed in only one direction at a time, evaporation is modeled only when the infiltration flux is zero.

The complex interaction between fluid flow and heat transfer during freezing and thawing (*i.e.* Hansson, *et al.*, 2004) cannot be simulated using VS2D. The period from May 5 to approximately July 12, while the waste rock pile was thawing, was modeled separately with the  $K_{sat}$  set to a value 45% of the  $K_{sat}$  for the thawed period. The times when the frozen conditions dominated the flow behaviour were neglected from the analysis: only the period from May 5 to October 27, 2007, were simulated.

Hydraulic parameters for the waste rock were assigned to the model by using the upscaling techniques described in Section 2.4.9 and Section 3.1.9. The porosity, residual moisture content, and initial moisture content values estimated for the matrix material were multiplied by an upscaling factor of 0.25 to yield the parameters provided in Table 3.4. Model calibration was then carried out with a trial and error approach to determine the  $K_{sat}$  and WRC parameters that produce a best fit between the simulated and

field measured wetting front propagation beneath the top of the pile and the outflow from the base of the pile. This modeling approach essentially neglects macropore flow. It is therefore expected to be capable of simulating only flow in response to rainstorms with a recurrence interval of approximately 30 years or less, under the rainfall conditions at the study site.

The wetting front that propagated into the initially dry Type 3 test pile was simulated with a velocity within 20% of the estimated velocity of the wetting front measured in the field (Figure 3.25). Table 3.5 summarizes the field estimates and model simulations for the average wetting front velocity, average groundwater velocity, average outflow rate from the base of the test pile, the cumulative outflow, and the cumulative evaporation, each for the year 2007. Figure 3.25 presents plots of the simulated evaporation using the VS2D model and the estimated evaporation using the FAO Penman-Monteith method, and field measurements and VS2D simulation results for outflow rate and cumulative outflow from the base of the pile. The outflow rate and cumulative outflow were simulated to within 10% of the field estimated values. Evaporation in 2007 was simulated to be 16% lower than the estimate of 95 mm made using the FAO P-M method. Transport of a conservative tracer (that does not correspond with any of the tracers actually applied to the Type 3 test pile) was simulated using the calibrated model to estimate an average groundwater flux within the upper 2 m of 8 mm/d from July to September, 2007. This estimate is approximately 50% of the value estimated over the same time period from data collected with tensiometer profiles and a field calibrated unsaturated hydraulic conductivity relationship (presented in the previous section).

### 3.9 Solute mass loading estimates

Flow behaviour may determine solute concentrations (Wagner *et al.*, 2006). Changes in the flow rate may be more significant than changes in solute concentrations in producing mass loading behaviour from the base of a waste rock pile. While mass loading is discussed here from the perspective of flow analysis, Smith (*in progress*) discusses mass loading from a geochemical perspective. In some cases, peak outflow at the base of the Type 3 test pile was associated with a decrease in specific conductance that may indicate a greater proportion of flow through waste rock with large pore spaces (Tran *et al.*, 2003, Wagner *et al.*, 2006). Measurements of specific conductance were related to major ion concentrations, including sulfate, in samples taken from the outflow at the Type 3 test pile (Smith, *in progress*). The analysis of these samples indicate that the specific conductance may be used to estimate the sulfate concentration in the outflow with an accuracy of approximately +/- 0.2 g SO<sub>4</sub><sup>2-</sup>/L (Smith, *in progress*). The relationship between specific conductance and sulfate concentration was used with continuous measurements of specific conductance to make an estimate of the sulfate mass loading rate using continuous measurements of the specific conductance in the outflow. The solute mass loading is calculated as:

$$\text{mass loading rate [g/d]} = \text{flow rate [L/d]} \cdot \text{solute concentration [g/L]}. \quad (3)$$

Mass loading may be normalized by the total mass of the waste rock (*e.g.* Wagner *et al.*, 2006) to aid in quantification of geochemical evolution. Mass loading is normalized by area here to avoid uncertainty in waste pile mass and bulk density while aiding in upscaling solute mass loading estimates to a full-scale pile:

$$\text{mass loading [g/m}^2\text{/d]} = \text{flow rate [L/m}^2\text{/d]} \cdot \text{solute concentration [g/L]}. \quad (4)$$

Outflow in response to a high-intensity applied rainfall event at the upper collection lysimeters had relatively constant specific conductance (Figure 3.26). Flow is inferred therefore to have been dominated by porewater displacement, and the change in solute mass loading with time was essentially controlled entirely by the change in the flow rate. The extremely rapid increase in flow (on Sep. 12, 2007, discussed in Section 3.7.5) during the recession from the more sustained peak in flow (from Sep. 5 to Sep. 7) generated a very modest decrease in specific conductance and resulted in an extremely short-duration peak sulfate mass loading rate of 200 g/d/m<sup>2</sup>. The average sulfate mass loading from the upper lysimeter was estimated to be 1.1 g/d/m<sup>2</sup> over the 20 day outflow period. The mass loading associated with the extreme peak in flow constituted 16% of the total loading during the period.

At the Type 3 test pile, outflow in response to a moderate-intensity natural rainfall event on August 21, 2007, included a rapid increase in flow rate and a sustained decrease in specific conductance (Figure 3.27a). The freshening of the outflow indicates an increase in the proportion of flow through large pores at the base of the batter, but the decrease in specific conductance was relatively insignificant in terms of the change in solute mass loading. During the event both the outflow rate and the estimated sulfate mass loading rate doubled. Over the course of the 2007 summer, both the outflow rate from the Type 3 test pile and the specific conductance of the outflow were at a maximum in late July to early August. The result was a maximum rate of sulfate mass loading of approximately 2.8 g/d/m<sup>2</sup> during the middle of the summer season (Figure 3.27b). The cumulative sulfate mass loading was normalized by the estimate of the area of the basal drain contributing to flow, which changed during the season. For 180 days of outflow

during the year 2007, the cumulative sulfate mass loading from the Type 3 test pile is estimated to be  $135 \pm 40 \text{ g/m}^2$ .

The average sulfate mass loading rate at the Type 3 test pile in 2007 is therefore estimated to be approximately  $0.8 \text{ g/d/m}^2$ . This value is 1.5 times lower than the mass loading rate estimated for the upper lysimeter, suggesting that an upscaling parameter may apply between the 2 m-scale and the 14 m-scale. However, since the outflow from the test pile flowed primarily through the batter of the pile, the lower mass loading rate may be associated with the high proportion of coarse material at the base of the pile or large proportion of the flow resulting from snowmelt.

**Table 3.1** Waste rock hydraulic parameters.

Sample scale	Saturated hydraulic conductivity		Porosity		Non-capillary pores $v_{max} / v_{avg}$	Water retention curve van Genuchten-Mualem model	
	mean m/s	SD m/s	m <sup>3</sup> pores / m <sup>3</sup> sample	m <sup>3</sup> matrix pores / m <sup>3</sup> large-scale sample	-	$\alpha$ kPa <sup>-1</sup>	$n$ -
large-scale waste rock	$1.5 \cdot 10^{-2}$	-	0.25	0.06 to 0.08	10	0.1	3
waste rock matrix	$9 \cdot 10^{-6}$	$1 \cdot 10^{-5}$	0.23	-	-	0.5	1.7
top surface of test piles	$5 \cdot 10^{-6}$	$8 \cdot 10^{-6}$	-	-	-	0.2	1.6

**Table 3.2** A summary of the model approaches and parameters used to analyze the flow response to a high-intensity rainfall event at the upper collection lysimeters. The success of each approach is presented in terms of the error in the wetting front velocity ( $v_{wf}$ ) and the cumulative outflow volume (Vol.).

<b>Simulation*</b>	<b>K<sub>sat</sub></b> m/s	<b>Porosity</b> m <sup>3</sup> /m <sup>3</sup>	<b>θ<sub>res</sub></b> m <sup>3</sup> /m <sup>3</sup>	<b>α<sub>VG-M</sub></b> m <sup>-1</sup>	<b>n<sub>VG-M</sub></b> --	<b>v<sub>wf</sub> Error</b> %	<b>Vol. Error</b> %
1	2.E-05	0.22	0.1	4.5	1.3	13	6
2	8.E-06	0.25	0.08	1	1.4	225	141

**\* Simulation Approach**

1. Matrix properties applied to a homogenous domain.
2. Matrix properties applied to 20% of the domain. No flow specified at the remaining fraction of the domain.

**Table 3.3** Infiltration periods and the flux specified in the VS2D models. Evaporation is simulated during the even-numbered periods, which are highlighted in grey.

	Model Period	Period Start Date	Period End Date	Top of Pile				Batter				Top	Batter
				Rainfall		Snowmelt		Rainfall		Snowmelt		Rain + Snowmelt	
				mm	mm/d	mm	mm/d	mm	mm/d	mm	mm/d	mm/d	mm/d
model for the thawing period	1	5-May-07	12-May-07	12	1.7	5	0.7	12	0.2	80	11.4	<b>2.4</b>	<b>11.6</b>
	2	12-May-07	20-May-07	0	0	0	0	0	0	0	0	<b>0</b>	<b>0</b>
	3	20-May-07	30-May-07	2.5	0.3	0	0	2.5	0.1	260	26.0	<b>0.3</b>	<b>26.1</b>
	4	30-May-07	13-Jun-07	0	0	0	0	0	0	0	0	<b>0</b>	<b>0</b>
	5		13-Jun-07	3.1	24.8	0	0	3.1	24.8	0	0	<b>24.8</b>	<b>24.8</b>
	6	13-Jun-07	12-Jul-07	0	0	0	0	0	0	0	0	<b>0</b>	<b>0</b>
model for the thawed period and the onset of freezing conditions	7	12-Jul-07	25-Jul-07	41.3	3.2	0	0	41.3	3.2	0	0	<b>3.2</b>	<b>3.2</b>
	8	26-Jul-07	7-Aug-07	0	0	0	0	0	0	0	0	<b>0</b>	<b>0</b>
	9	8-Aug-07	12-Aug-07	2.7	0.7	0	0	2.7	0.7	0	0	<b>0.7</b>	<b>0.7</b>
	10	12-Aug-07	16-Aug-07	0	0	0	0	0	0	0	0	<b>0</b>	<b>0</b>
	11	17-Aug-07	19-Aug-07	26.8	13.4	0	0	10.7	5.4	0	0	<b>13.4</b>	<b>5.4</b>
	12	19-Aug-07	20-Aug-07	0	0	0	0	0	0	0	0	<b>0</b>	<b>0</b>
	13		21-Aug-07	10.5	21.0	0	0	10.5	21.0	0	0	<b>21.0</b>	<b>21.0</b>
	14	22-Aug-07	27-Aug-07	0	0	0	0	0	0	0	0	<b>0</b>	<b>0</b>
	15	27-Aug-07	1-Sep-07	5	1.0	0	0	5	1.0	0	0	<b>1.0</b>	<b>1.0</b>
	16	1-Sep-07	4-Sep-07	0	0	0	0	0	0	0	0	<b>0</b>	<b>0</b>
	17		4-Sep-07	15	205.7	0	0	0	0	0	0	<b>205.7</b>	<b>0</b>
	18	4-Sep-07	12-Sep-07	0	0	0	0	0	0	0	0	<b>0</b>	<b>0</b>
	19		13-Sep-07	29.2	171.8	0	0	0.2	1.2	0	0	<b>171.8</b>	<b>1.2</b>
	20	14-Sep-07	25-Sep-07	0	0	0	0	0	0	0	0	<b>0</b>	<b>0</b>
	21	25-Sep-07	8-Oct-07	6	0.5	0	0	6	0.5	0	0	<b>0.5</b>	<b>0.5</b>
	22	9-Oct-07	9-Oct-07	0	0	0	0	0	0	0	0	<b>0</b>	<b>0</b>

**Table 3.4** The parameters used in the calibrated VS2D model to analyze the flow at the 14m-high test pile.

Simulation	Period	Saturated Hydraulic Conductivity	Porosity *	Residual Saturation *	Water Retention Parameters (van Genuchten - Mualem)	
		$K_{sat}$ m/d	$\theta_s$ m <sup>3</sup> /m <sup>3</sup>	$\theta_r$ m <sup>3</sup> /m <sup>3</sup>	$\alpha$ m <sup>-1</sup>	$n$ --
1: thawing	May 5, 2007 to July 12, 2007	$1 \cdot 10^{-7}$	0.06	0.01	10	1.8
2: thawed	July 12, 2007 to October 27, 2007	$3 \cdot 10^{-6}$	0.06	0.01	10	1.8

\* Values are applicable to the large-scale waste rock: Porosity is the volume of matrix pores per volume of large-scale waste rock. Residual Saturation is the moisture content of the large-scale waste rock at residual conditions.

**Table 3.5** Results of the calibration of the VS2D model used to simulate flow through the Type 3 test pile in 2007.

	<b>Average Wetting Front Velocity</b>	<b>Average Groundwater Velocity <sup>a</sup></b>	<b>Average Outflow Rate</b>	<b>Cumulative Outflow</b>	<b>Cumulative Evaporation</b>
	mm/d	mm/d	m <sup>3</sup> /d	m <sup>3</sup>	mm
<b>Field Measurements</b>	36	15 <sup>b</sup>	0.69	130	95 <sup>d</sup>
<b>Model Results</b>	29	8 <sup>c</sup>	0.76	126	80

Notes:

- <sup>a</sup> Groundwater flux through the upper several meters of the top of the test pile under thawed conditions.
- <sup>b</sup> Estimated from tensiometer measurements, field calibrated  $K(\phi)$ , and Darcy's Law.
- <sup>c</sup> Estimated from modeling the transport of a conservative tracer.
- <sup>d</sup> Cumulative evaporation modeled using field measurements and the FAO-Peman-Monteith model.

**Table 3.6** Summary of the flow behaviour in the Type 3 test pile and upper collection lysimeters in 2006 and 2007.

Measurement Location	Response to High-Intensity Rainfall				Summer Season				Annual Rate		
	wetting front velocity	peak flux	average flux	flow velocity	wetting front velocity	peak flux	average flux	flow velocity	wetting front velocity	flux	flow velocity
	m/d	mm/d	mm/d	mm/d	mm/d	mm/d	mm/d	mm/d	m/yr	mm/yr	m/yr
upper collection lysimeters 1.7 m depth	0.7 <b>(0.1)</b>	0.7 <b>(0.1)</b>	0.5 <b>(0.1)</b>	15 (10)	-	-	-	-	-	-	-
test pile top surface	1.1 <b>(0.8)</b>	14 <b>(3)</b>	1.4 <b>(0.15)</b>	200 * <b>(200)</b>	30 **	14 <b>(3)</b>	0.8 <b>(0.2)</b>	15 (10)	5 ** (1)	60 †	1 to 5 ††
test pile batter	10	1.2 (0.4)	0.7	-	-	2 to 10	1.5 (0.3)	-	-	270 (70)	-

values in parentheses: **(bold)** indicates a range of values measured at multiple locations; (plain font) indicates uncertainty in an estimate

\* preliminary results

\*\* wetting front propagating into dry waste rock

† estimated from evaporation analysis; represents average site conditions

†† range of estimates using average flux divided by porosity of the matrix at the large-scale (0.06) and by considering the flow velocity into dry waste rock equal to the wetting front velocity

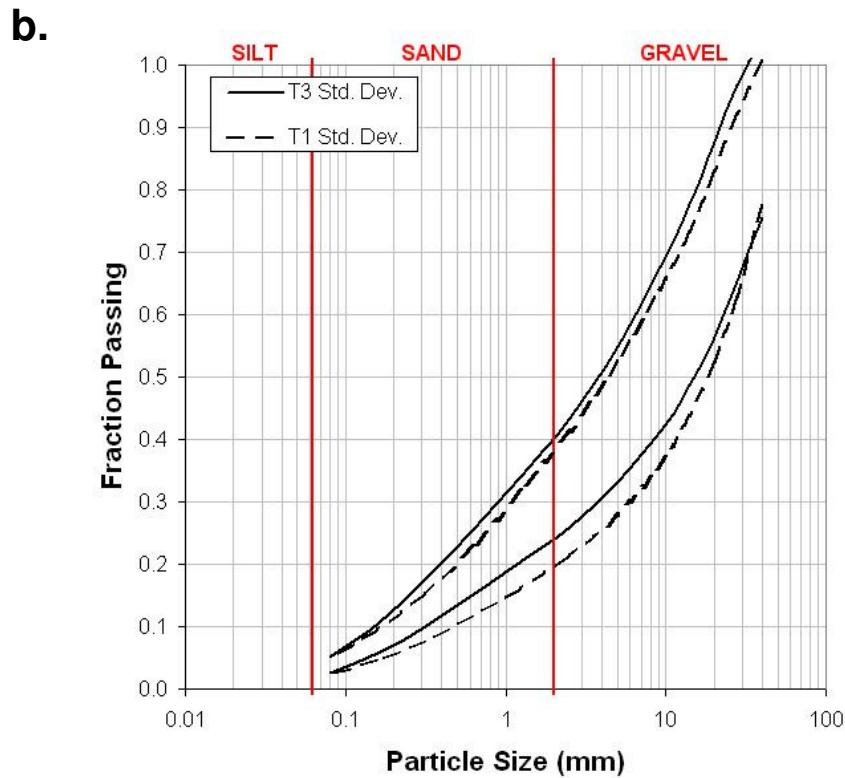
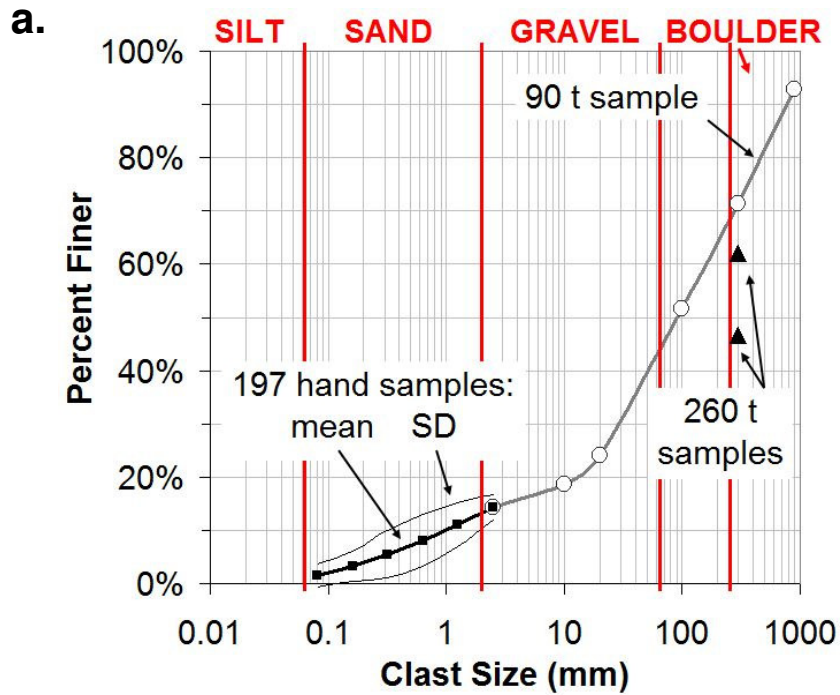


**Figure 3.1** (a) Grain size distribution of the waste rock where the hand sample distributions are shown as the fine portion of the 90 tonne sample distribution. (b) One standard deviation about the mean of Type 1 and Type 3 hand samples.

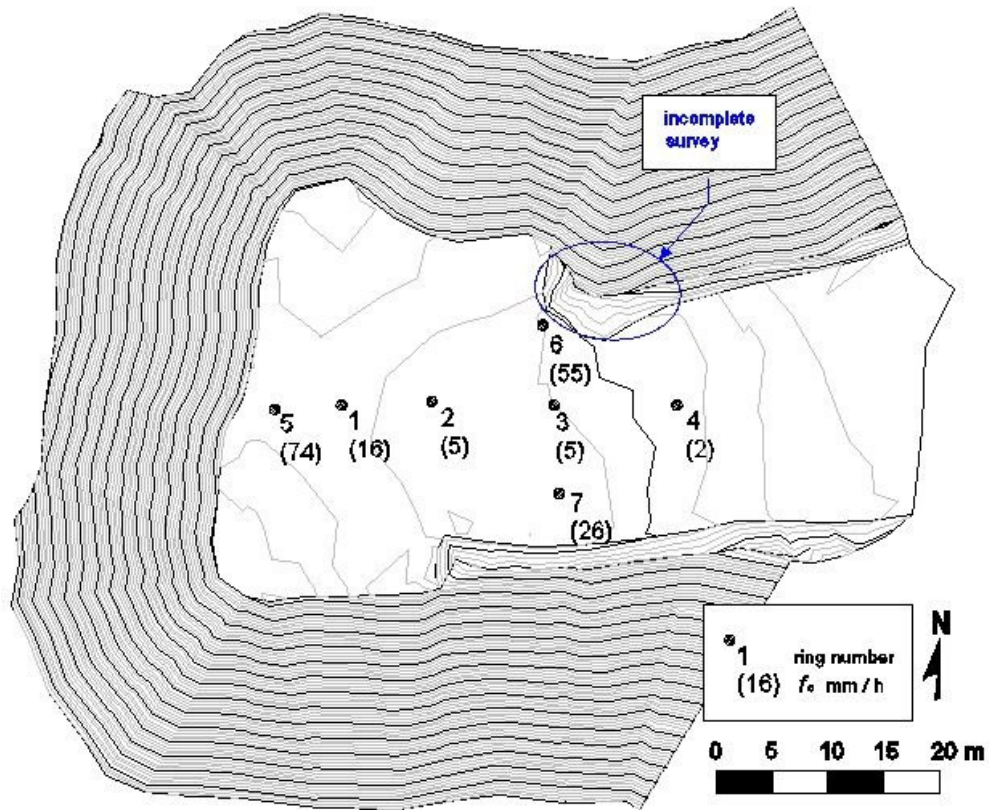


**Figure 3.2** Infiltration capacity (in parentheses [mm/h]) measured by ring infiltrometer tests at the top of the Type 3 test pile.

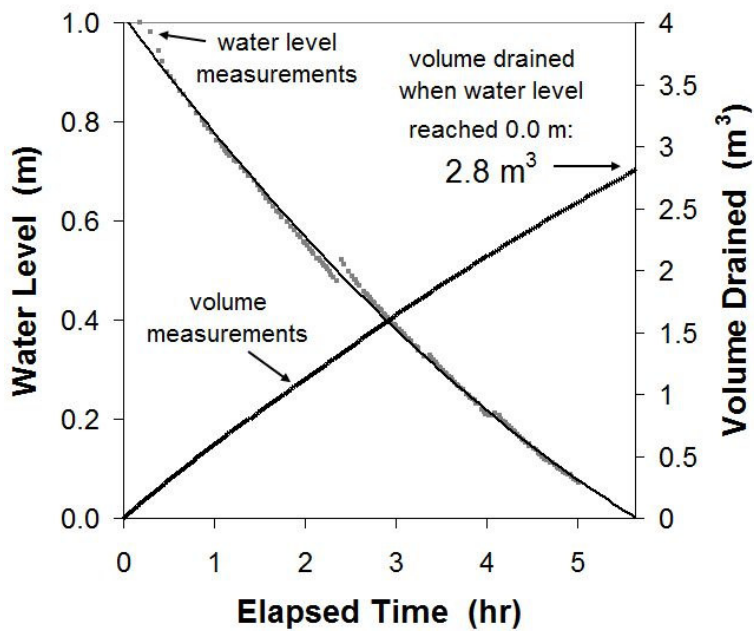


**Figure 3.3** The volume that drained rapidly from the 16 m<sup>3</sup> sample.

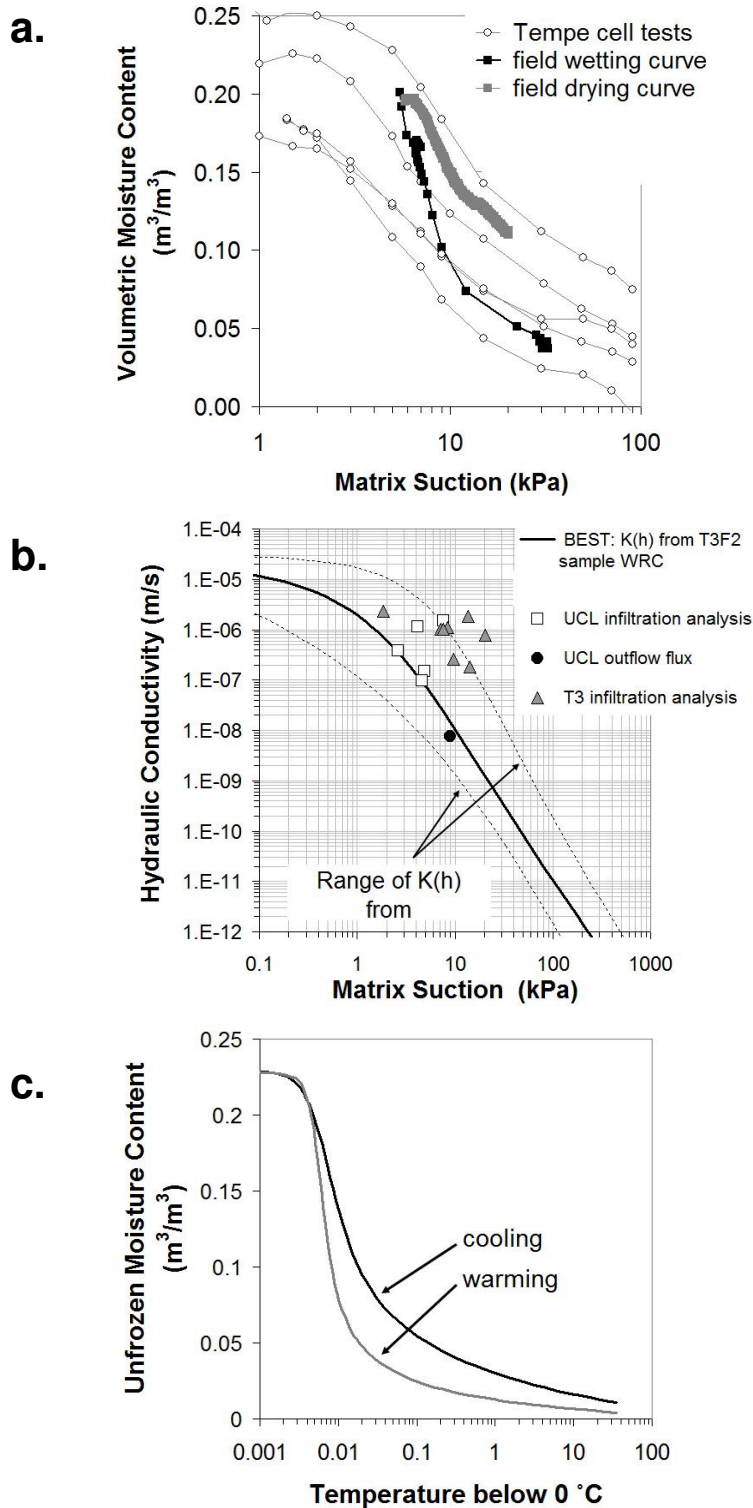
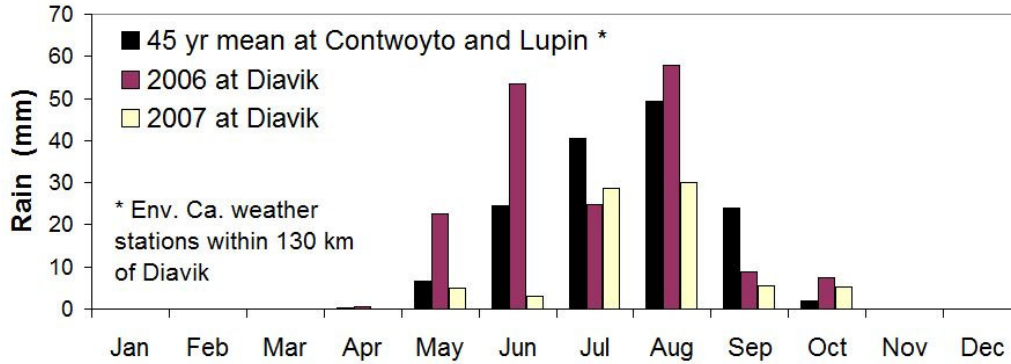


**Figure 3.4** (a) Water retention curves (WRC) measured from waste rock matrix material samples and measured in the field with a soil moisture sensor and a tensiometer. (b) A range of hydraulic conductivity curves determined using a pedotransfer function and the curve calibrated to an infiltration analysis. (c) The estimated portion of moisture remaining liquid due to strong capillary forces imparted by small mineral particles as the matrix freezes or thaws.

a.



b.

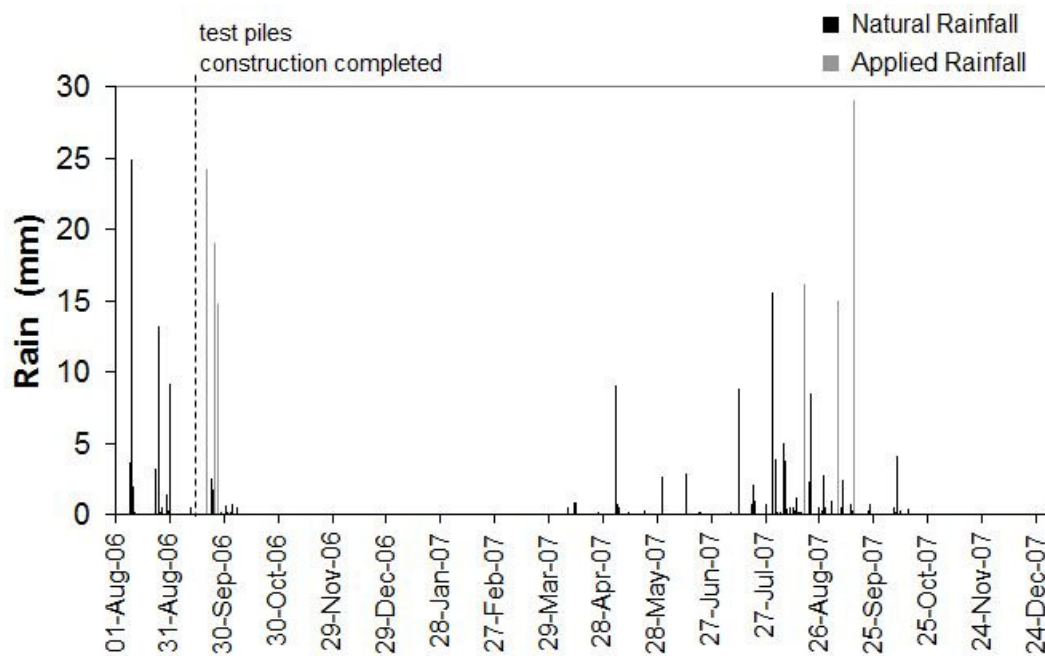


**Figure 3.5** (a) Rainfall in 2006 and 2007 compared to the mean monthly rainfall, and (b) daily rainfall since the construction of the test piles. Applied rainfall events conducted at the top of the Type 3 test pile are shown in gray.

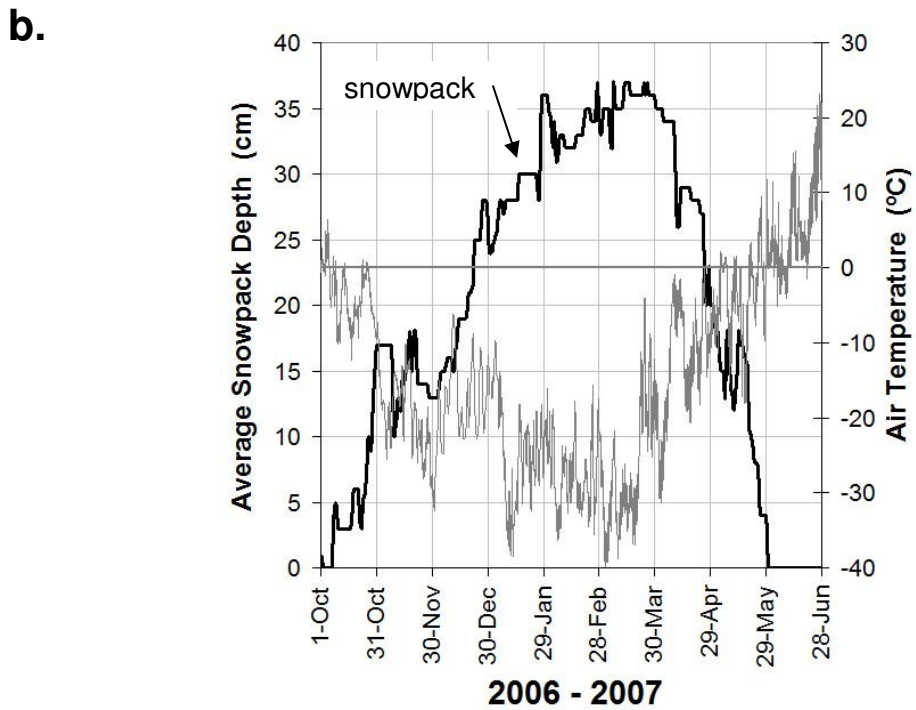


**Figure 3.6** (a) At the beginning of the melt period (April 27, 2007) snow remained on the top of the test piles only near berms, but over 1 m snow remained on the batters. (b) Snowpack depth at the Ekati meteorological station and hourly air temperature at Diavik.

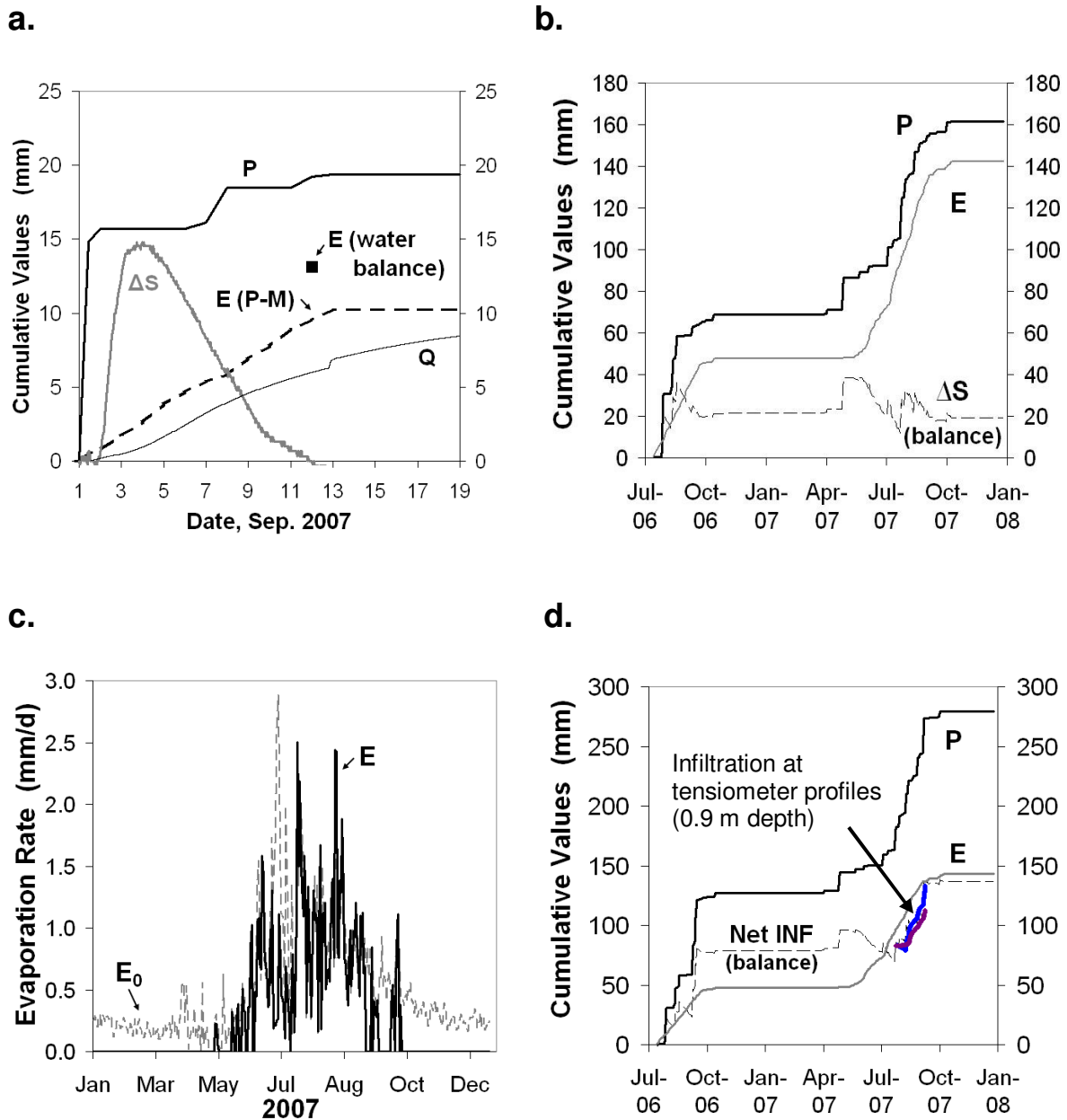


**Figure 3.7** (a) Estimation of evaporation at the Type 3 upper collection lysimeters after an applied rainfall event. (b) Estimated evaporation under natural conditions (drier than average) at the T1 upper collection lysimeters. (c) Estimated daily evaporation rate from the Type 3 test pile. (d) A water balance at the top of the Type 3 test pile under nearly average rainfall with estimated evaporation yields infiltration similar to that calculated using tensiometer profiles.



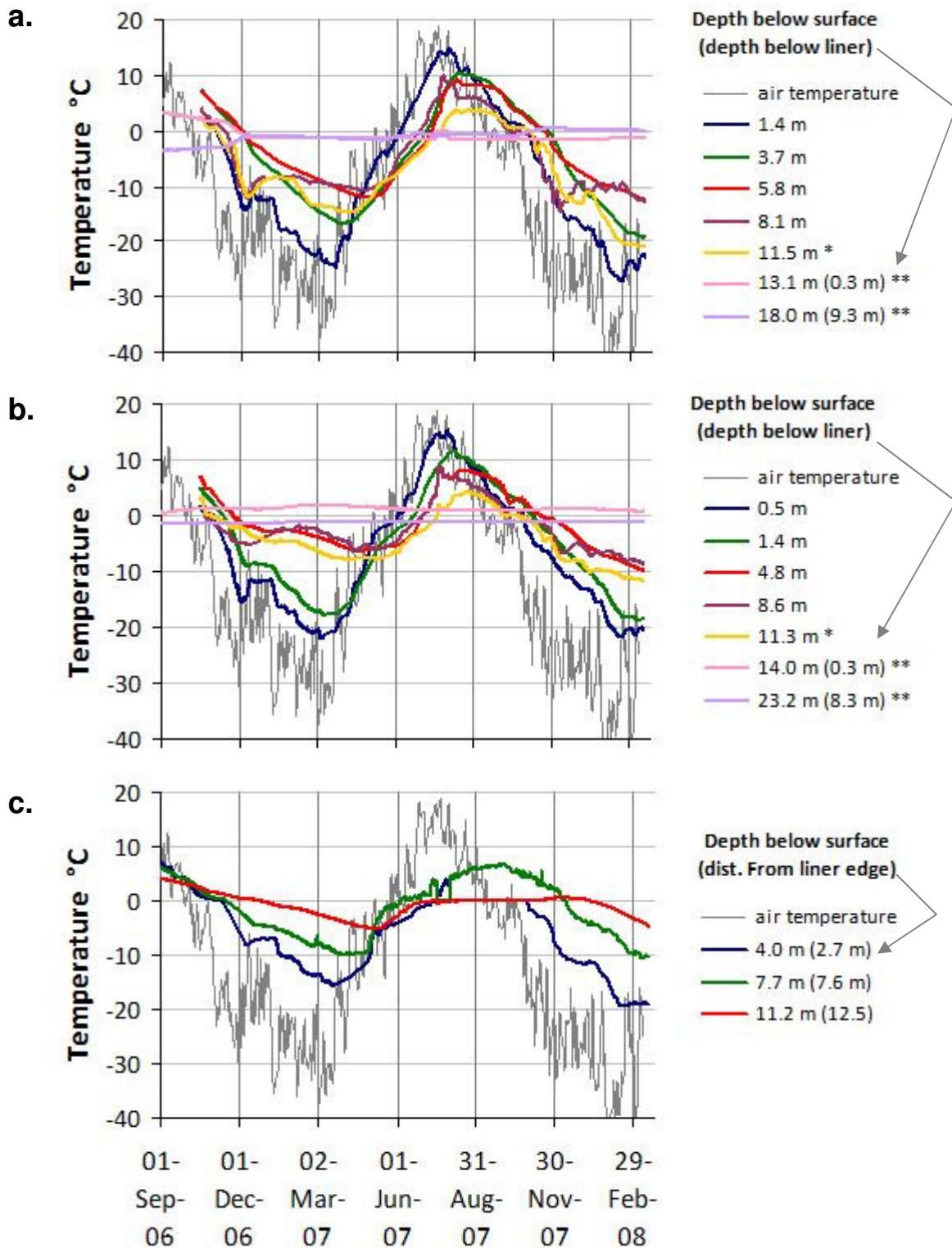


**Figure 3.9** Temperature within (a) the Type 1 test pile and (b) the Type 3 test pile. (In the parentheses are thermistor depth below the HDPE liner at the base of the piles.) (c) Temperature at the depth of the basal drain below the western aspect batter of the Type 1 test pile. (In parentheses are distances from the edge of the pile to the thermistor.)



Mike Gupton

**Figure 3.10** Vapor transport from a waste rock pile warmer than the atmosphere.

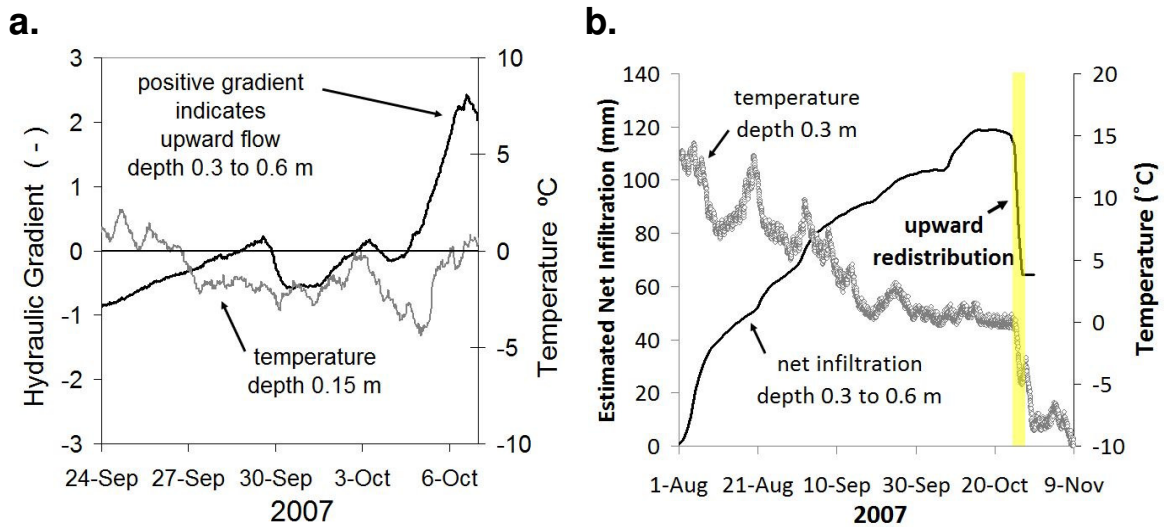


**Figure 3.11** (a) An upward (positive) hydraulic gradient measured with tensiometers when the waste rock above the porous cups froze. (b) Indication of further upward redistribution during five days prior to freezing, using moisture content data, the average WRC, and Darcy's Law.

a.



b.



c.

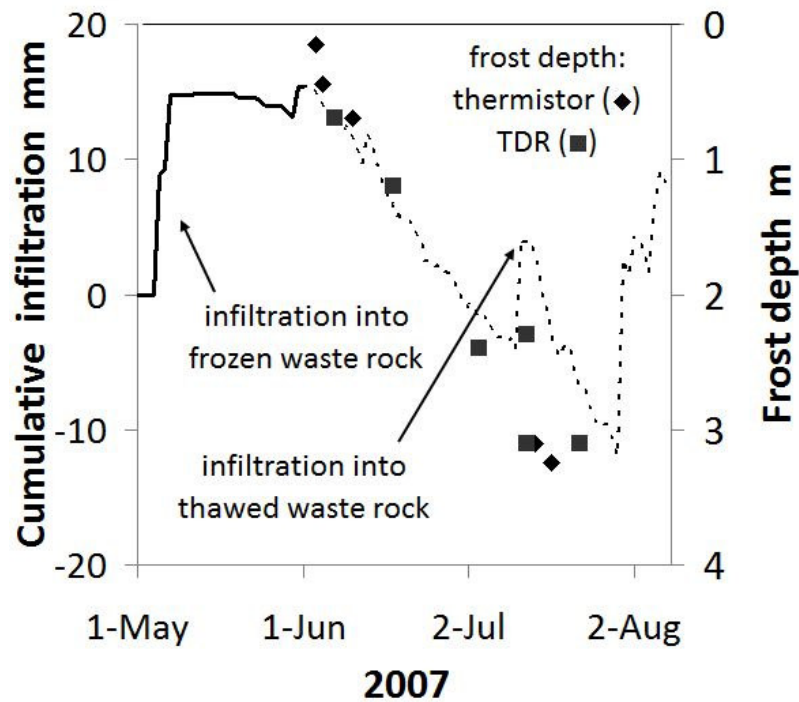
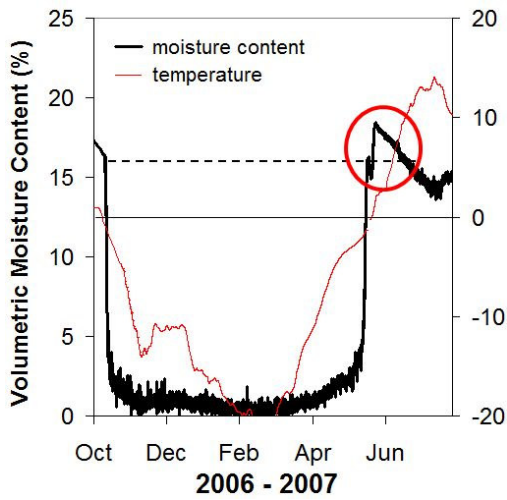
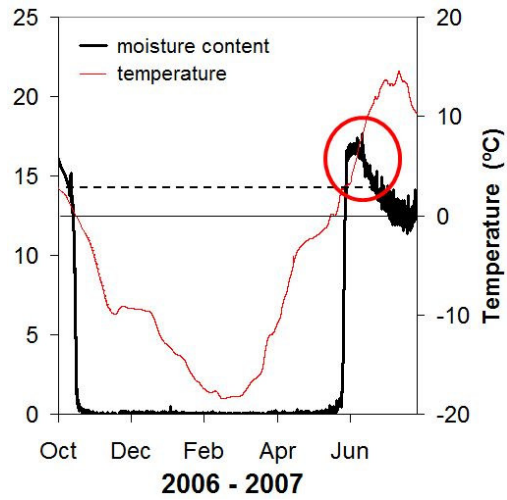


**Figure 3.12** (a and b) Ponding at the surface of the Type 3 test pile after 8 mm rain on May 5, 2007, when the pile was thawed only at the surface. (c) Infiltration during the thawing of the upper 3 m of the Type 3 test pile. The frost depth is determined using thermistors ( $T = 0^{\circ}\text{C}$ ) and TDR ( $\theta$  rises from  $\sim 0$  to level from before freezing). Infiltration trends downward due to evaporation.

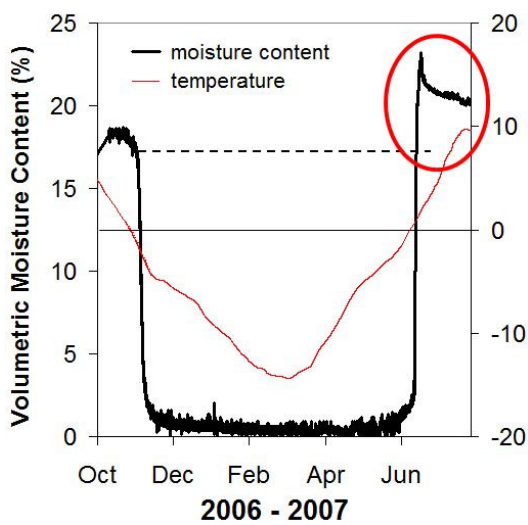
**a. 0.7 m depth**



**b. 1.2 m depth**



**c. 2.3 m depth**



**d. 3.2 m depth**

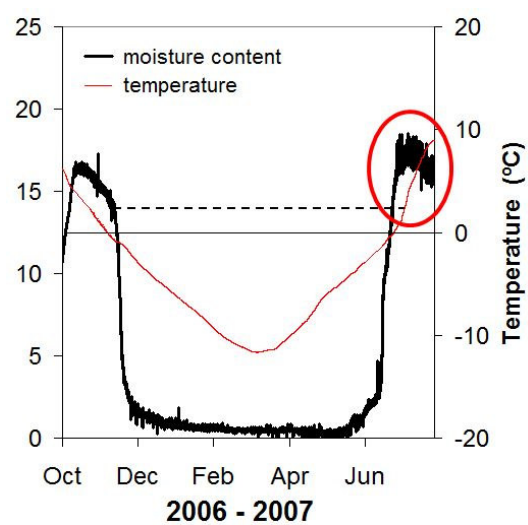


**Figure 3.13** When the 2007 thaw reached depths of (a) 0.7 m, (b) 1.2 m, (c) 2.3 m, and (d) 3.2 m, the moisture content was higher than it had been at the time of freezing the previous autumn. A dashed line marks the moisture content at the time of freezing.

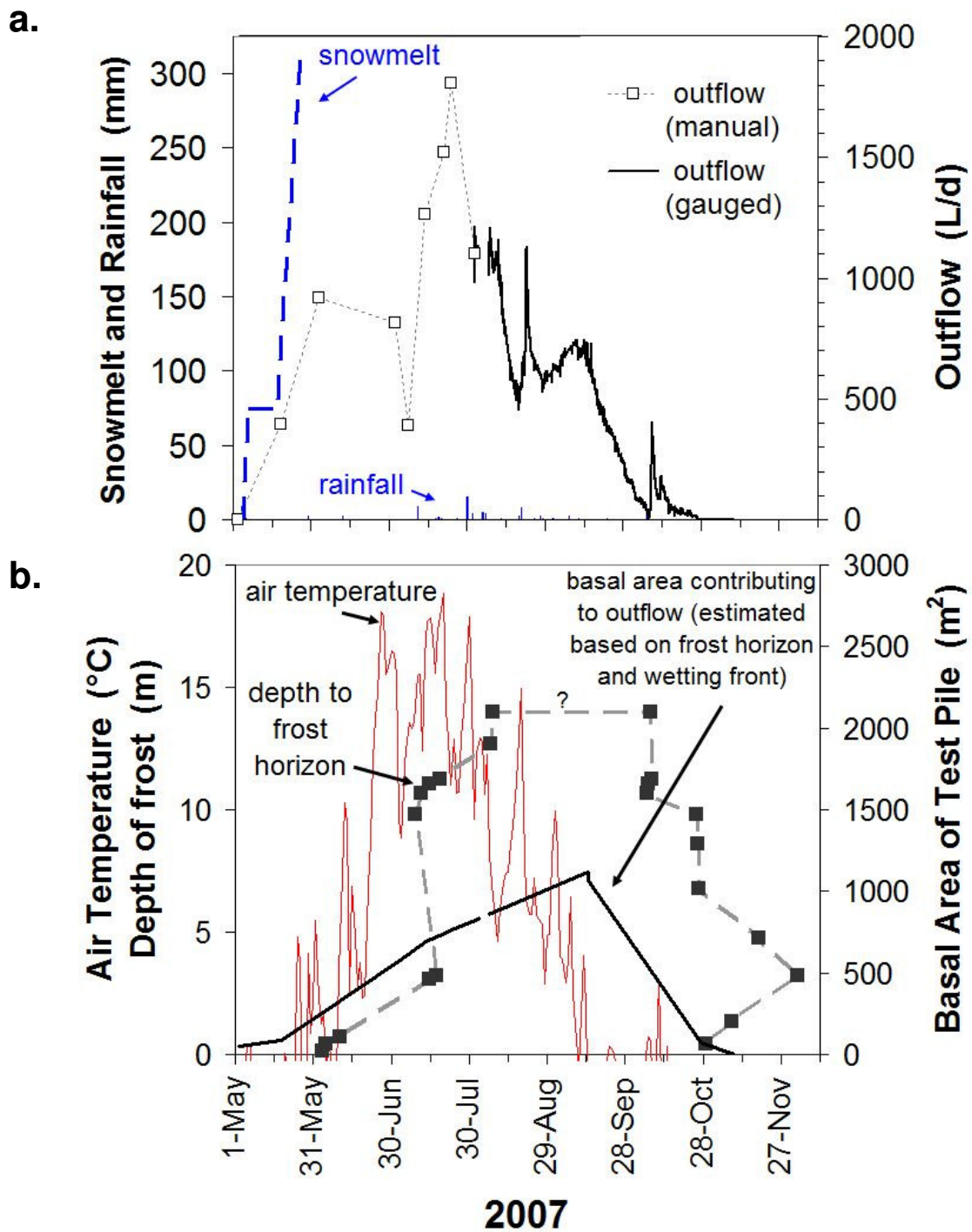
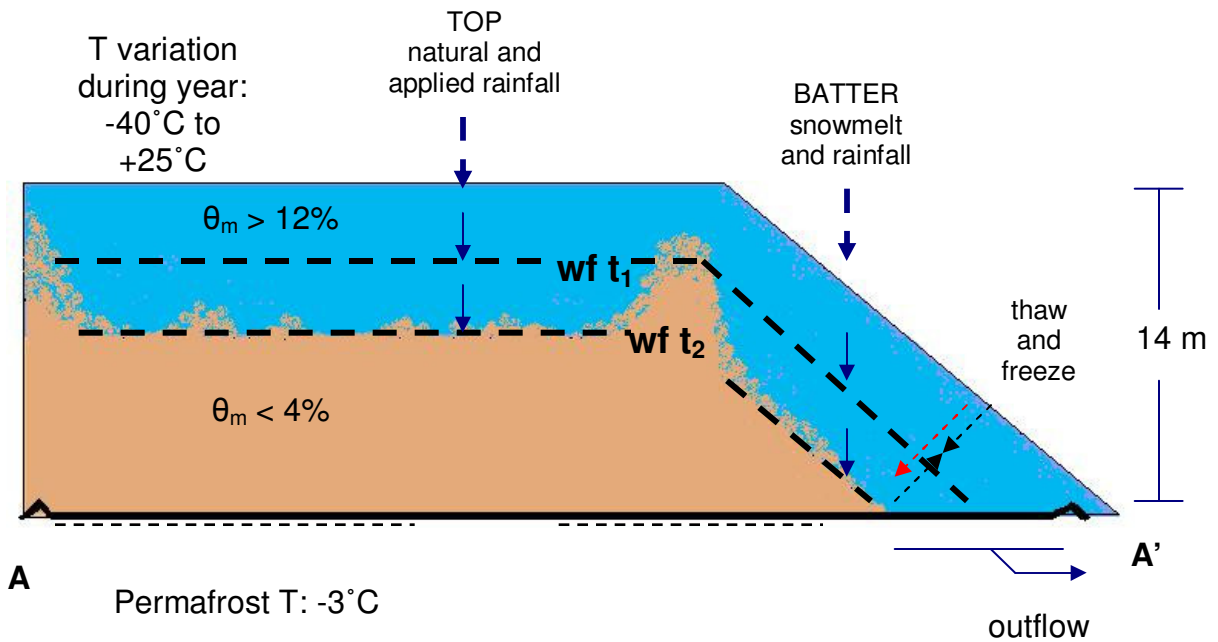


**Figure 3.14** Hydrologic and thermal interaction at the Type 3 test pile batters. (a) Estimated snowmelt into the (b) frozen batters of the test piles and (a) outflow measured from the Type 3 test pile. (b) Estimated area of the basal drain contributing to outflow.

## Cross Section



## Plan View

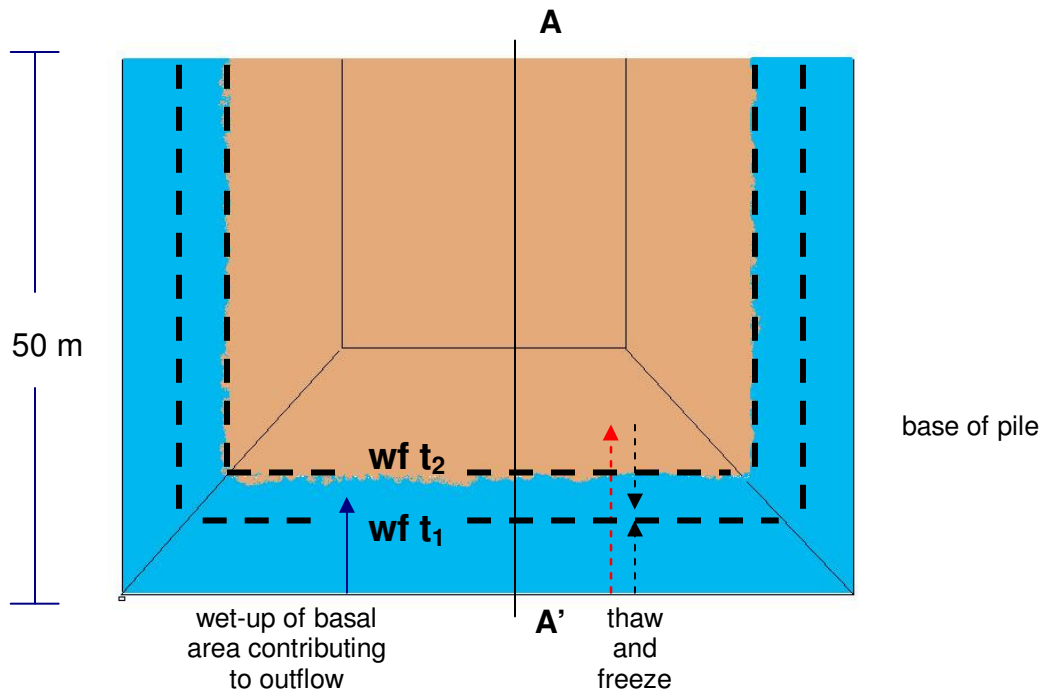


**Figure 3.15** Conceptual model (not to scale) for the portion of the test pile that contributes to outflow during the initial wet-up period. Factors controlling the leading wetting front (wf) include the initial moisture content of the matrix ( $\theta_m$ ), active layer depth ( $0^{\circ}\text{C}$  isograd), and the propagation of thaw and freeze fronts.

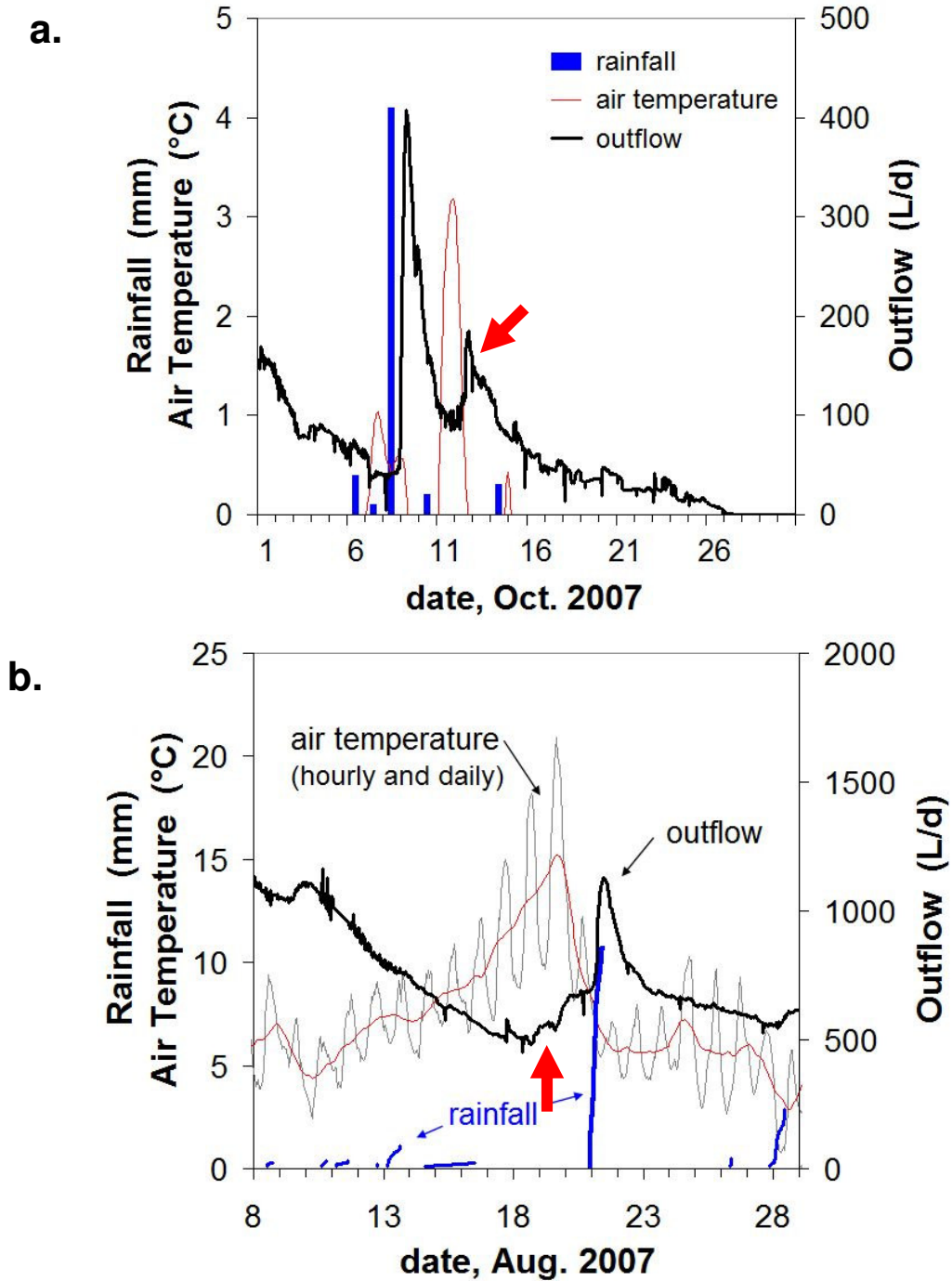


**Figure 3.16** The contribution of pore ice melting to outflow (marked by large arrows) at the Type 3 test pile, (a) during a time when air temperatures were near the freezing point, and (b) during a time when air temperatures were above the freezing point.

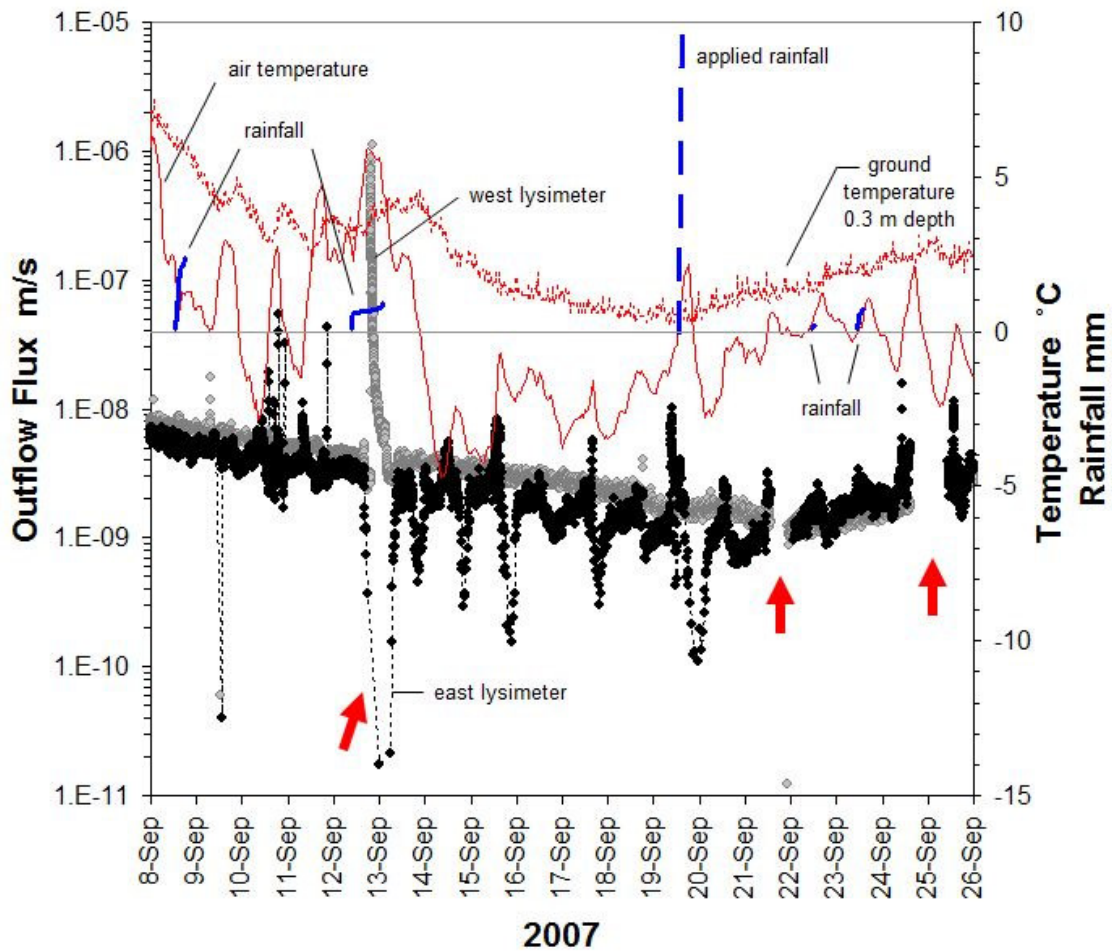


**Figure 3.17** Surface freeze and thaw effects on lysimeter outflow. Arrows mark times of significant decrease in flow, stoppage of flow, or macropore flow.

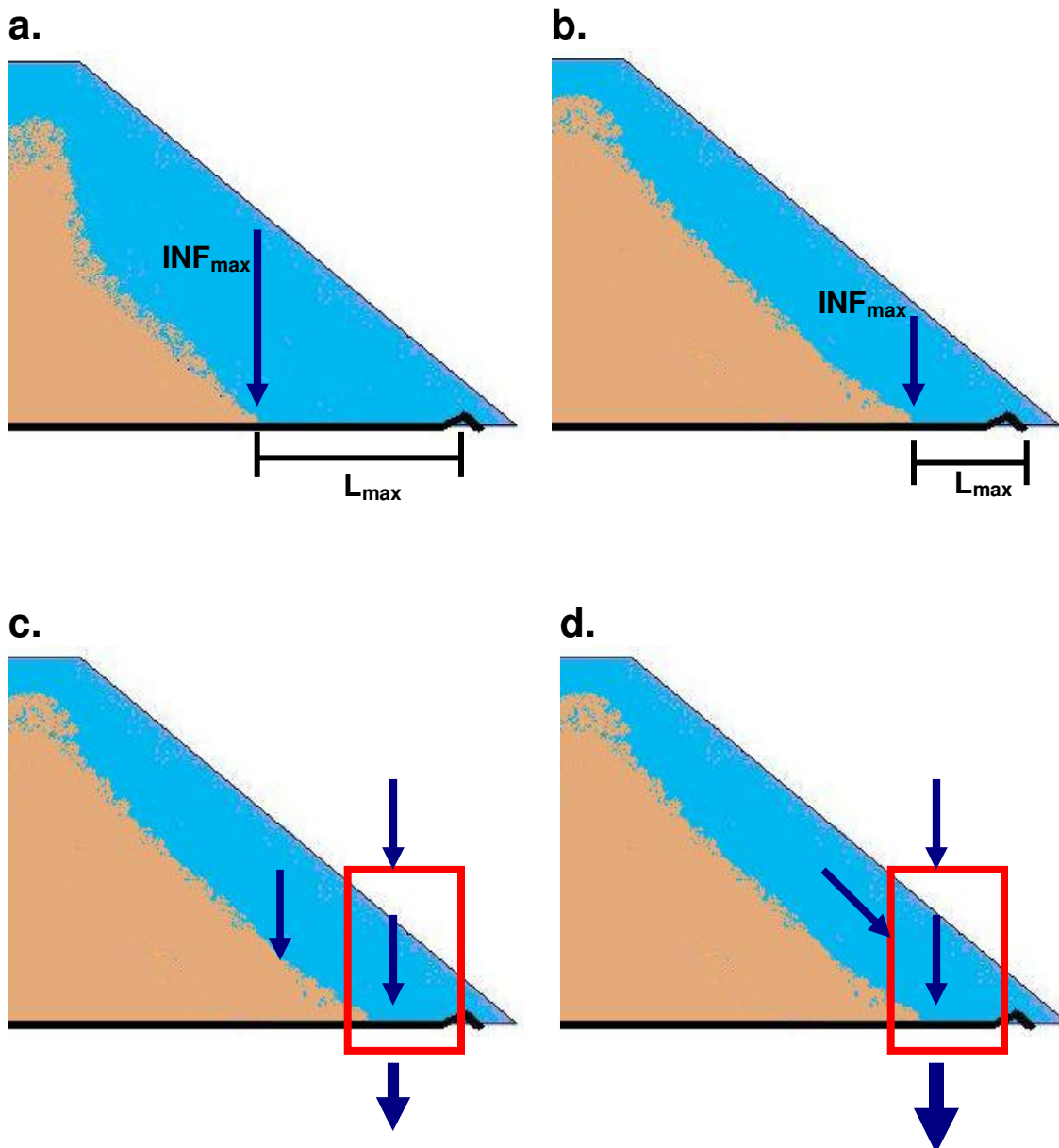


**Figure 3.18** Infiltration through the batter of the Type 3 test pile if the large-scale flow direction was vertical. (a) The maximum depth of infiltration at the maximum extent of infiltration in 2007 and (b) at the maximum depth of infiltration at some earlier time representing the average condition for the 2006 to 2007 period. (c) Outflow if flow was vertical and (d) outflow with a significant component of non-vertical flow.

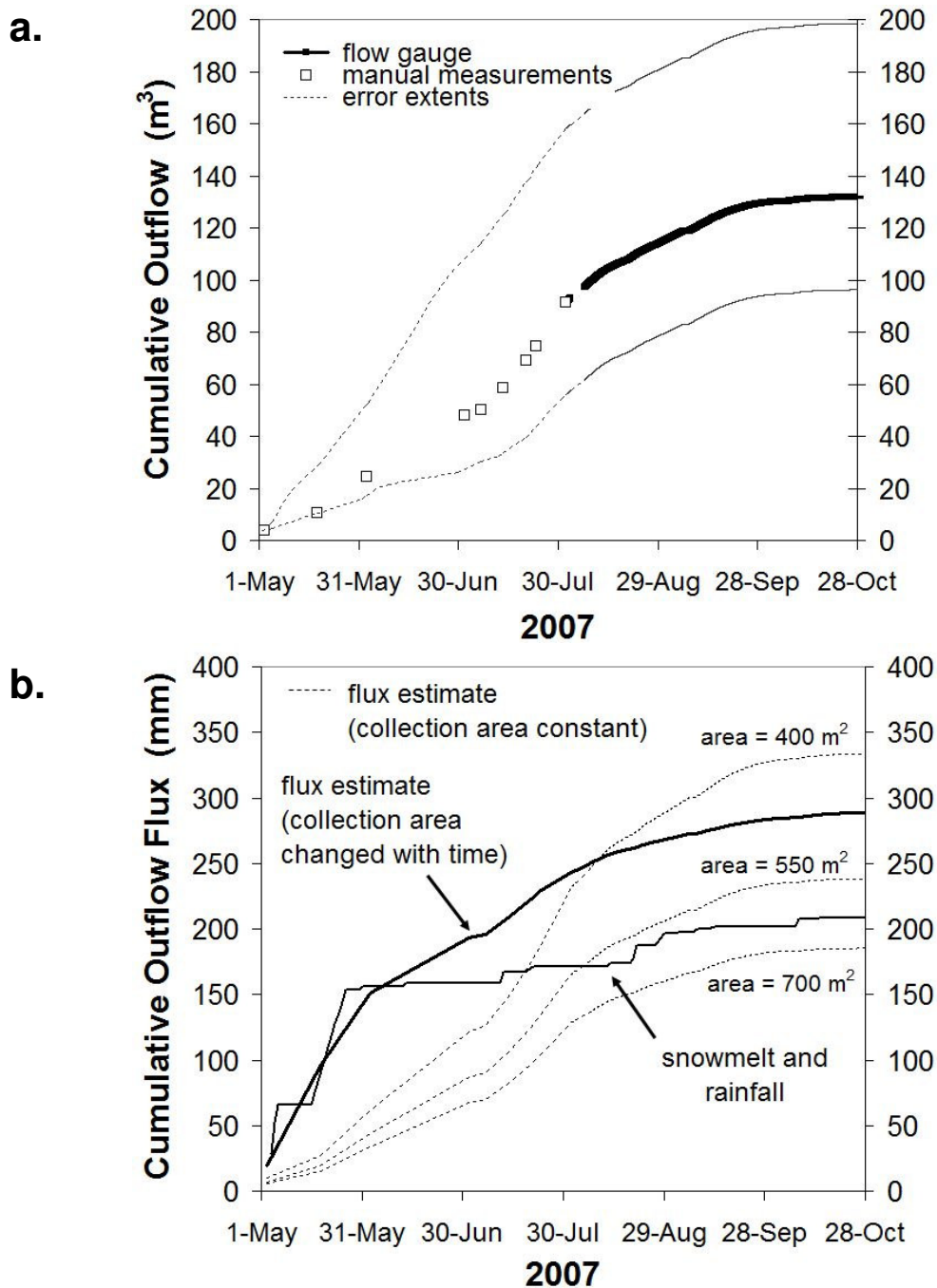


**Figure 3.19** (a) Cumulative outflow from the base of the Type 3 test pile and (b) the estimated cumulative outflow flux (volume divided by area). Error extents in (a) the volumetric outflow indicate the uncertainty in assuming a linear interpolation between the manual measurements. Uncertainty in (b) the outflow flux indicates the uncertainty in the collection area contributing to the outflow.

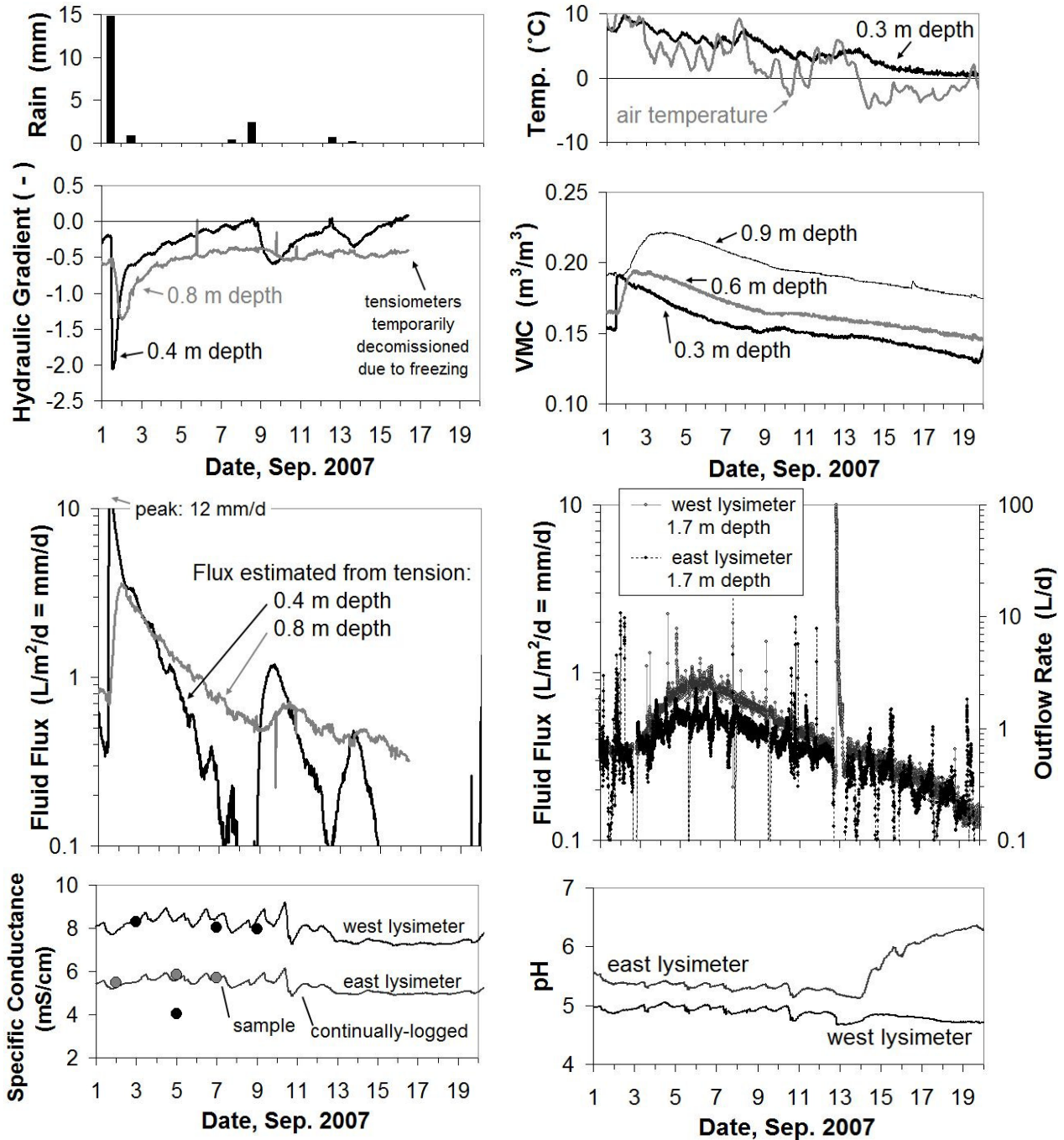


**Figure 3.20** The flow response at the upper collection lysimeters from a high-intensity applied rainfall event on September 1, 2007. VMC is the volumetric moisture content; fluid flux is calculated from tensiometer profiles and outflow from two lysimeters (divided by the collection area, plotted on logarithmic axis); and specific conductance and pH were measured at the outflow from the lysimeters.

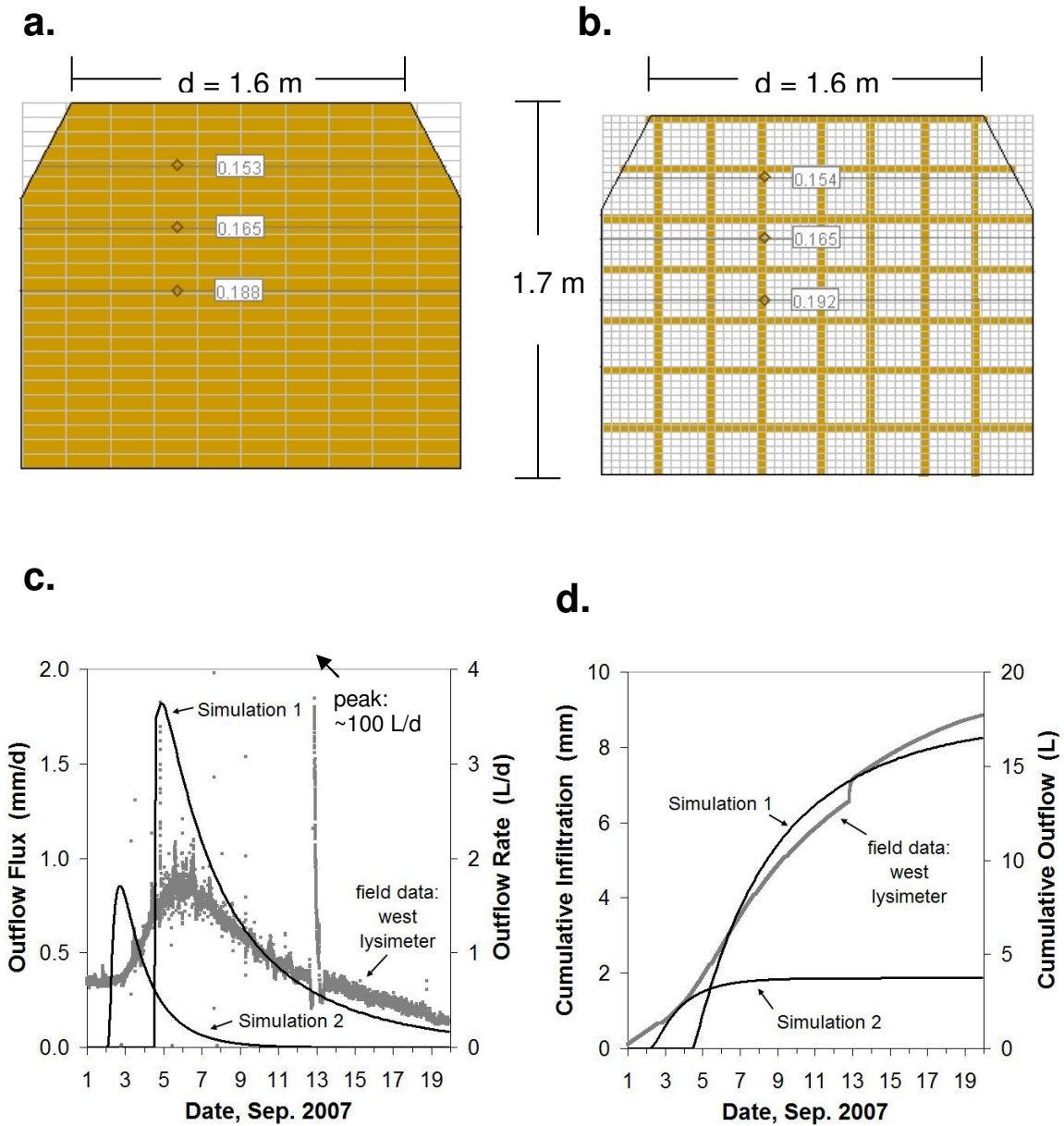


**Figure 3.21** Modeling flow in the upper collection lysimeters. (a) Model domain for Simulation 1: homogeneous; (b) model domain for Simulation 2: matrix zones (brown) surrounding zones of no flow. (c) Modeled lysimeter outflow rate compared to observed, and (d) modeled cumulative outflow volume compared to observed outflow volume.

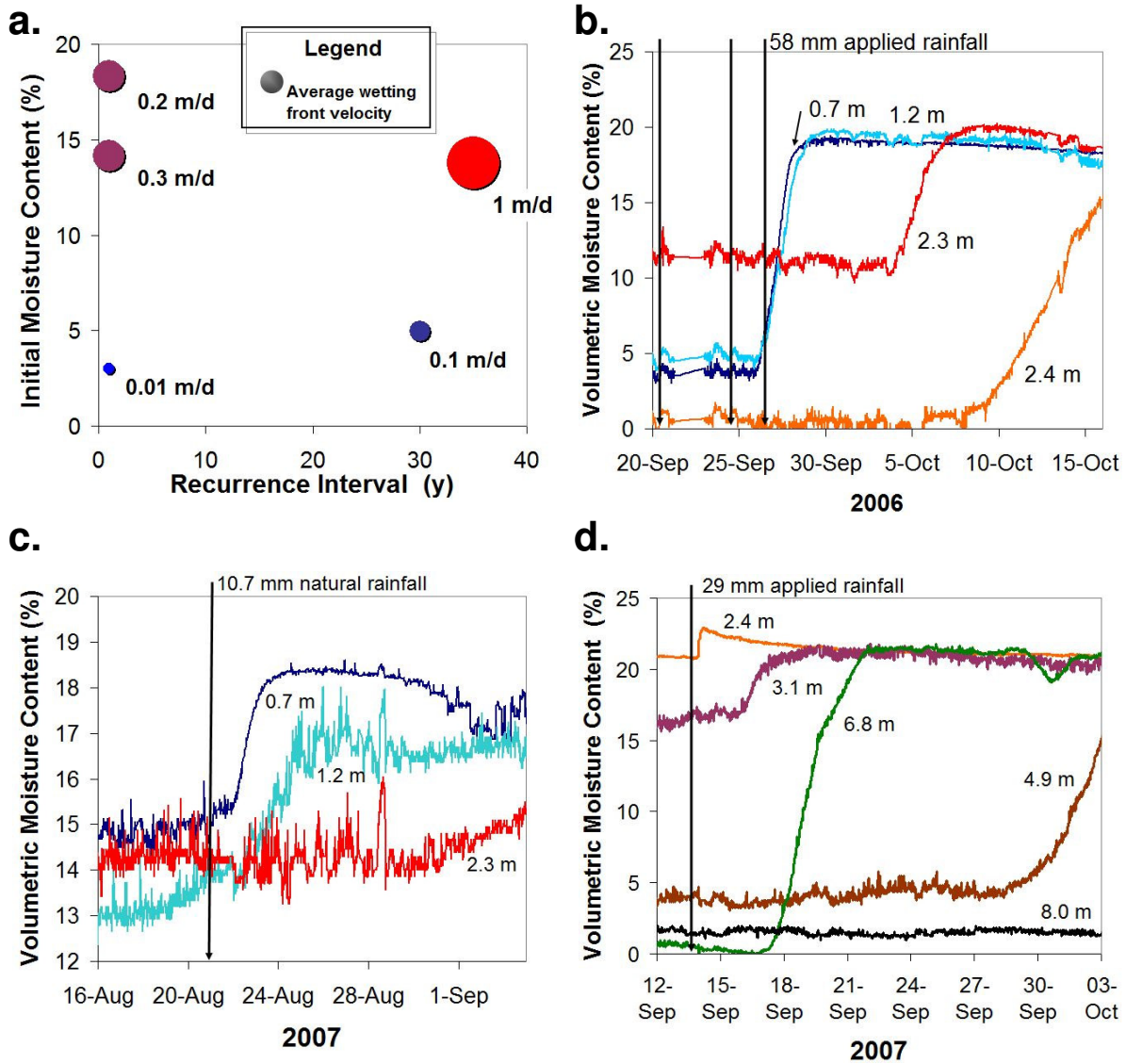


**Figure 3.22** (a) The relationship between rainfall recurrence interval for the region, matrix moisture content prior to the storm, and the average wetting front velocity. Wetting front propagation detected by TDR (b) after three high-intensity rainfall events at initially dry waste rock, (c) after a moderate-intensity rainfall at waste rock with matrix moisture content above field capacity, and (d) after a high-intensity rainfall with matrix moisture content above field capacity in the upper 4 m of the pile. The depth of each TDR probe is shown on each plot.

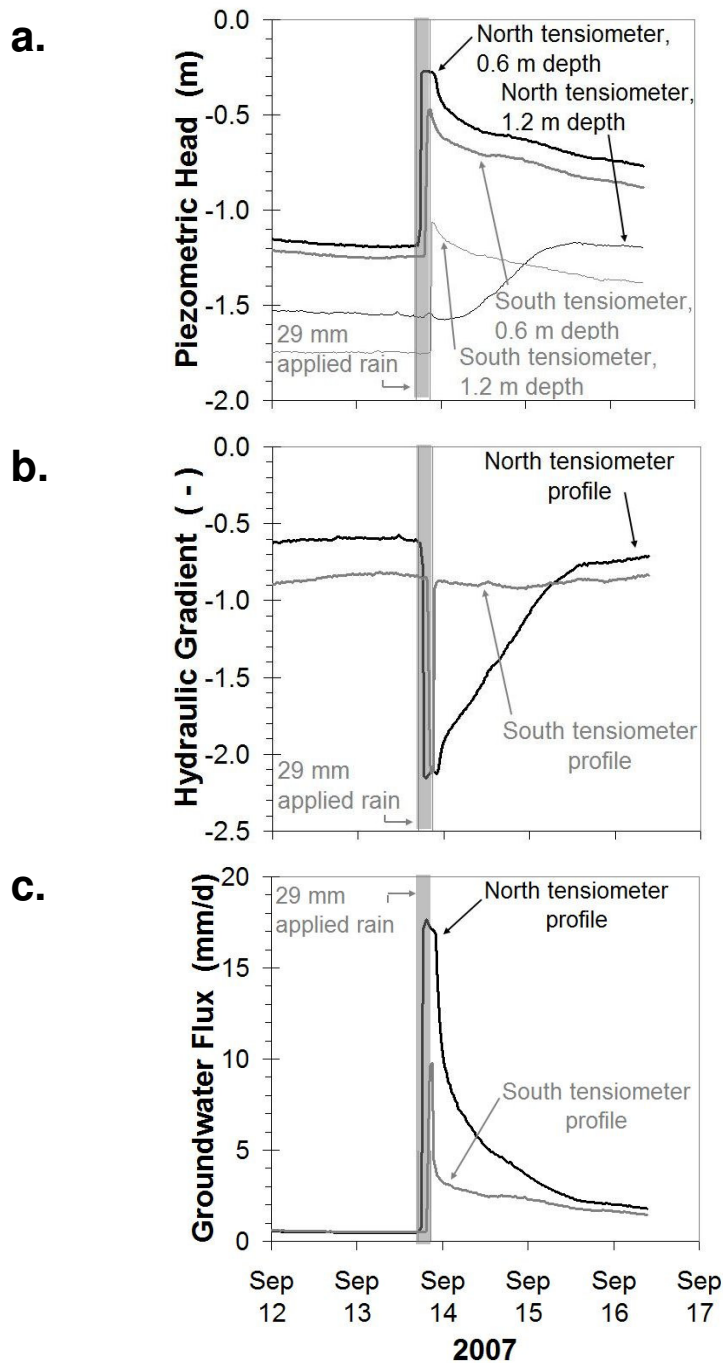
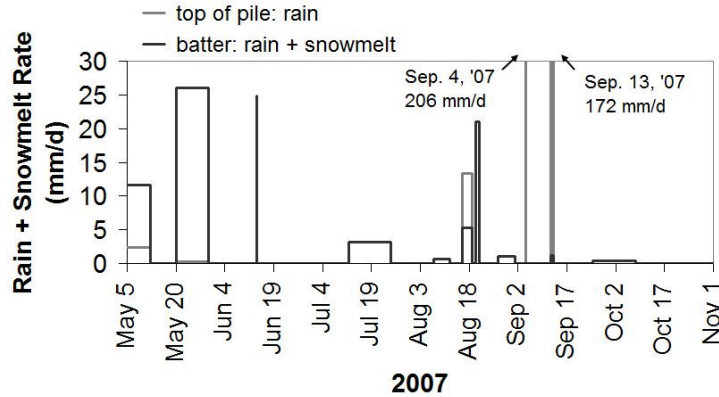
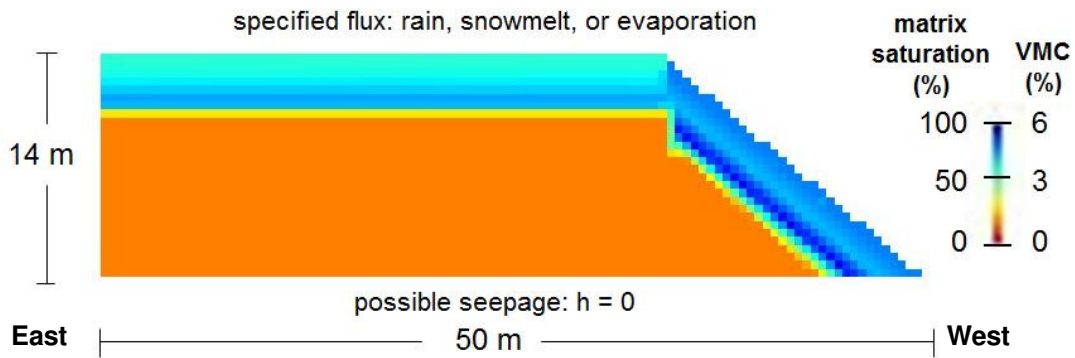


**Figure 3.23** Measurements at two tensiometer profiles in the Type 3 test pile of (a) hydraulic potential are used to determine the hydraulic gradient (b). The gradient indicates downward flow during the applied rainfall event on September 13, 2007, and is used to estimate (c) the groundwater flux within the upper 1.5 m of the waste rock pile.

a.



b.



c.

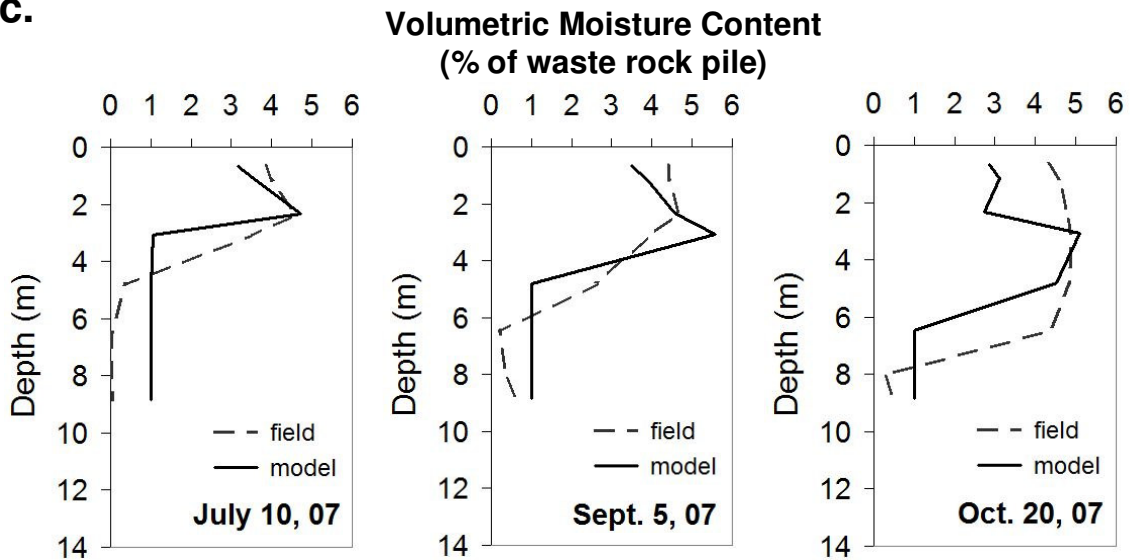


**Figure 3.24** Modeling the hydrologic behaviour in the Type 3 test pile. (a) The infiltration flux specified at the top boundaries, (b) VS2D boundary conditions and results, showing volumetric moisture content (VMC) in a cross section on September 5, 2007, and (c) moisture content profiles.

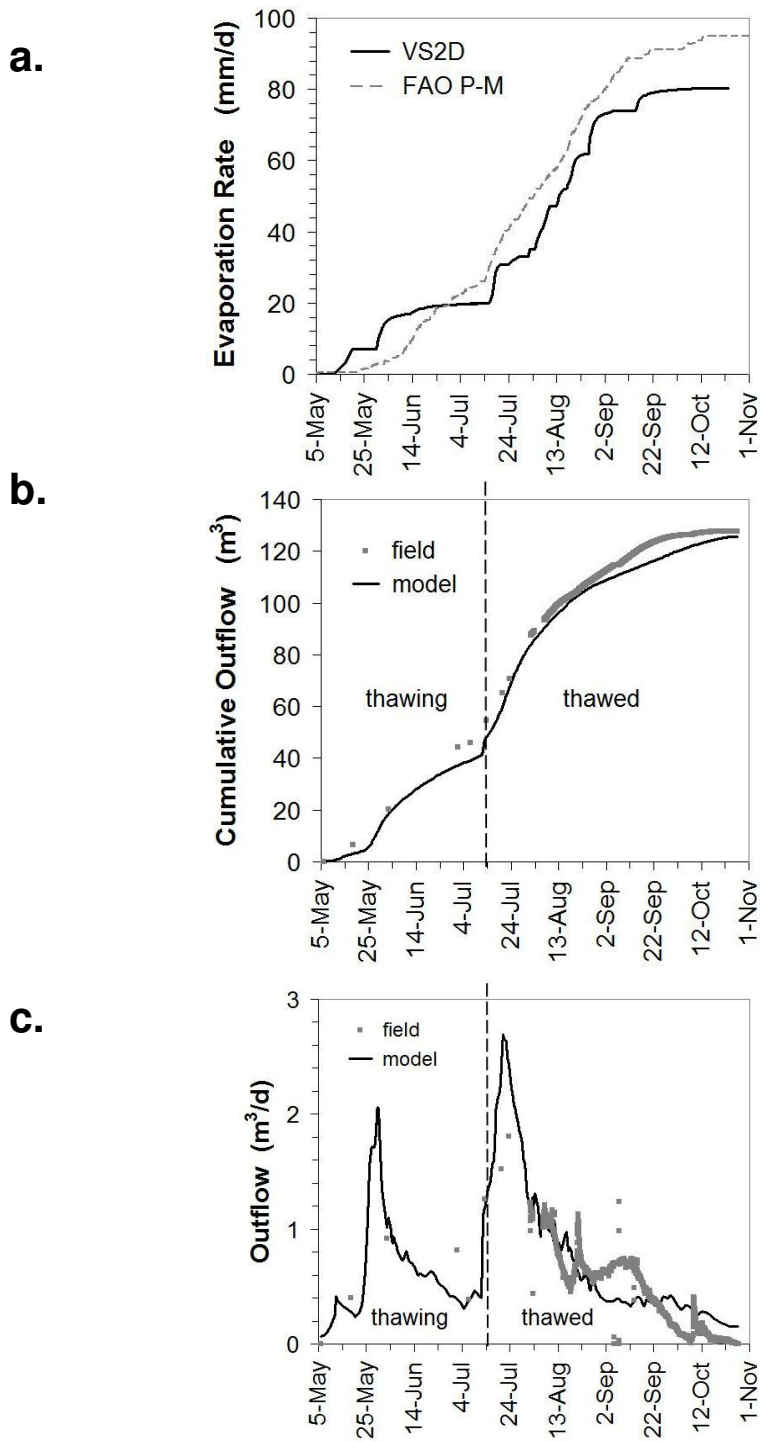


**Figure 3.25** Results of modeling flow through the Type 3 test pile using VS2D are compared to (a) evaporation modeled using the FAO Penman-Monteith method; and measurements made in the field of (b) the outflow rate at the base of the pile, and (c) the cumulative outflow.

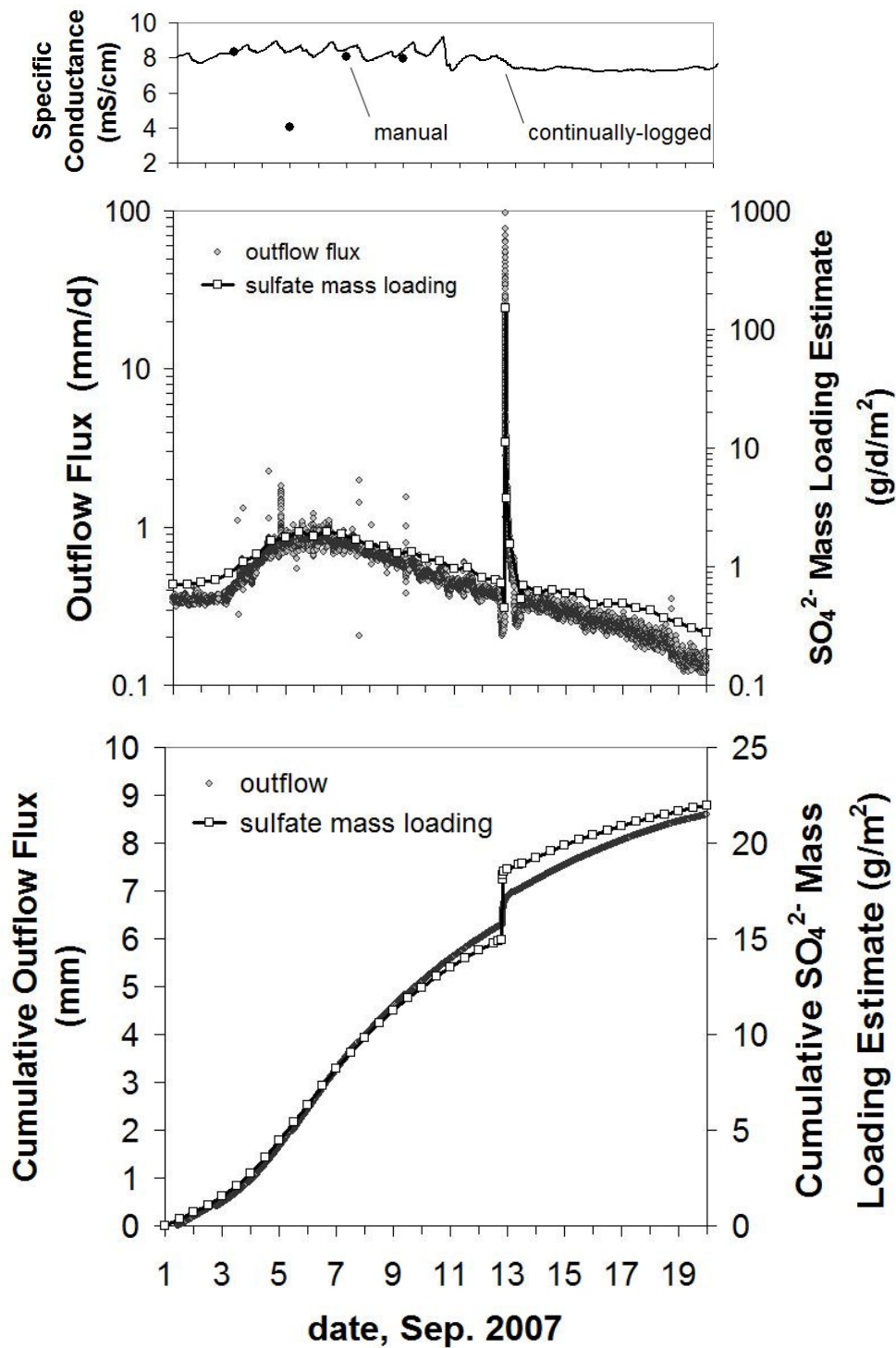
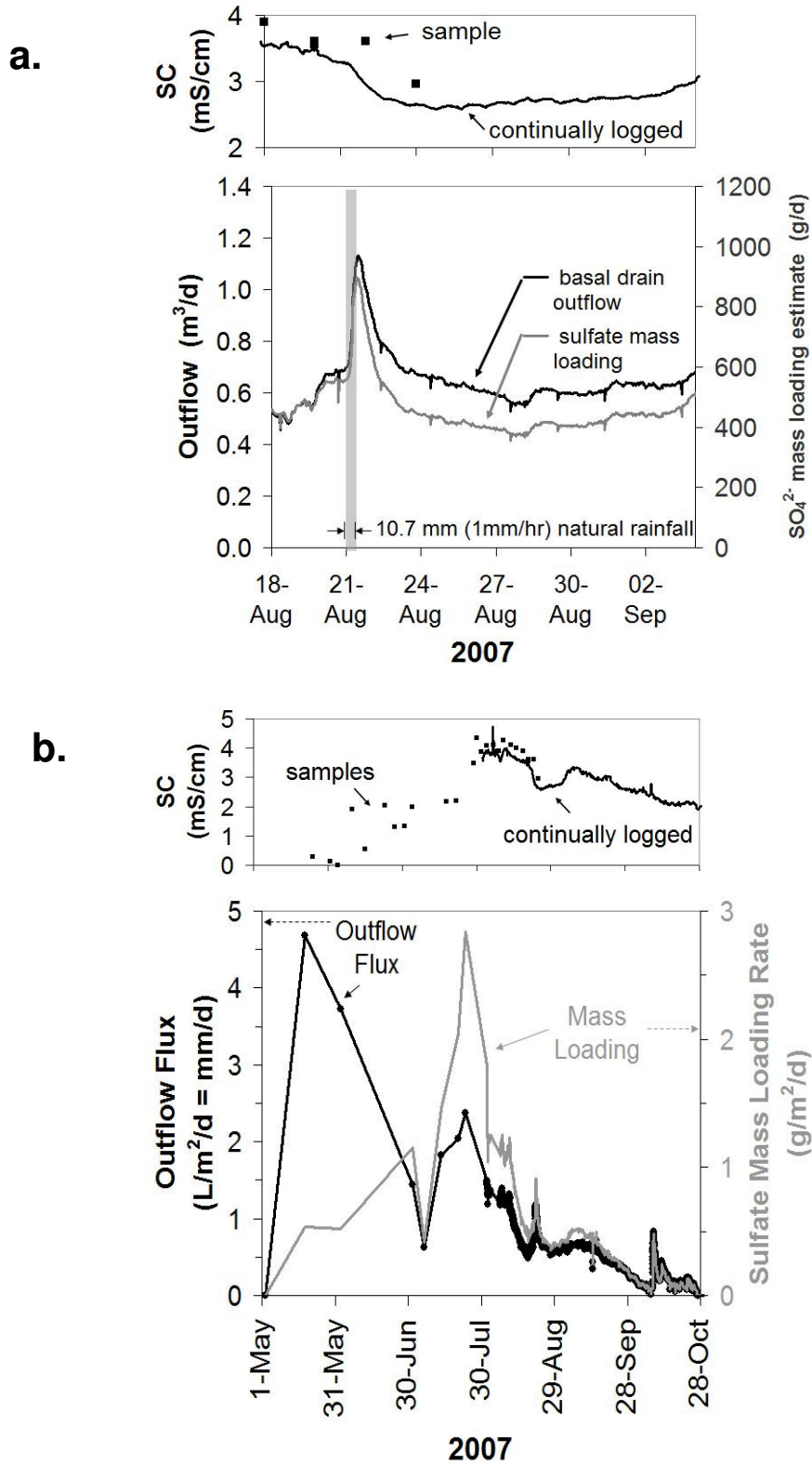


Figure 3.26 Solute mass loading estimate at the upper collection lysimeters.



**Figure 3.27** Sulfate mass loading estimated at the Type 3 test pile batters: (a) in response to a moderate-intensity rainfall, and (b) during the summer of 2007. (SC is the specific conductance).

## CHAPTER 4 DISCUSSION

### 4.1 Permafrost considerations: a long-term conceptual model

In order to address the question of how a projected increase in the depth of the permafrost active layer in the Arctic (e.g. Overpeck *et al.*, 1997, Lawrence and Slater 2005) may impact waste rock hydrogeological behaviour, a long-term conceptual model is required. While numerous questions remain concerning the estimation of long-term hydrogeological behaviour of large waste rock piles deposited onto permafrost, a preliminary conceptual model is proposed here for flow on a decade-to-century time scale. In temperate regions, it is understood that net infiltration through a waste rock pile generates exfiltration at the base of a pile that (1) flows along the natural ground surface at the base of the pile to seepage points and (2) recharges the saturated groundwater in the natural ground below the pile (Smith *et al.*, 1995). A waste rock pile, however, must first wet-up to field capacity before drainage occurs from the entire volume of the pile. Based upon results from the first 1.5 yr at the test piles (Table 3.4), for a 50 m-high waste rock pile in an semi-arid polar climate, 10 to 50 years may be required for the full volume of the pile to contribute to drainage. In a region of permafrost, a large portion of the pile may freeze during this time. Low seepage rates from waste rock in which permafrost develops may result from freezing of infiltration into the permafrost of an unsaturated waste rock pile. A long-term conceptual model for hydrogeological behaviour of a waste rock pile deposited onto permafrost is proposed here that recognizes three time periods: (1) *unlimited infiltration*, (2) *formation of an impermeable layer*, and (3) *dynamic equilibrium*.

#### 4.1.1 *Period 1: unlimited infiltration*

During the initial period, a waste rock pile deposited onto permafrost goes through two processes: wet-up and permafrost development. For a waste rock pile deposited with matrix saturation below field capacity, infiltration is retained in the matrix material until field capacity is reached. As infiltration continues into matrix material at field capacity, drainage delivers moisture lower into the pile. This initial wet-up process has been reported to occur at a percolation rate of 25 m/yr in a humid climate (Corazao Gallegos 2007), but occurred at a rate of less than 1 m/yr at the Diavik test piles under the 2006 to 2007 climatic conditions and at a rate of 1 to 5 m/yr at the Type 3 test pile where mean annual precipitation (153 mm rain) was achieved with three high-intensity applied rainfall events.

Permafrost development was observed in full-scale waste rock piles at the EKATI Diamond Mine, in conditions similar to those at Diavik, within the first few years after construction (SRK, 2007). After about 4 years, the waste rock piles remained frozen at depths greater than 4 to 14 m (SRK, 2007): permafrost has developed within the waste rock below those depths. After the first 5 to 10 years, then, infiltration in summer will generate drainage that infiltrates the waste rock with permafrost conditions and freezes. The depth of infiltration into frozen waste rock could be expected to be greater than the maximum 0.5 m observed in coarse frozen prairie soils (Granger *et al.*, 1984) and perhaps similar to the 2 m infiltration observed in porous media similar to the Diavik waste rock in an alpine permafrost environment (Woo *et al.*, 1994). Measurements of air-filled porosity of about 0.2 (Section 3.1) and observations of significant infiltration into frozen waste rock (Section 3.5) indicate that initially, flow from the active layer into

the underlying waste rock with permafrost conditions will be limited only by the flow rate through the active layer.

#### 4.1.2 *Period 2: formation of an impermeable layer*

The second period in the conceptual model is characterized by the formation of a frozen impermeable boundary below the active layer. Much uncertainty exists in estimation of whether such a boundary might evolve at a rate and extent to significantly impact mine site hydrology or to limit the transport of dissolved metals or acid through the active layer to the receiving environment. Nevertheless, flow into waste rock with permafrost conditions at a depth of the base of the active layer will likely produce ice-saturated conditions in the matrix material within a relatively short time period. Based on the results of column experiments reported by Fourie, *et al.* (2007) and the porosity and grain size distribution of the waste rock Diavik, ice-saturated conditions may be expected to form in material finer than 1 cm in the upper permafrost region within the waste rock after less than 100 mm of infiltration from the overlying active layer. Unfortunately, the study of Fourie, *et al.* (2007) could not conclude a rate of ice formation in larger gravel due to an underestimation of the required column height. Based on the mean annual rainfall at Diavik and an assumption of annual net infiltration through the active layer of 40% of rainfall (Section 3.4.3), ice-saturated conditions in the matrix material in the upper region of waste rock with permafrost conditions may develop within a few years. Due to yearly variation in active layer depth, regions with ice lenses and perched water tables may develop in the active layer (Tolstikhin and Tolstikhin, 1974), and the time required for ice-saturated conditions in the matrix at the

upper region of waste rock with permafrost to establish could be expected to be somewhat longer.

Subsequent drainage to the ice-saturated matrix below the active layer could generate saturated conditions atop ice lenses and focus flow into the larger air-filled pores of the waste rock with permafrost conditions. As this focused flow should also then freeze, however, the air-filled porosity of the larger pores would decrease incrementally. This process may continue to fill pores with ice for some time until a continuous layer becomes fully ice-saturated. The thickness of a continuous frozen layer could depend upon the limit of infiltration into frozen waste rock. This limit is unknown as of yet in very coarse sediments, but could be on the order of 5 m, based on a study of infiltration into frozen soils (Gray, *et al.*, 2001). For waste rock with a 0.25 porosity and infiltration into the upper region of waste rock with permafrost conditions of 60 mm/yr (about 40% of annual rainfall), ice saturation of a continuous layer 5 m-thick might occur after 15 years. However, if infiltrating water continues to find new pathways through the evolving ice-saturated layer, by for example ice melting by fractionation-produced brine, an ice-saturated boundary at the top of the permafrost may not form until much of the entire waste rock pile becomes ice-saturated. For a 50 m-high pile, hundreds of years may be required for this to happen, based on the estimated average rate of net infiltration (Table 3.6) and the porosity of the waste rock. It should be stressed that for a waste rock pile with an engineered cover including a layer of mostly fine-grained material such as glacial till, ice saturation could be expected after a time of perhaps several years, as discussed above.

When ice-saturation is eventually achieved in the upper region of the waste rock with permafrost conditions, it may promote the formation of a water table in the active layer, as has been observed in an alpine permafrost active layer (Woo *et al.*, 1994). An ice-saturated layer, and particularly the presence of a summer water table in the active layer, would cause an increase in exfiltration at the toe of the pile. An ice-saturated layer would enable the full area of the waste rock pile, rather than just a portion of the area of the batters, to act as a catchment supplying drainage at the toe of the pile. An increase in air temperature due to global climate change may cause the depth of the active layer to increase, resulting in the potential for water table development at a rate equal to the net infiltration through the active layer plus the rate of pore ice melting (Michel *et al.*, 1994). By the end of this period, when ice-saturated conditions are established, the active layer depth would change with climatic forcing in a manner similar to the surrounding natural permafrost active layer.

#### 4.1.3 *Period 3: dynamic equilibrium*

The final period in the long-term evolution of waste rock hydrogeology in a permafrost environment is dominated by flow in the active layer. The hydrogeological processes associated with infiltration into waste rock in a warmer climate occur in waste rock in a permafrost environment during the summer, but these processes are limited to the depth of the active layer. As the active layer thaws during summer discharge from the active layer to the toe of the pile could be expected to be similar to that of an alpine permafrost environment with coarse heterogeneous material.

Woo *et al.* (1994) studied an alpine permafrost catchment in the Tianshan Range, China, that has a climate and grain size distribution that is similar to the conditions of the

test piles at Diavik. After millennia since the previous glacial freeze in hydrologic activity, that catchment has reached a period of dynamic equilibrium. The catchment is characterized by boulder and gravel slopes with an ice-saturated “frost table” at a depth of approximately 2 m. The “frost table” enables the formation of a summer water table that saturates voids between the boulders and greatly increases the hydraulic conductivity, causing rapid lateral flow (*ibid*). The catchment-area-normalized outflow from the catchment ranged from about  $8 \cdot 10^{-9}$  m/s (0.7 mm/d) to about  $2 \cdot 10^{-7}$  m/s (17 mm/d) during the summer (Fig. 6 in Woo *et al.*, 1994). This range of discharge from coarse unsaturated material to an alpine stream is similar to the outflow from a constructed waste rock pile, under similar rainfall and evaporative conditions, where all of the discharge was collected (Fig. 3 in Nichol *et al.*, 2005).

When a large waste rock pile in a region of permafrost reaches a state of dynamic equilibrium, an ice-saturated layer at the base of the active layer would enable the entire area of the pile to contribute to the drainage from the toe of the pile. The most significant question remaining to be answered pertains to the timeframe in which this will happen. Column experiments may aid in better estimating the time required for infiltration into frozen waste rock to establish such an ice-saturated layer.

## **4.2 Non-vertical flow**

Three potential mechanisms exist that may have caused non-vertical flow at a large scale in the Type 3 test pile: (1) depositional structure, (2) contrasts in matrix moisture content, and (3) frozen conditions at the core of a pile. Alternating layers of coarse and fine waste rock, dipping at the angle of repose, have been observed inside waste rock

piles (Stockwell *et al.*, 2006) and these layers have been shown to create non-vertical flow paths in modeling studies (Fala *et al.*, 2005). At moderate matrix saturation, water flowing vertically down through dipping regions of fine-grained waste rock is redirected at an interface with waste rock with larger pore spaces due to a large difference in the capillary forces in each material. Higher tension in the fine waste rock allows the water to flow in a non-vertical trajectory rather than a vertical trajectory into the larger pores. At near-saturation conditions in the matrix, water is capable of overcoming the capillary barrier at the pore size interface and enter a macropore region, and may remain in the macropore region due to contrast in permeability with the underlying fine region. Non-vertical flow may occur, then, in dipping matrix regions due to contrasting capillary forces and in macropore regions due to contrasts in permeability.

Anisotropic flow under unsaturated conditions may occur as a result of a distribution of moisture content that is orientated at an angle to the primary flow direction (vertical). A contrast in matrix moisture content, particularly under the batter of a waste rock pile, may create a region in which the tension gradient and the moisture-content-dependent permeability act in opposition. A wetting front encountering such a region may flow toward a more permeable, higher moisture content region, particularly where this moisture content interface is at an inclined plane. McCord *et al.*, (1991) confirmed the stochastic-based theoretical arguments for saturation-dependent anisotropy (e.g. Montoglou and Gelhar 1987) with observation of macroscopic anisotropy in a sand dune hillslope. Two-dimensional simulations of flow through the Type 3 test pile in VS2D support the possibility for preferential flow along an inclined plane of waste rock with a high moisture content, located within a pile. The introduction of pore scale saturation-

dependent connectivity and tortuosity to the Richards equation model, such that tortuosity and lateral-component flow increase as pore space drains, could also describe this type of non-vertical flow (Zhang et al., 2003). However, given the large degree of heterogeneity and the transient thermal conditions in cold region waste rock piles, this mechanism may be less significant than the effect of depositional structure or the existence of a frost boundary.

Moisture content and temperature data from within the test piles show that much of the flow occurred at a time when a portion of each of the piles was frozen. Frost and thaw fronts propagated at a rate of approximately 0.2 m/d on a large spatial scale over the summer period. During frost propagation, moisture may flow upward towards the frozen soil (Dirksen and Miller, 1965; Kane, 1979), a process that may lead to the formation of a layer of soil with a higher volumetric ice content than the moisture content had been prior to the introduction of the frost (an ice lens). An upward hydraulic gradient was observed at the upper collection lysimeters (Section 3.5) and may have also occurred at the batters of the test piles to create a concentration of pore ice near the surface. During the subsequent snowmelt and thaw propagation, infiltrating water may have encountered ice-saturated matrix material and flowed preferentially along the plane of the frost horizon, parallel to the slope of the batter.

In waste rock piles, depositional structure and ice-saturated waste rock are likely the most significant mechanisms for non-vertical flow. In the long-term, non-vertical flow may contribute to a concentration of flow in the active layer of waste rock piles, particularly in the batters of a pile.

### 4.3 Waste rock hydrogeological characterization

Hydrogeological characterization of mine waste rock for unsaturated flow requires much effort and remains an area of active conceptual development. Measurement of the grain size distribution, saturated hydraulic conductivity, and porosity of the REV-scale waste rock requires significant effort, but greatly improve both the conceptual model and the calculations used to quantify the flow behaviour. Recall that the REV-scale refers to the scale at which small-scale properties may be replaced by parameters applied equally at any point within an approximate volume (Bear, 1972): an approximate volume of 80 m<sup>3</sup> for the waste rock at Diavik. Estimations of the water retention curve and hydraulic conductivity curve for REV-scale waste rock present a more difficult problem.

Systematic deconstruction of a waste rock test pile reported in Stockwell *et al.* (2006) found discontinuous regions of coarse material that were in some regions mixed with matrix material and in other regions contained large void spaces. For the regions of coarse material mixed with matrix material, Yazdani, *et al.* (2000) suggested that the water retention curve for the REV-scale material could be estimated by using only the fraction of the porosity at the REV-scale that contributes to capillarity in calculating the moisture content for each point in the WRC. In their report, they concluded that only the portion of the waste rock passing a 4.75 mm sieve contributes significantly to capillarity. Based on the large grain size distribution and the results from the drain-down test of a 16 m<sup>3</sup> sample (Section 3.1.9), approximately 20% of the porosity of Diavik waste rock at the REV-scale contributes significantly to capillarity. The method of Yazdani, *et al.* (2000) calls for the WRC to be scaled-up by multiplying the moisture content of each point on the WRC by the fraction of the waste rock at the REV-scale that is finer than

4.75 mm. The pore space contributing significantly to capillarity, referred to here as the matrix porosity, is therefore approximately 0.06 of the Diavik waste rock at the REV-scale.

Rather than incorporating the large pores into the flow system, this approach to scale-up the WRC utilizes the observation that large pores retain little water in capillarity to omit the large pores from the flow system. Utilization of a water retention curve determined with this approach to estimate the hydraulic conductivity curve yielded nearly linear curves (in log-log space) with hydraulic conductivities  $1 \cdot 10^{-8}$  to  $1 \cdot 10^{-11}$  m/s for the observed range of soil tension. Application of such low hydraulic conductivity estimates to Richards equation-based VS2D models yielded simulations that in some cases (*i.e.*, for the upper lysimeters) did not converge or were incapable of reproducing observed flow behaviour. However, the success of the application of this scale-up approach in simulating flow through the Type 3 test pile indicates that difficulty with the simulations for the upper lysimeters may have been due to the limitations inherent in the trial-and-error approach taken to attempt to calibrate the scaled-up model for the upper lysimeters (which has not been presented in this thesis). While difficulties remain in estimating the water retention curve and the unsaturated hydraulic conductivity curve for waste rock at the REV scale, measurement of properties at this large scale, particularly the grain size distribution and the porosity, greatly improve estimations of the flow behaviour through a waste rock pile.

#### 4.4 Flow mechanisms

At a less-than-2 m scale, the hydraulic response to a high-intensity rainfall when matrix saturation was high showed no signs of significant macropore flow at two lysimeters and three moisture content sensors. Estimations of wetting front velocity and cumulative outflow volume from a high-intensity rainfall event were made with Richards equation modeling using measured waste rock matrix properties with reasonable success. This relative success may have been due to the apparent lack of preferential flow paths in upper lysimeters. The placement of waste rock into the collection lysimeters using an excavator may have created waste rock with either a random or fining upward spatial particle distribution. This type of material placement, however, would not necessarily preclude the presence of preferential flow paths. The studies of Nichol *et al.* (2005) and Marcoline (2008) revealed that waste rock lacking inclined gradation structures typical of end-dumping deposition is capable of significant macropore flow at a 5 m scale. Another explanation for the lack of macropore flow at the upper collection lysimeters in response to the high-intensity applied rainfall event could be a lack of surface ponding.

At a 15 m scale, over the course of the 2007 summer season, wetting front propagation and pile outflow occurred in a manner that was adequately characterized by modeling with a single set of waste rock hydraulic properties. A modeling approach utilizing up-scaled waste rock matrix properties was able to characterize the flow with errors on the order of 50% or less in the wetting front velocity, the pile outflow rate, and the cumulative outflow volume for the year 2007. This relative success highlights the dominant nature of flow through the matrix, even for very coarse waste rock, under average semi-arid conditions over a time period of months.

Model calibration for the Type 3 test pile required a  $K_{sat}$  value lower than the average estimate for both the matrix and the large-scale waste rock. The low  $K_{sat}$  value in the model might be explained by an underestimation of the porosity, but it may also be due to the presence of large pores in the pile that are not accounted for in the model. Flow through waste rock may be slowed by zones of void spaces that are large enough to remain air-filled at most times. Wilson (2003) explains the effectiveness of large pores in the creation of flow barriers in engineered waste rock pile covers that consist of fine-grained material placed over coarse-grained material (i.e. material with large pores). Fala *et al.*, (2005) explains the role of matrix-macropore boundaries as barriers to flow, but focuses on large-scale barriers formed by stratification of waste rock parallel to batters and the resulting large-scale non-vertical flow. In a region where water flowing downward through matrix material reaches a boundary between matrix and a large air-filled pore, the matric potential in the matrix must exceed the potential in the void for water to flow into the void. If the pressure in the void is equal to the atmospheric pressure, water will not flow into it until the overlying matrix is nearly saturated. (The qualifier “nearly” is used in consideration of the gravitational potential that exists due to the position of the matrix above the void.) The time required for this process to occur may result in a net slowing of the groundwater flow, particularly if many relatively small air-filled pores are present. The concept of a high degree of matrix and large pore interaction is in agreement with the results from the large permeameter, which found that the volume of large pores accounts for five times the matrix porosity.

Vapor transport between the matrix and the atmosphere through highly-connected macropore and matrix zones may play a significant role in the waste rock water budget.

There are two indicators of significant potential for gas flow, which may drive vapor transport, in the waste rock at Diavik: (1) a 3-orders-of-magnitude difference in permeability between the bulk waste rock and the matrix and (2) the high proportion of macropore to matrix porosity (section 2.4.2). Vapor transport driven by heat transfer may easily be observed as steam vents that generally form in the pile batters during October and November. This process was not discernable as a trend to lower moisture content at the test piles, but such a trend may have occurred at the upper collection lysimeters, where the matrix water retention was relatively low. The rate in decrease of moisture content after the passage of a wetting front (the slope of the moisture content recession) was higher in October, when the temperature gradient between the subsurface sensors and the atmosphere averaged  $10^{\circ}/\text{m}$ , than it was in August or September, when the thermal gradient was lower. Based on this difference in the slope of the moisture content recession, vapor transport may account for fluxes estimated to be as high as 0.5 mm/d. Marcoline (2008) stresses the importance of evaporative flux in the water budget of a waste rock pile, but a more complete conceptual model may be one that extends the role of evaporation to the zero tension air-filled macropores in the waste rock subsurface.

The numerical simulations performed in the analysis presented here made a crude approximation of the conceptual model for flow in unsaturated mine waste rock. A heterogeneous, dual porosity, or flow path continuum model may be required to accurately model spatial variability observed in response to high-intensity rainfall infiltrating into waste rock with matrix saturation greater than field capacity. A more accurate approach would also include coupled unsaturated flow and evaporative flux as

well as coupled unsaturated flow and heat transport by conduction, convection, and wind-advection.

## CHAPTER 5 CONCLUSIONS

A field experiment was constructed to investigate water flow through unsaturated mine waste rock piles in a permafrost region. Test piles 14 m-high were built above drainage collection systems 60 m by 50 m, with instrumentation installed in the piles including moisture content sensors, thermistors, and tensiometers. Lysimeters were installed near the test piles to investigate infiltration, evaporation, and the effect of the thermal regime in the upper 2 m of the waste rock. Hydrogeological characterization of the waste rock was performed at multiple scales, with samples ranging in volume from 250 cm<sup>3</sup> to 100 m<sup>3</sup>, and with tests conducted at the test piles. During the first 1.5 year of monitoring, the core of the piles remained dry while the waste rock in the batters and in the upper 7 m wetted up. Infiltration into the waste rock and drainage occurred between May and October in 2007, where the material was thawed. The following five conclusions are highlighted from the initial 1.5 year of the study:

1. Net infiltration into the top of the Type 3 test pile in 2007, under approximately the mean annual rainfall (153 mm), is estimated to be approximately 60 mm/yr (39% of rainfall). Under conditions drier than average for the study site, no net infiltration reported to the 2 m depth at the top of the Type 1 test pile and upper collection lysimeters.

2. Flow was temperature-dependent on a yearly time scale and shorter. At the yearly-scale, a wetting front froze in winter and was remobilized the following summer. During the hydrologically active period (May to October in 2007), outflow from the Type

3 test pile increased as early-season infiltration that had frozen in the upper portion of the pile melted to reach a maximum outflow when the pile mostly thawed in late July, 2007. At the daily time scale, warming air temperatures appeared to cause pore ice to melt, resulting in increases in outflow.

3. In response to rainfall with a recurrence interval of less than 10 years, flow through the flat top surface of the Type 3 test pile and upper collection lysimeters had relatively little spatial variability (based on TDR measurements at the Type 3 test pile) and an average fluid flux of 0.6 +/- 0.2 mm/d. In response to applied rainfall with a recurrence interval of about 35 years onto a pile with matrix saturation of approximately 60%, peak fluid flux is estimated to have been between 10 and 15 mm/d, and macropore flow led to high spatial variability with flow velocities as high as 400 mm/d.

4. A scale-up method has been used to develop a calibrated numerical model capable of simulating flow through the uncovered test piles in the absence of extreme flow events.

5. Sulfate mass loading from Type 3 waste rock is estimated to have averaged 0.9 +/- 0.1 g SO<sub>4</sub><sup>2-</sup>/m<sup>2</sup>/d in 2007. After a storm of moderate intensity, loading increased by a factor of about 2 for a day. Loading from the Type 3 test pile during July 2007 was twice the average rate of approximately 0.8 g SO<sub>4</sub><sup>2-</sup>/d/m<sup>2</sup>.

## RECOMMENDATIONS

- Conduct a tracer test at the Type 3 upper collection lysimeters to compare flow velocity determined by conservative transport with velocity determined by dividing the lysimeter outflow flux by the moisture content of the matrix as a fraction of the large-scale unit waste rock volume (0.06 +/- 0.01).
- New instrumentation: install thermistors at the surface of the test pile top, test pile batters, and at the surface of the upper collection lysimeters to improve the ability to determine the effect of surface freezing and melting on the hydrogeologic behaviour. Install moisture content sensors (ECH<sub>2</sub>O probes) within the upper 0.3 m at the upper collection lysimeters to better enable calibration of an integrated evaporative flux and infiltration model.
- Conduct large column experiments to investigate the net infiltration required to create ice-saturated conditions in Diavik waste rock.
- Measure the snow depth at the batters of the test piles just before the melt starts. The method used to take these measurements would depend upon the outcome of a job hazard analysis that may require approval from mine safety personnel.
- Further data collection and analysis are required to determine whether numerical modeling must include the following processes to adequately predict flow in waste rock piles deposited onto permafrost, to a level required for accurate prediction of geochemical transport:
  1. heterogeneous or dual-porosity modeling
  2. coupled flow and heat transport modeling
  3. coupled unsaturated flow and evaporative flux modeling.

## REFERENCES

Adams, E.E., and Gelhar, L.W., 1992. Field study of dispersion in a heterogeneous aquifer, 2. Spatial moments analysis, *Water Resources Research*, v. 28, n. 12, pp. 3293-3307.

Allen, R.G., Pereira, L.S., Raes, D., and Smith, M., 1998. Crop evapotranspiration - Guidelines for computing crop water requirements, FAO Irrigation and drainage paper 56, Food and Agriculture Organization of the United Nations, Rome, Italy.

American Society for Testing and Materials (ASTM), 2001. Standard Test Method for Particle Size Analysis of Natural and Man-Made Riprap Materials (D 5519), Annual Book of ASTM Standards, v. 04.08.

American Society for Testing and Materials (ASTM), 2002. Standard Test Method for Particle-Size Analysis of Soils (D422-63). Annual Book of ASTM Standards, v. 04.08.

Andrina, J., Wilson, G.W., Miller, S., Neale, A., 2006. Performance of the acid rock drainage mitigation waste rock trial dump at Grasberg Mine, In: Proceedings of the 7th International Conference on Acid Rock Drainage, St. Louis, MO.

Bear, J., 1972. Dynamics of fluids in porous media, Dover Publications, Inc., New York, 764 p.

Bellehumeur, T., 2001. Mechanisms and spatial variability of rainfall infiltration on the Claude waste rock pile, MSc. dissertation, University of British Columbia, Vancouver.

Birkholzer, J., and Tsang, C.-F., 1997. Solute channeling in unsaturated heterogeneous porous media, *Water Resources Research*, v. 33, n. 10, pp. 2221–2238.

Black, P.B., and Tice, A.R., 1989. Comparison of soil freezing curve and soil water curve data for Windsor Sandy Loam, *Water Resources Research*, v.25, n.10, pp. 2205-2210.

Blowes, D.W., C.J. Ptacek, J.L. Jambor and C.G. Weisener, 2003. The Geochemistry of Acid Mine Drainage, Treatise on Geochemistry, Ed. H.D. Holland and K.K. Turekian, v. 9, pp. 149-204.

Blowes, D., L. Smith, D. Segó, L. Smith, M. Neuner, M. Gupton, M. Moncur, M. Moore, R. Klassen, T. Deans, C. Ptacek, A. Garvie, and J. Reinsen, 2007, Prediction of effluent water quality from waste rock piles in a continuous permafrost region, from the Proceedings of IMWA Symposium 2007: Water in Mining Environments, R. Cidu & F. Frau (Eds), 27th - 31st May 2007, Cagliari, Italy.

Carey, S.K., S.L. Barbour, and M.J. Hendry, 2005. Evaporation from a waste-rock surface, Key Lake, Saskatchewan, *Can. Geotech. J.*, v. 42, pp. 1189–1199.

Cary, J.W., 1965. Water flux in moist soil: thermal versus suction gradients, *Soil Science*, v. 100, n. 3, pp. 168-175.

Corazao Gallegos, J.C., 2007. The design, construction, instrumentation, and initial response of a field-scale waste rock test pile, M.A.Sc. dissertation, University of British Columbia, Vancouver, Canada.

Coulombe-Pontbriand, Moise, Robert Reid, and Francis Jackson, 1998. Overview of the Hydrology and Water Quality of the Coppermine River, BHP Ekati Diamond Mine internal report, 1998.

Dawson, R.F., and K.A. Morin, 1996. Acid Mine Drainage in Permafrost Regions: Issues, Control Strategies and Research Requirements. Canadian Mine Environment Neutral Drainage (MEND) Report 1.61.2.

Diavik Diamond Mines, Inc., 2005. Environmental Assessment Review and Revised Effects Assessment, internal report, P.O. Box 2498, 5007 50<sup>th</sup> Ave., Yellowknife, NT, X1A 2P8, Canada.

Diavik Diamond Mines, Inc., 2006. Interim closure and reclamation plan, Report ICRP-Sep06 submitted to Wek'èzhí Land and Water Board, c/o Mackenzie Valley Land and Water Board, 7th Floor – 4910 50th Avenue, PO Box 2130, Yellowknife, NT, Canada, X1A 2P6, <http://www.mvlwb.ca/WLWB/Registry.aspx>.

Dingman, S.L., 2002. Physical Hydrology, 2<sup>nd</sup> Ed., Prentice Hall, Upper Saddle River, NJ, 646p.

Dirksen, C., and Miller, R.D., 1966. Closed-system freezing of unsaturated soil, *Soil Sci. Soc. Am. J.*, v. 30, pp. 168-173.

Earman, S., and Hershey, R.L., 2004. Water quality impacts from waste rock at a Carlin-type gold mine, Elko County, Nevada, *Environmental Geology*, v. 45, n. 8, pp. 1043-1053.

Environment Canada, 2008. Climate Data Online, National Climate Data and Information Archive, <[http://climate.weatheroffice.ec.gc.ca/climateData/canada\\_e.html](http://climate.weatheroffice.ec.gc.ca/climateData/canada_e.html)>.

Fala, O., Aubertin, M., Molson, J., Bussière, B., Wilson, G.W., Chapuis, R., and Martin, V., 2003. Numerical modeling of unsaturated flow in uniform and heterogeneous waste rock piles, from the Proceedings from the 6th International Conference of Acid Rock Drainage, pp 903-910 (The Australasian Institute of Mining and Metallurgy: Melbourne).

Fourie, W.F., Barnes, D.L., Shur, Y., 2007. The formation of ice from the infiltration of water into a frozen coarse grained soil, *Cold Regions Science and Technology*, v. 48, pp. 118-128.

Fredlund, D.G., and H. Rahardjo, 1993. *Soil Mechanics for Unsaturated Soils*, John Wiley and Sons, Inc., New York, 519p.

Fredlund, D.G., Anqing Xing, and Shangyan Huang, 1994. Predicting the permeability function for unsaturated soils using the soil-water characteristic curve, *Canadian Geotechnical Journal*, v. 31, n. 3, pp. 521-532.

Fredlund, M.D., W. S. Sillers, D. G. Fredlund, and G.W. Wilson, 1996. Design of a Knowledge-based system for unsaturated soil properties, 3rd Canadian Conference on Computing in Civil and Building Engineering, Montreal, Quebec, Aug. 26-28.

Fredlund, Murray D., G. Ward Wilson, and Delwyn G. Fredlund, 2002. Use of the grain-size distribution for estimation of the soil-water characteristic curve, *Can. Geotech. J.*, v. 39, pp. 1103–1117.

Golder Associates, 1997. *Baseline Data of Climate and Surface Water Hydrology for the Diavik Diamond Mines EIA*, report prepared by Golder Associates, 4260 Still Creek Drive, Burnaby, BC, Canada, V5C 6C6.

Golder Associates, 2005. *Baseline hydrology update – Diavik Diamond Mines*, technical memorandum prepared by D’Aoust, S., and D. Walker, Golder Associates, 4260 Still Creek Drive, Burnaby, BC, Canada, V5C 6C6, 44p.

Golder Associates, 2008. *Report on 2007 review of baseline climate and surface water hydrology for the Diavik Diamond Mine*, prepared by Golder Associates, Burnaby, BC, submitted to Diavik Diamond Mines Inc., Yellowknife, NWT, Canada.

Gray, D.M., Toth, B., Zhao, L., Pomeroy, J.W., Granger, R.J., 2001. Estimating areal snowmelt infiltration into frozen soils, *Hydrological Processes*, v. 15, pp. 3095-3111.

Gupton, M., in progress. M.A.Sc. thesis, University of British Columbia, Vancouver, Canada.

Hansson, K., Šimánek, J., Mizoguchi, M., Lundin, L.-C., and van Genuchten, M.Th., 2004. Water flow and heat transport in frozen soil: numerical solution and freeze-thaw applications, *Vadose Zone Journal*, v. 3, pp. 693-704.

Harlan, R.L., 1974. Dynamics of water movement in permafrost: a review, from *Permafrost Hydrology*, the Proceedings of the workshop seminar for the Canadian National Committee and the International Hydrological Decade, February 26-28, Calgary, Alberta..

Kane, D.L., 1979. Snowmelt infiltration into seasonally frozen soils, from Proceedings of the Conference on Cold Regions Soil Water Problems, American Geophysical Union, September 19-20, Calgary, Alberta.

Kyhn, C., Elberling, B., 2001. Frozen cover actions limiting AMD from mine waste deposited on land in Arctic Canada, *Cold Regions Science and Technology*, v. 32, Is. 2-3, pp. 133-142.

Lapalla, E.G, Healy, R.W., and Weeks, E.P., 1987. Documentation of computer program VS2D to solve the equations of fluid flow in variably saturated porous media, U.S. Geological Survey Water Resources Investigations Report 83-4099, 131 p.

Lawrence, D.M., and Slater, A.G., 2005. A projection of severe near-surface permafrost degradation during the 21st century, *Geophysical Research Letters*, v. 32, doi:10.1029/2005GL025080.

LeBlanc, D.R., Garabedian, S.P., Hess, K.M., Gelhar, L.W., Quadri, R.D., Stollenwerk, K.G., and Wood, W.W., 1991. Large-scale natural gradient tracer test in sand and gravel, Cape Cod, Massachusetts, 1. Experimental design and observed tracer movement, *Water Resources Research*, v. 27, n. 5, pp. 895-910.

Liston, G.E., and Sturm, M., 2002. Winter precipitation patterns in Arctic Alaska determined from a blowing-snow model and snow depth observations, *Journal of Hydrometeorology*, v. 3, pp. 646-659.

Mace, A., D. L. Rudolph, and R. G. Kachanoski, 1998. Suitability of parametric models to describe the hydraulic properties of an unsaturated coarse sand and gravel, *Ground Water* v. 36 n. 3, pp. 465-475.

Marcoline, J., 2008. Investigations of water and tracer movement in covered and uncovered unsaturated waste rock, PhD. dissertation, University of British Columbia, Vancouver, Canada.

Mackenzie Valley Land and Water Board, 2002. Decision of the McKenzie Valley Land and Water Board Panel Meeting of May 30, 2002; Re: Water License N7L2-1645, pursuant to the Northwest Territories Waters Act.

McCord, J.T., Stevens, D.B., Wilson, J.L., 1991. Hysteresis and state-dependent anisotropy in modeling unsaturated hillslope hydrologic processes, *Water Resources Research*, v. 27, n. 7, pp. 1501-1518.

McKnight, T.L., 2002. *Physical Geography: a landscape appreciation*, 7<sup>th</sup> Ed., Prentice Hall, Upper Saddle River, New Jersey, 629 p.

Meldrum, J.L., H.E. Jamieson, and L.D. Dyke, 2001. Oxidation of mine tailings from Rankin Inlet, Nunavut, at subzero temperatures, *Can. Geotech. J.*, v. 38, pp. 957-966.

Michel, F.A., and van Everdingen, R.O., 1994. Changes in hydrogeologic regimes in permafrost regions due to climatic change, *Permafrost and Periglacial Processes*, v. 5, pp. 191-195.

Mantoglou, A., and L. Gelhar (1987), *Stochastic Modeling of Large-Scale Transient Unsaturated Flow Systems*, *Water Resour. Res.*, v. 23, n.1, pp. 37-46

Morin, K.A., Gerencher, E., Jones, C.E., Konasewich, D.E., 1991. Critical literature review of acid drainage from waste rock. MEND Report 1.11.1, CANMET, 175 p.

Morin, K.A., 2003. Problems with acid rock drainage predictions at the Ekati Diamond Mine, Northwest Territories, Canada, from the Proceedings from the 6th International Conference of Acid Rock Drainage, pp. 663-669 (The Australasian Institute of Mining and Metallurgy: Melbourne).

Nichol, Craig F., 2002. Transient flow and transport in unsaturated heterogeneous media: Field experiments in mine waste rock. Ph.D. dissertation, University of British Columbia, Vancouver.

Nichol, C.F., Smith, L., and Beckie, R., 2005. Field scale experiments of unsaturated flow and solute transport in a heterogeneous porous medium, *Water Resources Research*. v. 41.

O'Kane, M., and Barbour, S. L., 2003. Predicting field performance of lysimeters used to evaluate cover systems for mine waste, from the Proceedings from the 6th International Conference of Acid Rock Drainage, pp. 663-669 (The Australasian Institute of Mining and Metallurgy: Melbourne).

Philip, J.R., 1975. Stability analysis of infiltration, *Soil Sci. Soc. Am. J.*, v. 39, pp. 1042-1049.

Price, William A., 2003. Challenges posed by metal leaching and Acid Rock Drainage, and approaches used to address them, In J.J. Jambor, D.W. Blowes, and A.I.M. Ritchie, *Environmental Aspects of Mine Wastes*, Short Course Series v. 31.

Raats, P.A.C., 1973. Unstable wetting fronts in uniform and nonuniform soils, *Soil Sci. Soc. Am. J.*, v. 37, pp. 681-685.

Ritchie A. I. M., 1994. Sulfide oxidation mechanisms: controls and rates of oxygen transport, in *The Environmental Geochemistry of Sulfide Mine-wastes* (eds. J. L. Jambor, and D. W. Blowes). Mineralogical Association of Canada, Nepean, ON, vol. 22, pp. 201-246.

Roscoe, and Postle, 2005. Diavik Diamond Mines mineral reserve and mineral resource audit, Report NI 43-101 prepared for Harry Winston Diamond Corporation (formerly

Aber Diamond Corporation), Rosceo Postle Associates Inc., [www.rpacan.com](http://www.rpacan.com), Suite 501, 55 University Avenue, Toronto, Ontario, M5J 2H7, Canada.

Smith, Leslie, Dina L. Lopez, Roger Beckie, Kevin Morin, Richard Dawson, and William A. Price, 1995. Hydrogeology of Waste Rock Dumps, British Columbia Acid Mine Drainage Task Force.

Smith, Leslie, and Roger Beckie, 2003. Hydrologic and geochemical transport processes in mine waste rock, Environmental Aspects of Mine Wastes, Ed. J.J. Jambor, D.W. Blowes, and A.I.M. Ritchie, Short Course Series v. 31, Ed. R. Raeside, Mineralogical Association of Canada, 2003.

Smith, Lianna, 2008. Test piles project 2006 construction summary, report prepared for FDA Engineering, Ltd., 38 Sheep River Cove, Okotoks, AB T1S 2G7, Canada, and submitted to Diavik Diamond Mines, Inc., P.O. Box 2498, 5007 50<sup>th</sup> Ave., Yellowknife, NT, X1A 2P8, Canada.

Smith, Lianna, *in progress*, M.Sc. thesis, University of Waterloo, Waterloo, Canada.

SoilCover, 1997. The design of soilcover systems. SoilCover Version 4.0 User Manual. Unsaturated Soils Group, Department of Civil Engineering, University of Saskatchewan, Saskatoon.

Stähli, M., Jansson, P.E., and Lundin, L.C., 1996. Preferential water flow in a frozen soil – a two-domain model approach, Hydrological Processes, v. 10, pp. 1305-1316.

Steffen Robertson Kirsten Consulting (SRK), 2003. 2002 Waste Rock Storage Area Seepage and Waste Rock Survey Report, report submitted by BHP Billiton Diamonds, Inc., to the Wek'eezhii Land and Water Board, P.O. Box 2130, Yellowknife, NT, Canada, X1A 2P6.

Steffen Robertson Kirsten Consulting (SRK), 2007. EKATI Diamond Mine 2006 Waste Rock Storage Area Seepage and Waste Rock Survey Report, report submitted as requirement for License MV2003L2-0013 to the Wek'eezhii Land and Water Board, <http://www.mvlwb.ca/WLWB/Registry.aspx>.

Stockwell, J., Smith, L., Jambor, J.L., and Beckie, R., 2006. The relationship between fluid flow and mineral weathering in heterogeneous unsaturated porous media: a physical and geochemical characterization of a waste rock pile, Applied Geochemistry, v. 21, pp. 1347-1361.

Tolstikhin, N.I., and Tolstikhin, O.N., 1976. Groundwater and surface water in the permafrost region, Technical Bulletin n. 97, Inland Waters Directorate, National Research Council of Canada, translated by V. Poppe, 25p.

Tokunaga, T.K., Wan, J., and Olson, K.R., 2002. Saturation-matric potential relations in gravel, *Water Resources Research*, v. 38, n. 10, p.1214, doi:10.1029/2001WR001242.

Tran, A.B., Miller, S., Williams, D.J., Fines, P., and Wilson, G.W., 2003. Geochemical and Mineralogical Characterization of Two Contrasting Waste Rock Dumps – The INAP Waste Rock Dump Characterization Project, Proceedings from the 6th International Conference of Acid Rock Drainage, pp 903-910 (The Australasian Institute of Mining and Metallurgy: Melbourne).

van Genuchten, M. Th., 1980. A closed-form equation for predicting the hydraulic conductivity of unsaturated soils, *Soil Sci. Soc. Am. J.*, v. 44, pp. 892-898.

Wagner, K. 2004, Characterization of the geochemistry of discharge waters, pore waters, primary and secondary minerals of an experimental waste rock pile, Cluff Lake Mine, Saskatchewan, Canada. M.Sc. dissertation, University of British Columbia, Vancouver, Canada.

Wagner, K., Smith, L., Beckie, R., 2006. Hydrogeochemical characterization of effluent from mine waste rock, Cluff Lake, Saskatchewan. In: Proceedings of the 7th International Conference on Acid Rock Drainage, St. Louis, MO.

Walvoord, M. A., and R. G. Striegl (2007), Increased groundwater to stream discharge from permafrost thawing in the Yukon River basin: Potential impacts on lateral export of carbon and nitrogen, *Geophys. Res. Lett.*, 34, L12402, doi:10.1029/2007GL030216.

Weller, G., and Holmgren, B., 1974. The microclimates of the Arctic tundra, *Journal of Applied meteorology*, v. 13, pp. 854-862.

Wilson, G.W., Fredlund, D.G., and Barbour, S.L., 1994. Coupled soil-atmosphere modelling for soil evaporation, *Canadian Geotechnical Journal*, v. 31, pp. 151-161.

Wilson, G.W., 2003. The design and performance of mine-waste cover systems, *Environmental Aspects of Mine Wastes*, Ed. J.J. Jambor, D.W. Blowes, and A.I.M. Ritchie, Short Course Series v. 31, Ed. R. Raeside, Mineralogical Association of Canada, 2003.

Woo, M., and Marsh, P., 1978. Analysis of error in the determination of snow storage from small High Arctic basins, *Journal of Applied Meteorology*, v. 17, pp. 1537-1541.

Woo, M., Yang, Z., Xia, Z., Yang, D., 1994. Streamflow processes in an alpine permafrost catchment, Tianshan, China, *Permafrost and Periglacial Processes*, v. 5, pp. 71-85.

Woo, M., Marsh, P., and Pomeroy, J.W., 2000. Snow, frozen soils and permafrost hydrology in Canada, 1995–1998, *Hydrological Processes*, v. 14, pp. 1591-1611.

Yazdani, J., Barbour, L, and Wilson, G.W., 2000. Soil water characteristic curve for mine waste rock containing coarse material, from Proceedings of the 6<sup>th</sup> Environmental Engineering Specialty Conference of the Canadian Society of Civil Engineers, London, ON, Canada.

Zegelin, S., I. White, and D.R. Jenkins, 1989. Improved field probes for soil-water content and electrical conductivity measurement using time domain reflectometry. *Water Resour. Res.*, v. 25, pp. 2367–2376, 89WR01417.

Zhang, Z.F., Ward, A.L., and Gee, G.W., 2003. A tensorial connectivity-tortuosity concept to describe the unsaturated hydraulic properties of anisotropic soils, *Vadose Zone Journal*, v. 2, pp. 313-321.

## **APPENDIX A CONSTRUCTION DETAILS**

### **A.1 Construction of the test piles**

From 2004 to 2007 Diavik Diamond Mines, Inc. (Diavik), researchers from the University of Waterloo, the University of British Columbia, and the University of Alberta, and engineers from FDA Engineering, Ltd. (FDA), constructed three mine waste rock test piles and six upper collection lysimeters. The construction was managed by FDA and is reported in detail by Smith 2008. The test piles were constructed with waste rock based upon the classification system required by the mine water license (Mackenzie Valley Land and Water Board 2002) and described in the Environmental Assessment (Diavik Diamond Mines, Inc., 2005). Diavik refers to mine waste rock as country rock. Geologists and environmental technicians classify waste rock at Diavik by sulfur content into three categories: Type 1, Type 2, and Type 3. The Type 1 test pile (T1) consists of rock classified by geologists as rock that is not likely to generate acid rock drainage (ARD), and is intended to have sulfur content less than 0.04%. The Type 3 test pile (T3) consists of rock classified as having the potential to generate ARD, and is intended to have sulfur content greater than 0.08%. A third test pile was built to investigate the mine closure plan. A end-dumped and push-dumped Type 3 pile was re-sloped into a 3 : 1 horizontal to vertical aspect, covered by a 1.5 m-deep glacial till layer, which was then covered by a 3 m Type 1 layer.

A basal drain and basal lysimeters collect the outflow from each test pile, using the zero-tension pan lysimetry method (Figures A.1 and A.2). The Type 1 and Type 3 test piles were built upon 40 Mil high-density polyethylene (HDPE) liners with a 2680m<sup>2</sup> and 3050m<sup>2</sup> collection surface, respectively. Each liner consists of overlapping 7 m-wide

sheets of HDPE that were welded together to form a single sheet (Figure A.7). The T1 liner was installed on graded T1 waste rock fill covered with a 30 cm-thick layer of processed kimberlite and sand from local esker deposits. The T1 liner sloped at a 1% minimum grade towards a perforated 6" polyvinyl chloride (PVC) drainpipe located at the center of the pile base (Figure A.1). The T1 liner was covered with a permeable geotextile for protection. The Type 3 pile liner was installed on a T1 fill pad covered with a 50 cm-thick layer of esker sand. The T3 liner sloped at a 0.7% minimum grade towards a drainpipe located near the outside edge of the liner (Figures A.2 and A.7). Thermostat-regulated mineral-insulated heat-trace was installed inside each basal drain PVC drainpipe. Berms 30 cm-high at the outside edge of the liner of each test pile direct pile outflow to the basal drain. The low liner berm height may allow a capillary rise to direct flow to an evaporative seepage face, but this potential effect would be limited to less than five percent of the liner area (O'Kane 2003). The PVC drainpipe exited the liner by passing through the berm at a sleeve in the liner sealed to the pipe. The drainage from the T1 basal drain flows to a flow-through monitoring system inside the T1/T3 instrument building located between the T1 and T3 piles. The drainage from T3 basal drain flows to flow-through monitoring systems located in two instrument huts: the north drain hut and the south drain hut (Figure A.8). A 30 cm-thick protective layer of crushed Type 1 rock 2 in.-and-finer covered the T1 liner. A 30 cm-thick protective layer of 1¼ in. clean crushed Type 1 rock covered the T3 liner. Waste rock was deposited onto the protective layer of each test pile liner.

Basal lysimeters were constructed to collect water flow that reached the base of the central region of each test pile in discrete collection areas (Figures A.1 and A.2). Four 4

m by 4 m basal lysimeters and four 2 m by 2 m basal lysimeters, with a total collection area of 72m<sup>2</sup>, are located beneath the flat top of each pile. Two 4 m by 4 m basal lysimeters and two 2 m by 2 m basal lysimeters, with a total collection area of 36m<sup>2</sup>, are located near or below one of the batters of each pile. Each lysimeter drains at a minimum 1% grade in 1.5” PVC pipes, kept above freezing with thermostat-controlled heat trace located inside the drain pipes (Figure A.9). The volume of water that pools inside the drain pipes at low points and joints between pipe segments ranged from 0.1 L to 1.4 L. The drain pipes are housed inside 14-inch diameter insulated double-wall HDPE pipe to minimize heat transfer from the heated collection system to the waste rock pile. Each basal lysimeter (Figure A.10) was constructed at least 60 cm deep to keep the capillary fringe within the lysimeter. The basal lysimeters were constructed with 40 Mil HDPE liner about a plywood frame (Figure A.11). Heat trace was placed inside a sand layer below each lysimeter to keep the saturated bottom of each lysimeter thawed at times when water may flow through an unfrozen pile core to a frozen pile base. Thermistors were placed inside the lysimeters to allow monitoring of this heat trace. Each basal lysimeter drains to a zero-tension standpipe with a 20cm screen. The drainage from the basal lysimeters flows to flow-through monitoring systems inside the T1/T3 instrument building (Figure A.12).

A 2m-high protective layer of waste rock was push-dumped over the 0.3m-thick crushed rock layer atop the HDPE liner, using haul trucks and a bulldozer (Figure A.13). The basal lysimeters were filled with waste rock by hand around the standpipe drains and by an excavator. The moderate-traffic layer created at the top of this 2 m lift was subsequently partially ripped when trenches were excavated to install gas sampling

instrumentation. The piles were then built in five stages by end-dumping and push-dumping from an access ramp 15m above the HDPE liner (Figure A.14).

After each stage of test pile construction, instrumentation was installed on the tip face (Figure A.15). Instrumentation included time domain reflectometry (TDR) probes, which measure moisture content. Each test pile contains four instrumented tip faces, but TDR probes were installed on only two or three of the tip faces. Instrumentation was installed using a fall-arrest system and a manlift. TDR sensors were placed inside permeable nylon bags filled with <20mm waste rock to ensure that the exposed rods would not be surrounded by void space. Instrument lines were anchored to boulders at the top of the pile to minimize displacement during burial.

Due to a signal attenuation limitation to the TDR cable length and other logistical reasons, instrumentation was required to exit the pile at the top surface, rather than at the base. Instrument leads were buried at a level 0.5 m below the design elevation of the top of the pile, each covered with HDPE pipe cut in half with a chain saw. After the pile construction was completed by end-dumping and push-dumping, much of the top surface was excavated to recover the instrument leads. After instrument lead excavation, waste rock was re-deposited to create a relatively level top surface (Figure A.17). These activities resulted in waste rock at the top surface of the test piles which may have a depositional structure different than the rest of the pile.

TDR probes were installed on the batter (waste rock slope) from a man lift. Each probe was checked after shipment to the site by observing good reflected waveforms before installation. Coaxial cables for the TDR probes were protected with flexible PVC pipe. Protecting the coaxial cable for each probe individually significantly improved the

survival rate upon burial in waste rock. Individually protected TDR probes (in the covered test pile) survived burial at a rate of 91% while only 45% of the probes that shared a common protective flexible PVC housing (as shown in Figure A.15) survived burial. TDR probe survival rate in the Type 3 and Type 1 piles was 45% (Table A.1).

Four tensiometers were installed into shallow boreholes drilled into the top of the Type 3 test pile ten months after construction of the pile. Each tensiometer was installed into a separate borehole, which was drilled using a compressed-air jack hammer drill. Two tensiometers were installed at the northern profile of TDR probes and above the basal lysimeters at depths of 0.60 m and 1.20 m (Figure A.4). Two tensiometers were installed at the southern profile of TDR probes and above the basal lysimeters at depths of 0.60 m and 1.20 m. Instrumentation details are discussed in Appendix B.

## **A.2 Construction of the upper collection lysimeters**

Upper collection lysimeters were constructed at a location about 100 m from the test piles in waste rock with a surface at the same elevation as the top of the piles (Figures A.17 and A.19). The lysimeters were constructed by removing the tops from 1000 gal HDPE water tanks (Figure A.20). Drains were constructed using screened standpipes like the one shown in Figure A.11e connected to 2" fittings installed in each tank by the manufacturer. PVC pipes connected to the tank drain directed the outflow at a 1% minimum grade to a heated instrument building. Drain pipes were heat traced and insulated to keep from freezing in the spring and autumn when air temperatures drop considerably lower than subsurface temperatures. Two thermistors were installed near the heat trace to monitor any heat transfer to the waste rock from the heat trace around

the insulated drain pipes. At the west T3 and west T1 upper lysimeter thermistors were installed in the waste rock at the outside of the lysimeter, 5 cm and 40 cm above the top of the insulated drain pipe. At each of the east T3 and east T1 upper lysimeters, one thermistor was installed inside the insulated pipe near the heat trace and 40 cm above it, the other thermistor was installed.

Two lysimeters were filled with Type 1 material and two lysimeters were filled with Type 3 material using a Komatsu PC600 track-mounted excavator (Figure A.21). The Type 3 lysimeters are located to the west of the Type 1 lysimeters. Waste rock coarser than about 1 m was not deposited into the lysimeters. The screened drains were buried with waste rock by hand before waste rock was deposited by the excavator. During waste rock deposition, the east Type 1 lysimeter wall was torn from the top down 50 cm. This tear was repaired by welding a sheet of 40 Mil HDPE geomembrane to the lysimeter wall over the tear. The Type 1 lysimeter walls extend from the waste rock surface to a depth of 1.50 m. The Type 3 lysimeter walls extend from the waste rock surface to a depth of 1.75 m. The bottom of the drain fitting at each lysimeter was 5 cm above the base of the lysimeter. Therefore the effective depth below the ground surface was 1.45 m for the Type 1 upper collection lysimeters and 1.70 m for the Type 3 upper collection lysimeters. The collection area was 3.6 m<sup>2</sup> for the Type 1 upper collection lysimeters and 2.09 m<sup>2</sup> for the Type 3 upper collection lysimeters. The lysimeter drainage monitoring flow-through systems are described in Appendix B.

Three ECH<sub>2</sub>O probes and three tensiometers were installed into a single borehole located between the Type 3 upper collection lysimeters (Figure A.19). ECH<sub>2</sub>O-TE probes measure moisture content, temperature, and pore water electrical conductivity.

Tensiometers measure matric potential. The borehole was drilled with a gasoline-powered Pionjar jack-hammer drill to a depth of 1 m. The diameter of the borehole was 20 cm at the bottom and 60 cm at the top. An ECH<sub>2</sub>O probe and the porous cup of a tensiometer was installed 20 cm from each other at a depth of 0.90 m, 0.60 m, and 0.30 m. Each ECH<sub>2</sub>O probe and tensiometer porous cup was surrounded by waste rock matrix material finer than 5 mm to ensure that a probe was not installed in a large air-filled pore.

**Table A.1** A list of the TDR probes that survived construction.

<b>Instrument Label</b>	<b>Array ID</b>	<b>Northing</b>	<b>Easting</b>	<b>Depth</b>	<b>Survived</b>	<b>Failed</b>
		m	m	m		
<b>Type 1 Test Pile</b>						
11W2TDR04	79	7151224.54	533421.23	4.24		X
11W2TDR06	80	7151226.08	533419.61	5.65	X	
11W2TDR07	81	7151228.03	533418.49	6.99		X
11W2TDR08	82	7151229.55	533418.61	8.14		X
11W2TDR09	83	7151231.02	533418.47	8.71	X	
12W2TDR01	84	7151226.53	533421.04	0.98		X
12W2TDR02	85	7151227.21	533421.05	1.46		X
12W2TDR2A	86	7151227.96	533420.74	2.18	X	
12W2TDR03	87	7151228.93	533420.97	2.86	X	
12W2TDR06	88	7151232.42	533421.42	5.64		X
<b>Total</b>					<b>4</b>	<b>6</b>
<b>Type 3 Test Pile</b>						
31N2TDR01	51	7151165.59	533357.47	0.67	X	
31N2TDR03		7151165.35	533354.54	2.41		X
31N2TDR05		7151166.13	533351.66	4.48		X
31N2TDR07	52	7151165.65	533349.15	6.13	X	
31N2TDR09	53	7151166.06	533347.30	8.04	X	
31S2TDR01	54	7151159.72	533356.39	1.18	X	
31S2TDR03	55	7151160.83	533354.49	2.39	X	
31S2TDR05	56	7151160.45	533346.71	4.76	X	
31S2TDR07		7151159.46	533349.09	6.80		X
31S2TDR09	57	7151160.93	533351.60	8.85	X	
32S2TDR01		7151166.44	533349.11	1.56		X
32S2TDR03		7151163.96	533346.04	2.69		X
32S2TDR05		7151165.98	533343.77	5.18		X
32S2TDR07		7151164.23	533341.62	6.81		X
32S2TDR09		7151164.74	533350.67	8.82		X
32N2TDR01		7151159.18	533348.45	1.20		X
32N2TDR03		7151159.04	533350.92	2.90		X
32N2TDR05		7151159.32	533345.98	4.60		X
32N2TDR07	58	7151159.91	533343.03	6.79	X	
32N2TDR09		7151160.35	533340.29	8.57		X
33N2TDR01	59	7151165.76	533343.02	1.16	X	
33N2TDR02		7151164.93	533341.78	2.19		X
33N2TDR03	60	7151165.11	533339.80	3.06	X	
33N2TDR05	61	7151165.25	533344.80	4.86	X	
33S2TDR01		7151159.96	533342.34	1.10		X
33S2TDR02	62	7151161.16	533341.23	2.32	X	
33S2TDR03	63	7151160.33	533339.18	3.09	X	
33S2TDR05		7151160.00	533344.39	4.96		X
<b>Total</b>					<b>13</b>	<b>15</b>

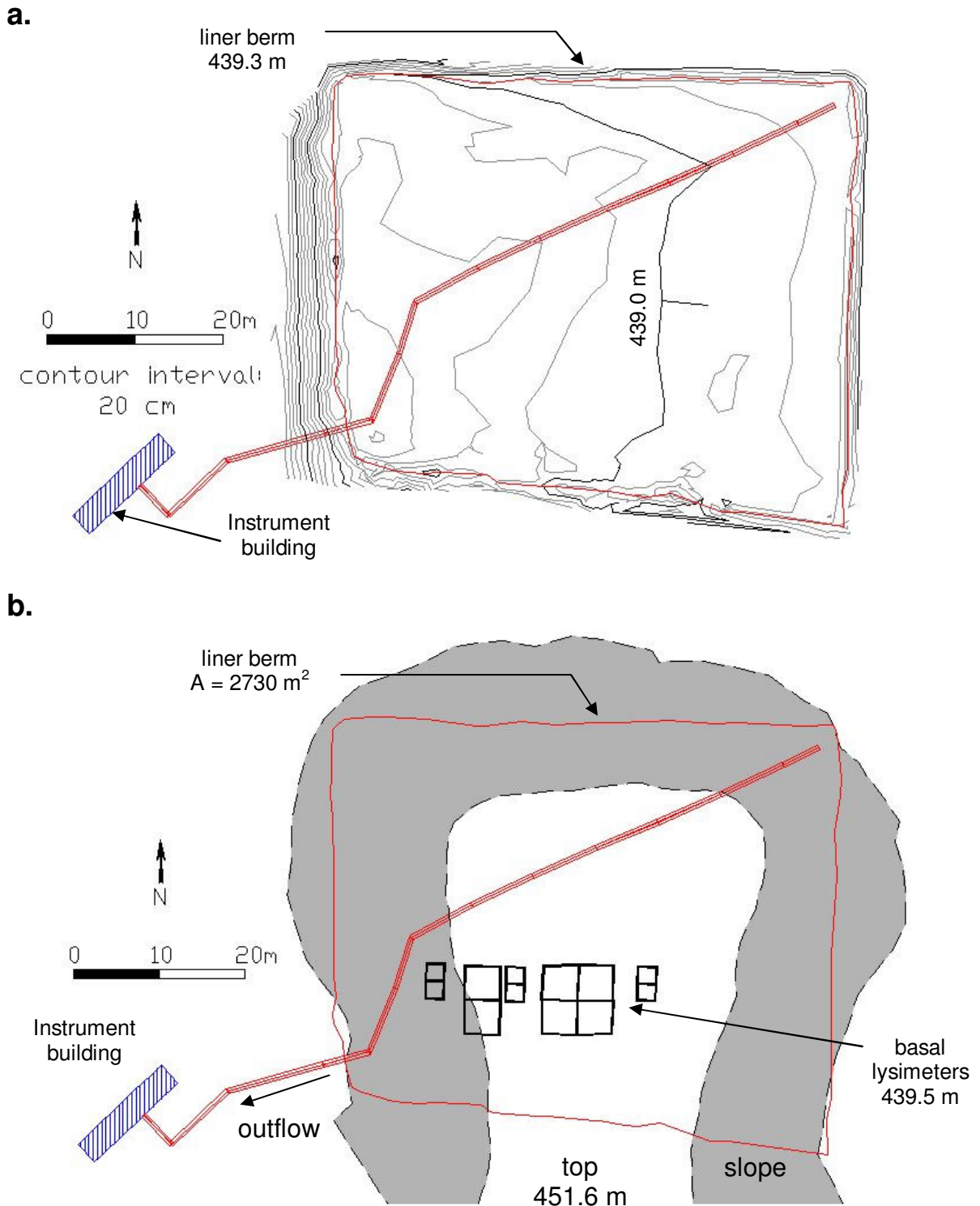


**Figure A.1** As-built drawings of the Type 1 test pile (a) basal drain HDPE liner and (b) the liner and basal lysimeters relative to the outline of the pile top and batters. The basal lysimeters drain to the instrument building: drain lines were omitted from drawing for clarity.

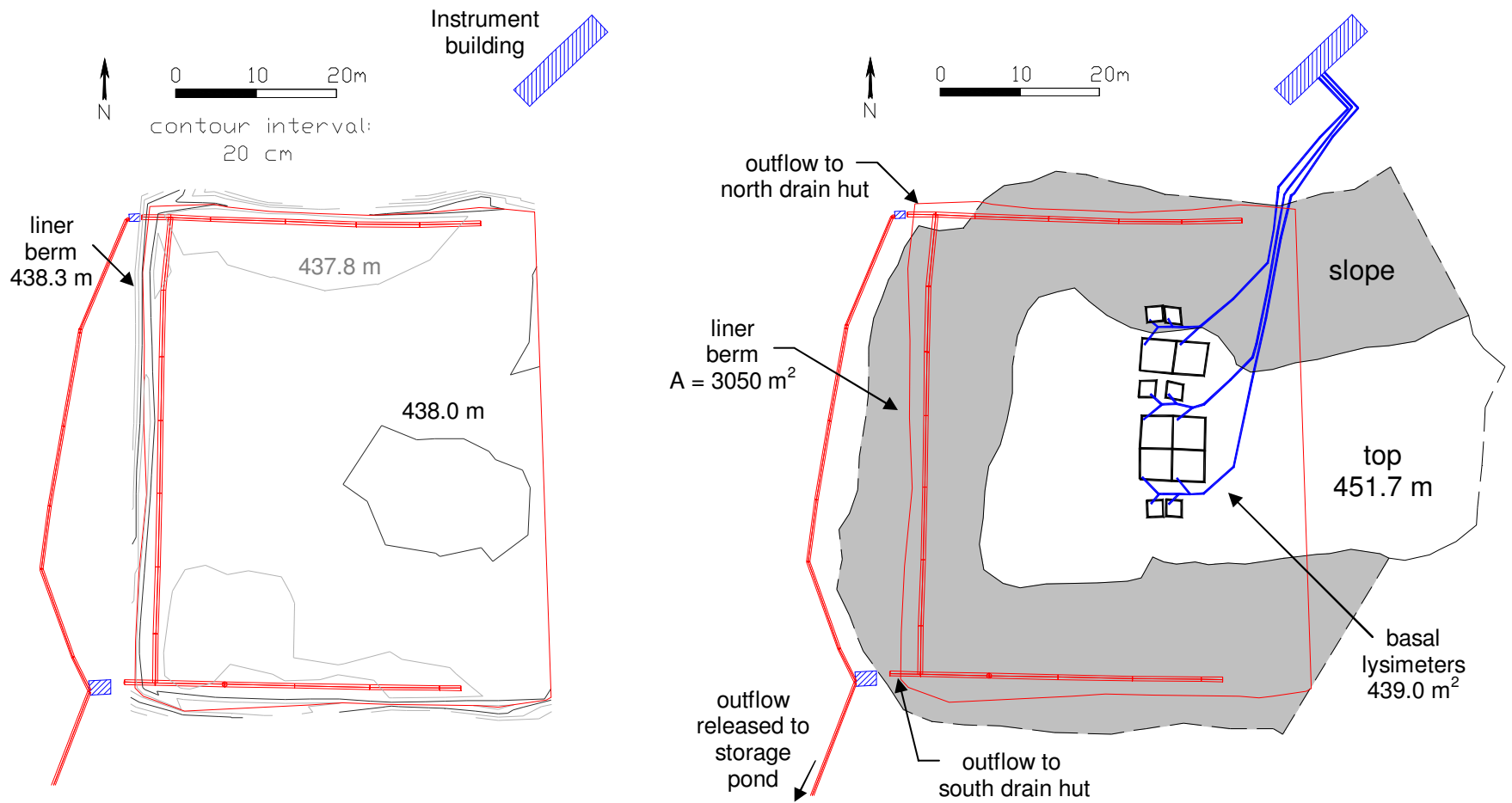


**Figure A.2** As-built drawings of the Type 3 test pile (a) basal drain HDPE liner and (b) the liner and basal lysimeters relative to the outline of the pile top and batters.

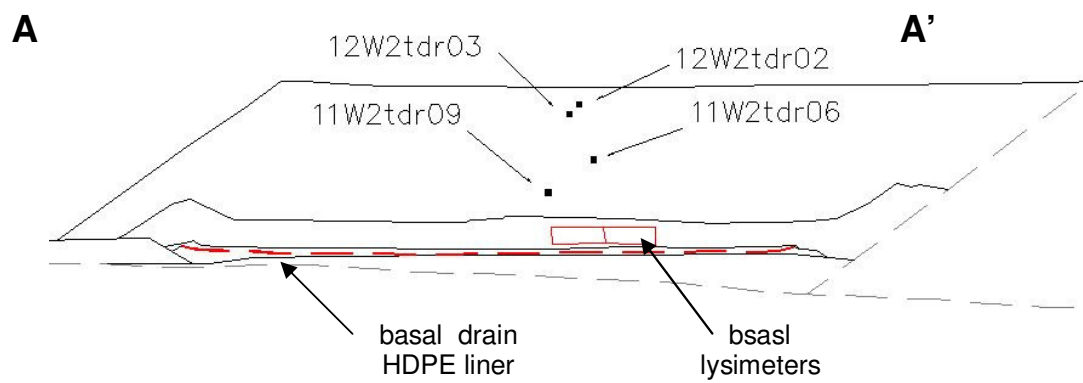
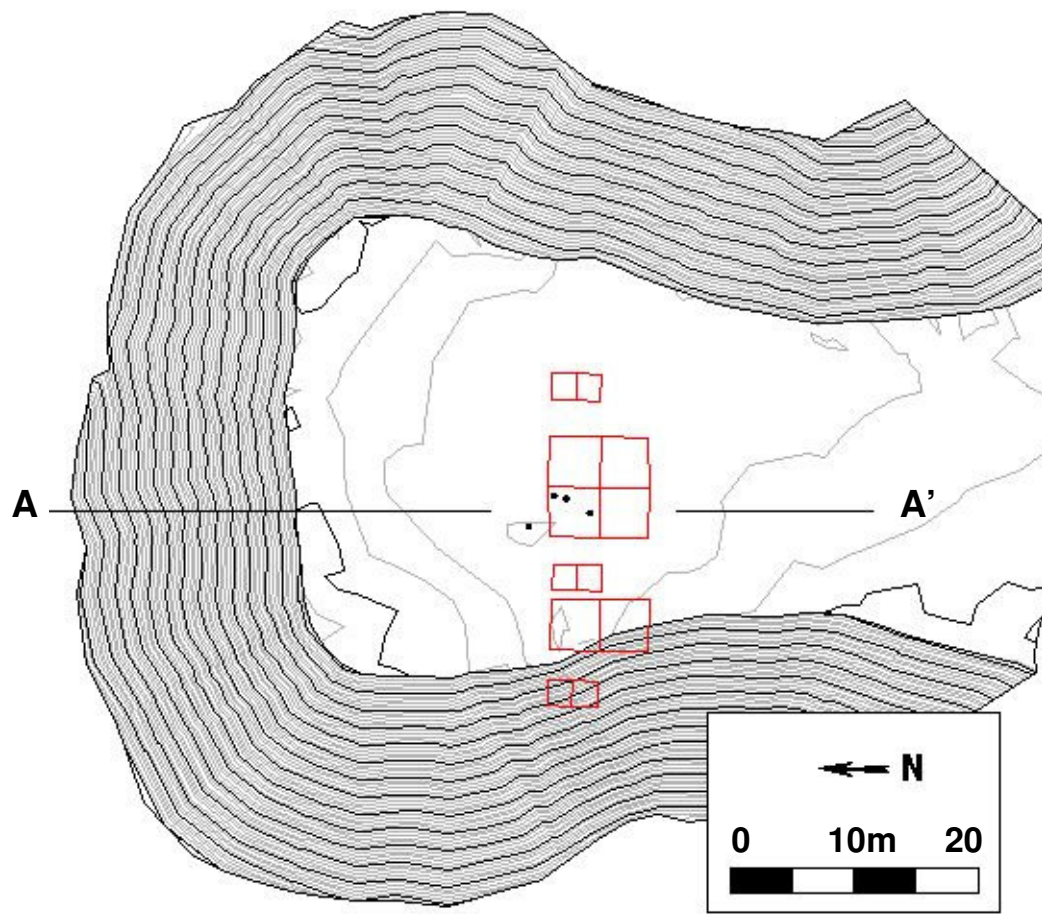


**Figure A.3** As-built positions of TDR probes in the Type 1 test pile.

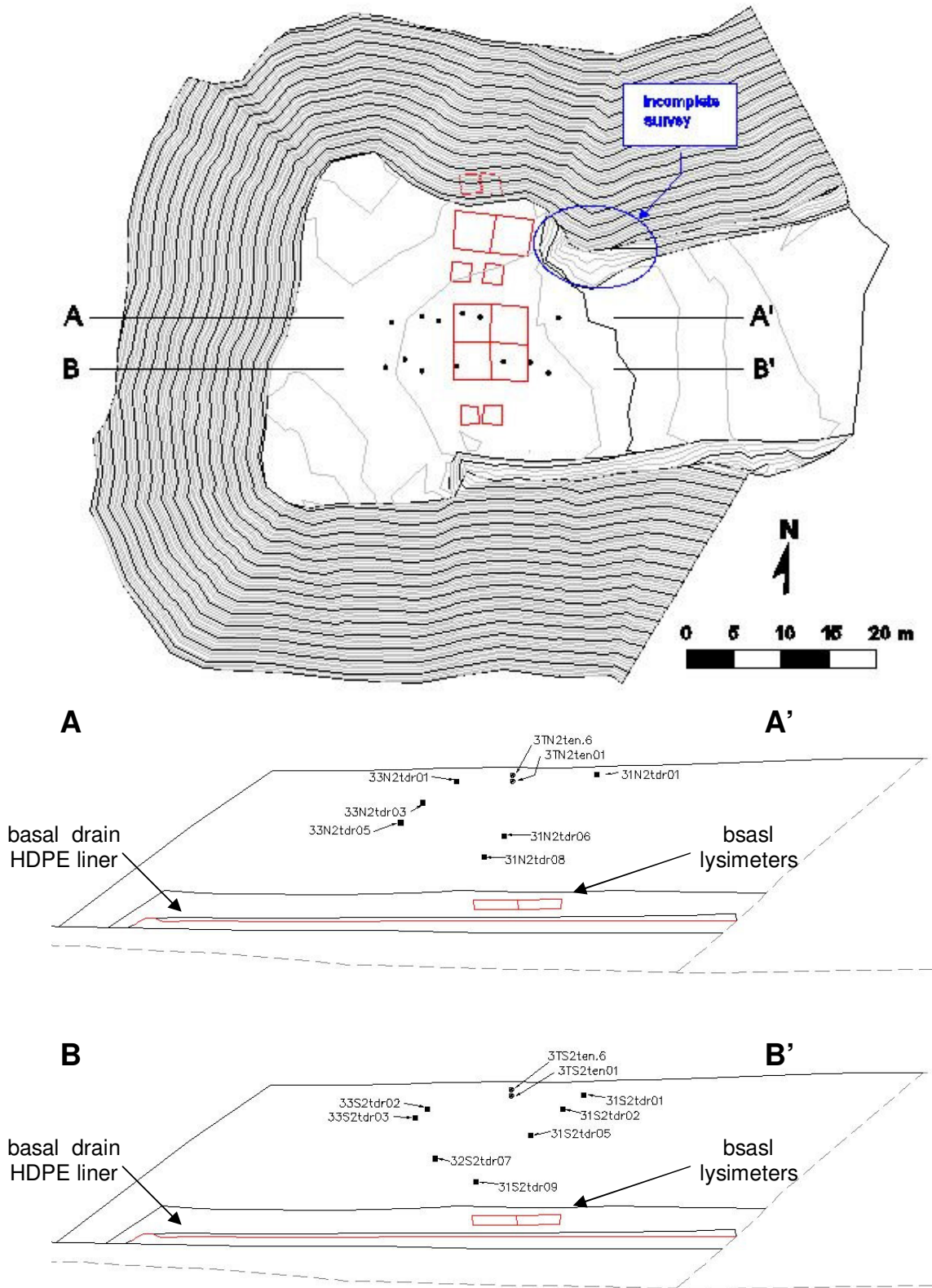


**Figure A.4** Positions of TDR probes and standpipe tensiometers in the T3 pile.

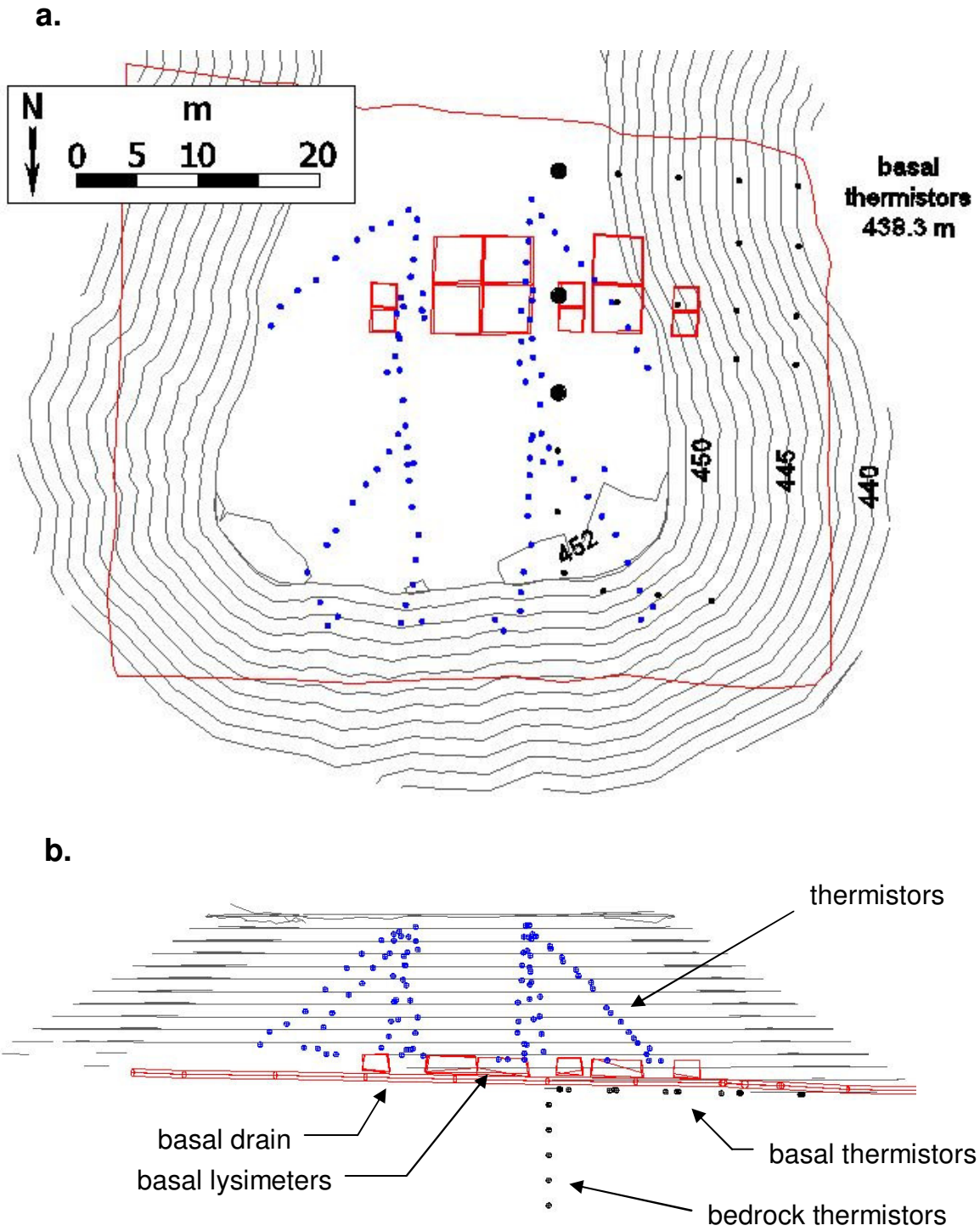


**Figure A.5** (a) Plan view of the T1 thermistor positions and (b) transparent side view of the thermistors looking from the north at the front face of the T1 test pile.

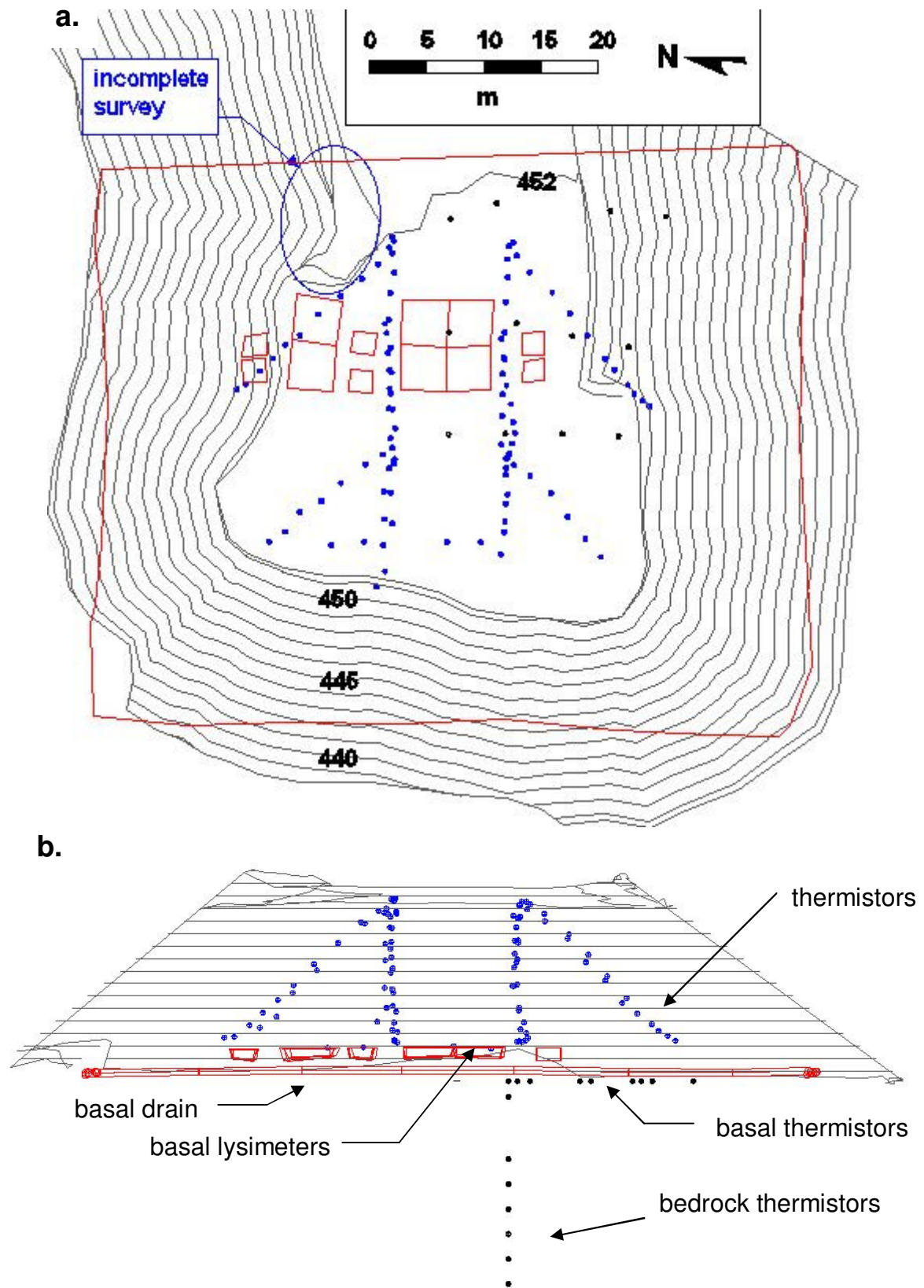


**Figure A.6** (a) Plan view of the T3 thermistor positions and (b) transparent side view of the T3 thermistors looking from the west at the front face of the T3 test pile.

a.



*Lianna Smith*

b.

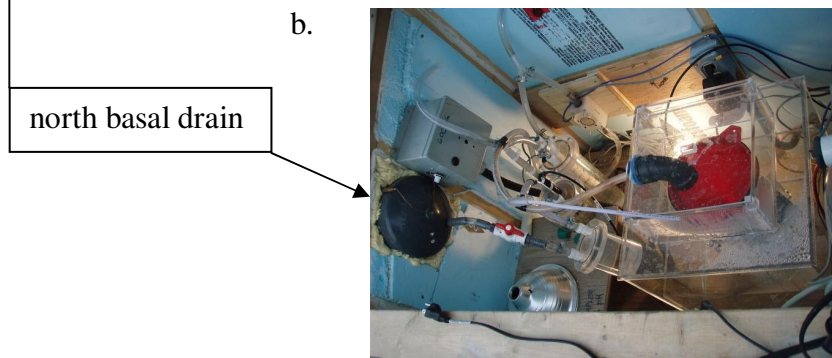


**Figure A.7** Construction of the basal drain at one of the test piles. (a) Sheets of HDPE were laid upon a bed of sand or processed kimberlite, welded together, and covered by 2 in. crushed rock before deposition of waste rock commenced. (b) Perforated drain pipe delivers drainage water from low areas of the liner to instrumentation buildings.

a.



b.



c.

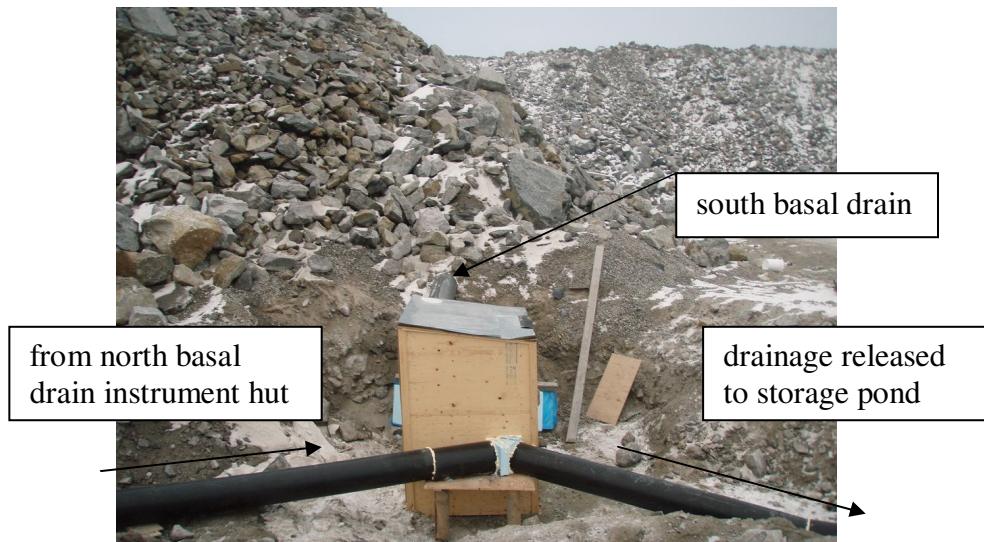


**Figure A.8** (a) The T3 north basal drain instrument hut, (b) the flow-through system inside the north drain hut, and (c) the T3 south basal drain hut. All drain plumbing was heat traced and insulated. Outflow from both drains mixes in a 1000 L bulk storage tank located in the south drain instrument hut.

a.



b.



d.



**Figure A.9** Basal lysimeter drain plumbing and insulation: (a) construction of the basal lysimeter drains at the T3 pile, (b) cementing PVC drain pipe within insulated pipe, (c) insulation at pipe junctions, (d) wooden protection for pipe junctions.

a.



b.

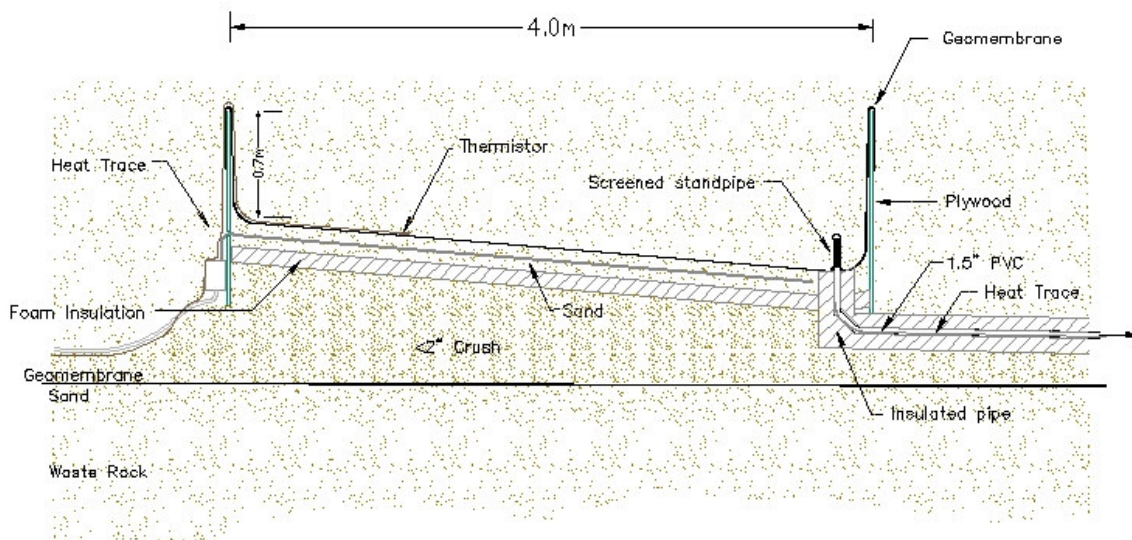


**Figure A. 10** (a) The basal lysimeters during construction of the T3 pile, and (b) a typical cross section of a basal lysimeter.

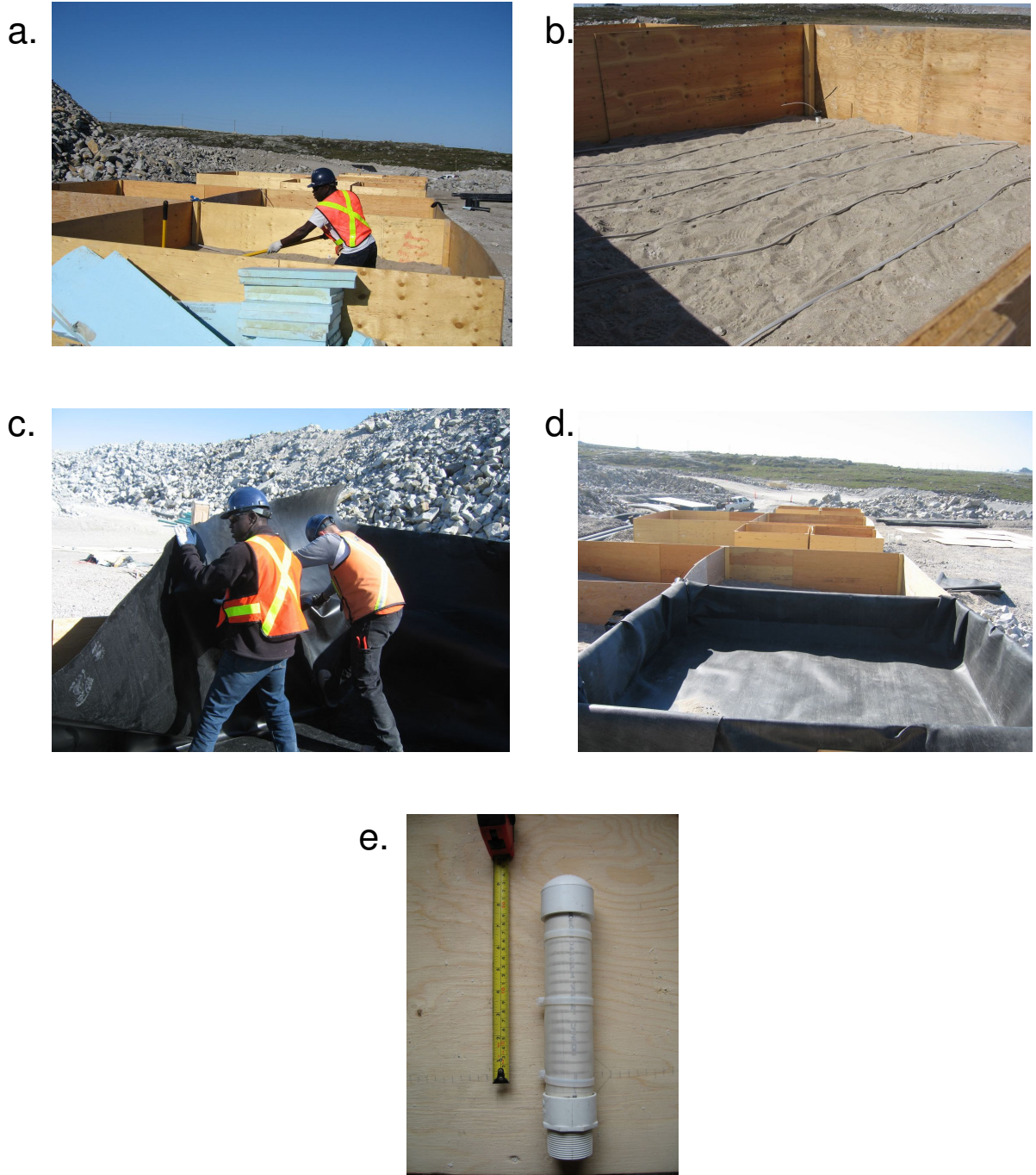
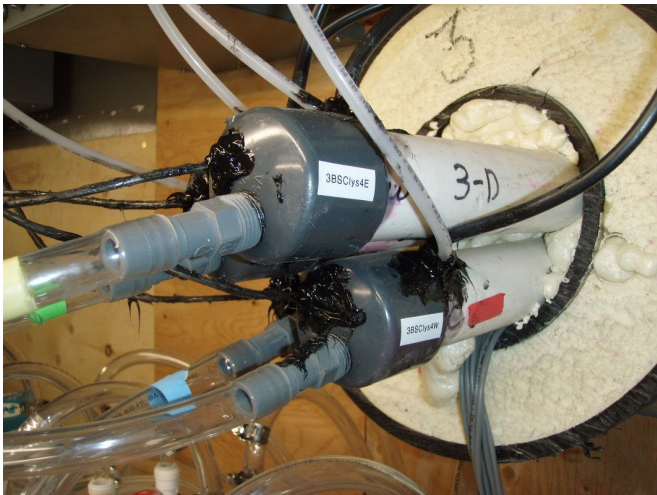


**Figure A.11** Basal lysimeter construction: (a) grading sand inside the plywood frame. The sand was installed above foam insulation and (b) self-regulating heat trace was installed within the sand layer. (c) Installing the HDPE liner into a lysimeter. (d) A lined lysimeter before installing geotextile, and (e) a screened PCV drain standpipe.

a.



b.



c.



**Figure A.12** (a) Basal lysimeter drainage plumbing to the T1 and T3 instrument building. (b) Basal lysimeter drainpipe at the entrance to the instrument building. Heat trace and purge tubing were installed inside the drainpipes from this point to just below the lysimeter drain. Heat trace thermostat bulbs were installed inside the drainpipes to about 3 m from the building. Leads from thermistors installed to monitor the lysimeter pad heat trace are also visible in the photograph. (c) Heat trace thermostats and the flow-through systems for the basal lysimeters.

a.



b.



c.



d.



**Figure A.13** (a) A 2 m lift of waste rock covered the basal collection system. (b and c) The basal lysimeters were filled with waste rock using an excavator. (d) The surface of the 2 m lift was ripped with an excavator to install gas instrumentation.

a.



b.



**Figure A.14** The test piles were constructed using both (a) end-dumping and (b) push-dumping techniques.

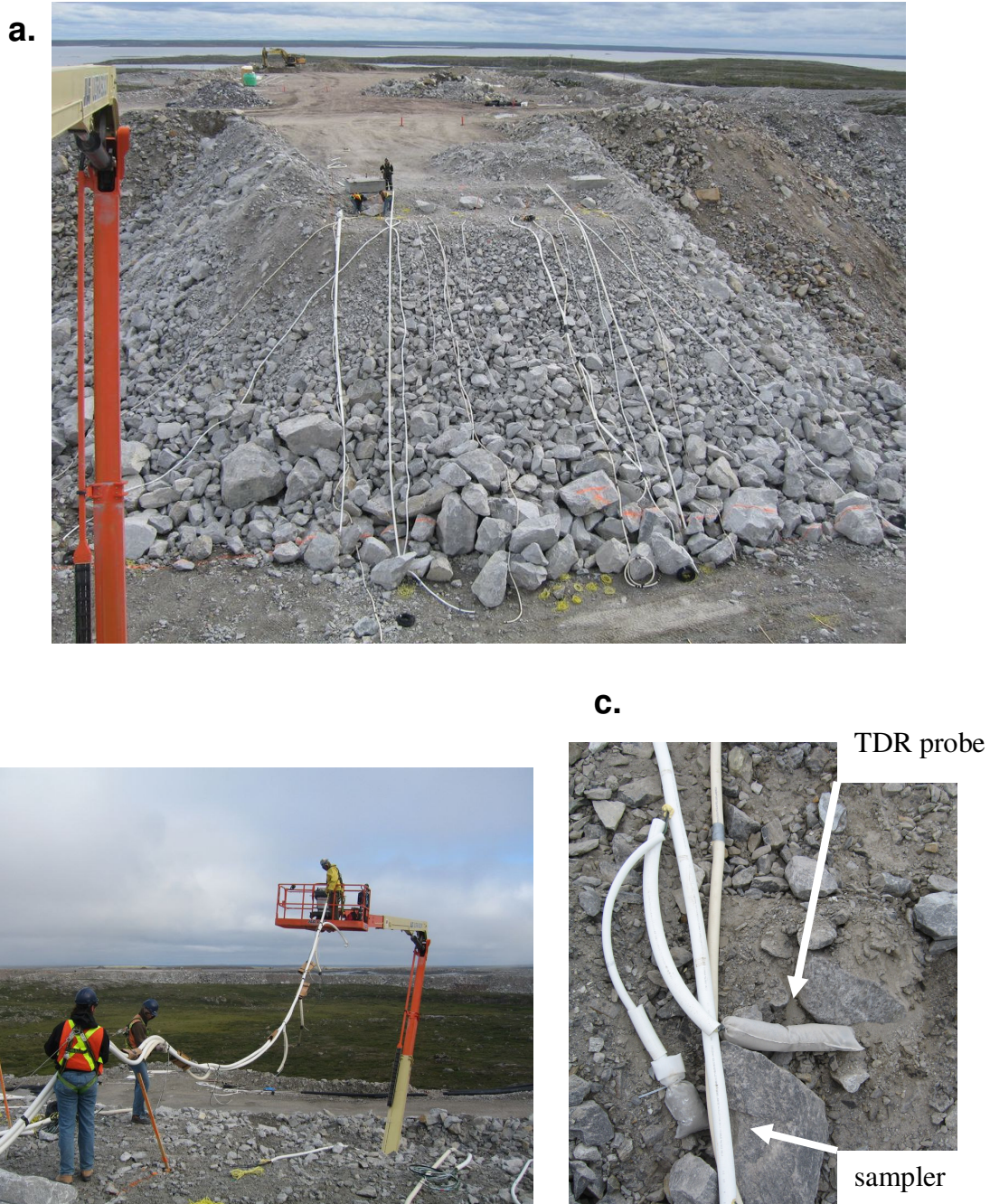
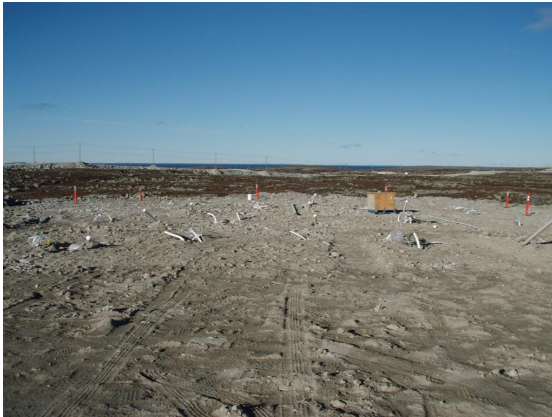


**Figure A.15** (a) Typical tip face instrumentation (photo taken from manlift). (b) TDR probes were installed using a fall-arrest anchor system at the top of the pile and a manlift. (c) Each soil water sampler and TDR probe was placed inside a permeable nylon bag filled with waste rock finer than about 1 cm.



**Figure A.16** (a and b) Instruments were covered with waste rock by an excavator, and (c) the instrument leads were buried before pile construction with haul trucks and bulldozer continued. After completion of test pile construction, (d) the buried instrument leads were excavated by an excavator and (e) by hand. (f) TDR leads were buried in PVC housing to the instrument hut.

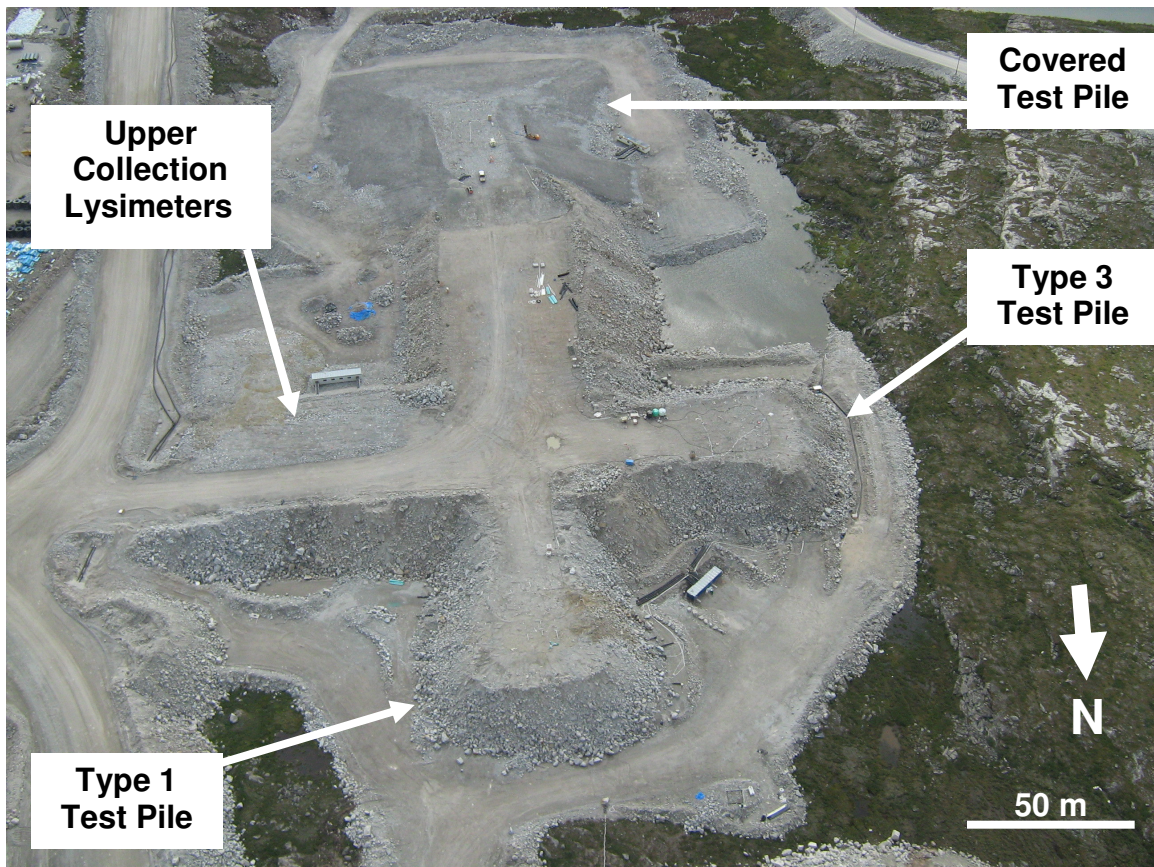
a.



b.



c.



Mike Gupton

**Figure A.17** The top surface of (a) the Type 3 test pile and (b) the Type 1 test pile after the instrument leads were excavated. (c) Overview of the waste rock test piles research site after completion of the construction (high resolution image).



*Leslie Smith*

**Figure A.18** The Type 3 waste rock test pile.

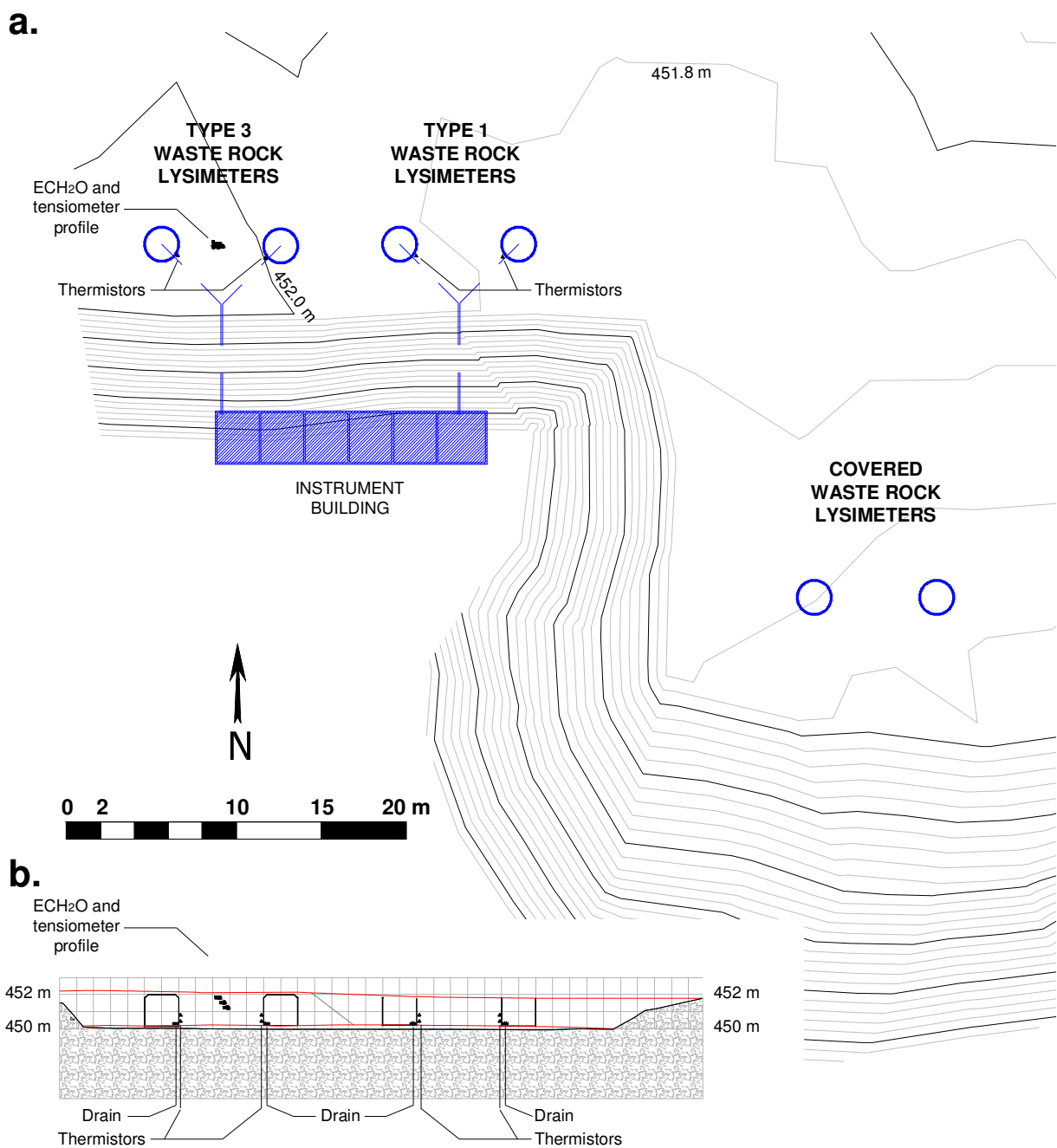


**Figure A. 19** As-built (a) plan of the upper collection lysimeters and (b) cross section of the Type 1 and Type 3 upper collection lysimeters.

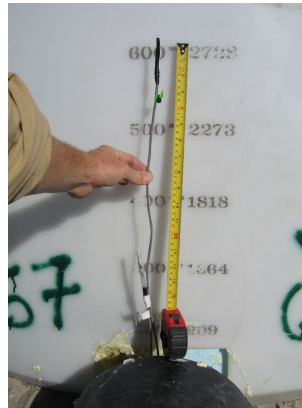
a.



b.



c.



d.



**Figure A.20** (a) Construction of the T3 (foreground) and T1 upper lysimeters, (b) sawing off the top of a 1000 gal tank, (c) thermistors installed to monitor the heat traced and insulated drain lines, and (d) a lysimeter drain protected by perforated PVC.

a.



b.



**Figure A. 21** (a) The 2 westerly upper collection lysimeters were filled with Type 3 waste rock and the two easterly lysimeters were filled with Type 1 waste rock by an excavator. (b) The T3 and T1 upper collection lysimeters after completion of construction.



**Figure A. 22** Drilling a 1 m-deep borehole near the collection lysimeters for installation of ECH<sub>2</sub>O probes and tensiometers.



**Figure A. 23** Nested tensiometers with jet fill reservoirs and strain gauge tension transducers and ECH<sub>2</sub>O probes with cables protected by 1" PVC.

## APPENDIX B INSTRUMENTATION DETAILS

### B.1 Moisture content sensors

#### B.1.1 Time Domain Reflectometry (TDR)

Time domain reflectometry (TDR) instruments send a radio frequency (~1GHz) pulse along a conductor and detect the pulse or pulses that reflect from discontinuities in the conductor. A pulse that travels along a coaxial cable to a moisture content probe in soil is partially reflected at the head of the probe, where the pulse first encounters a conductor surrounded by soil. The remainder of the initial pulse travels along the conductor in the soil, reflects off the probe end, and returns to the TDR instrument nanoseconds after the first reflection. The impedance of the pulse along the conductor by the soil determines velocity of the pulse through the probe, and hence the time between the two reflections detected by the instrument. Like the insulator in the coaxial cable, the soil acts as a dielectric. Impedance of an electromagnetic pulse through a dielectric material is defined by the relative permittivity of the material, which is the ease with which the material transmits an electric field. It has a real and imaginary component (Kraus 1984 in Topp *et al.*, 2000):

$$\epsilon_r = \epsilon_r'(\omega) - i \left( \epsilon_r''(\omega) + \frac{\sigma_0}{\omega \epsilon_0} \right), \quad (1)$$

where  $\epsilon_r$  is the relative permittivity,  $\epsilon_r'(\omega)$  is the real component as a function of the angular frequency,  $\epsilon_r''(\omega)$  is the imaginary component,  $\sigma_0$  is the DC electrical conductivity of the soil water,  $\epsilon_0$  is the dielectric permittivity of free space, and  $i = \sqrt{-1}$ . The real component represents the permittivity caused by dipolar relaxation that is significant in water molecules, while the imaginary component represents conductance

that is significant in conductive pore water and charged mineral grains (i.e. clays). Due to the polarized nature of the water molecule, the dielectric permittivity of water is much higher (dielectric constant ( $\kappa$ ) = 80) than that of air, the coaxial insulator (polyethylene), ice, and mineral grains ( $\kappa$  = 1 to 5, respectively). Therefore a wet soil transmits more of the current from the central conductor of the probe to the ground conductors of the probe than does a dry soil, resulting in a slower pulse velocity along the probe central conductor. The difference in pulse travel time along the probe, therefore, is dependent on the moisture content of the soil.

High pore water electrical conductivity is typical in mine waste rock piles and creates two problems with TDR measurement of moisture content: and 1. signal attenuation and 2. high component of imaginary permittivity. Signal attenuation is the loss of signal strength, or amplitude. Attenuation may be high enough for measurements made in conductive pore water to cause the reflected pulses to be indiscernible from the signal noise. Hook *et al.*, 1992 developed the diode difference technique, which improves signal reflections by making multiple measurements with remotely shorted diodes at the probe head and end. Nichol *et al.*, 2002 developed a design for a three-rod TDR probe with diodes at the probe head and end and featuring a coated central conductor to minimize the conductive losses causing signal attenuation while enabling the electric field to extend into the soil. The TDR probes used in this research were built by research personnel using the design of Nichol *et al.*, 2002, with an average exposed rod length of 360mm, a 23mm rod spacing, and 65mm diameter epoxy housing around the probe head and end (Figure B.1).

The calculation of moisture content from the measurement of the relative permittivity by TDR must either account for the imaginary component of permittivity or assume that it is insignificant. Relative to the real component in permittivity, the imaginary component is at a minimum for electromagnetic signals with a frequency of 100MHz and remains low at 1GHz. In validating the TDR method, Topp *et al.*, 1980 found that neglecting salinity effects for pore water with electrical conductivity up to 8dS/m (4000ppm NaCl) and neglecting the temperature dependency in the 10 to 35°C range leads to errors in moisture content of less than 0.013. They therefore proposed the simplified relationship between apparent dielectric permittivity and the propagation velocity of an electromagnetic wave in a conductor, commonly referred to as the Topp equation:

$$v = \frac{c}{\sqrt{\kappa'}}, \quad (2)$$

where  $v$  is the velocity,  $c$  is the speed of light in free space, and  $\kappa'$  is the apparent dielectric permittivity. A proportional approach may then be taken to convert the apparent dielectric of the soil to that of the mineral, air, and water components to arrive at the volumetric moisture content.

In practice, the Topp equation, or similar relationships which account for specific soils (e.g. Young 1995), are used less than relationships derived from soil-specific calibration. The presence of a lag time between the shorting of a diode and the true reflection at the interface between the probe head or end and the soil and the presence of the central rod coating complicate the application of the theoretical relationships. Nichol 2002 proposed theoretical solutions for these complications, but conducted a soil calibration to relate the pulse travel time along the probe from field experiments to the

moisture content. Attempts at applying this solution to field data from the field data from the Diavik test piles yielded moisture content values higher than the measured porosity.

A calibration was conducted at several moisture contents using waste rock samples taken during the construction of the test piles that consisted of particles finer than 20mm. Several samples were oven-dried, weighed to a precision of 0.01kg, and then mixed together on a table. The waste rock was then placed around a TDR probe in the center of a 55cm x 35cm x 22cm plastic container. The container was significantly larger than the one used in a similar calibration performed by Nichol *et al.*, 2003, which found the effective TDR electromagnetic field cross section to be less than 2.4 times the probe width. The waste rock was then removed from the container and spread out on the table. A 5dS/m KCl solution was applied evenly using a hand spray bottle, and the waste rock was thoroughly mixed with a hand trowel before, weighed, and re-packed around the TDR probe. Pore water specific conductance measured from samples taken from within the test piles at locations near the TDR probes range from 1dS/m to 25dS/m. This process was repeated at eleven different moisture contents. The volumetric moisture content was measured by gravimetrically determining the mass of water in each calibration, calculating the volume of water using the density of the KCl solution, and dividing by the bulk volume. The waste rock was re-packed to the same bulk volume throughout the calibration, which corresponded to a dry bulk density of 1840kg/m<sup>3</sup>.

Several checks were made during the calibration to simulate possible conditions around the probes in the test piles. Each probe installed in the test piles was placed in a 15cm diameter permeable nylon fabric sock filled with 1cm minus waste rock prior to placement on the tip face to ensure that no probe was positioned partially or fully within

air space. Calibration trials were done with the probe inside a permeable nylon sock filled with 1cm minus waste rock. No deviation from the calibration curve was found when the sock was surrounded by matrix or by a mixture of cobbles and matrix. But when the TDR probe and matrix-filled sock were surrounded by cobbles and air-filled pores, the pulse travel time through the probe was significantly less than the travel time through a larger volume of matrix with the same moisture content. Therefore, the electromagnetic field generated during a measurement extends outside the matrix in the permeable nylon sock.

The pulse travel time along the probe is presented in terms of the term  $t/t_{air}$  so that the calibration may be applied to probes of different lengths.  $t/t_{air}$  is defined as:

$$t/t_{air} = \frac{t_{dd} - t_{offset}}{t_{air}}, \quad (3)$$

where  $t_{dd}$  is the diode-difference travel time from the probe head to end and back (the output of the TDR instrument),  $t_{offset}$  is the difference between the travel time measured with a probe surrounded by air and the travel time calculated using the Topp equation (Equation 2), and  $t_{air}$  is the travel time in air calculated using the Topp equation. A polynomial regression was fit to the calibration data shown in Figure B.3 to determine the following relationship between the TDR probe pulse travel time and volumetric moisture content ( $\theta$ ):

$$\theta = 0.093 (t/t_{air})^4 - 0.983 (t/t_{air})^3 + 3.74 (t/t_{air})^2 - 5.90(t/t_{air}) + 3.29 \quad (4)$$

Neglecting the uncertainty due to potential placement of a probe near large air-filled pores, the uncertainty in the volumetric moisture content determined by TDR using this

soil calibration is estimated to be  $0.05\text{m}^3/\text{m}^3$ . Sources of error include the variation in waste rock conditions in the vicinity of the probe during calibration, uncertainty in the calibration bulk volume, soil and water losses during calibration, and scale accuracy. Application of the matrix calibration to a probe surrounded by large rocks and air-filled pores would underestimate the moisture content of the matrix in the immediate vicinity of the probe (inside the nylon sock) by as much as  $0.07\text{m}^3/\text{m}^3$ . This uncertainty and the uncertainty due to variation in the probe head offset between probes yield a total uncertainty of  $0.07\text{m}^3/\text{m}^3$ .

TDR measurements were made using the Moisture Point MP-917, manufactured by Environmental Sensors, Inc. (ESI), 2071C Malaview Avenue, Sidney BC V9L 5X6 Canada. The instrument has a precision of about 15 picoseconds, which corresponds to a precision of  $0.0004\text{ m}^3/\text{m}^3$ , but in practice the precision over several hours is about  $0.005\text{ m}^3/\text{m}^3$ . The measurements were controlled and multiplexed using the ESI Interconnect Module and the CR10X data logger and SDMX50 multiplexer from Campbell Scientific, 11564 - 149 Street NW, Edmonton, AB, Canada T5M 1W7. Data logger programs and wiring diagrams are shown in Appendix D.

Application of the calibration to the field data from multiple probes of varying lengths requires the calculation of  $t/t_{\text{air}}$  (Equation 3). Temperature dependence in the dielectric permittivity of water requires a correction to account for the difference between the temperature during the laboratory calibrations and the temperature in the field. Since the dielectric constant of ice is closer to air than water, the moisture content measured by TDR appears to drop sharply when the waste rock around the probe freezes. Therefore, the TDR method is effective only for liquid phase pore water. The effective temperature

range for TDR measurements, then is 0 to 15°C, and the average temperature was about 5°C. The correction for the temperature variation from the average effective TDR temperature was less than the 0.005m<sup>3</sup>/m<sup>3</sup> measurement precision, and was therefore neglected. An empirically derived temperature correction was applied to account for the difference between the temperature in the laboratory during calibration (T<sub>lab</sub>) and the average TDR temperature (T<sub>fld</sub>):

$$t/t_{\text{air}}' = t/t_{\text{air}} - (T_{\text{lab}} - T_{\text{fld}}) \times [(2.645 \times 0.006) - 0.006 (t/t_{\text{air}})], \quad (5)$$

where  $t/t_{\text{air}}'$  is the temperature-corrected travel time normalized by the probe length.



**Figure B. 1** Coated three-rod TDR probes with remotely-shorted diodes (above), built at the University of British Columbia.



**Figure B. 2** Soil calibration of a TDR probe (left) in waste rock sampled during the construction of the Diavik test piles.

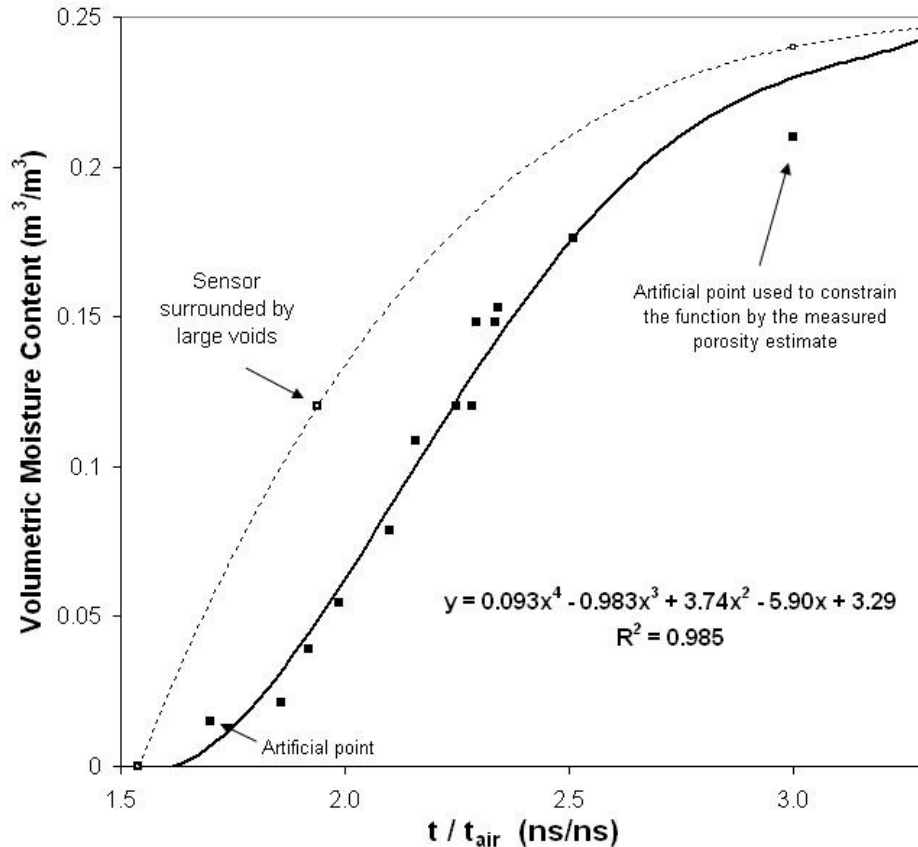


**Figure B.3** The soil calibration curve for Diavik waste rock.

### B.1.2 Capacitance sensors

Capacitance sensors measure the moisture content in the waste rock matrix using the same relationship between dielectric properties and the moisture content of soils that are used by TDR measurements. But rather than measuring the impedance of a pulse along a conductor, capacitance sensors such as the ECH<sub>2</sub>O-TE from Decagon Devices, Inc., measure the capacitance in the soil as an alternating current (AC) is applied across it. The rate of change of voltage measured between the two prongs of the ECH<sub>2</sub>O probe is related to the dielectric constant, and hence moisture content, of the soil between the prongs (Decagon 2007, Decagon 2007a). Decagon maintains a competitive advantage in

the moisture content sensor market while providing limited information on the theory and circuitry of the sensors. The following is inferred from general knowledge of electromagnetics and circuitry. Application of a step voltage alternating current creates a constant charge gradient across the capacitor. Current, and therefore voltage, increases in the capacitor with time. A reference capacitor is likely included in the circuitry to allow the sensor to know when to stop measuring the voltage increase while reducing thermal effect errors. The change in voltage with time is inversely related to capacitance. Capacitance (C) is directly related to the dielectric permittivity of the soil, by (Serway 2003):

$$C = \kappa \epsilon_0 (A/d), \quad (6)$$

where  $\kappa$  is the dielectric constant (in F/m),  $\epsilon_0$  is the permittivity of free space ( $8.854 \times 10^{-12}$  F/m), A is the area of each capacitor plate (ECH<sub>2</sub>O prong), and d is the distance between the plates or prongs. A microprocessor in the sensor detects the rate of change of voltage at the prongs and outputs a corresponding value as serial data.

Measurements from capacitance sensors are subject the same difficulties as TDR and other dielectric methods. ECH<sub>2</sub>O-TE sensors (Figure B.5) are well-equipped to deal with the temperature dependency and the conductive imaginary component of dielectric permittivity. The sensors include a thermistor that measures the temperature of the soil at the same interval as the moisture content measurement. The current applied to the soil alternates at a frequency of 70 MHz. The imaginary component of the complex permittivity is at a minimum relative to the real component that represents the dipolar relaxation significant in water molecules at this frequency. Fiberglass prong coating offers protection while lowering the DC conductive permittivity component. The

ECH<sub>2</sub>O-TE sensors also measure the bulk soil electrical conductivity, which may be used to calculate the pore water specific conductance.

As with other dielectric methods of determining porous media moisture content, an empirical relationship between the apparent dielectric measurement and the moisture content is favored over a theoretical approach in practice. Some manufacturers offer relationships with a physical basis in the electromagnetic refraction by minerals, air, and water (Regaldo 2007), but these models nevertheless require a porosity estimate of the soil. Relationships derived empirically for several soil types are available for the ECH<sub>2</sub>O-TE sensors that offer accuracy of 0.03 m<sup>3</sup>/m<sup>3</sup> for soils with pore water conductivity less than 8 dS/m (Decagon 2007). But site-specific soil calibrations are recommended, particularly for material with high sand content and the potential for conductive pore water (Campbell 2006).

Prior to installation at the Diavik waste rock test piles research site, ECH<sub>2</sub>O sensors were calibrated in the < 5mm fraction of waste rock samples taken during construction of the test piles. The calibration followed the procedure described by Cobos 2006 (Figure B.5), with the notable exception that the entire sample container was weighed at each calibration point to measure volumetric moisture content, rather than weighing a core of the sample. The calibration generated a relationship between the sensor output (E) and volumetric moisture content ( $\theta$ ) best described by the logarithmic function (Figure B.6):

$$\theta = 0.268 \times \log[2.3 \times 10^{-4}(E - 560)] + 0.548. \quad (7)$$

This relationship is accurate to within  $0.02 \text{ m}^3/\text{m}^3$  and is essentially indistinguishable from the linear mineral soil relationship for moisture content up to about  $0.20 \text{ m}^3/\text{m}^3$ . Uncertainty in the sensor output (the x-axis error bars in Figure B.6) represents the extents of the observed variation between several probes at the same moisture content. Sources of uncertainty in the volumetric moisture content include variation in the soil volume, soil losses, evaporation and other water losses, and scale accuracy.



**Figure B.4** The ECH<sub>2</sub>O-TE moisture content, electrical conductivity, and temperature sensor (image provided by Decagon Devices, Inc.).



**Figure B.5** Soil calibration for ECH<sub>2</sub>O probes performed with samples from the Diavik test piles.

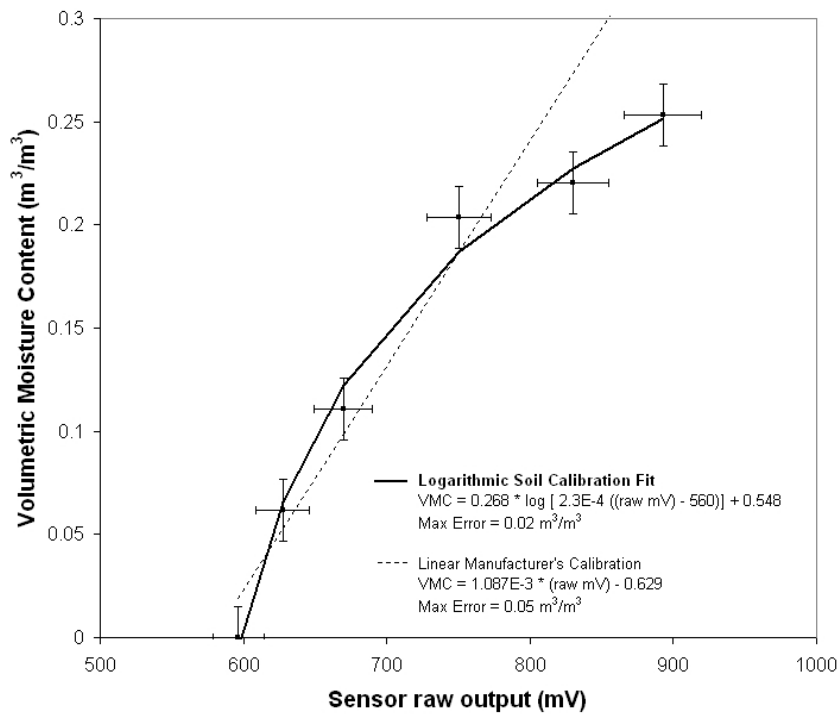


**Figure B.6** The soil calibration curve for moisture content measured by ECH<sub>2</sub>O probes in Diavik waste rock.

## **B.2 Tensiometers**

### *B.2.1 Standpipe tensiometers*

Standpipe tensiometers were used to measure the negative pressure head, or tension, within the waste rock porous media. Tensiometers were installed into shallow boreholes drilled into the top of the Type 3 test pile and into a single borehole located between the two Type 3 collection lysimeters. Model 2725 tensiometers were purchased from Soil Moisture, Corp. (P.O. Box 30025, Santa Barbara, CA, 93105, USA; [www.soilmoisture.com](http://www.soilmoisture.com)), at standard dimensions of 2.2cm diameter by 2ft., 2.2cm diameter by 3ft., and 2.2cm diameter by 4ft (Soil Moisture, Corp., 1997). A jet fill reservoir allows water to be added to the body of the tensiometer without exposing it to atmospheric pressure. The tension inside the tensiometer was maintained at equilibrium with the waste rock matric suction by means of a porous ceramic cup. The model 5301 current transducer was used to obtain a continuous record of matric suction that was logged with a Campbell Scientific CR10X data logger. The transducer is vented to the atmosphere causing tension readings to be relative to the atmospheric pressure (i.e. no correction is necessary). The solid-state pressure transducer has a range of 0 to 1000 mb (0 to 100kPa, similar to the ceramic porous cups that are the sampling point), and precision was found to be 0.01m of head. The transducer consists of a strain gauge with electrically conductive plates that contact each other such that the contact surface area changes with differences in tension. A greater strain gauge contact area causes a greater current in the transducer circuit (Soil Moisture, Corp., 1989).

The current output from the transducer varies linearly with tension. The current must pass through a reference resistor to be measured by the data logger. The transducer output circuit is shown in Figure B.9. By Ohm's law, the voltage ( $V_X$ ) in the transducer output circuit equals the product of the current output by the transducer ( $I_\phi$ ) and the reference resistance ( $R_f$ ):

$$V_X = I_\phi R_f \quad (11)$$

In Figure B.9,  $V_G$  is assumed to be zero. Alternatively, a differential voltage could be made across the reference resistor. A  $120 \Omega$  reference resistor was chosen to ensure that  $V_X$  would remain within the 2.5V range of the data logger for all possible current output from the transducer. With a  $120 \Omega$  reference resistor, the transducer output ( $V_X$ , in mV) to tension ( $\phi$ , in kPa) relationship was found to be:

$$\phi = 0.0521V_X - 25. \quad (12)$$

Water level in the tensiometer was maintained within 1 cm of full using jet fill reservoirs, causing small false spikes in suction in general every few days. The matric suction data was added to the elevation of the porous ceramic cup relative to the height of the top of the tensiometer body (the top of the water column, assuming it was full) to determine the piezometric head, or tension head, at each tensiometer.

The tensiometers at the upper collection lysimeters were heated during a time when air temperature was below freezing but the waste rock temperature near the porous cup was above freezing. Two 100 Watt light bulbs were placed near the tensiometers under a cardboard box and plastic tarp. This hasty heating system allowed for a two-week extension in the application of the tensiometers that included the monitoring of infiltration into partially-frozen waste rock.

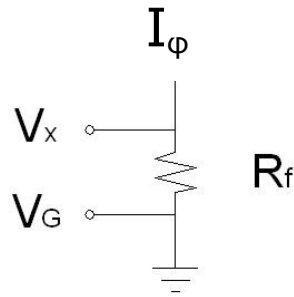


**Figure B.7** Wiring diagram for measurement of the current output from the Soil Moisture, Inc. model 5301 current transducer with a Campbell Scientific data logger.

### B.2.2 *Using suction samplers as tensiometers*

Tension measurements were made sporadically at suction samplers that were installed during test pile construction at depths of 1m to 9m. A typical installation is shown in Figure B.4. The ceramic porous cup that acts as a membrane between the porous media and the sampler was coated with a paste of silica flour and distilled water to promote hydraulic connection. The porous cup was then placed into a nylon mesh bag and surrounded by waste rock finer than 2cm. The 2cm minus material acts as a safeguard against a potential placement of the sampler in a large air-filled void space while providing some protection of the ceramic cup. Tension readings may show bias towards the tension within the fine material inside the mesh bag. But a hydraulic connection between the fine material inside the bag and the fine material around it would provide a more representative tension reading. This condition, however, is unknown.

Tension measurements were made by collecting a pore water sample into a Soil Moisture Model 1920 pressure-vacuum soil water sampler (Soil Moisture Corp., 1997a),

allowing the tension in the sample water to equilibrate with the adjacent porous media, then measuring the tension in the sampler using a Tensimeter (older version of the Tensicorder, Soil Measurement Systems 2006). Figure B.9 illustrates the procedure. The Tensimeter consists of a tension gauge, a needle probe, and a digital screen that displays pressure sensed at the needle with a resolution of 1 mbar (0.1kPa). The gauge is vented so that pressure relative to atmospheric pressure is displayed. The needle was inserted through a septum stopper into the sampling tube of the soil water sampler. Tension readings were taken until a maximum tension value was determined, generally over the course of several hours.

In 2007 this method was used only once at the Type 3 test pile with success. Several subsequent attempts yielded virtually all readings of very nearly atmospheric pressure. Problems in making tension measurements may have been due to a lack of available soil moisture. If the porous ceramic cup of the sampler is not fully saturated, as the case would be if less than 100mL of pore water is drawn into the sampler, a direct connection between the sampler and the air-filled pore space is made. Pressure of the gas phase of pore space in the unsaturated zone is generally about equal to the atmospheric pressure, except where regions of saturated conditions or very low permeability zones isolate an unsaturated zone from connection with the atmosphere. In these instances additional water must be introduced into the sampler to saturate the porous cup. However, the addition of water to the sampler from the ground surface by means of the sampling tube would compromise subsequent samples taken for geochemical analysis. Therefore application of a higher tension in step 1 is recommended to draw water from smaller pore spaces.

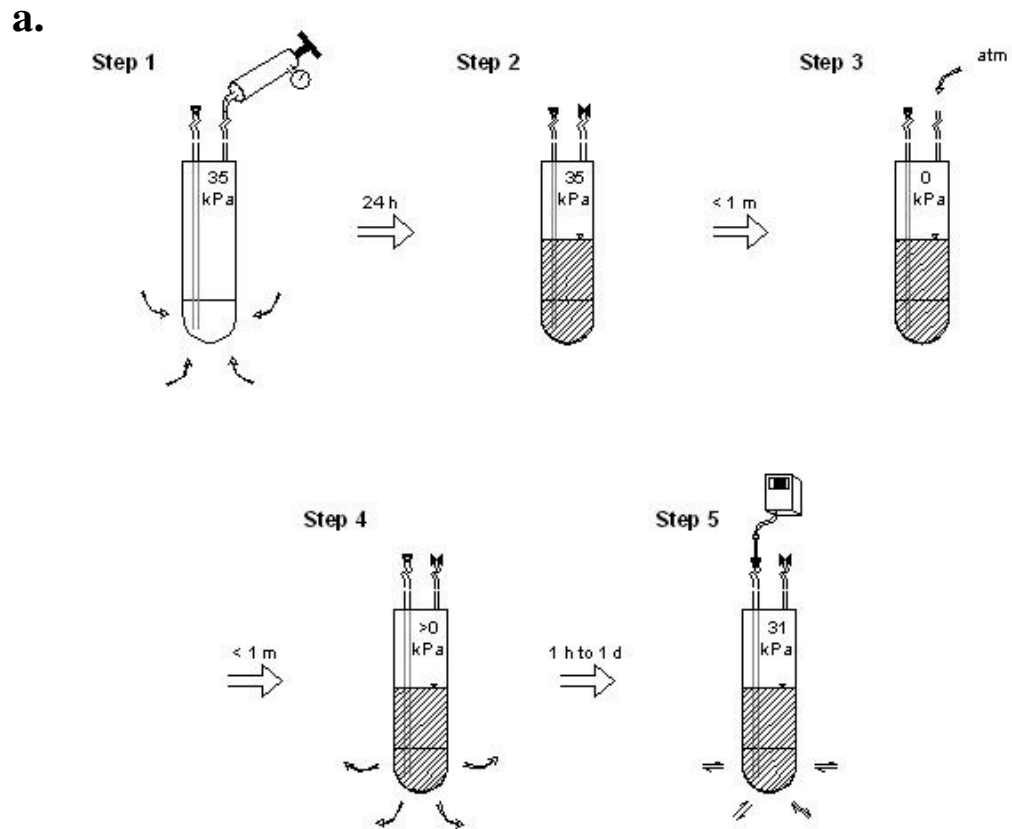


**Figure B.8** (a) Procedure for measuring matric suction in a soil water sampler, and (b) the Tensiometer displaying the pressure sensed in the tubing connected to a sampler.

### **B.3 Instrument positions**

Table B.1 lists the positions of the TDR probes, ECH<sub>2</sub>O probes, and tensiometers in the test piles and at the collection lysimeters. The instrument identifier uses the system that is consistent for all of the instrumentation within the Diavik test piles project. The format gives the general location and type of instrument (or location of sample). The system lists the test pile (1, 3, C, or U), the instrumentation tip face, in order of construction (1 to 4), the direction offset from the pile centerline (N, S, E, or W), the approximate offset from the centerline in meters, an abbreviation of the instrument, and the approximate depth in meters. The Diavik waste rock test piles site is located at latitude 64°29'N, longitude 110°18'W, elevation 450 m above sea level. The instrument position coordinates are of the Zone 12 Universal Transverse Mercator (UTM) projection of the North American Datum of 1983 (NAD83). The instrument elevation and surface elevation directly above each instrument are given in meters above sea level, and the depth is the difference. The survey was performed using real time kinematic (RTK) differentially-corrected global position system (GPS), which has typical precision of 0.02m. Due to instrument size and surface topography variation all positions are accurate to 0.1 to 0.2m.

**Table B.1** Surveyed positions of TDR probes and tensiometers at the Type 3 test pile.

Instrument Label	Array ID	UTM Zone 12 / NAD83 Coordinates		Elevation m.a.s.l.	Surface $El_0(N,E)$ m.a.s.l.	Depth m
		Northing (m)	Easting (m)			
Type 3 test pile TDR probes						
31N2TDR01	51	7151165.59	533357.47	451.13	451.80	0.67
33N2TDR01	59	7151165.76	533343.02	450.49	451.65	1.16
31S2TDR01	54	7151159.72	533356.39	450.57	451.75	1.18
33S2TDR02	62	7151161.16	533341.23	449.30	451.62	2.32
31S2TDR02	55	7151160.83	533354.49	449.33	451.72	2.39
33N2TDR03	60	7151165.11	533339.80	448.59	451.65	3.06
33S2TDR03	63	7151160.33	533339.18	448.56	451.65	3.09
31S2TDR05	56	7151160.45	533346.71	446.99	451.75	4.76
33N2TDR05	61	7151165.25	533344.80	446.79	451.65	4.86
31N2TDR06	52	7151165.65	533349.15	445.62	451.75	6.13
32S2TDR07	58	7151159.91	533343.03	444.93	451.72	6.79
31N2TDR08	53	7151166.06	533347.30	443.71	451.75	8.04
31S2TDR09	57	7151160.93	533351.60	442.87	451.75	8.88
Type 3 test pile tensiometers						
3TN2ten.6	121	7151164.0	533348	451.1	451.7	0.60
3TN2ten01	121	7151164.5	533348	450.5	451.7	1.20
3TS2ten.6	121	7151160.0	533348	451.1	451.7	0.60
3TS2ten01	121	7151159.5	533348	450.5	451.7	1.20

*Surface  $El_0(N,E)$  refers to the elevation of the surface of the waste rock pile vertically above each sensor.*

**Table B. 2** Surveyed positions of TDR probes at the Type 1 test pile and ECH<sub>2</sub>O probes and tensiometers at the Upper Collection Lysimeters.

Database Label	Array ID	UTM Zone 12 / NAD83 Coordinates		Elevation m.a.s.l.	Surface El <sub>0</sub> (N,E) m.a.s.l.	Depth m
		Northing (m)	Easting (m)			
Type 1 test pile TDR probes						
12W2TDR02	86	7151227.96	533420.74	449.42	451.4	1.98
12W2TDR03	87	7151228.93	533420.97	448.74	451.4	2.66
11W2TDR06	80	7151226.08	533419.61	445.95	451.4	5.45
11W2TDR09	83	7151231.02	533418.47	442.90	451.4	8.51
Upper Collection Lysimeter tensiometers *						
U3C0ten.3	113	7151134.0	533469.4	451.65	451.95	0.30
U3C0ten.6	113	7151134.0	533469.4	451.35	451.95	0.60
U3C0ten.9	113	7151134.0	533469.4	451.05	451.95	0.90
Upper Collection Lysimeter ECH <sub>2</sub> O probes *						
U3C0eco.3	113	7151134.0	533469.4	451.65	451.95	0.30
U3C0eco.6	113	7151134.0	533469.4	451.35	451.95	0.60
U3C0eco.9	113	7151134.0	533469.4	451.05	451.95	0.90

\* Approximate borehole location. Tensiometer and ECH<sub>2</sub>O probes located at the same depth are horizontally within 0.2m of each other.

*Surface El<sub>0</sub>(N,E) refers to the elevation of the surface of the waste rock pile vertically above each sensor.*

#### B.4 Continually-logging specific conductance

Custom sensors were built at the University of British Columbia, using the Werner array design of Masaki Hayashi (University of Calgary). A schematic and wiring diagram for the probe is shown in Figure B.10, and an image of a probe in a flow-through system is shown in Figure B.11. Using a Campbell scientific data logger, a 2.5V excitation is applied to the electrode at the bottom of the probe, labeled “E<sub>2.5V</sub>”. The current is grounded (through a reference resistor) at the upper electrode, labeled “H<sub>1</sub>”, by creating an electrical field through the dissolved ions in the water in the flow-through cell. A half bridge measurement evaluates the differential voltage through the water ( $V_2 = H_2 - L_2$ ) relative to the differential voltage through the reference resistor ( $V_1 = H_1 - L_1$ ). The measurement output (X) logged by the data logger, in mV, is (Campbell Scientific 2003):

$$X_{mV} = V_2 / V_1. \quad (12)$$

The following calculations must be made to determine the specific conductance from the measurement output. For clarity, the calculations are made in *SI* units:

$$X_V = X_{mV} / 1000. \quad (13)$$

By Ohm’s Law for the same current,

$$X_V = R_s / R_f. \quad (14)$$

The resistance in the reference resistor should be within an order of magnitude of the resistance of the water. The reference resistor used in the electrical conductivity circuit,  $R_f$ , had a resistance of 469.3Ω. The resistance, in Ω, in the water in the flow-through cell is:

$$R_s = X (R_f) / 1000. \quad (15)$$

Electrical conductivity, in S, is the reciprocal of the resistance multiplied by a cell factor  $k$ :

$$EC_{\text{raw}} = k / R_s. \quad (16)$$

The cell factor is related to the geometry of the probe (Won 1987):

$$k = \frac{2}{\pi^2 d} \ln \left( \frac{4a + \pi d}{4a + \pi d / 2} \right), \quad (17)$$

where  $d$  is the diameter of the probe and  $a$  is the length between each electrode, each in meters. The probes made for the Diavik project had a cell constant of  $1.884\text{m}^{-1}$ . This cell factor does not account for truncation of the electrical field by the walls of the flow-through cell. A calibration was done to account for this boundary effect. Each EC probe was inserted into flow-through cells with solutions of 0.001 M KCl, 0.01 M KCl, and 0.1M KCl. These solutions have a specific conductance of  $147 \mu\text{S}/\text{cm}$ ,  $1.4 \text{ mS}/\text{cm}$ , and  $12 \text{ mS}/\text{cm}$ , respectively. From the calibration, an average calibration factor  $C$  of 3.96 was determined. Calibrated electrical conductivity is:

$$EC_{\text{cal}} = EC_{\text{raw}} (C). \quad (18)$$

The electrical conductivity of the water is directly related to the concentration of total ions in solution, and hence the total dissolved solids. The measurement is highly dependent on temperature. The temperature of the water in the flow-through cell is measured by a thermistor, and a correction is made to evaluate what the electrical conductivity would be at  $25^\circ\text{C}$ . The temperature-normalized electrical conductivity, the specific conductance (SC), is calculated with the following relationship:

$$SC(t) = \frac{EC_{\text{cal}}(t)}{1 + m(T(t) - 25^\circ\text{C})}, \quad (19)$$

where  $SC(t)$  is the specific conductance at time  $t$ ,  $EC$  is the electrical conductivity at time  $t$ ,  $T(t)$  is the water temperature at time  $t$  in degrees celcius, and  $m$  is the slope of the temperature correction (typically about 0.02). The  $m$  parameter is related to the geochemistry of the water, and was set to 0.0245 to fit the continuously-logged  $SC$  to the  $SC$  measured in samples taken during 2007.

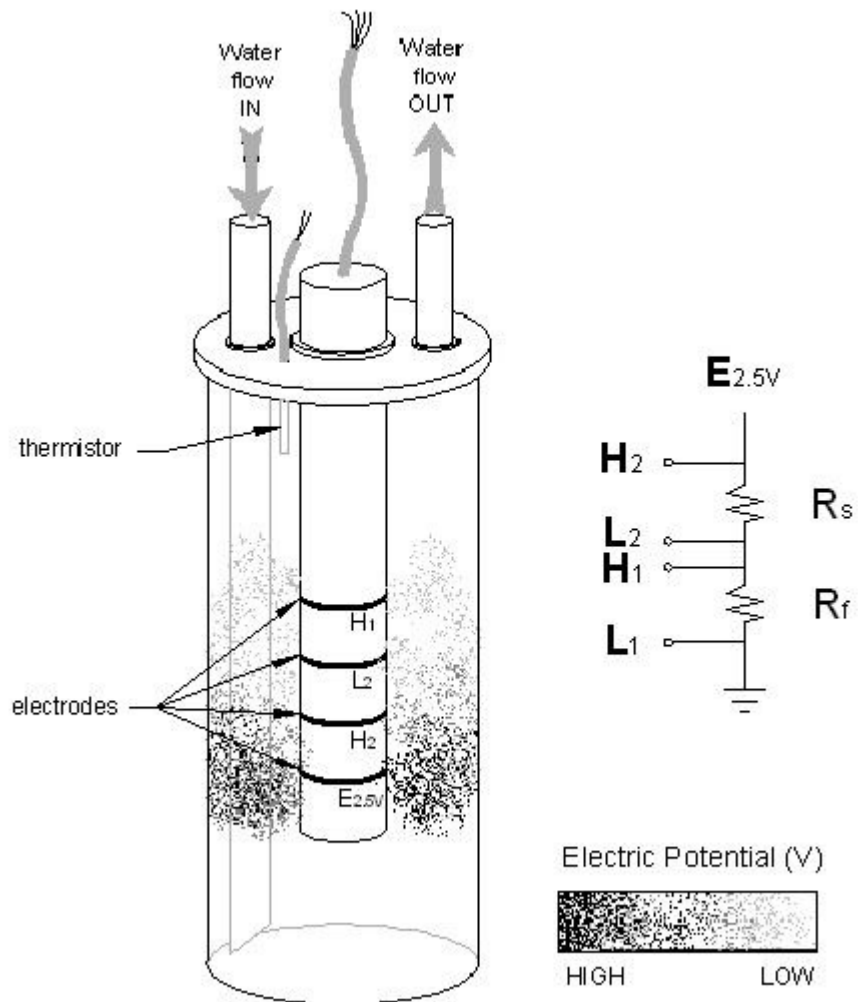


**Figure B.9** Custom-built electrical conductivity probe inside a flow-through cell. For clarity, the electrical field is shown in only cross-section.

The thermistors used in the specific conductance measurements were model 44007 precision interchangeable thermistors, manufactured by Omega Engineering, Inc. (1 Omega Dr., Stamford, CT, 06907, USA, [www.omega.com](http://www.omega.com)). Temperature is related to resistance in a thermistor by the Steinhart-Hart equation:

$$T = \frac{1}{a + b \ln(R_s) + c \ln^3(R_s)}, \quad (20)$$

where T is temperature in kelvin,  $R_s$  is the resistance in the thermistor in Ohms, and a, b, and c, are constants specific to a particular type of thermistor. For the Omega model 44007, a is  $1.285 \times 10^{-3}$ , b is  $2.362 \times 10^{-4}$ , and c is  $9.285 \times 10^{-8}$ . A wiring diagram for a thermistor is shown in Figure B.11. For a single-ended measurement circuit with a 2.5 V excitation, resistance in the thermistor ( $R_s$ ) is (Campbell Scientific 2003):

$$R_s = R_f \left( \frac{2.5V}{V_s} - 1 \right). \quad (21)$$

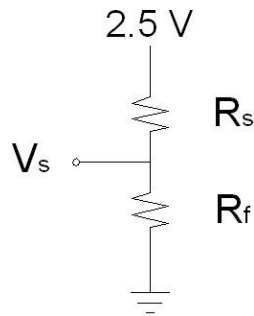


**Figure B.10** Wiring diagram for thermistor measurement. Temperature is related to the resistance in the thermistor ( $R_s$ ) and measured by the voltage in a circuit ( $V_s$ ) with a reference resistor ( $R_f$ ).

## **B.5 Continually-logging pH**

The pH of the drainage was measured continually using Model CSIM11 pH probes manufactured by Campbell Scientific, Inc. An image of a Model CSIM11 pH probe in a flow-through system is shown in Figure B.11. The pH probes have a specified accuracy of 0.1 pH units and a drift of less than 2 mV (less than 0.04 pH units) per week (Campbell Scientific 2003). But microbial growth around the electrode may cause an apparent drift significantly greater than this rate. Cleansing and calibration of the probes may be done following the procedure in the instruction manual (Campbell Scientific 2003). The calibration is applied to the probe by changing the offset in the data logger program or by changing this offset in data post-processing. The offset is initially set at 7.00. It is recommended to redirect the outflow during the calibration so that the flow bypasses the flow-through cells and flows directly to the flow gauge.

## **B.6 Flow gauges**

### *B.6.1 Gauge requirements*

Predictions of extreme outflows were made for the test pile basal collection lysimeters, test pile basal drains, and the upper collection lysimeters to determine the gauging requirements. Two approaches were taken for the high flow extreme: 1. calculation of infiltration during the largest daily rainfall on record into waste rock with saturation at field capacity, and 2. published flux extremes for flow through waste rock in similar meteorological conditions. The onset of permafrost conditions at the base of the

test piles was also considered, based on thermal modeling predictions made by ANSTO and observations made during the 2006-2007 winter. The low flow extreme requirement was estimated from a published flux extreme.

The calculation for infiltration during the largest daily rainfall on record followed the form:

$$q = P \times IF \quad (22)$$

$$Q = q \times A, \quad (23)$$

where  $q$  is the groundwater flux,  $P$  is the rainfall rate,  $IF$  is the infiltration fraction,  $A$  is the collection area draining to the flow gauge, and  $Q$  is the volumetric flow to the gauge. The highest daily rainfall for the region on record was 40mm, observed at the Lupin A meteorological station July 9, 1983. An infiltration fraction of 0.5 was used based on the average infiltration rate observed at the Cluff Lake constructed pile experiment (Nichol 2002).

The flux calculated using (8) is in close agreement to the flux observed by Nichol (2002) at the Cluff Lake waste rock hydrogeology experiment on several occasions in response to a 40mm applied rainfall event. Permafrost conditions were expected to form at the base of the Type 1 test pile before the waste rock saturation reached values near field capacity, based on convective thermal modeling. Maximum active zone depth was set to 8m in the calculations, based on two years of data from thermistor profiles in the waste rock piles 30km north of Diavik at the BHP Ekati Diamond Mine (Steffen Robertson and Kristen (Canada), Inc. 2003). Higher outflows were predicted at the T3

test pile due to anticipated applied rainfall events and a slower onset of basal permafrost conditions due to a larger contribution of heat from the enthalpy of sulfide oxidation.

Flow at the Type 3 test pile basal drain in 2007 focused almost entirely at the south basal drain. If this condition persists while the pile continues to wet-up, the prediction for the Type 1 pile may be more applicable. At a depth of about 0.2 m below the basal drain HDPE liner, permafrost conditions appeared to be present at 13 of 15 thermistors under the core of the T3 test pile and at 12 of 19 thermistors under the core of the T1 test pile. However, it is possible that almost the entire depth of the test piles remain in the active zone, due to higher than expected heat transport during summer. The initial wetting front at the T3 test pile is currently expected to reach the basal drain at the core of the pile during the 2009 summer. However significant uncertainty in this prediction exists due to uncertainty in future rainfall and uncertainty in flow characterization. The Type 1 test pile is less likely to wet-up before the onset of permafrost conditions at the pile base.

**Table B.3** A summary of the calculations made to estimate the flow gauge requirements.

Gauging location	Gauging Requirement	Collection Area	Rainfall Intensity	Infiltration Fraction	Rainfall Flux	Cluff Lake Flux ('99 to '01)	Predicted Extremes		Flow
							m <sup>2</sup>	mm/d	
T3 basal drain	maximum flow for unfrozen wetted pile	1500	40	0.5	2.E-07	2.E-07	300	26000	
	maximum flow for partially-frozen pile	850	40	0.5	2.E-07	2.E-07	170	15000	
	minimum flow during pile wet-up	1500				1.E-11	0.015	1	
	minimum flow after pile wet-up	1500				1.E-09	1.5	130	
T3 basal lysimeter	large maximum flow	16	40	0.5	2.E-07	2.E-07	3	280	
T3 basal lysimeter	small maximum flow	4	40	0.5	2.E-07	2.E-07	1	70	
T1 basal drain	maximum flow for partially-frozen pile	1700	40	0.5	2.E-07	2.E-07	340	30000	
	maximum flow for unfrozen wetted pile	3000	40	0.5	2.E-07	2.E-07	600	52000	
T1 basal lysimeter cluster	maximum flow for partially-frozen pile	2	40	0.5	2.E-07	2.E-07	0.4	35	
	maximum flow for unfrozen wetted pile	40	40	0.5	2.E-07	2.E-07	8	700	
upper collection lysimeter	maximum flow	2	40	0.5	2.E-07	2.E-07	0.4	35	

### B.6.2 Flow-through drainage monitoring system

Drainage from the basal drain, basal collection lysimeters, and upper collection lysimeters flowed through a series of flow-through cells before reaching the flow gauges. Drainage flowed through ½" OD flexible PVC tubing to a sample collection cell, a continuous pH measurement cell, and a continuous specific conductance (SC) measurement cell before reaching the flow gauge. Tipping bucket rain gauges were chosen for use as flow gauges to meet the high-resolution requirements at flow rates from 0 to 3 mL/s predicted for the basal lysimeters and upper collection lysimeters. The flow-through systems for the lysimeters are shown in Figure B.12 and B.13.

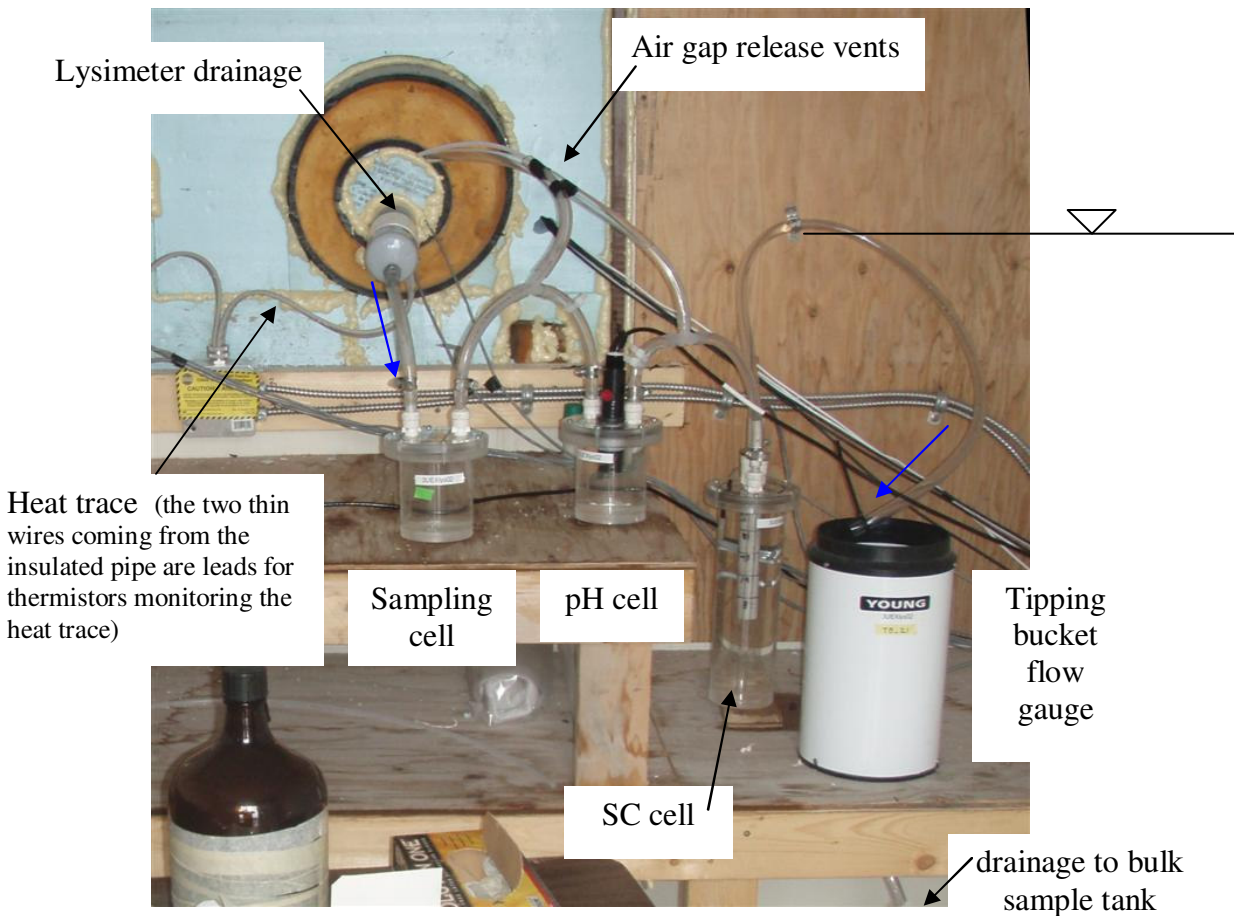


**Figure B.11** Flow-through drainage monitoring system at one of the upper collection lysimeters. Blue arrows indicate flow direction.

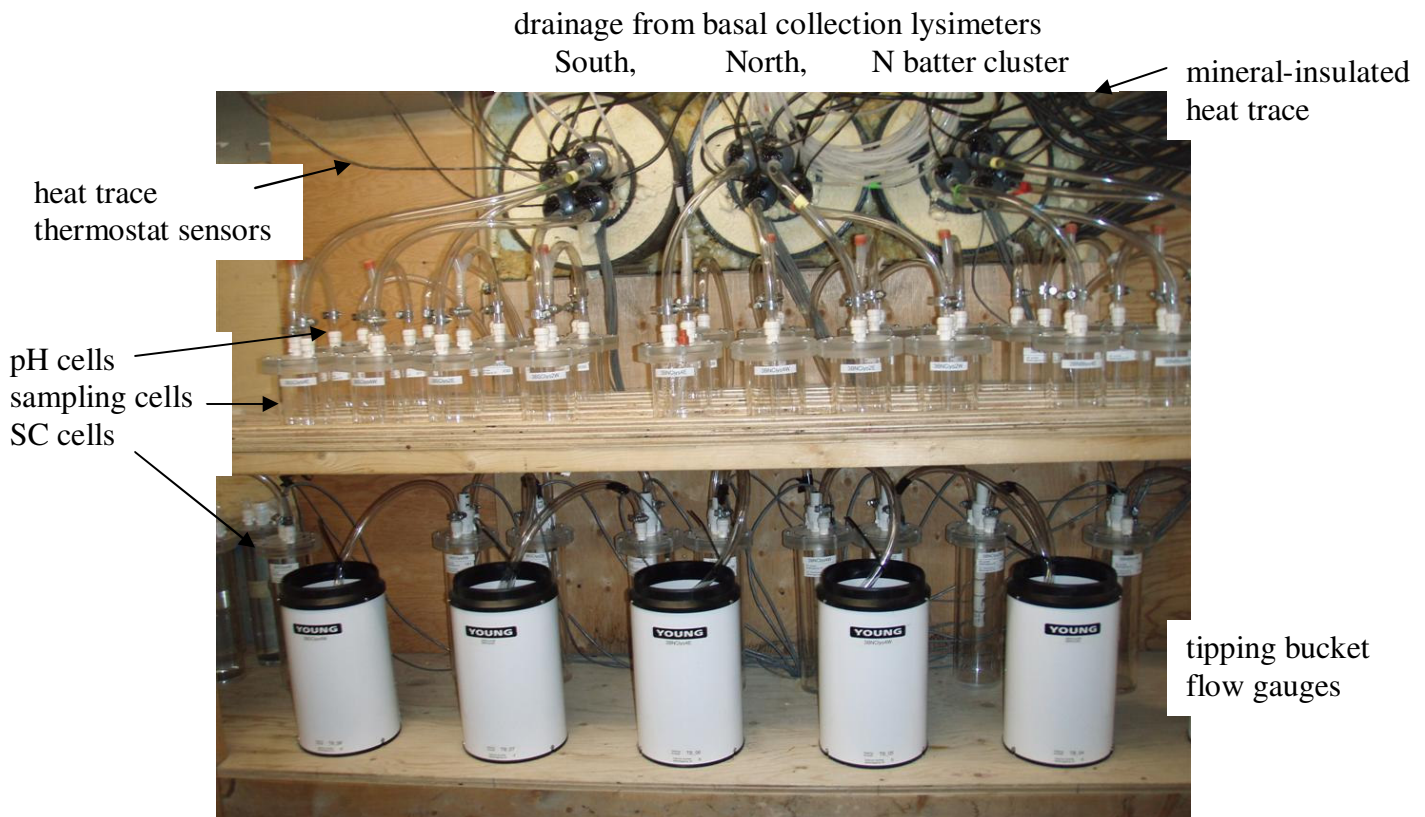


**Figure B.12** Flow-through drainage monitoring system for the Type 3 test pile basal lysimeters. The drainage from each lysimeter may flow through dedicated sampling, pH, and SC cells and a flow gauge. But drainage from the 2m x 2m lysimeters from each cluster is joined together at the flow gauge. Since no flow had yet arrived at the basal lysimeters by the end of 2007, pH probes were not yet inserted into the cells.

To meet the wide range of gauging requirements for the basal drain, the flow was directed through a paddlewheel gauge and a custom tipping bucket gauge. The custom tipping bucket measures flow from 0 to 100 mL/s, a range that likely includes all flow rates that will be observed during the course of the experiment. The paddlewheel measures flow from 19 to 600mL/s, and is incorporated in the system to measure any extremely high flow. One of the flow-through systems for basal drain is shown in Figure B.14.

basal drain

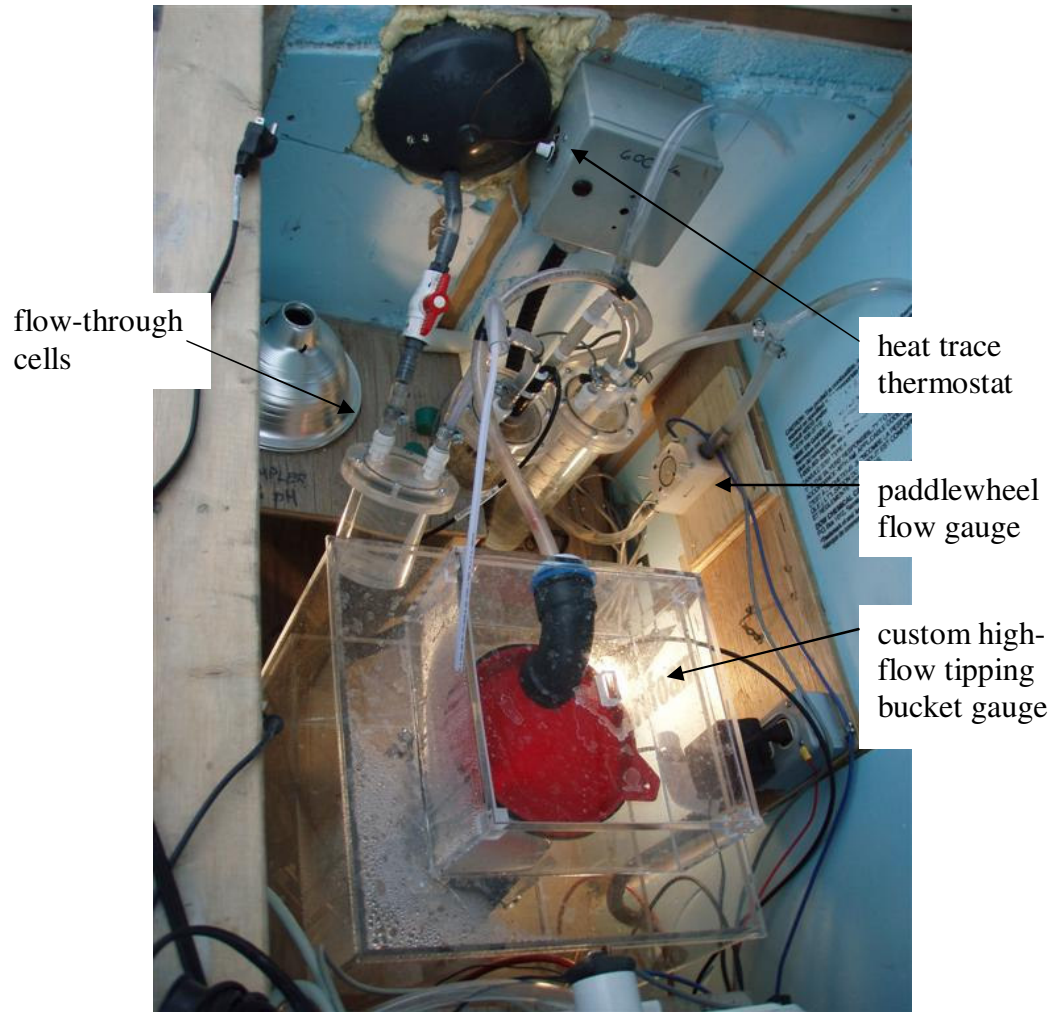


**Figure B.13** The Type 3 test pile north basal drain.

It should be noted that flow restriction in the ½” tubing and the flow-through cells would occur at flow rates higher than about 100 mL/s. Table B.4 summarizes tests done with ½” tubing and fittings to determine the functional flow capacity of the flow-through system.

**Table B.4** The rise in head that would accompany extremely high flow as outflow would back up in the drain pipe due to resistance in the flow-through system.

<b>h</b>	<b>Q</b>
cm	mL/s
30	96
43	147
66	198
105	205

### *B.6.3 Gauging problems in 2007*

Initially, a paddlewheel flow gauge and a Hydrological Services TB4 tipping bucket rain gauge gauged outflow at the basal drains. However much of the flow was in a range between the flow capacity of the tipping bucket and below the minimum functional range of the paddlewheel. The intended use of the tipping bucket is as a rain gauge, and the specified resolution of 0.2mm rain per tip is related to the size of the bucket. Based on the 0.2mm rain per tip resolution of the Hydrological Services TB4 gauge and the 0.1mm rain per tip resolution of the Young Model 52202 tipping bucket gauges, which were calibrated to a flow capacity of about 4 mL/s, a flow capacity for the TB4 gauges of about 8 mL/s was inferred. The paddlewheel flow gauges have a specified minimum range extent of about 6 mL/s. A small overlap of gauge range was expected.

However, calibration of the gauges determined that a large gap existed between the functional range of the paddlewheel gauge and the TB4 tipping bucket gauge. The TB4 gauge had a flow capacity of about 6 mL/s. Despite the specified minimum of 6 mL/s, the Muis paddlewheel had a functional minimum of about 19 mL/s. A larger custom-made tipping bucket gauges was installed at the T3 south basal drain on August 1, 2007. During May, June, and July, flow measurements were made using a graduated cylinder and a stopwatch.

Air gaps introduced into the flow-through cell tubing created pressure locks that caused stoppage of the outflow, particularly during the large changes in flow rate that occurred during snowmelt. Air gap release vents were placed in the flow-through system (in July 2007) to prevent such pressure locks from occurring (Figure B.12).

#### *B.6.4 Low flow tipping bucket gauges*

Young Model 52202 tipping bucket rain gauges were used to gauge the outflow from the basal collection lysimeters and the upper collection lysimeters. When used as a rain gauge, the water collected in the funnel at the top of the gauge flows to the tipping bucket. When the bucket reaches a certain volume, it tips and causes a magnet to pass a reed switch that sends a pulse to a data logger. During an intense rainfall, the tipping bucket may tip about every five minutes. When used as a flow gauge, the volume per tip increases at flow rates above about 0.5 mL/s, and a calibration is required to relate the time between tips to flow rate. The calibration procedure below follows the procedure described by Nichol 2002. When used as flow gauges, tipping bucket gauges have very high resolution and are functional even at slow drips.

## Low Flow Tipping Bucket Calibration Procedure

### A. Materials

1. Laptop computer
2. Data logger with power supply
3. Digital watch with seconds display
4. Datalogging field book

### B. Setup

1. Level the tipping bucket platform using the level bubble and the tri-brach nuts.
2. Connect the pulse input leads from the tipping bucket to the data logger. For the Young Model 52202 gauge:
  - black: IN channel on SW8A multiplexer or P channel on data logger
  - white and clear: ground
3. Turn on the datalogging system with the power switch on the power supply.
4. Connect the datalogger to the computer using a 9pin serial cord connected to the “computer” side of the SC32B interface.
5. On the computer, open PC208W from the shortcut on the desktop.
6. Select connect to open the CR10X datalogger connection window. Select connect. If connection problems exist, see Details section below.
7. Set your watch to the datalogger clock, shown at the lower right of the PC208 window.
8. Use a peristaltic pump to deliver water from the supply bucket to the constant head bucket.
9. Ensure that the upper outflow from the constant head bucket is draining back into the supply bucket.
10. Direct the lower outflow from the constant head bucket to one of the tipping bucket flow gauges. This line has a valve that controls the flow rate. The flow into the tipping bucket should stream into the funnel perpendicular to the tipping bucket swing arm to avoid flow that swirls down into the gauge.

### C. Calibration Procedure

1. Open the valve on the line flowing to the tipping bucket. Start with a low flow rate – a tip about every 10 seconds. Ensure that the flow rate to the tipping bucket is steady: count the time between tips, at several times over the course of a few minutes. (A tip may be easily heard as a clicking sound.)
2. Start the calibration trial by directing the tipping bucket outflow into a 500mL or 1000mL graduated cylinder. This should be done so that the graduated cylinder collects the flow at a discrete tip. Record the time, to the second, that the outflow begins to flow into the cylinder.
3. Allow 150mL or more to flow into the cylinder.
4. Remove the graduated cylinder from the tipping bucket outflow exactly as a tip occurs. Do not collect the discharge water from this last tip in the graduated cylinder. Record the time, to the second.
5. In the PC208 window, press Collect. Use the stopwatch start and stop times to determine the start and stop times in the data file. Determine the average tip time during the calibration trial by dividing the number of data entries by the time of the trial. Evaluating the tip time at each tip may check the assumption of a constant flow rate delivered by the constant head reservoir.
6. The flow rate for the trial is the volume of water measured with the graduated cylinder divided by the time of the trial.

#### Approximate Flow Rates:

0.2mL/s	10 s/tip
0.4mL/s	6 s/tip
0.5mL/s	4 s/tip
1.2mL/s	2 s/tip
1.5mL/s	1.5 s/tip
2.0mL/s	1.3 s/tip
3.5mL/s	0.8 s/tip

OR HIGHEST FLOW RATE POSSIBLE

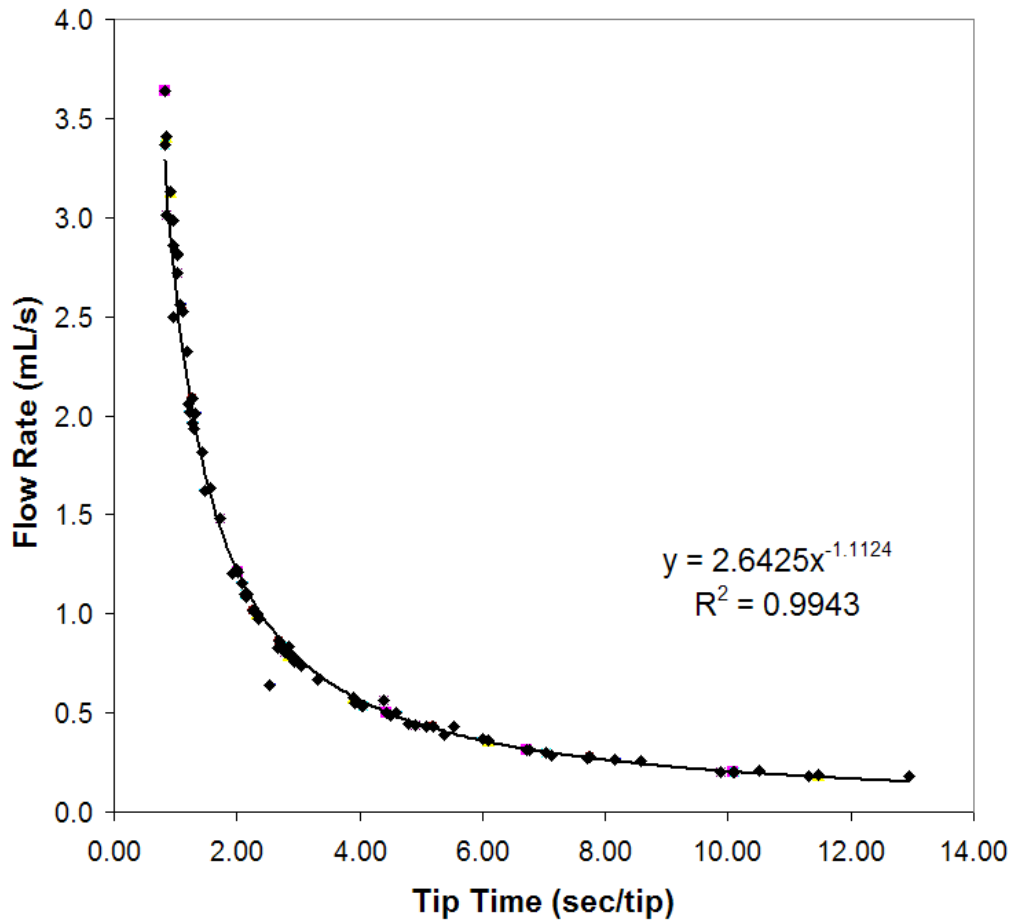
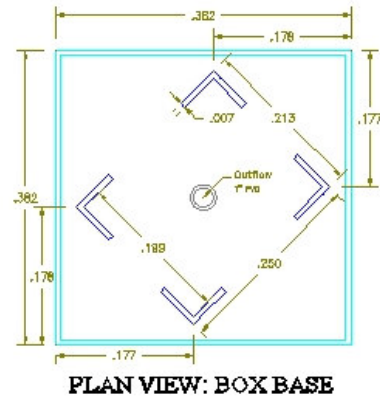
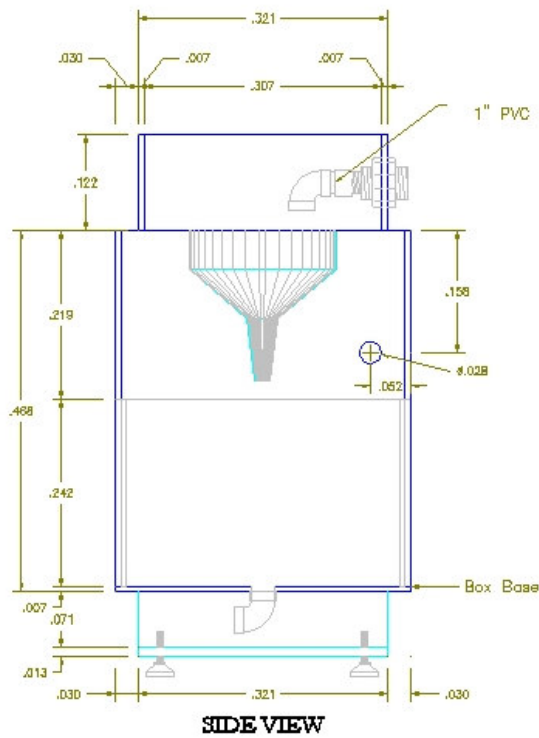


**Figure B. 14** Low flow tipping bucket gauge calibration curve.

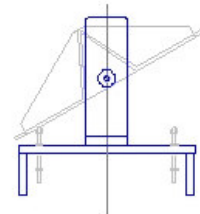
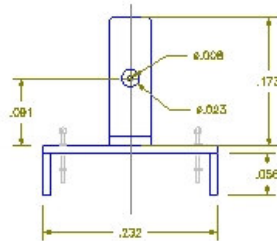
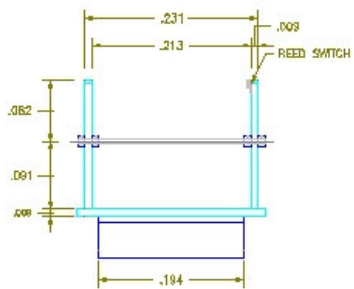
*B.6.5 High flow tipping bucket gauges*

Tipping bucket gauges for high flow capacity were custom-made by PlasticSmith, Inc. (17 East 6th. Ave., Vancouver B.C. V5T1J3, 604 876-4494). The gauges were fabricated with acrylic and the axle for the bucket mechanism was stainless steel. A rare earth magnet was cemented to the bucket so that as the bucket tips, it passes a Texas Electronics reed switch, which sends a pulse to the data logger.

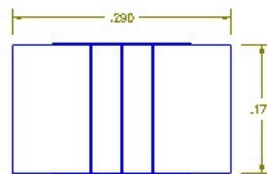
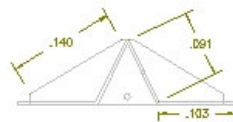


UBC TIPPING BUCKETS Diavik Project  
Matt Neuner

units: meter



Tipping bucket  
mechanism



rare-earth  
magnet

Figure B.15 Design for the high flow tipping bucket flow gauges.

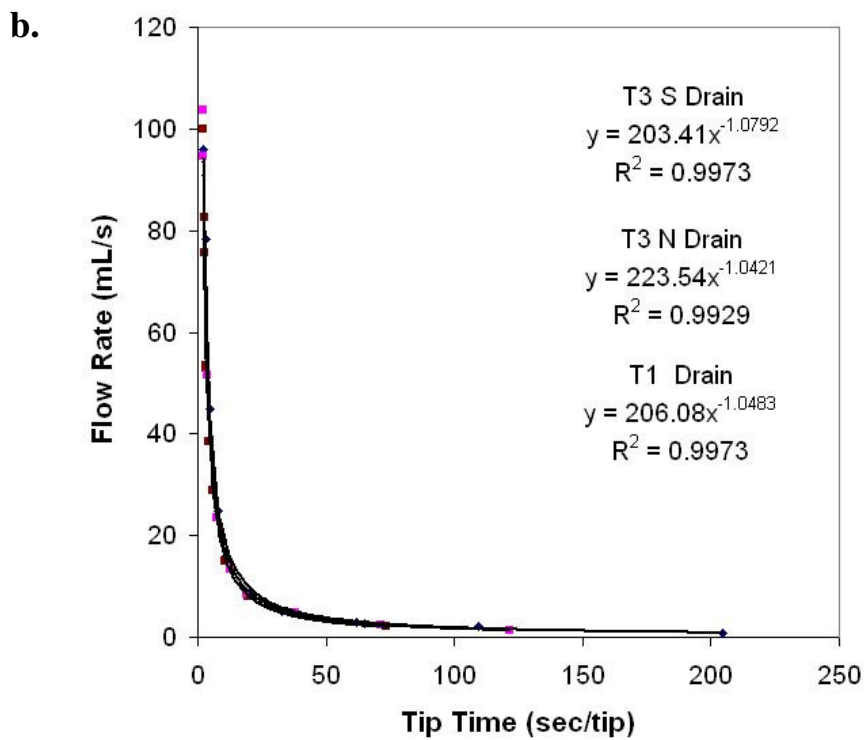
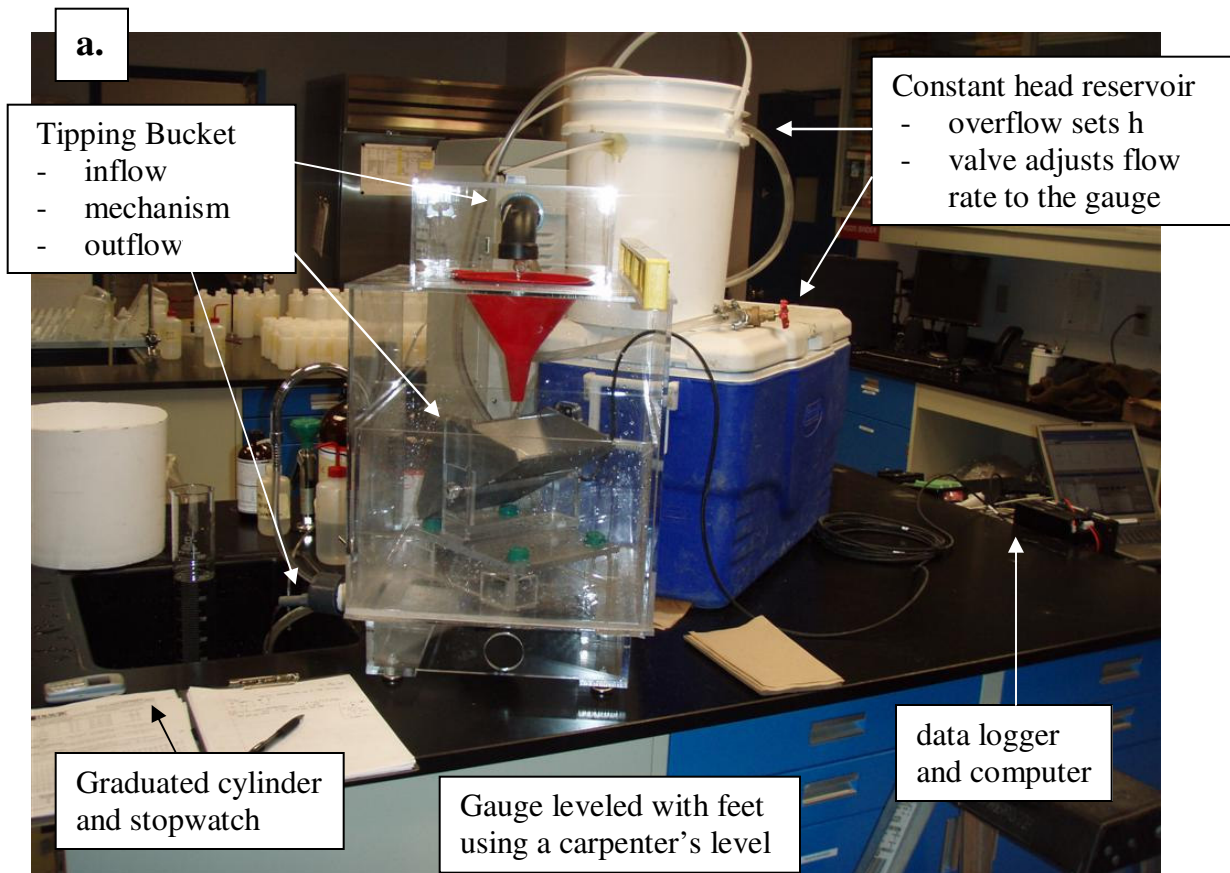


**Figure B.16** (a) Calibration of the high flow tipping bucket flow gauge and (b) the resulting relationship between tip time and flow rate for each gauge.

### B.6.6 Paddlewheel gauges

Paddlewheel flow gauges were installed at the test pile basal drains to capture any extreme flow event that was out of range of the high flow tipping bucket gauges. The gauges were Muis SPX Low Flow Meters, with ½”NPT fittings (10610 -172 Street, Edmonton, AB Canada T5S 1H8, 780 486-2400 [www.muiscontrols.com](http://www.muiscontrols.com)). The gauges are made of polypropylene and acrylic and feature a magnet on the paddlewheel which passes a reed switch. The low flow limit of the gauge is listed as 0.4 L/min, or 6 mL/s, in the brochure, but was found to be 19 mL/s in my calibration.

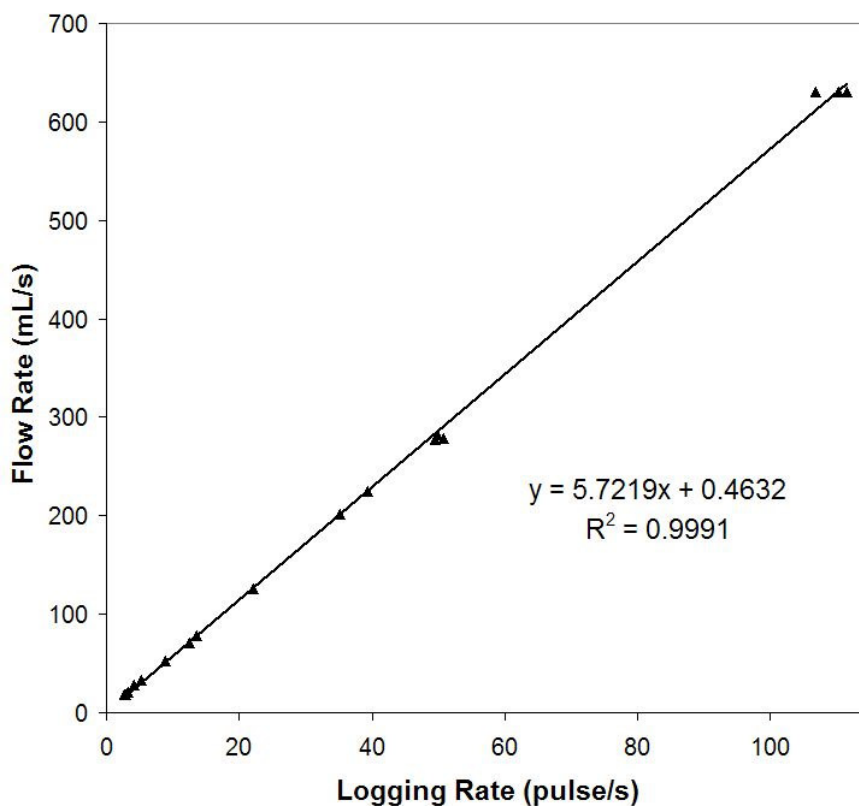
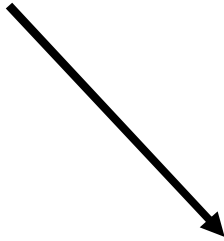


**Figure B.17** Calibration curve for the paddlewheel flow gauges.



*Mike Gupton*

**Figure B.18** A rain gauge was installed on the roof of the instrument hut at the top of each test pile

## APPENDIX C DETAILS OF CHARACTERIZATION OF THE WASTE ROCK

### C.1 Grain size distribution

#### C.1.1 Boulder fraction of 100 m<sup>3</sup> samples

Three haul-truck loads of Type 3 waste rock and three haul-truck loads of Type 1 waste rock from the A154 pit were taken during the construction of the test piles and placed into separate piles to estimate the fraction of the waste rock in the boulder size class. Komatsu 830E haul trucks were used, which have a typical payload of 250 t, equivalent to a payload volume of 100 m<sup>3</sup>. Two of the Type 1 boulder fraction analysis piles, however, were mistakenly bulldozed during the construction of the covered test pile. Each of the remaining loads was split into two separate piles: a pile of waste rock clasts with a diameter larger than about 30 cm and a pile of the clasts and particles finer than about 30 cm. Under the Unified Soil Classification System, the boulder class is defined as clasts larger than 25.6 cm. The material was sorted using a Komatsu PC600 track-mounted excavator. The 30 cm sorting criteria was evaluated visually by the operator, generally from inside the excavator cab.

The mass of the coarse and fine fractions of the 830E haul-truck loads were measured using the calibrated payload meter of a Komatsu HD785 haul-truck. One truck was used for all measurement. The payload meter determines the mass inside the box using calibrated pressure transducers inside the front and rear suspension. The suspension in the truck used for the measurements was recharged, and the payload pressure transducers were calibrated immediately prior to use in the measurements, following the instructions in the HD785 instruction manual. The payload meter was tared while the truck drove on level ground. The waste rock fractions were loaded into the

HD785 haul truck using a Caterpillar 345C track-mounted excavator. Research personnel rode with the haul truck operator to record the payload measurement, which was made as the truck drove on level ground. Payload meter resolution was 1 t, but a direct test of the accuracy was not performed. Due to limited availability of the haul-truck for this research purpose, only two of the samples were measured. The results of the boulder fraction measurements are summarized in Table C.1, and the average of the two measurements is included in the summary particle size table, Table C.2.

A portion of one of the coarse splits was weighed using a drive-on truck scale and 6m<sup>3</sup> payload volume trucks (Figure C.1). The trucks were weighed empty and loaded to determine the mass of the load. This method was abandoned due to concern for the condition of these smaller trucks. The method using a haul-truck payload meter described above was used for the remaining measurements.

**Table C.1** The fraction of 100 m<sup>3</sup> samples with particle size finer than 30 cm.

<b>Sample</b>	<b>Mass &gt; 30 cm</b> [t]	<b>Mass &lt; 30 cm</b> [t]	<b>Total Mass</b> [t]	<b>Sample</b>	<b>% Finer than 30 cm</b>
Type 3 Sample 1	- sample T3 (1) mass not fully measured -				
Type 3 Sample 2	141	123	264		<b>47</b>
Type 3 Sample 3	99.5	163	263		<b>62</b>
Type 1 Sample 1	- sample T1 (1) mass not fully measured -				

a.



b.



**Figure C.1** Determining the boulder fraction of 100 m<sup>3</sup> samples of waste rock. (a) Splitting a sample visually using an excavator. (b) Loading waste rock from each split into a truck to determine the mass of the load with a drive-on truck scale.

### *C.1.2 Grain size distribution of a 40 m<sup>3</sup> sample*

A size-mass mass distribution of a Komatsu HD785 haul truck load was determined by following the procedure described as Test Method A in ASTM standard method D 5519 (ASTM 2001). Project management, sample collection, waste rock sieving, and data synthesis were performed by Nishi-Khon/SNC-Lavalin Limited. The particle size analysis was performed on a 90 Tonne Type 1 waste rock sample that included all clasts and particles in the haul-truck load, including boulders larger than 0.9 m. The distribution of clasts and particles in this sample was the best representation of the distribution of the waste rock on the large-scale. The grain size distribution for this 40 m<sup>3</sup> sample is plotted in Figure C.4a and summarized, with the size distribution of the hand samples described below, in Table C.2.

### *C.1.3 Grain size distribution of hand samples*

Hand samples were taken during construction of the test piles using a large trowel and 60 cm by 40 cm sample bags. Typical sample mass was 10 kg and consisted of waste rock finer than 100 mm. Approximately 244 samples were taken from the Type 1 test pile, 313 samples from the Type 3 test pile, and 5 samples from the Upper Collection Lysimeters. Hand samples were collected for analysis of grain size distribution, hydraulic testing, sulfur content, mineralogy, rock classification, and microbiology. A complete analysis of the grain size distribution and sulfur content of the hand samples is provided by Smith (in progress). The results from analysis of 91 samples from the Type 1 test pile, 101 samples from the Type 3 test pile, and 5 samples from the Upper Collection Lysimeters are presented here. The samples analyzed are listed in Table C.3.

Samples were collected from the 2m basal lift, each of Faces 1, 2, 3, 4, and 5, and the top surface of the piles (Figure C.2). Samples were collected from the test pile face using a 125 ft. JLG man lift (Figure C.2a). However, since the matrix material tended to deposit in the voids between the boulders, little was available for sampling. No attempt was made to sample matrix material by reaching into void spaces between boulders due to significant risk of personal injury posed by the unstable boulders. The limited number of hand samples taken directly from the face were supplemented by samples taken at dump piles before the material was pushed down the face by the dozer (Figure C.2b). Many of the samples are therefore representative of the material finer than 100 mm in the region of the test pile where the dump pile was pushed (a region perhaps 5 m wide by 1 m deep by 20 m along the slope), rather than at a discrete location. For this analysis, the data were organized into samples that were taken from the material that was deposited during the six construction stages of each test pile: the basal 2 m lift, tip face 1, tip face 2, tip face 3, tip face 4, and tip face 5, and those taken from the top of the piles (Figure C.3). For example the T3F2 grain size data consists of the samples taken from the material dumped between tip face T3F1 and T3F2 and the samples taken from the T3F2 tip face.

Samples were split for various analyses using a riffle splitter, which divides a sample into halves without bias. Grain size distribution analysis was done by sieving according to the ASTM standard method D422 (ASTM 2002). Typical mass of a subsample analyzed for grain size distribution was 5 kg. A large Gilson TS-1 sieve shaker was used to sieve from 40 mm to 5 mm. The fraction finer than 5 mm was oven dried before being sieved from 5 mm to 0.08 mm using an auto-tapping sieve shaker. The mass retained on each sieve was measured with a calibrated scale with 0.1 g resolution.

The mean grain size distribution and the range of distributions of Type 3 hand samples were somewhat finer than that of the Type 1 waste rock. Figure C.4b shows the standard deviation about the mean grain size distribution for 91 Type 1 samples and 101 Type 3 samples. The distribution at one standard deviation coarser than the mean distribution of Type 1 material was slightly coarser than that of the Type 3 material, and the same was true for each of the distributions at one standard deviation finer than the mean distribution. The mean particle size by weight ( $D_{50}$ ) for the mean Type 3 hand sample was 7mm, while the  $D_{50}$  for the mean Type 1 hand sample was 9mm. The range of the  $D_{50}$  for all 197 hand samples, at one standard deviation from the mean of all samples, was from 4 mm to 15 mm.

The mean grain size distribution of the matrix material (defined here as the material finer than 5mm) for the Type 3 material was very similar to the mean distribution of the Type 1 material. The matrix material in the Type 3 test pile with a mean grain size distribution was 26% gravel, 67% sand, and about 7% silt and clay. The mean matrix material in the Type 1 test pile was 28% gravel, 65% sand, and about 7% silt and clay.

Three samples were analyzed from the top of each of the test piles. But the matrix material at the tops of the piles was finer than the mean matrix grain size distribution for all samples (Figure C.5). It should be noted that the samples at the top of the piles were sampled after much of the top of the piles had been excavated to a depth of about 1 m and re-deposited to recover the instrumentation leads. The hand samples from T3F1 and T3F2 were finer than those from the rest of the pile and the samples from the base of the pile were coarser than the rest of the pile (Figure C.6). The variability in the grain size distribution of the hand samples from the Type 1 pile showed less spatial bias amongst

the stages of the test pile construction (Figure C.7). The data are summarized in Table C.2.

**Table C. 2** A summary of the grain size distribution of the waste rock at the large-scale, at the hand sample-scale, and at the matrix-scale. Variability in the grain size distributions is presented as one standard deviation about the mean.

Sample	% Boulder	% Cobble	% Gravel	% Sand	% Silt and Clay
large-scale samples					
100 m <sup>3</sup>	54				
40 m <sup>3</sup>	32	34	30	13	1
hand samples					
T3 mean			67	30	3
T1 mean			72	25	3
coarse extent of one Std. Dev. about the mean T3 distribution			75	23	2
coarse extent of one Std. Dev. about the mean T1 distribution			80	18	2
fine extent of one Std. Dev. about the mean T3 distribution			60	36	4
fine extent of one Std. Dev. about the mean T1 distribution			63	33	4
< 5mm fraction					
T3 mean			26	67	7
T1 mean			28	65	7
coarse extent of one Std. Dev. about the mean T1 distribution			32	62	6
fine extent of one Std. Dev. about the mean T3 distribution			24	66	10

a.



b.



**Figure C.2** Collecting waste rock hand samples (a) from the tip face and (b) from a dump pile before the material was pushed down the tip face by a bulldozer.

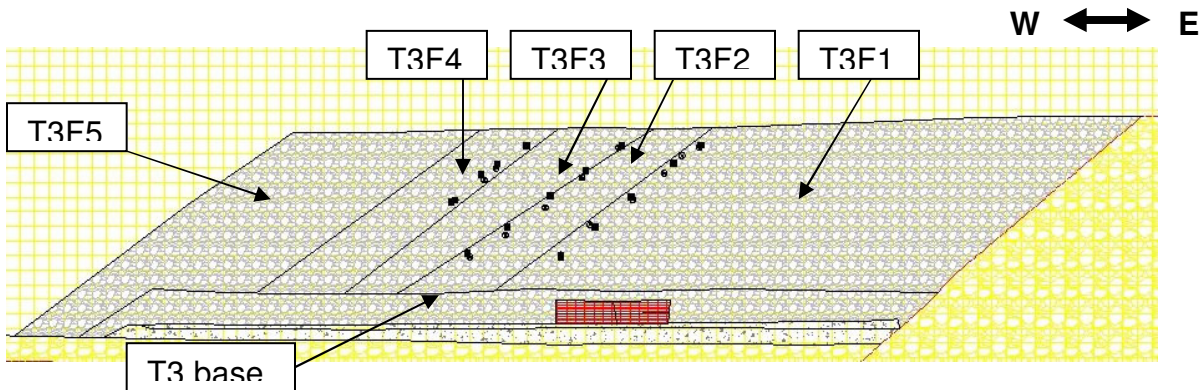


**Figure C.3** A longitudinal cross-section of the Type 3 test pile: the pile was built by end-dumping from right to left. The location of the sampling regions are labeled.

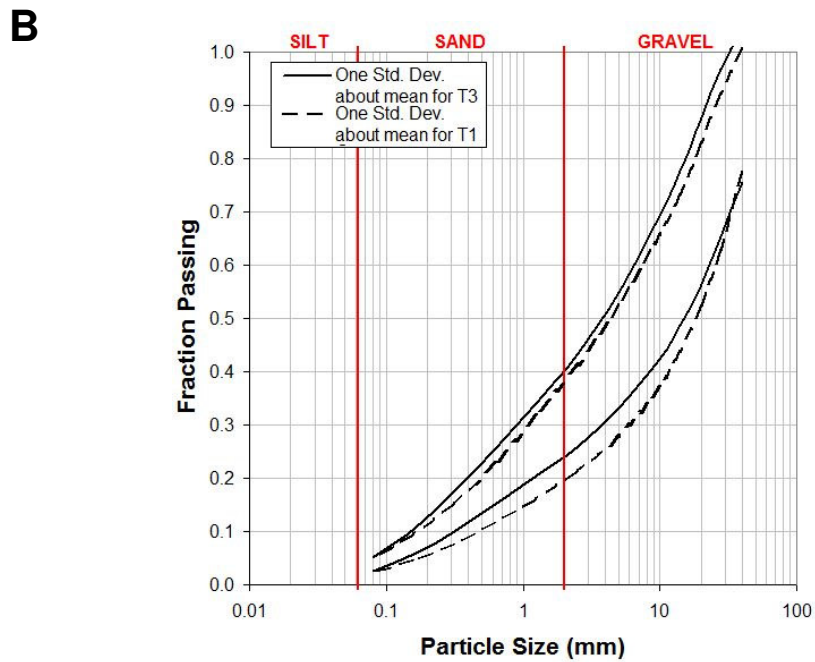
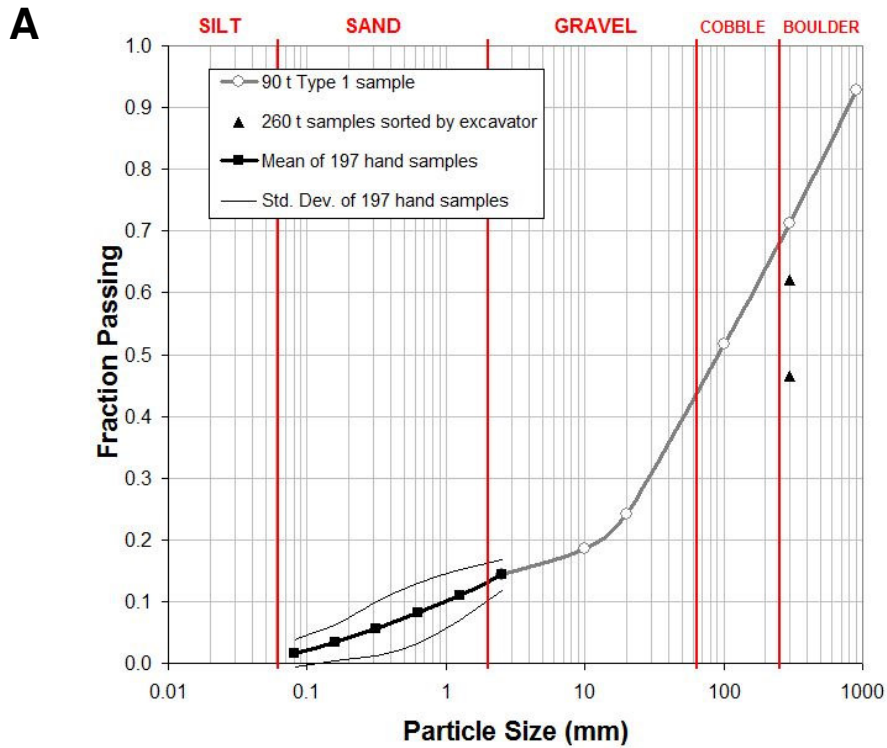
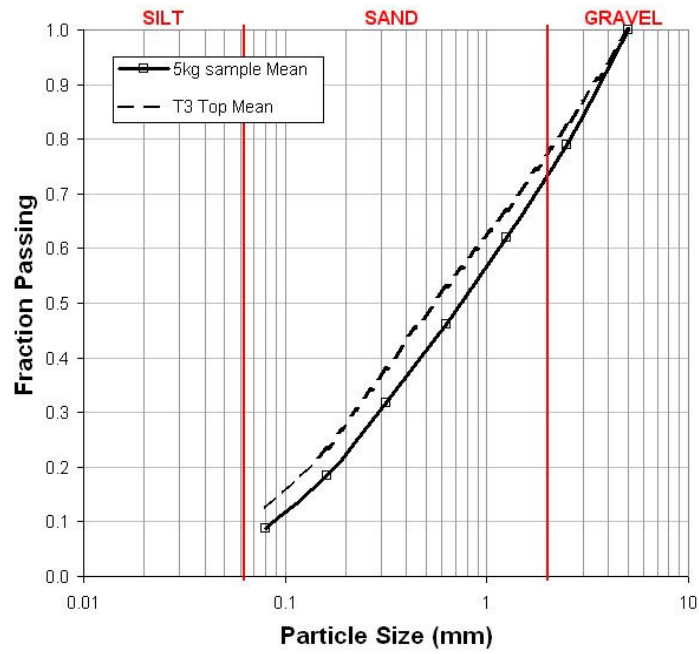


**Figure C.4** (A) Grain size distribution of a 90 Tonne T1 sample, the boulder fraction of two 250 Tonne T3 samples, and the mean and SD of 197 hand samples as an extension of the 90 t sample curve. (B) The standard deviation of 91 T1 hand samples and 101 T3 samples.

**A**



**B**

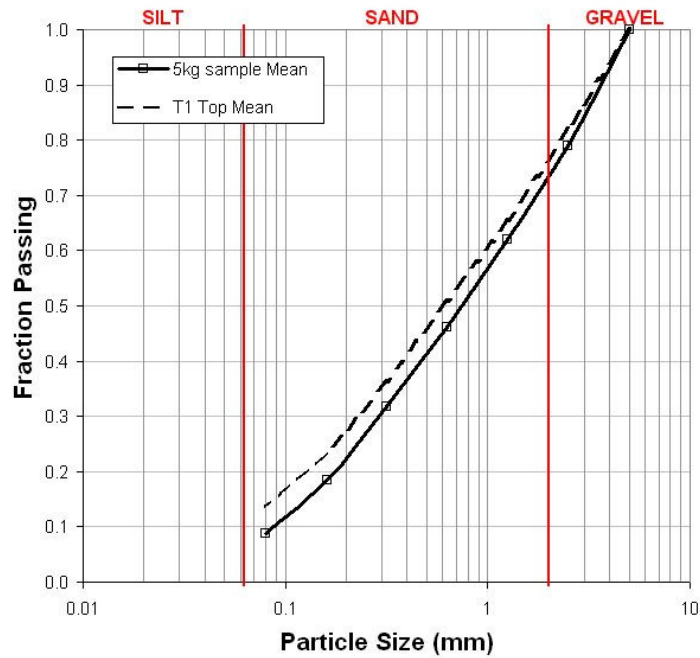


**Figure C.5** The fraction finer than 5mm: mean of 197 samples from the T1 and T3 and (A) the mean of 3 samples from the top of the T3 and (B) the mean of 3 samples from the top of the T1.

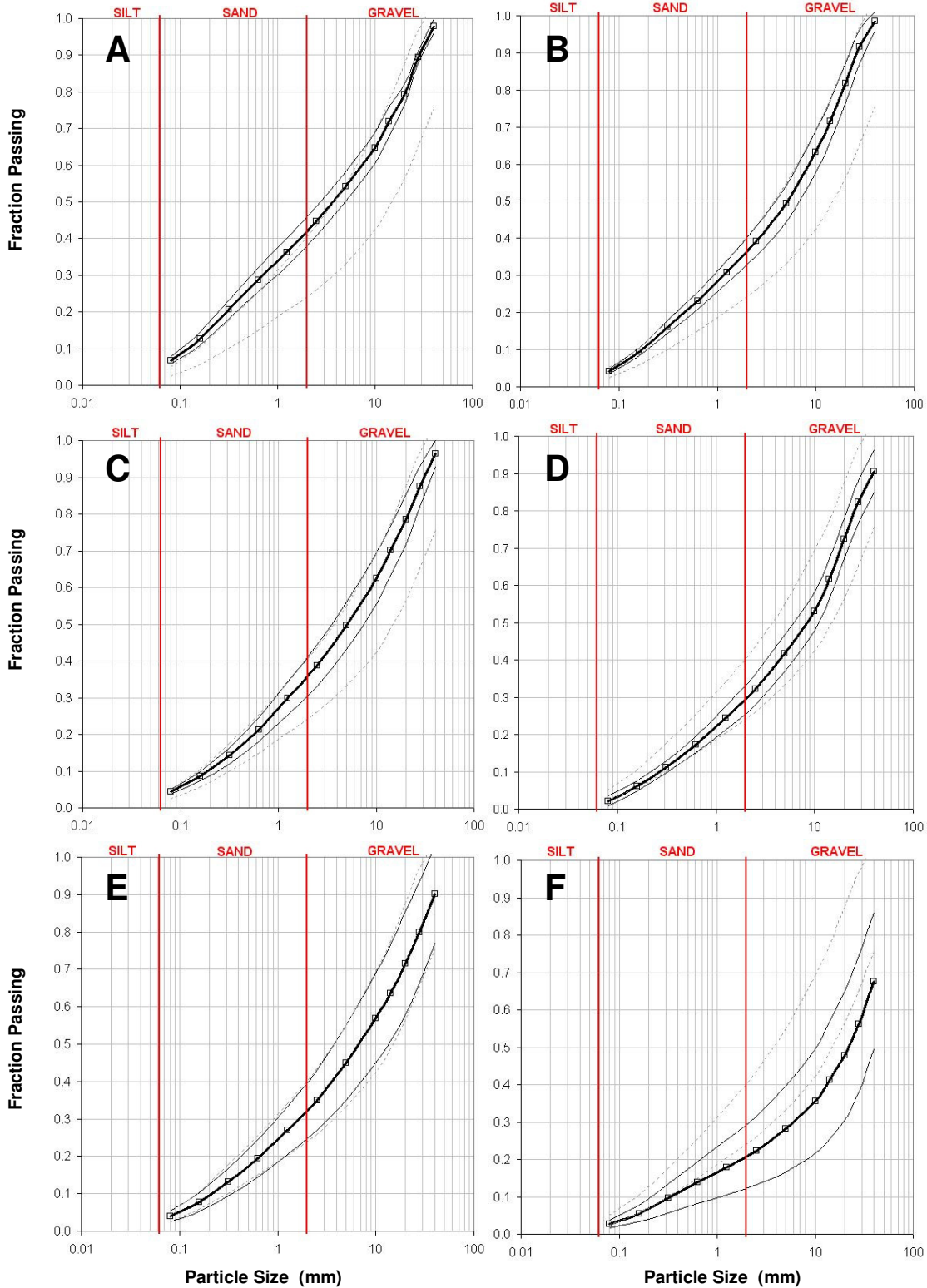


**Figure C.6** Grain size distribution of hand samples at the T3 (A) top, (B) F1, (C) F2, (D) F3, (E) F4 and F5, and (F) base. The dark line is the mean, the light line is the standard deviation of samples from each region, and the light dashed line is the standard deviation of all T3 hand samples (same for all plots).

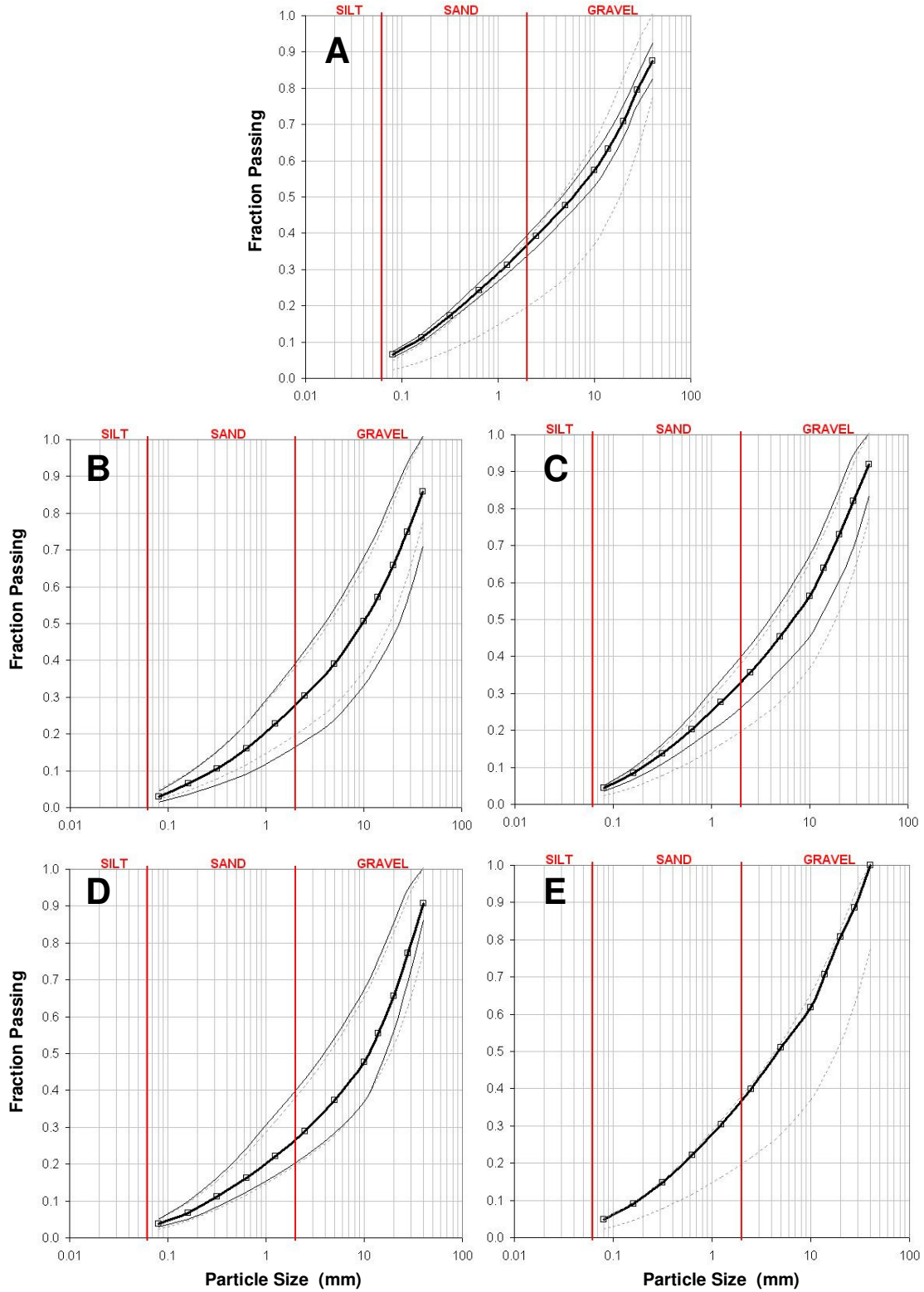


**Figure C.7** Grain size distribution of hand samples at the T1 (A) top, (B) F1, (C) F2, (D) F3, and (E) F4. The dark line is the mean, the light line is the standard deviation of samples from each region, and the light dashed line is the standard deviation of all T1 hand samples (same for all plots).

**Table C.3** List of hand samples analyzed.

TYPE 3		TYPE 3		TYPE 1		TYPE 1	
Sample Number	Location	Sample Number	Location	Sample Number	Location	Sample Number	Location
189105	T3-B	190277	T3F2	190174	T1F1	190674	T1F2
189109	T3 B	190278	T3F2	190176	T1F1	190699	T1F2
189111	T3 B	190279	T3F2	190249	T1F1	190702	T1F2
189112	T3 B	190280	T3F2	190250	T1F1	190706	T1F2
189113	T3 B	190281	T3F2	190251	T1F1	190708	T1F2
189114	T3 B	190282	T3F2	190252	T1F1	190748	T1F2
189115	T3 B	190283	T3F2	190253	T1F1	190750	T1F2
189315	T3 B	190284	T3F2	190254	T1F1	190875	T1F2
189317	T3 B	190288	T3F2	190255	T1F1	190876	T1F2
189319	T3 B	190289	T3F2	190256	T1F1	190877	T1F2
189320	T3 B	190290	T3F2	190257	T1F1	190878	T1F2
189323	T3 B	190295	T3F2	190258	T1F1	190879	T1F2
189325	T3 B	190296	T3F2	190259	T1F1	191450	T1F3
189328	T3 B	190781	T3F2	190260	T1F1	191480	T1F3
189332	T3 B	190782	T3F2	190261	T1F1	191481	T1F3
189333	T3 B	190783	T3F2	190262	T1F1	191482	T1F3
189335	T3 B	190799	T3F2	190263	T1F1	191483	T1F3
189336	T3 B	190800	T3F2	190264	T1F1	191486	T1F3
189338	T3 B	191058	T3F3	190265	T1F1	191488	T1F3
189339	T3 B	191059	T3F3	190266	T1F1	191489	T1F3
189357	T3 B	191061	T3F3	190267	T1F1	191490	T1F3
189820	T3F1	191062	T3F3	190268	T1F1	191492	T1F3
189822	T3F1	191063	T3F3	190269	T1F1	191495	T1F3
189844	T3F1	191065	T3F3	190270	T1F1	191497	T1F3
189845	T3F1	191066	T3F3	190271	T1F1	191500	T1F3
189846	T3F1	191067	T3F3	190272	T1F1	191501	T1F3
189847	T3F1	191070	T3F3	190273	T1F1	191502	T1F3
189848	T3F1	191100	T3F3	190274	T1F1	191648	T1F3
189850	T3F1	191104	T3F3	190275	T1F1	191649	T1F3
189851	T3F1	191107	T3F3	190277	T1F1	191651	T1F3
189852	T3F1	191160	T3F3	190298	T1F1	191652	T1F3
189853	T3F1	191163	T3F3	190299	T1F1	191655	T1F3
189854	T3F1	191164	T3F3	190299	T1F1	191749	T1F3
189855	T3F1	191170	T3F3	190301	T1F1	191751	T1F3
189856	T3F1	191174	T3F3	190301	T1F1	191752	T1F3
189857	T3F1	191360	T3F3	190302	T1F1	191753	T1F3
189858	T3F1	191361	T3F3	190302	T1F1	191755	T1F3
189859	T3F1	191362	T3F3	190304	T1F1		
189860	T3 F1	191363	T3F3	190304	T1F1	070627_2	T1 Top
189861	T3 F1	191455	T3F4	190306	T1F1	070627_1	T1 Top
189862	T3 F1	191456	T3F4	190306	T1F1	070627_3	T1 Top
189863	T3 F1	191473	T3 F4	190312	T1F1		
189864	T3 F1	191474	T3 F4	190656	T1F2	<b>Upper Lysimeters</b>	
189865	T3 F1	191475	T3 F4	190657	T1F2	<b>Sample</b>	<b>Material</b>
189866	T3 F1	191923	T3 F5	190658	T1F2	<b>Number</b>	
189867	T3 F1	191924	T3 F5	190659	T1F2	UCL 1	T1
189869	T3 F1	191948	T3 F5	190660	T1F2	UCL 2	T1
189870	T3 F1	193120	T3 F5	190662	T1F2	UCL 3	T1
189871	T3 F1	192410	T3 Top	190663	T1F2	UCL 4	T3
189951	T3F1	192201	T3 Top	190665	T1F2	UCL 5	T3
190261	missing data	192421	T3 Top	190668	T1F2		

## C.2 Hydraulic testing of a 16 m<sup>3</sup> sample

A 4 m x 4 m x 1 m tank was constructed to conduct porosity measurements, large-scale permeameter tests, and a drain-down test on a sample of waste rock at a scale on the order of the representative elemental volume (REV). This tank is referred to as the 16 m<sup>3</sup> permeameter or the field permeameter. Bear (p.20, 1972) defines an REV as the approximate volume at which the particle-scale properties of a porous media may be replaced by a fictitious continuum in which we may assign values of any property that apply equally to any point inside the volume. An REV is the scale at which we may parameterize a porous media. The waste rock at the Diavik mine includes boulders up to about 3m<sup>3</sup>. An estimate of the REV was made by considering a basic REV parameter, the porosity (n):

$$n = V_v / V_t , \quad (1)$$

and the porosity (n') if an additional clast of the largest possible volume (V<sub>c</sub>) is included:

$$n' = V_v' / V_t , \quad (2)$$

where V<sub>v</sub> is the volume of the void space, V<sub>t</sub> is the total volume of the particles and voids, and V<sub>v</sub>' is the volume of the voids minus the volume of the largest clast (V<sub>c</sub>). This statement makes the simple assumption that a large clast has essentially no pore space, and therefore reduces the total volume of voids. Using this method, and assuming the largest clast size is 3 m<sup>3</sup>, a reduction of 1% (approximately a 95% confidence) in the porosity estimation (by the addition of a large clast) was attained with a volume of 80 m<sup>3</sup>. This calculation was carried out prior to filling the 16 m<sup>3</sup> permeameter with waste rock, assuming a large-scale porosity of 0.3, to determine the largest acceptable clast. The

calculation was done again using the measured porosity (see below) to determine the approximate volume of an REV of 80 m<sup>3</sup>.

Hydraulic tests were performed on a sample with a volume smaller than the representative elemental volume due to practical considerations. The 16 m<sup>3</sup> permeameter was constructed using a design similar to that of the basal lysimeters. The permeameter was the largest size that could be made without requiring HDPE geomembrane, which was available in sheets 7m wide, to be fused. A 0.5 m<sup>3</sup> (0.8 m x 0.8 m x 0.8 m) maximum particle size acceptable for the 16 m<sup>3</sup> permeameter was calculated using the method described above.

A drawing of the 16m<sup>3</sup> permeameter is shown in Figure C.8. The plumbing is drawn as it was set to estimate permeability. A plywood frame was built atop a base of 2” crushed rock. A 1½” PVC lower drain pipe with a rubber gasket compression fitting was buried in the crushed rock. A 10 cm layer of sand was deposited atop the crushed rock and graded towards the drain pipe (Figure C.9). A single sheet of 40 Mil HDPE geomembrane liner was fit into the plywood frame. Rubber gasket compression fittings were used to seal the HDPE liner to the lower drain and upper drain. The seals at the fittings were also covered with a silicone caulk seal. The bottom of the inside of the permeameter was filled with a 5 to 25 cm thick layer of 3/8” clean crushed rock that was level at the top surface. The clean crush was installed to provide a highly permeable layer to allow the water flowing upward through the overlying waste rock to be applied uniformly across the lower boundary of the waste rock.

The clean crush layer was saturated by pumping about 650 L of water through the lower drain. While the clean crush was fully saturated, the permeameter was filled with

Type 1 waste rock using a Caterpillar 345C track-mounted excavator (Figure C.9). Some large boulders were not placed into the permeameter. The largest particle size was about 0.5 m. Three manometers, made of 1" PVC with a 5 cm screened interval at the level of the base of the waste rock, were installed with the waste rock. The waste rock was filled as close as possible to the level of the upper drain. Waste rock was placed around the sides of the permeameter for support.

Porosity was measured by pumping a volume of water into the 16 m<sup>3</sup> permeameter until the waste rock was saturated (Figure C.10a). The total volume of the sample was determined to be 16.0 m<sup>3</sup> by measuring the dimensions of the tank prior to filling with waste rock, from the top of the saturated gravel to the spillway at the upper drain. Water was pumped from a 1000 L tank graduated to 50 L increments into the waste rock from the bottom of the permeameter. The 1000 L tank was graduated by marking the water level as it was filled with 10 L increments from a graduated bucket. The 1000 L tank was re-filled by a tanker truck three times during the porosity measurement. 3870 L +/- 200 L of water were pumped into the 16 m<sup>3</sup> permeameter to saturate the waste rock. Assuming that the waste rock was dry when placed into the 16.0 m<sup>3</sup> permeameter, the porosity of the sample was 0.24. Accounting for the initial moisture content in the sample was done by factoring the estimated moisture content of 0.02 to 0.04 for the < 100 mm material by the fraction of the large-scale material < 100 mm. Using the large-scale grain size distribution, about 50% of the material was < 100 mm, so the initial moisture content at the large-scale was 0.01 to 0.02. The porosity of the waste rock at the large-scale was therefore estimated 0.25 to 0.26.

Saturated hydraulic conductivity ( $K_{\text{sat}}$ ) was estimated by conducting constant head tests while using the 16.0 m<sup>3</sup> permeameter (Figure C10b). A 200 L barrel provided a constant head for the supply of water to the base of the waste rock sample for two trials. To apply a higher flow rate, water was pumped directly into the sample, from the bottom, for three trials. Flow was upwards and was measured with a graduated bucket and a stop watch at the upper drain. The difference in head through the 1 m thick waste rock sample was measured as the average head at three manometers, screened at the bottom of the waste rock, and the head over the top of the sample, which was set by the spillway of the upper drain. The head difference was on the order of a few millimeters. To minimize the error in the head measurement due to slack in the water level tape, the manometers were cut short so that the measurement was made at a section of measuring tape fixed to the rigid metal housing of the needle that senses the water level. The very small difference in head measured across the depth of the sample introduced uncertainty to the measurement. Furthermore, the flow rate through the sample was about the same when supplied by a ½ horsepower pump and a 5 horsepower pump. This suggests that the screened PVC at the lower drain (Figure C.9a, b) may have limited the maximum flow rate, and may therefore have limited the conductivity measurement. Williams (1981) found that well screens with open area less than 3 to 5% of the well wall area limit the water flow. The slotted PVC at the lower drain of the permeameter consisted of three areas of slots around the circumference with slots 1 to 2 mm wide spaced at about 1 cm intervals along the length of the standpipe. The open area of the slotted drain screen was estimated 3 to 7% of the well wall area. Therefore the saturated hydraulic conductivity of the 16.0 m<sup>3</sup> waste rock sample was at least  $1 \times 10^{-2}$  m/s.



**Table C.4** Results from permeameter tests with a 16.0 m<sup>3</sup> sample.

		<b>Trial 1 *</b>	<b>Trial 2 *</b>	<b>Trial 3 **</b>	<b>Trial 4 #</b>	<b>Trial 5 #</b>
Q measurement (m <sup>3</sup> /s)	1	9.0E-05	9.8E-05	2.5E-04	2.4E-04	2.6E-04
Q measurement (m <sup>3</sup> /s)	2	7.1E-05	1.0E-04	3.1E-04	1.3E-04	2.6E-04
Q average		8.0E-05	1.0E-04	2.8E-04	1.8E-04	2.6E-04
dh at manometer a	1	1	3	3	2	
dh at manometer b	4	3	2	1	2	
dh at manometer c	2	0	0	2	0	
dh average		2.3	1.3	1.7	2.0	1.3
dh/dL		0.0023	0.0013	0.0016	0.0019	0.0013
<b>K<sub>sat</sub></b>		<b>2.3E-03</b>	<b>5.0E-03</b>	<b>1.1E-02</b>	<b>6.1E-03</b>	<b>1.3E-02</b>

dh is the difference in head measured at the top and bottom of the sample  
waste rock sample thickness (dL) and area orthogonal to flow (A):

dL (mm) 1030  
A (m<sup>2</sup>) 15.5

\* Flow supplied by head 0.9 m above sample water level

\*\* Flow supplied by 1/2 horsepower pump

# Flow supplied by 5 horsepower pump

The drain-down of the 16.0 m<sup>3</sup> waste rock sample was monitored to estimate the portion of the porosity that is significantly affected by capillary forces. A rhodamine dye tracer was applied to the surface of the sample in two locations above the lower drain to determine the average flow velocity and fastest flow velocity through macropores under

saturated conditions. During the drain-down test, the water level was monitored at one of the manometers near the lower drain of the 16.0 m<sup>3</sup> permeameter using a Solonist water level tape, and the outflow was measured with a graduated 20 L bucket and watch with a digital seconds reading (generally at every 10 L of outflow). Cumulative volume drained was derived by summing the 10 L increments of outflow measured. Figure C.11 shows the falling water level and outflow rate drained during the test. A rapid decrease in the outflow rate occurred after the waste rock became unsaturated because additional time was required to drain the clean crushed rock below the waste rock. The outflow rate was limited by the outflow plumbing, which included ½ in. tubing, to allow accurate detection of the time when the sample drained and to allow sampling for dye tracer transport in a practical manner. The water level in the waste rock dropped below the point measurable using the water level tape in the manometer after 5.03 hours (Figure C.12a). This point was 8 cm above the base of the waste rock. The time that the water level reached the base of the waste rock was determined by quadratic regression of the water-level data to be 5.66 h after the start of the test. At that time, the cumulative water drained from the sample was 2900 L.

The volume of water that drained rapidly (2900 L) was 75% of the total porosity. This portion of the total volume represents the rapidly-draining contribution of the specific yield from large pores, where little capillarity exists, and from the small pores, where capillarity is more significant. For comparison, 30 to 35% of the porosity of a soil with a similar grain size distribution as the < 5 mm fraction of the waste rock (a loamy sand) would drain rapidly (in 5 to 10 h) (Nachabe 2002). The remaining 25% of the total waste rock pore water was significantly retained by capillary forces. This portion of the

porosity was greater than the field capacity of the matrix (since drainage continued slowly after the end of the rapid drain-down) and less than the porosity of the matrix. The porosity of the matrix was the portion of the total porosity that was retained plus the portion of rapidly-drained water that may have drained from the matrix. Based on the portion of a loamy sand that drains rapidly, the porosity of the matrix may be 30 to 35% greater than the volume retained in the 16.0 m<sup>3</sup> permeameter. The porosity of the matrix was therefore estimated 6% of the total waste rock volume (25% x total porosity = 6%) to 8% of the total waste rock volume ((25% + 33% of 25%) x total porosity = 8%). A matrix porosity 25 to 33% of the total volume of the waste rock was qualitatively consistent with the grain size distribution of a 40 m<sup>3</sup> waste rock sample (Figure C.5a) that had 15 to 30% matrix material, depending upon the size definition of the term matrix.

The drainage was sampled to analyze the transport of a rhodamine dye tracer through the 1.03 m thickness of the saturated waste rock sample. The dye used was 40% rhodamine WT in methanol. 25 mL of rhodamine was applied to the top surface of the saturated waste rock at two locations, each about 50 cm from one another, at the start of the drain-down of the waste rock. Tracer was applied at one location that consisted of some fine-grained material and at another location that consisted of very little fine-grained material to ensure connection with rapidly-draining water. Tracer was observed in the first sample, which was taken 6 minutes after the start of the drain-down (Figure C.12b). The concentration of the tracer in each sample, relative to the maximum outflow tracer concentration, was determined using a Hach DR/2400 photospectrometer. A maximum absorbance of 0.36 in one of the samples was obtained with a beam wavelength of 557 nm. Beer's law describes absorbance of light by a substance as:

$$A = \epsilon l C , \quad (3)$$

where  $A$  is the absorbance,  $C$  is the concentration of the substance absorbing a portion of the photospectrometer beam,  $\epsilon$  is the specific absorptivity of that substance, and  $l$  is the path length of the light through the sample containing the substance. Since the specific absorptivity and path length were the same for all samples,

$$C_n / C_{\max} = A_n / A_{\max} . , \quad (4)$$

where  $C_n/C_{\max}$  is the concentration of the rhodamine dye in the  $n^{\text{th}}$  sample relative to the maximum concentration of the dye sampled and  $A_n/A_{\max}$  is the absorbance measured in the  $n^{\text{th}}$  sample relative to the maximum absorbance measured in the samples.

For an instantaneous slug introduction of the rhodamine dye into a saturated groundwater flow system, the maximum concentration of the dye would have transported by advection are transported at the average flow velocity. The maximum relative concentration of rhodamine drained from the 16.0 m<sup>3</sup> at an elapsed time of 1.0 h (Figure C.12b). At that point in the drain-down test, only the upper 15% of the sample had drained. Most of the dye was therefore transported well in advance of the dropping phreatic surface. Rhodamine transported to the base of the 1.03 m thick waste rock sample at a maximum velocity of 10 m/h and an average velocity of 1 m/h under essentially saturated conditions, relative to the conditions of flow in unsaturated waste rock piles. Because the flow velocity was limited by the plumbing of the permeameter drain (1/2" tubing to direct the flow through a flow gauge), the tracer test results are best considered as a relative measurement. Water moved through the most permeable flow paths 10 times faster than water flowing at the average velocity, at saturated conditions. For saturated waste rock this implies that dispersion is significant, even in only the most

permeable portion of the media. For unsaturated waste rock piles, this suggests that at a 1 m scale continuous macropore flow paths may exist, but macropore and matrix interaction appears to be significant. However, repetition of this experiment in waste rock with angle of repose deposition and comparison with tracer transport in homogenous porous media with consistent experimental design, would offer more quantitative results.

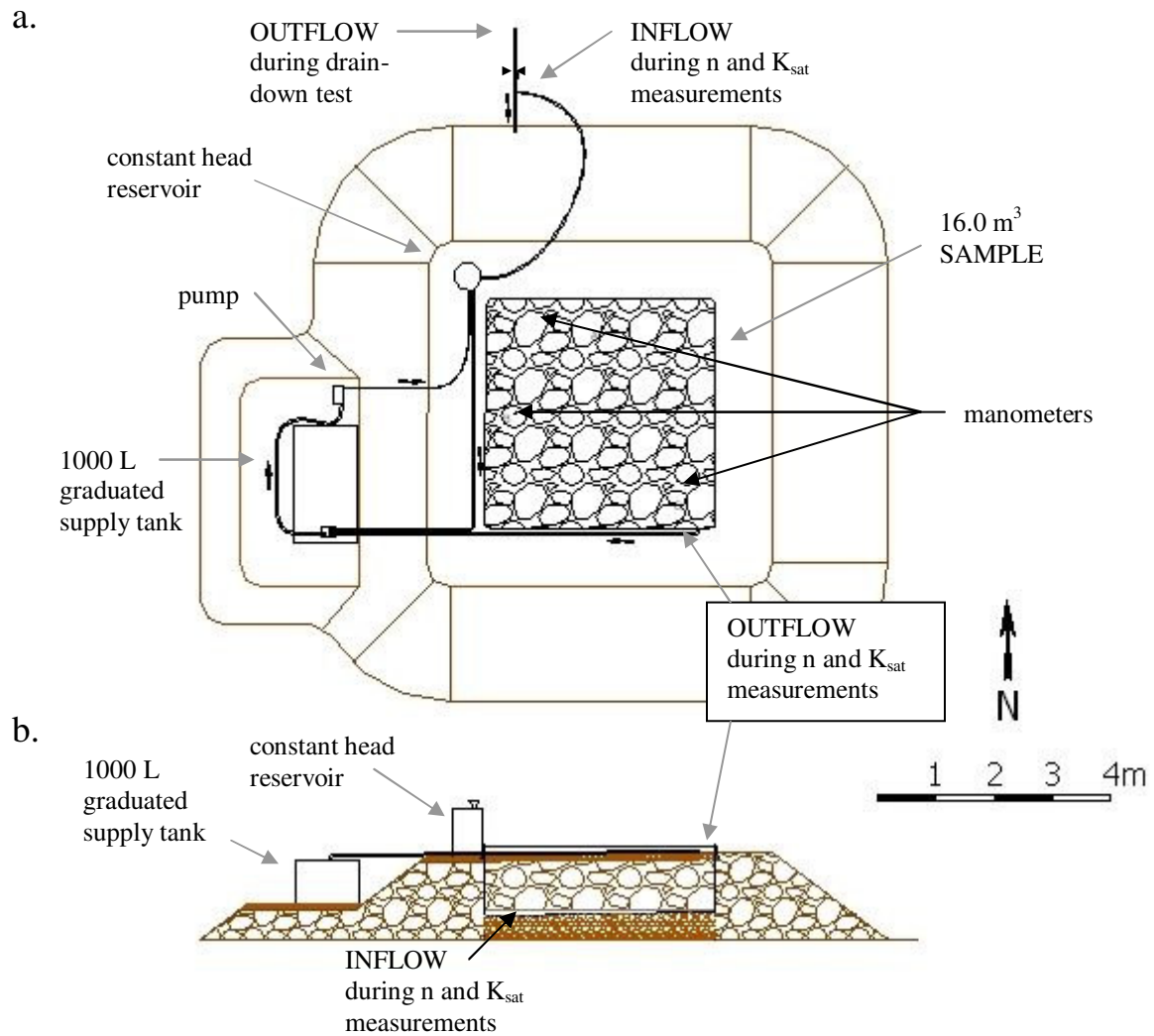


**Figure C.8** (a) Plan view and (b) cross section of the 16.0 m<sup>3</sup> permeameter used to estimate REV-scale hydraulic parameters of the waste rock.

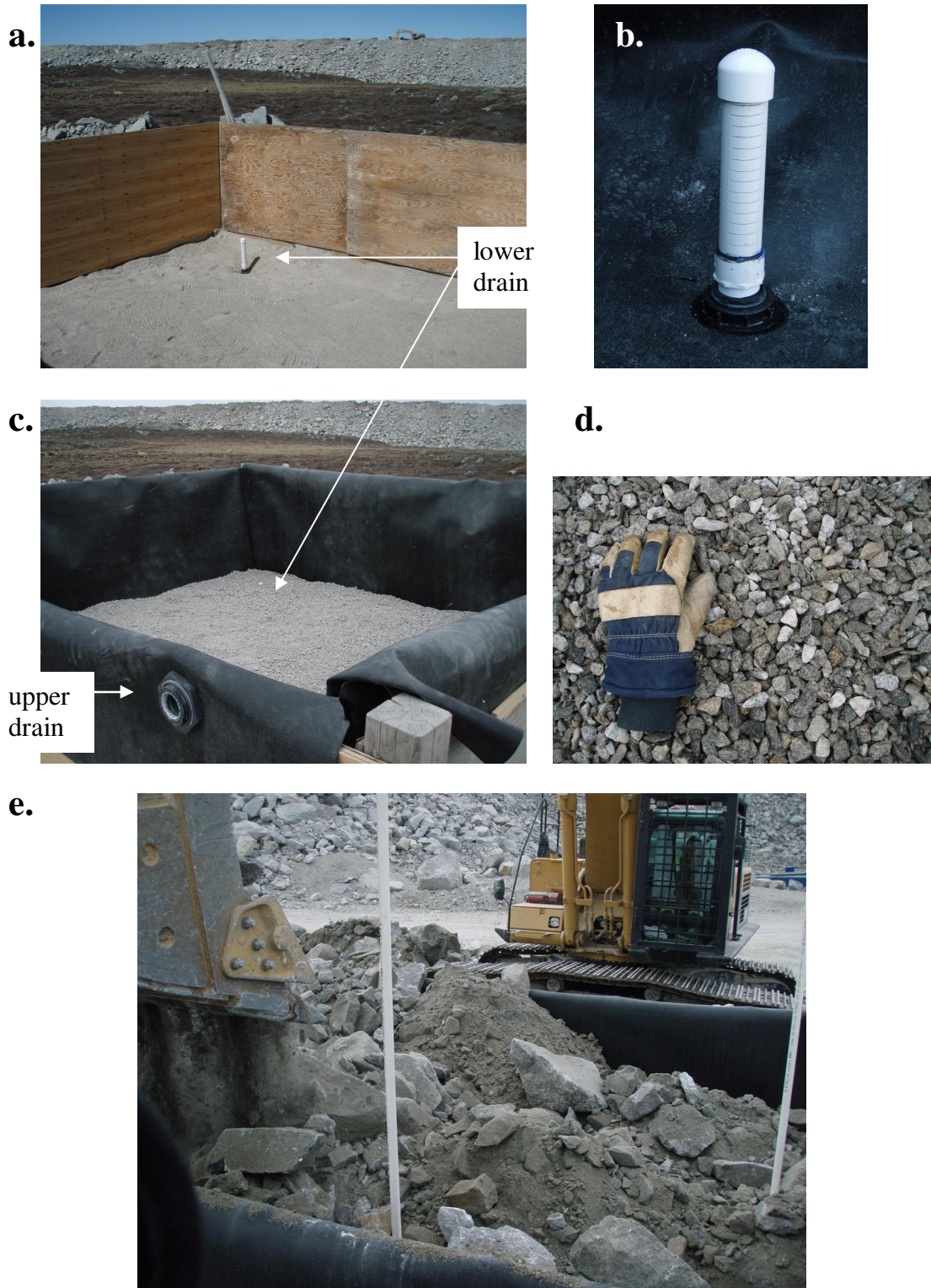
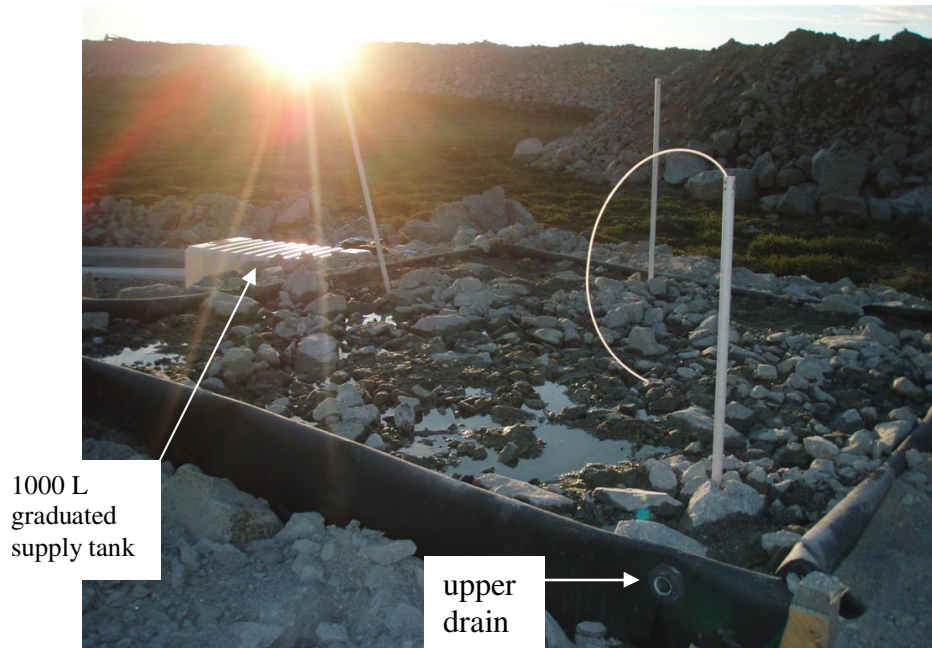


**Figure C.9** Construction of the 16.0 m<sup>3</sup> permeameter: (a) graded sand base, (b) screened lower drain sealed to HDPE liner, (c) clean crush layer, (d) detail of the clean crush, and (e) waste rock loaded into the permeameter.

a.



b.

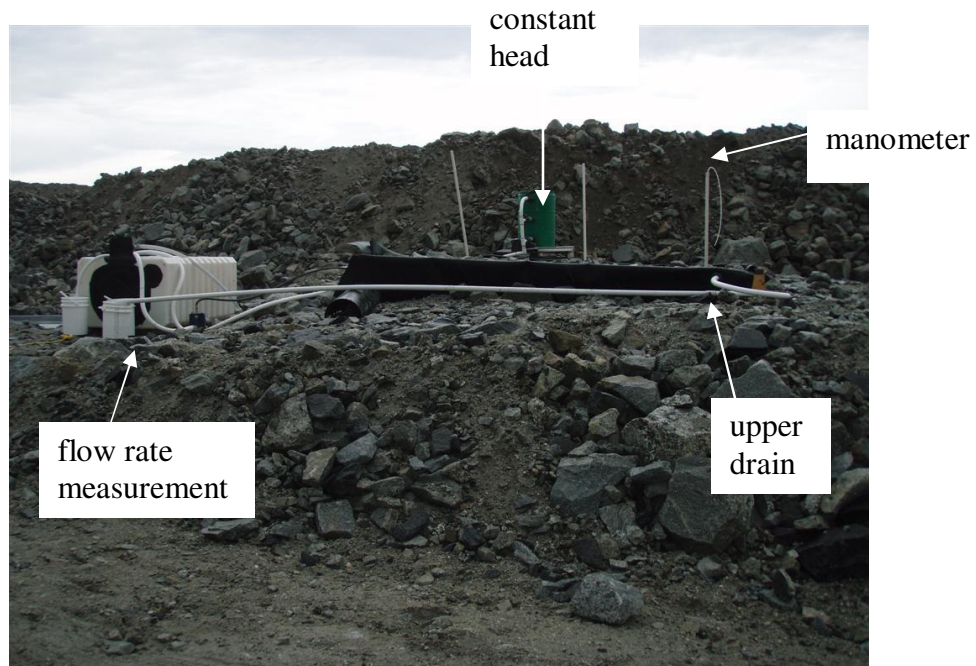


**Figure C.10** Hydraulic testing of a 16 m<sup>3</sup> waste rock sample: (a) Porosity was measured by pumping water from a graduated tank into the sample to the spillway at the upper drain. (b) Saturated hydraulic conductivity was measured by conducting a constant head test.

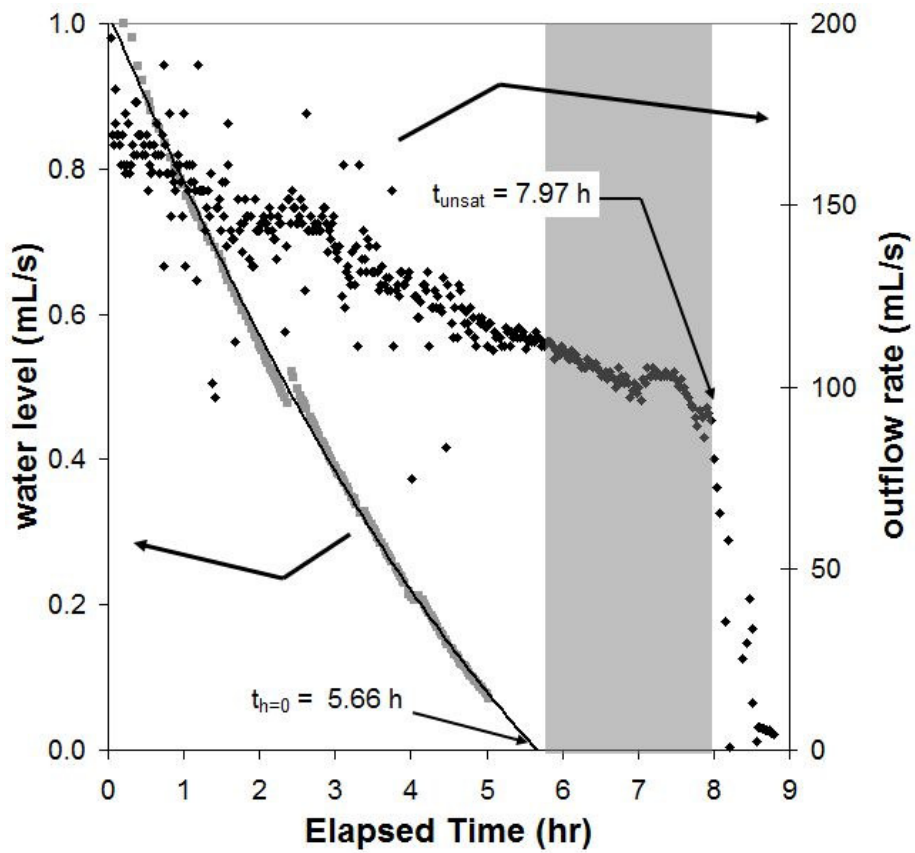
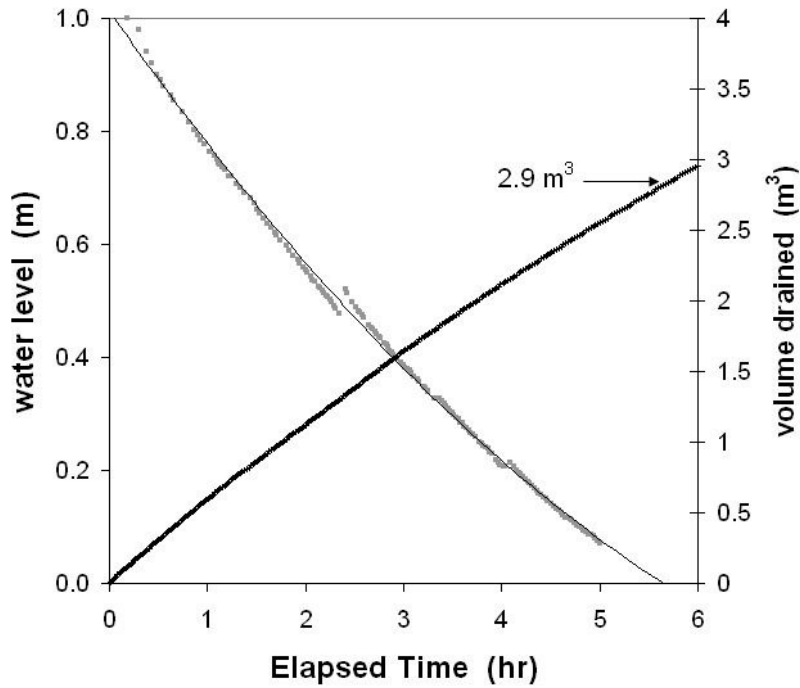


**Figure C.11** Results from the drain-down test conducted with the 16 m<sup>3</sup> sample. The gray portion of the plot indicates the time when the clean crushed rock below the waste rock was draining.

a.



b.

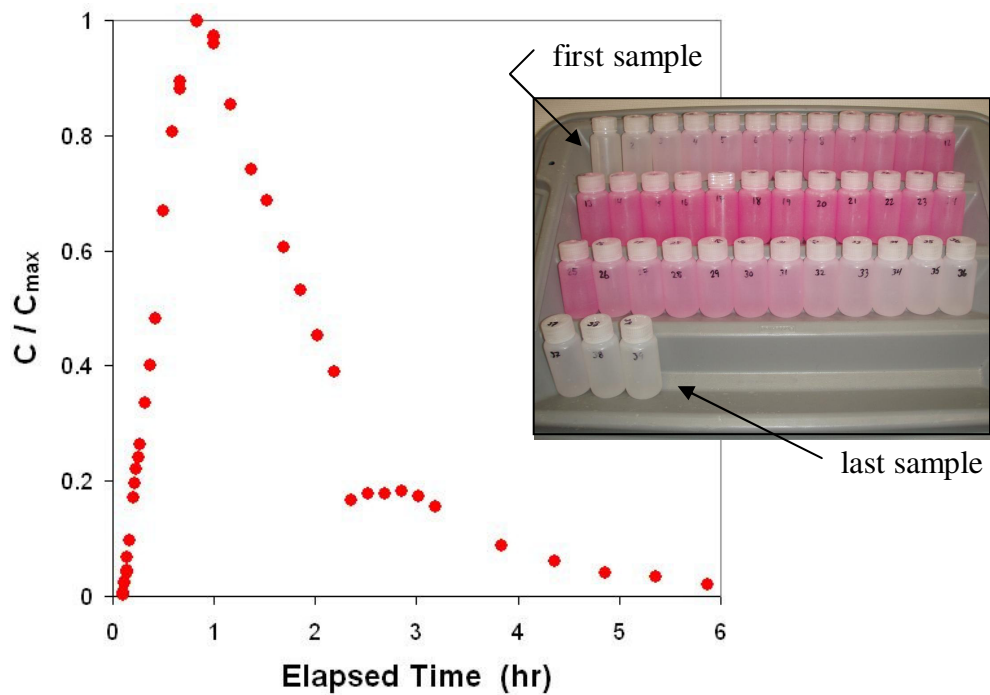


**Figure C.12** Hydraulic testing of a 16 m<sup>3</sup> waste rock sample: (a) Cumulative volume of water drained from the 16 m<sup>3</sup> waste rock sample. After 5.67 hours, the full depth of the sample became unsaturated and 2.9m<sup>3</sup> water, 75% of the total waste rock pore water, had drained. (b) Dye tracer relative concentration in the drainage.

### C.3 Laboratory permeameter tests

The saturated hydraulic conductivity of 18 waste rock matrix material samples was measured using laboratory permeameter tests. Waste rock matrix samples were collected from the Type 1 test pile, the Type 3 test pile, and the Upper Collection Lysimeters during the construction of the test piles using the methods described in Section C.1.3. The samples were sieved to 5 mm. The permeameters used were columns with a cross-sectional area of  $36 \text{ cm}^2$  (6.8 cm diameter) and the length of the sample ranged from 9 cm to 23 cm (Figure C.13). Constant head tests were conducted so that upward flow through the sample was driven by a hydraulic gradient of 0.08 to 0.5, set by adjusting the height of the water level in the Mariotte constant head vessel, relative to the longitudinal length of the sample ( $L$ ). In the tests, the hydraulic gradient through the sample was measured as the difference in head between the point measured with a manometer ( $h_1$ , near the bottom of the sample, though the head level itself is near the level set by the Mariotte vessel) and the head at the top of the waste rock ( $h_2$ , the level of the water at the outflow from the column), divided by the length of the waste rock sample from the manometer sample point and the top of the waste rock sample. Flow rate was measured at the outflow from the permeameter at the top of the sample using a graduated cylinder and a stopwatch. Three trials were conducted on each sample, each with a different gradient applied. Hydraulic conductivity was calculated using Darcy's law. Table C.5 lists the results from the tests.

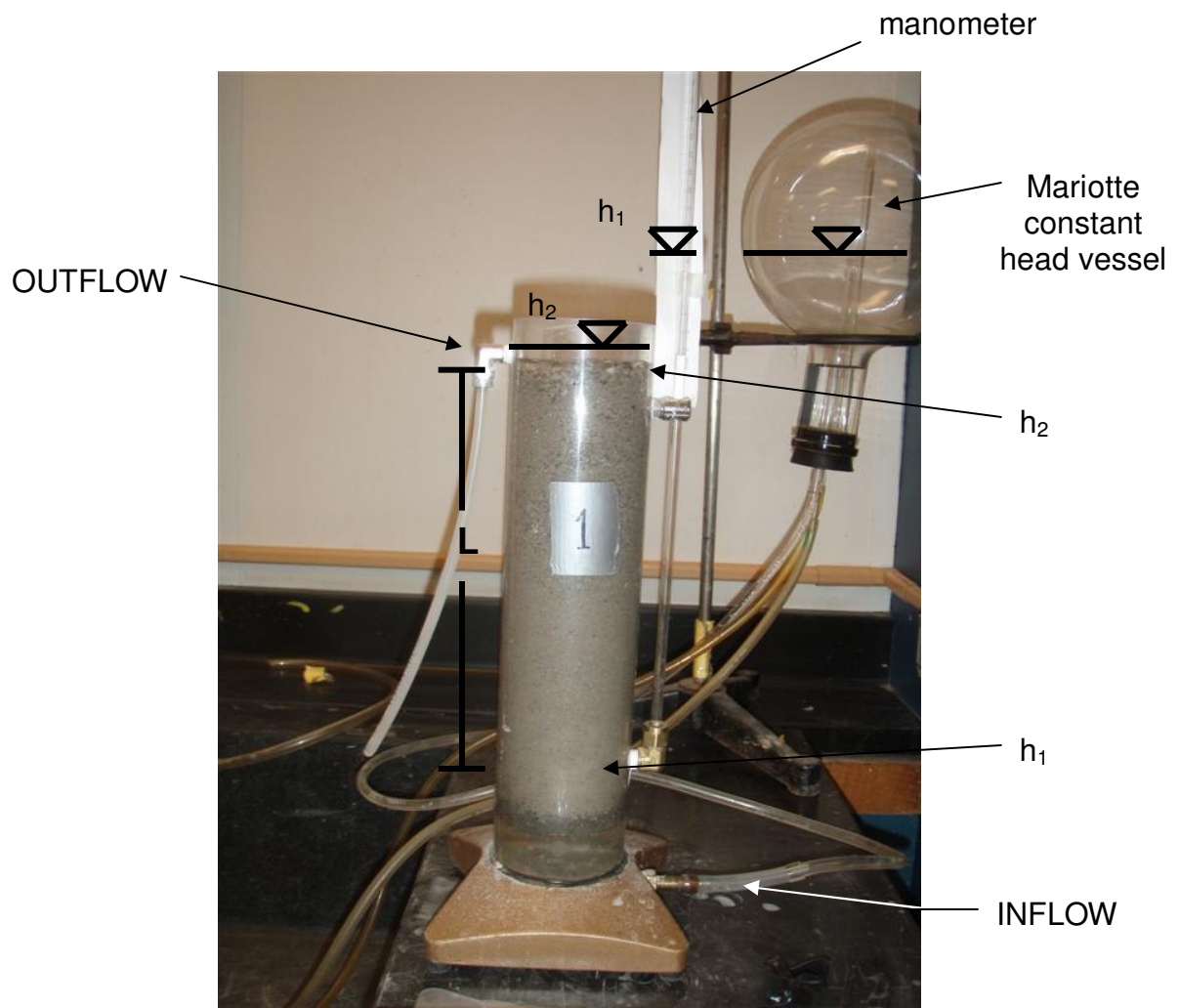


**Figure C.13** A constant head permeameter test conducted to measure the saturated hydraulic conductivity of a waste rock matrix sample taken during construction of the test piles.

**Table C. 5** Results from constant head permeameter tests conducted on the < 5mm fraction of waste rock hand samples.

Sample Name	Location	Packed dry bulk density g/cm <sup>3</sup>	D <sub>20</sub> * µm	Hydraulic Gradient			Flow Rate			Saturated Hydraulic Conductivity			Average Hydraulic Conductivity m/s
				Trial 1	Trial 2	Trial 3	Trial 1	Trial 2	Trial 3	Trial 1	Trial 2	Trial 3	
				-	-	-	mL/min	mL/min	mL/min	m/s	m/s	m/s	
192421	T3 Top	1.66	130	0.37	0.15	0.55	0.25	0.08	0.42	3.2E-06	2.4E-06	3.6E-06	<b>3.1E-06</b>
192410	T3 Top	1.73	140	0.31	0.21	0.56	0.32	0.15	0.59	5.0E-06	3.4E-06	5.0E-06	<b>4.5E-06</b>
189867	T3F1	1.52	150	0.59	0.42	0.09	0.66	0.45	0.10	5.6E-06	5.5E-06	5.6E-06	<b>5.6E-06</b>
190279	T3F2	1.45	-	0.39	0.25	0.09	1.42	1.31	0.47	1.8E-05	2.5E-05	2.5E-05	<b>2.3E-05</b>
191170	T3F3	1.52	170	0.53	0.33	0.09	1.35	0.78	0.21	1.2E-05	1.1E-05	1.2E-05	<b>1.2E-05</b>
191948	T3F5	1.69	210	0.18	0.09	0.46	1.39	0.46	3.20	3.7E-05	2.4E-05	3.3E-05	<b>3.1E-05</b>
189338	T3 Base	1.56	140	0.25	0.13	0.38	0.15	0.11	0.43	2.8E-06	4.0E-06	5.5E-06	<b>4.1E-06</b>
070627_01	T1 top	1.61	120	0.18	0.25	0.30	0.12	0.21	0.34	3.2E-06	3.9E-06	5.3E-06	<b>4.1E-06</b>
070627_02	T1 top	1.57	130	0.17	0.29		0.05	0.16	0.00	1.4E-06	2.5E-06		<b>2.0E-06</b>
070627_03	T1 top	1.56	120	0.13	0.29	0.26	0.06	0.19	0.14	2.3E-06	3.1E-06	2.6E-06	<b>2.6E-06</b>
190263	T1F1	1.51	240	0.11	0.21	0.38	0.50	0.63	2.52	2.1E-05	1.4E-05	3.2E-05	<b>2.2E-05</b>
190275	T1F1	1.56	160	0.08	0.16	0.26	0.71	0.54	1.01	4.2E-05	1.6E-05	1.9E-05	<b>2.6E-05</b>
190665	T1F2	1.59	220	0.18	0.31	0.47	0.84	1.80	1.87	2.3E-05	2.8E-05	1.9E-05	<b>2.3E-05</b>
191480	T1F3	1.72	200	0.54	0.26	0.12	0.72	0.28	0.16	6.3E-06	5.1E-06	6.4E-06	<b>5.9E-06</b>
191482	T1F3	1.66	160	0.19	0.12	0.37	1.47	0.24	1.38	3.7E-05	9.4E-06	1.8E-05	<b>2.1E-05</b>
192176	T1F4	1.54	180	0.14	0.25	0.35	0.49	0.91	1.38	1.7E-05	1.8E-05	1.9E-05	<b>1.8E-05</b>
Upper Lys 2	T1	1.47	140	0.24	0.11	0.42	0.66	0.45	0.10	1.3E-05	2.0E-05	1.1E-06	<b>1.1E-05</b>
Upper Lys 4	T3	1.57	130	0.25	0.12	0.43	0.22	0.16	0.51	4.0E-06	6.0E-06	5.7E-06	<b>5.2E-06</b>
Geometric Mean of the T3 samples												<b>7.8E-06</b>	
Geometric Mean of the T1 samples												<b>9.7E-06</b>	
Geometric Mean of all samples												<b>8.8E-06</b>	

\* D<sub>20</sub> is the maximum particle size of the finest 20% of the sample.

#### **C.4 Ring infiltrometer tests**

Ring infiltrometer tests were conducted at the top of the Type 3 test pile to determine the infiltration capacity of the surface. The infiltration capacity of a surface is the flux at which ponding and runoff begins. Infiltration capacity varies at a single location primarily due to the dependency of permeability and soil suction on moisture content, and infiltration capacity for non-vegetated surfaces varies from one location to another primarily due to variation in intrinsic permeability of the ground surface (Loague and Gander 1990, Bellehumeur 2001). The infiltration capacity of a surface is usually high at the beginning of rainfall, but declines to a steady state infiltration capacity (Dingman 2002, p. 245). The tests conducted at the top of the Type 3 test pile were done to determine the steady state infiltration capacity.

Single ring infiltrometers with a 90 cm diameter were used to measure infiltration capacity of the waste rock surface over an area as large as could be efficiently tested. Double ring infiltrometers are typically used in natural soils to limit lateral flow under the edge of the ring, which causes an overestimation of the vertical infiltration. Bower (1986) found that lateral flow has a negligible effect on the infiltration measurement for rings with a diameter larger than 30 cm. Bellehumeur (2001) found lateral flow to be insignificant for ring infiltrometer tests conducted at the top surface of a waste rock pile using 58 cm diameter rings by excavating to a depth of 50 cm to analyze the flow path of rhodamine dye used in the tests.

Rings were fabricated by cutting scrap culvert sections with a welding torch into 30 cm high cylinders. The test procedure followed that of Bellehumeur (2001) and Loague (1990). Figure C.15 illustrates the procedure for installation and operation of the ring

infiltrometers on a waste rock surface. Attempts at driving the rings into the waste rock surface with a sledge hammer failed due to the coarse nature of the material. The rings were set into the surface to a typical depth of 1 cm by twisting the ring under the weight of one or two people. During installation, some rocks dislodged under the ring were removed. The disturbed material was limited to the area within about 5 cm of the ring. This material was compacted around the inside and outside edge of the ring. Some trials found that compacted waste rock alone was insufficient to seal the ring to the ground surface. A bentonite clay paste was used to seal the outside edge of the ring to the ground surface in all cases, and the inside edge of the ring except where infiltration was less than about 5 mm/h or less. At lower infiltration rates bentonite flocculation and deposition at the surface was observed, and the test site was abandoned. The bentonite seal performed best when left to dry after application, and rewetted and compacted into the ground surface prior to the test. During preparation of the rings, the ground surface at the outside of the ring was thoroughly wetted to reduce lateral flow during the test.

Rings were filled to an average depth of 5 cm using a 1000 gal water tank and a hose with a valve at the outflow, a system that enabled several tests to be run simultaneously. Water filling the ring was deflected with the lid of a bucket to minimize surface disruption (Figure C.15g). A tape measure was fixed to the inside of each ring for manual measurement of the water level drop during the test. For most tests, when the water level dropped to the bottom of the tape measure, the test was continued by refilling the ring. Several tests failed due to leakage under the ring to adjacent topographic lows. The results from these tests are omitted in the analysis. Photographs of the waste rock surface at each ring before the test was conducted are shown in Figure C.16. The results

from the tests are plotted in Figure C.14 and summarized in Table C.6. Although the surface of the test pile was excavated to access the instrumentation leads, the ring infiltrometer results show a relationship of lower infiltration capacity at the middle of test pile surface, where the haul-truck and bulldozer traffic was highest.

**Table C.6** Results from single ring infiltrometer tests conducted at the top of the Type 3 test pile.

Ring number	Approximate location	Steady state infiltration capacity			Sorptivity
		mm/m	mm/h	m/s	mm/min <sup>1/2</sup>
4 *	F1 center	0.04	2	6.5E-07	0.6
3	F2 center	0.08	5	1.3E-06	0.6
2	F3 center	0.09	5	1.5E-06	0.7
1	F4 center	0.26	16	4.3E-06	1.4
5	F5 center	1.24	74	2.1E-05	6.5
6	F2 7m N	0.92	55	1.5E-05	4.5
7	F2 7m S	0.43	26	7.2E-06	3.1
geometric mean **		0.44	26	5.E-06	2.5
standard deviation **		0.47	28	8.E-06	2.3
standard error (%) **		107	107	153	93

\* Ring was located on a moderate traffic surface. All other rings located on a waste rock surface that was excavated a year before the tests were conducted.

\*\* calculated for all rings except number 4

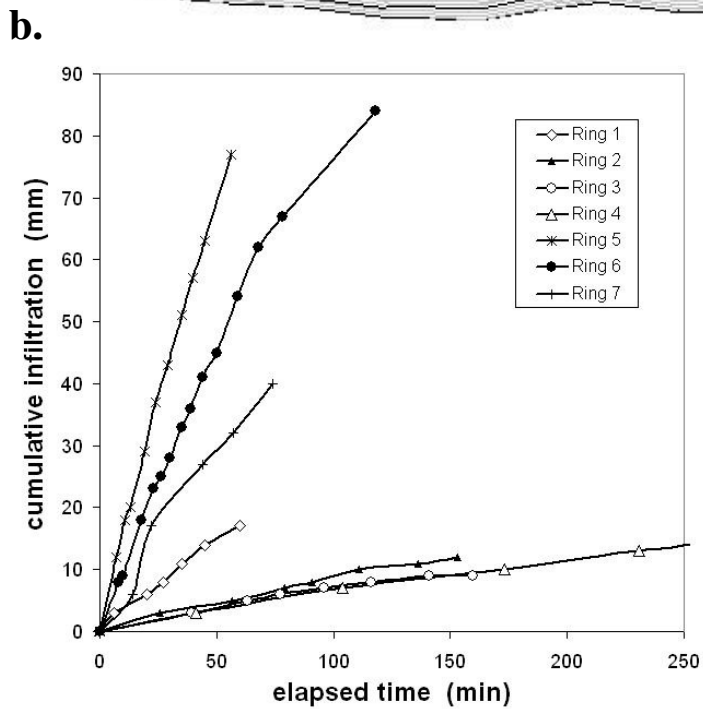
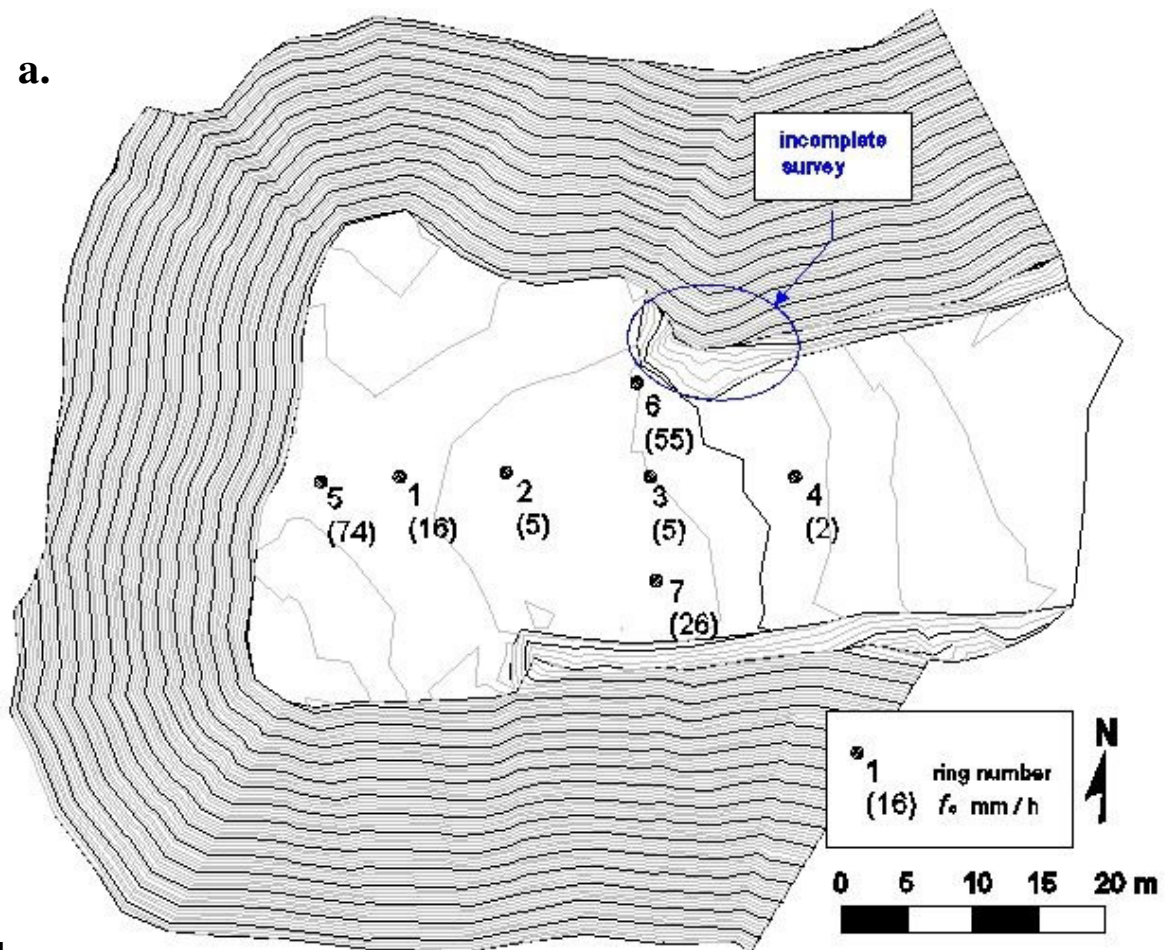


**Figure C.14**

(a) Results of the ring infiltrator tests conducted at the top of the Type 3 test pile:  $f_c$  is the steady state infiltration capacity in mm/h.

(b) Measurements made during the ring infiltrator tests, in terms of cumulative infiltration.

**Ring 1**  $4.3 \times 10^{-6}$  m/s



**Ring 2**  $1.5 \times 10^{-6}$  m/s



**Ring 3**  $1.3 \times 10^{-6}$  m/s



**Ring 4**  $6.5 \times 10^{-7}$  m/s



**Figure C.15** Ring infiltrometry tests (part 1): rings 1, 2, 3, and 4. Continued next page.

**Ring 5**

$2.3 \times 10^{-5}$  m/s



**Ring 6**

$1.5 \times 10^{-5}$  m/s



**Ring 7**

$7.2 \times 10^{-6}$  m/s



**Figure C.15 (continued)** Ring infiltrometry tests (part 2): rings 5, 6, and 7.

**a.**



**b.**



**c.**



**d.**



**Figure C.16** Ring infiltrometry procedure (part 1): (a) The ground surface before ring installation, (b) installation by twisting under pressure, (c) compaction of the material around the ring, (d) the outside of the ring sealed to the ground surface with bentonite clay. Figure continued on next page.

e.



f.



g.



h.



**Figure C.16 (continued)** Ring infiltrometry procedure (part 2): (e) the inside of the ring sealed if necessary, (f) ground surface around the ring thoroughly wetted, (g) ring filled with water to a depth of about 5 cm without disturbing the surface, and (h) the infiltration rate was monitored with a fixed tape measure and a watch. Additional water was added as needed, and the test proceeded until equilibrium infiltration rate was reached.

## C.5 Water retention curves

### C.5.1 Tempe cell tests

Water retention curves were estimated for five samples of the matrix material from the Type 3 test pile using Soil Moisture Corp. Model 1405 Tempe Pressure Cells. A Tempe cell test determines the moisture content of a porous material at various applied suctions. The tests were conducted using the method described by Fredlund and Rahardjo (1993) and by Soil Moisture Corp. (1995). Waste rock samples were collected using the methods described in Section C.1.3. The samples were split using a riffle splitter and sieved to 5 mm. Yazdani *et al.*, 2000 found that the fraction of waste rock coarser than 5 mm does not have a significant effect on water retention in waste rock. About 200 g of waste rock matrix material (finer than 5 mm) was packed into a 6.4 cm diameter cylinder to a height of 3.1 +/- 0.1 cm atop a saturated porous ceramic plate (Figure C.17). Each sample was packed to a bulk density of 1.7 +/- 0.05 g/cm<sup>3</sup>. The sample was fully saturated inside the cylinder, and the cylinder was sealed between the top and bottom caps.

In the first part of the test, a head difference was applied across the sample with a difference in gravitational potential ( $z_1 - z_2$ ) (Figure C.18). A head difference was applied by gravitational potential while maintaining atmospheric pressure inside the Tempe cell and inside the drainage bottle. Hydraulic connection was maintained between the sample and the drainage bottle by means of a saturated porous ceramic plate, tubing, and a needle through a septum. The ceramic plate used had an air entry pressure of 1 b (100 kPa), which caused it to remain saturated throughout the test. Care was taken so that the air bubbles were not able to form an air gap in the tubing connected to the porous

at any time. The head difference was maintained for at least 24 hours to allow pressure equilibrium between the waste rock sample and the porous disk to establish. The moisture content was measured gravimetrically after equilibrium was established for each increment in head difference by weighing the entire Tempe cell and subtracting the mass of the cell and the oven-dried soil (measured at the end of the test).

The second part of the test, conducted for suction greater than 10 kPa, followed the procedure described by Soil Moisture Corp. 1995. The drainage bottle and the Tempe cell were kept at the same elevation while a pressure difference was applied by maintaining atmospheric pressure in the drainage bottle and a higher pressure in the Tempe cell. Compressed gas was delivered to the top valve of each Tempe cell through a pressure regulator and a manifold. Pressure transducers vented to the atmosphere read the pressure in the Tempe cell. For each pressure difference applied across the sample, equilibrium was allowed to be established in the waste rock sample. The moisture content was then measured gravimetrically as described above. The suction range of the test was limited to 100 kPa by the air entry pressure of the porous ceramic disk. After completion of the tests, each waste rock matrix sample was oven-dried for over 48 hours and the material was weighed. Each Tempe cell was weighed without the sample, in conditions consistent with those during the tests, which included moisture condensation on the wall of the cell, saturated porous disc, and tubing full of water.

The measurements from the Tempe cell tests are plotted in Figure C.19. The data were fit to the van Genuchten (1980) water retention function with the Mualem (1976) assumption applied using the Soil Vision software (Fredlund *et al.*, 1996):

$$\theta = \theta_r + \frac{(\theta_s - \theta_r)}{[1 + (\alpha\phi)^n]^{1-\frac{1}{n}}}, \quad (5)$$

where  $\theta$  is the volumetric moisture content ( $\text{m}^3/\text{m}^3$ ),  $\theta_r$  is the residual moisture content,  $\theta_s$  is the moisture content at saturation (the porosity),  $\alpha$  is a curve fitting parameter ( $\text{kPa}^{-1}$ ) related to the air-entry pressure,  $\phi$  is the hydraulic potential expressed as tension (kPa), and  $n$  is a dimensionless curve fitting parameter related to the maximum slope of the curve. The water retention curve parameters for each waste rock matrix sample are listed in Table C.7.

### C.5.2 *Field water retention curves*

A water retention curve was also estimated at a location 60 cm below the ground surface between the two T3 upper collection lysimeters (Figures A.19 and A.23). The curve was constructed using simultaneous measurement of moisture content with an ECH2O probe and hydraulic potential with a tensiometer and tension gauge. The tensiometer porous cup was installed about 20 cm laterally from the ECH2O probe in a 60 cm-diameter borehole backfilled with waste rock (Figure B.7 and B.8). The wetting curve plotted in Figure C.19 was developed with measurements made every 30 minutes during a 60 hour period in which the wetting front from the August 4, 2007, applied rainfall event approached the sensors. The drying curve plotted in Figure C.19 was made with measurements from a drying period from August 7 to August 21, 2007, and from a drying period from October 3 to October 7, 2007.

## C.6 Unsaturated hydraulic conductivity

### C.6.1 Estimation from the water retention curve

Estimation of the unsaturated hydraulic conductivity function from the range of water retention curves measured in waste rock samples in the lab and with sensors in the field was done using the relationship derived by van Genuchten (1980):

$$K_r(\varphi) = \frac{\left\{1 - (\alpha\varphi)^{1-n} \left[1 + (\alpha\varphi)^n\right]^{\frac{1}{n}-1}\right\}^2}{\left[1 + (\alpha\varphi)^n\right]^{\frac{1-\frac{1}{n}}{2}}}, \quad (6)$$

where  $K_r(\varphi)$  is the relative hydraulic conductivity [ $K_r(\varphi) = \cdot K_{sat} / K(\varphi)$ ],  $\varphi$  is the hydraulic potential expressed as tension (kPa),  $\alpha$  is a water retention curve fitting parameter ( $\text{kPa}^{-1}$ ) related to the air entry pressure, and  $n$  is a dimensionless water retention curve fitting parameter related to the slope of the water retention curve. This estimation was done using Soil Vision software (Fredlund *et al.*, 1996).

### C.6.2 Field calibration of the unsaturated hydraulic conductivity

The range of unsaturated hydraulic conductivity functions determined for the Diavik test piles site, using Equation 6, was about three orders of magnitude in  $K(\varphi)$  for any value of  $\varphi$  observed in the field (Figure C.20). This range yields great uncertainty in estimates of groundwater flux calculated from tensiometer profiles (Figure C.21) and therefore warrants field calibration. Figure C.21 shows flux calculated using Darcy's Law, by multiplying the unsaturated hydraulic gradient measured at tensiometer profiles by the  $K(\varphi)$  evaluated at the average of the tension at the two tensiometers using two  $K(\varphi)$  curves developed using Equation 6. In the figure, the flux is compared to, in a(i) and b(i), the outflow flux at the lysimeter and in a(ii) and b(ii) the cumulative infiltration (the time

integral of the flux) is compared to the cumulative rainfall. The flux and cumulative infiltration calculated at the tensiometer profiles were low (Figure C.21a) relative to lysimeter outflow flux and rainfall using the  $K(\phi)$  curve using Equation 6 and the T3F3 WRC, and were high (Figure C.21b) relative to outflow flux and rainfall using Equation 6 and the field WRC. A method for field calibration of the unsaturated hydraulic conductivity was developed to improve flux calculations and to upscale the  $K(\phi)$  estimate to the 1 to 2 m-scale.

The field calibration was guided by the principle that for flow that is not focused into channeled pathways (i.e. for Richard's equation-type flow), the flux should be less than or equal the rainfall rate at all locations. The Green-Ampt model for infiltration was used to relate rainfall rate to infiltration rate, and Darcy's law was used to relate the infiltration rate to the unsaturated hydraulic conductivity. First, the condition observed at the upper collection lysimeters is considered, where significant ponding was never observed at the ground surface during high-intensity rainfall events. From Dingman 2002, for  $t_0 < t < t_w$ :

$$\text{if } w < K_{sat}, \quad \text{then } f(t) = w, \quad (7)$$

where  $w$  is the rainfall rate,  $f(t)$  is the infiltration rate, and  $t_w$  is the time at the end of the rainfall. During a rainfall event, if no ponding occurs,  $K_{sat}$  at the surface is greater than the rainfall rate and the infiltration rate near the surface is equal to the rainfall rate. Therefore the infiltration rate near the surface is less than  $K_{sat}$ .

This concept is extended for depths greater than the near-surface, and hence for infiltration occurring after the rainfall period ( $t > t_w$ ) with the following assumption made by the author:

$$f_M = w = K(\phi_w)_M \cdot i_w, \quad (8)$$

where  $f_M$  is the maximum possible flux (or infiltration rate at depth),  $K_h(\varphi_w)_M$  is the maximum possible hydraulic conductivity at the wetting front, and  $i_w$  is the hydraulic gradient at the wetting front. In other words, the maximum possible  $K(\varphi)$  is the rainfall rate divided by the gradient at the wetting front generated in response to the rainfall. This assumption was used to constrain the  $K(\varphi)$  curve, as described below.

Maximum possible hydraulic conductivity at the wetting front ( $K_h(\varphi_w)_M$ ) may be calculated with available rainfall rate and soil tension data. In the absence of soil tension data, the hydraulic gradient at the wetting front may be assumed to be 1 with about an order of magnitude uncertainty in the estimate of maximum possible hydraulic conductivity, based upon the data available for this analysis. Hydraulic gradient measured between two tensiometers and the average hydraulic potential measured at two tensiometers were evaluated at the low values (minima) observed as wetting fronts passed the tensiometers (Figure C.22). Note that if the sign convention for the gradient were reversed and the hydraulic potential were calculated as m of head rather than kPa, these quantities would have been evaluated at the high values (maxima) that occurred as the wetting fronts passed. The rainfall rate for the events driving each wetting front and the hydraulic gradient and hydraulic potential minima are summarized in Table C.8. These  $K_h(\varphi_w)_M$  points are plotted in Figure C.23.

Since

$$f(t) \leq f_M, \quad (9)$$

$$K(\varphi) \leq K(\varphi_w)_M. \quad (10)$$

Therefore, the  $K(\phi)$  function must fall below the  $K_h(\phi_w)_M$  points. A  $K(\phi)$  curve that fits these criteria was the curve estimated by application of the WRC from the T3F2 sample Tempe cell test (values in Table C.7) and  $K_{sat}$  measured with the T3F2 sample (2E-5 m/s) to Equation 6.

Calculation of the groundwater flux using the T3F2  $K(\phi)$  function (Figure C.23b) yielded values that are reasonable relative to the measured lysimeter outflow flux. The cumulative infiltration was calculated using the following equation:

$$F(t) = \int_0^t f(t) \cdot dt \quad (11)$$

The calculated cumulative infiltration (Figure C.23c) was reasonable relative to both the cumulative rainfall and the cumulative lysimeter outflow flux.

The validity of the assumption expressed in Equations 8 and 10 is addressed below by comparison of a range of  $K(\phi)$  functions (Figure C.21) and a calibrated mathematical model (figure C.24). A VS2D simulation was carried out with a model calibrated by the lysimeter outflow flux. The flux modeled at the observation points that represent the tensiometer location was similar to the flux values calculated using the Green-Ampt approach to determine a field calibrated  $K(\phi)$  function. The assumption made in Equation 8 therefore is valid for this case. This method improved the accuracy of the estimate of hydraulic conductivity from three orders of magnitude to better than one order of magnitude and extended the scale of the estimated curve from the Tempe cell-scale to a 1 to 2 m-scale.

Infiltration capacity at the Type 3 test pile was measured by ring infiltrometry to range from 2 mm/h to 77 mm/h (Figure C.14). Ponding was observed at the surface of

the Type 3 test pile during several applied rainfall events with rainfall rate greater than 7 mm/h (Figure C.25a). It is uncertain whether the ponding was significant enough to limit the maximum possible hydraulic conductivity at the wetting front. The Green-Ampt model for infiltration was used to relate rainfall rate to infiltration rate, and Darcy's law was used to relate the infiltration rate to the unsaturated hydraulic conductivity. Here, the condition of ponding is considered in calculation of the maximum infiltration rate. From Dingman 2002:

$$|\varphi_{fth}| = \frac{2 \cdot b + 3}{2 \cdot b + 6} \cdot |\varphi_e| , \quad (12)$$

$$z_f(t_p) = \frac{K_{sat} \cdot |\varphi_{fth}|}{w - K_{sat}} , \quad (13)$$

$$t_p = \frac{K_{sat} \cdot |\varphi_f| \cdot (\theta_s - \theta_0)}{w \cdot (w - K_{sat})} , \quad (14)$$

$$f(t) = K_{sat} - K_{sat} \cdot \frac{|\varphi_{fth}| + H(t)}{z_f(t)} , \quad (15)$$

where  $|\varphi_{fth}|$  is the theoretical hydraulic potential at the wetting front,  $b$  is the water retention curve power from the Campbell model (4.4 cm<sup>-1</sup> for waste rock matrix with grain size distribution similar to a loamy sand),  $z_f(t)$  is the depth of the wetting front,  $t_p$  is the time of the onset of ponding where  $t_0$  is the onset of rainfall, and  $H(t)$  is the height of ponding, which may be neglected. The infiltration rate calculated using this method is considered the maximum possible infiltration rate, by making the same assumption made by Equation 8. However, for the condition of ponding, the assumption is modified to:

$$f_M = f(t_w) = K(\varphi_w)_M \cdot i_w , \quad t > t_w , \quad (16)$$

where  $f(t_w)$  is the infiltration rate during ponding, which is a rate between the rainfall rate and the saturated hydraulic conductivity. Table C.9 summarizes the calculations made to determine the  $K(\phi_w)_M$  points plotted in Figure C.27a.

Due to the heterogeneity of the surface of the waste rock test piles, ponded water will run-off to regions of higher infiltration capacity. At regions of higher infiltration capacity, infiltration may occur as macropore or as more rapid Darcian, or capillarity-controlled, infiltration. This uncertainty in flow response leads to an uncertainty in the  $K(\phi)$  function of at least an order of magnitude. A  $K(\phi)$  function was determined for the condition where ponding was significant, and a  $K(\phi)$  function was determined for the condition where ponding in the low permeability regions was insignificant in evaluating the maximum possible  $K(\phi)$  (Figure C.27a).

Groundwater flux calculated by using a  $K(\phi)$  function that is between these two functions and the hydraulic gradient measured at the tensiometer profiles in the Type 3 test pile is reasonable (Figure C.27b) relative to the flux values calculated at the upper collection lysimeters, where outflow flux measurements were available. Cumulative infiltration calculated using this infiltration rate is reasonable relative to cumulative rainfall (Figure C.27c).

**Table C.7** Water retention curve fitting parameters using the van Genuchten (1980) model with the Mualem (1976) assumption applied.  $\alpha$  and  $n$  are curve fitting parameters,  $\varphi_e$  is the air entry pressure, the slope is the maximum slope of the function, and  $\theta_r$  is the residual saturation.

<b>Sample number</b>	<b>Sample location</b>	<b><math>\alpha</math></b> kPa <sup>-1</sup>	<b><math>n</math></b> -	<b><math>\varphi_e</math></b> kPa	<b>Slope</b> kPa <sup>-1</sup>	<b><math>\theta_r</math></b> m <sup>3</sup> /m <sup>3</sup>
189867	T3 F1	0.28	1.40	1.6	0.47	0.00
190279	T3F2	0.72	1.45	0.6	0.50	0.00
191170	T3F3	0.65	1.53	0.7	0.52	0.01
191948	T3F5	0.89	1.42	0.5	0.48	0.00
189338	T3 Base	0.23	1.56	1.9	0.58	0.00
	field WRC	0.12	2.28	4.0	0.88	0.01



**Figure C.17**

(a) The porous ceramic disk and sample cylinder of the Tempe cell.

(b) A saturated waste rock matrix sample packed into a Tempe cell sample cylinder.

(c) Moisture content was measured gravimetrically after each interval of suction had been applied at least 24 hours.

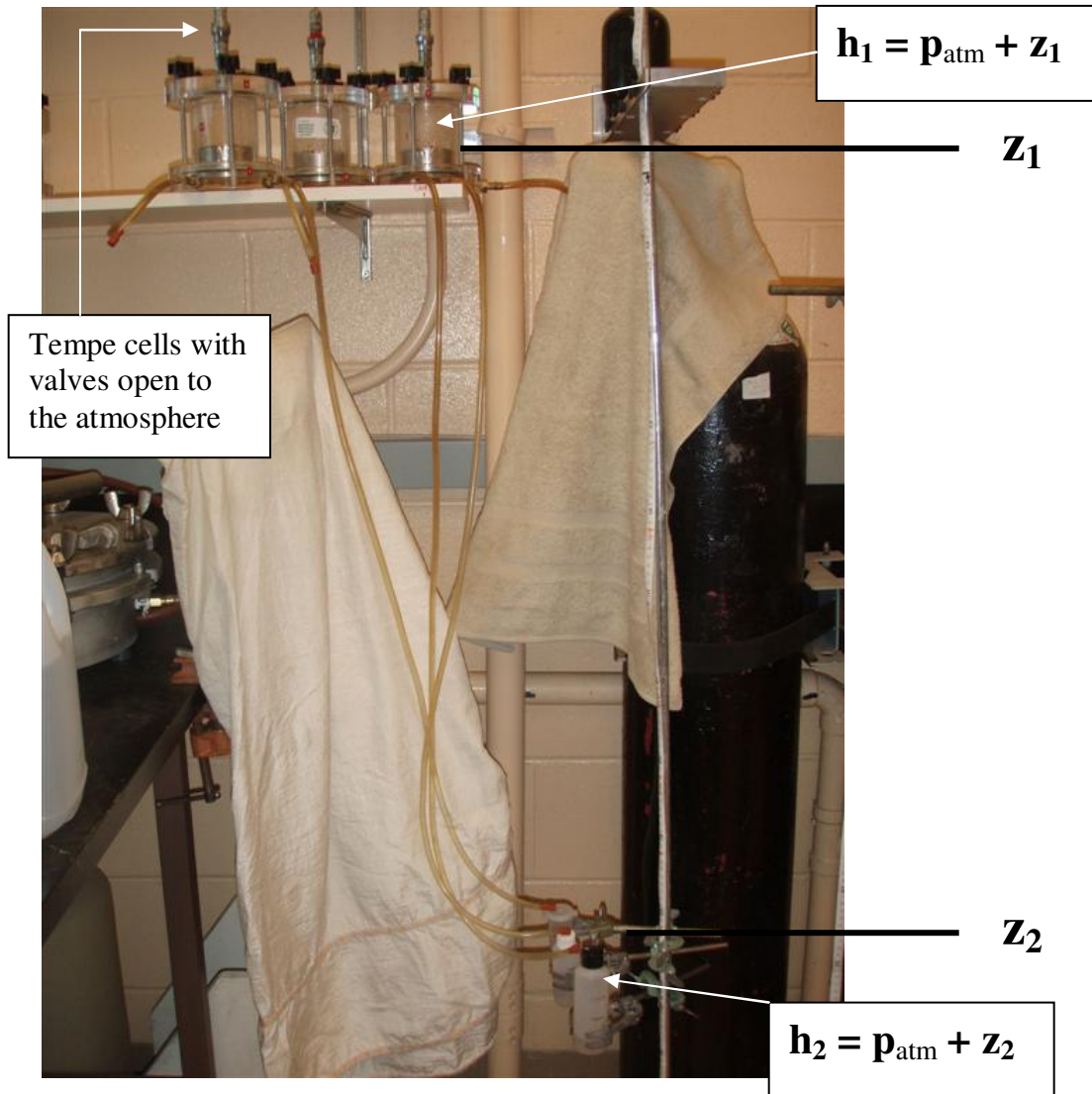


**Figure C.18** Tempe cell test, part 1.

Suction is applied to the sample by setting the head at the top of the sample in the Tempe cell ( $h_1$ ) greater than the head in the drainage bottle ( $h_2$ ). (10 cm head = 1 kPa).

The tubing is full of water. Connection with the drainage bottle is made by a needle through a septum, and connection with the sample is made via a porous disk.

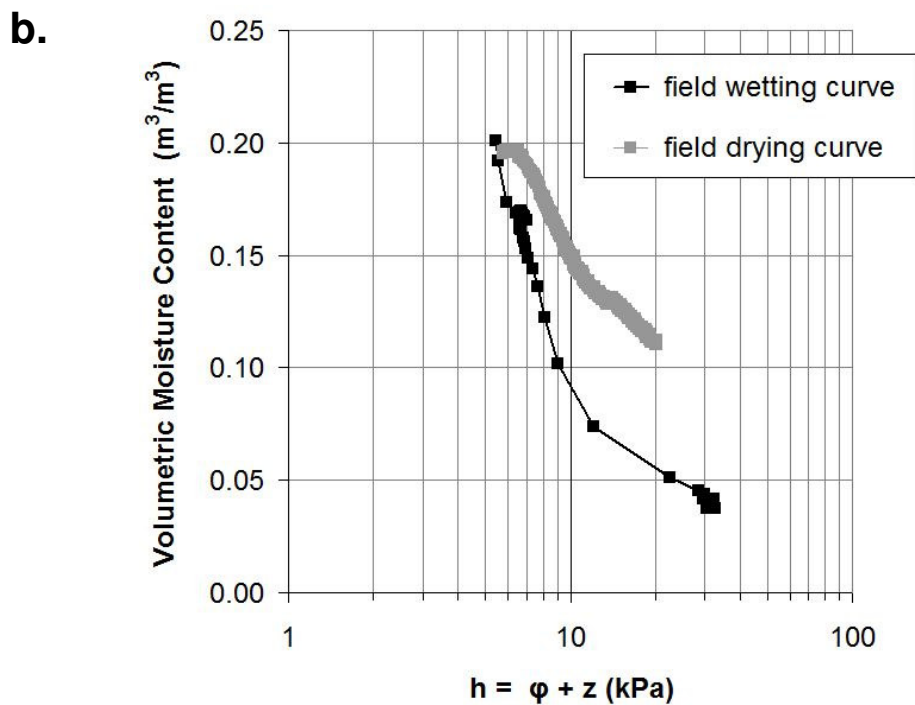
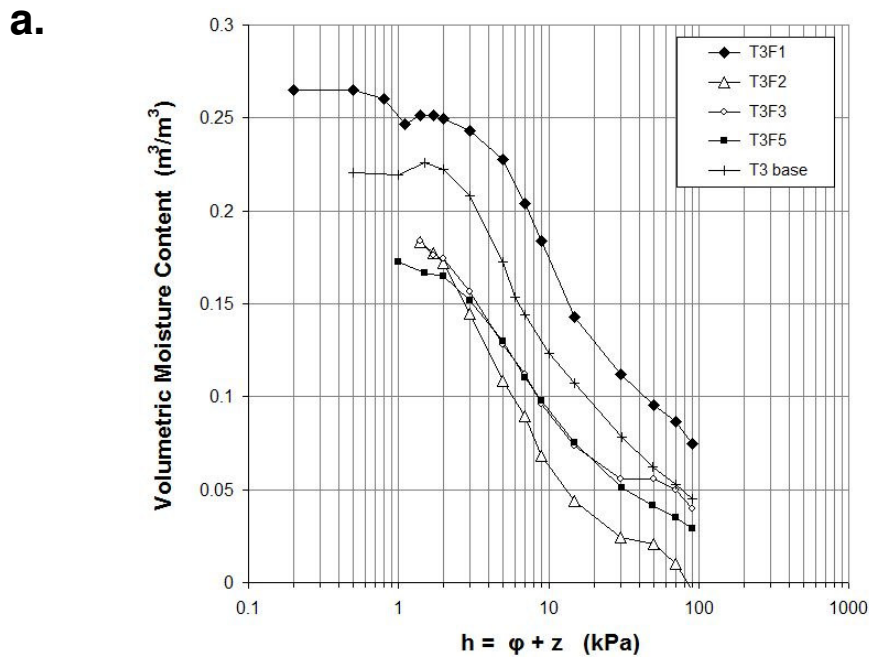


**Figure C.19** Water retention curves (a) measured in five waste rock matrix samples taken from the Type 3 test pile by conducting Tempe cell tests, and (b) measured in the field with an ECH<sub>2</sub>O probe and tensiometer located within 20 cm of each other at a 60 cm depth between the two T3 upper collection lysimeters.

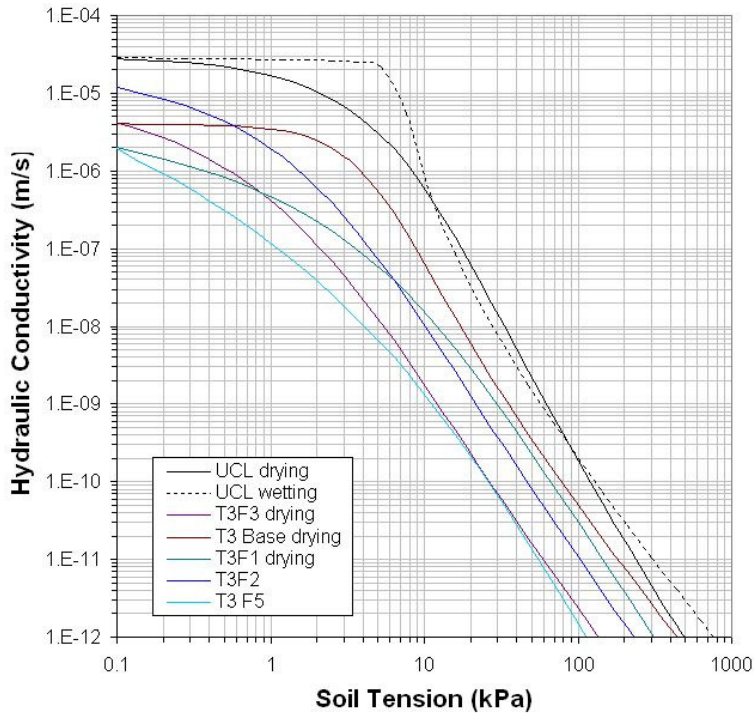


**Figure C.20** Hydraulic conductivity curves generated using Equation 6 for matrix materials. Parameters used to derive these functions were taken from the water retention curves measured from waste rock matrix samples in Tempe cell tests, from a water retention curve generated at one location in the field, and from the saturated hydraulic conductivity measured with each of these samples in laboratory permeameter tests.

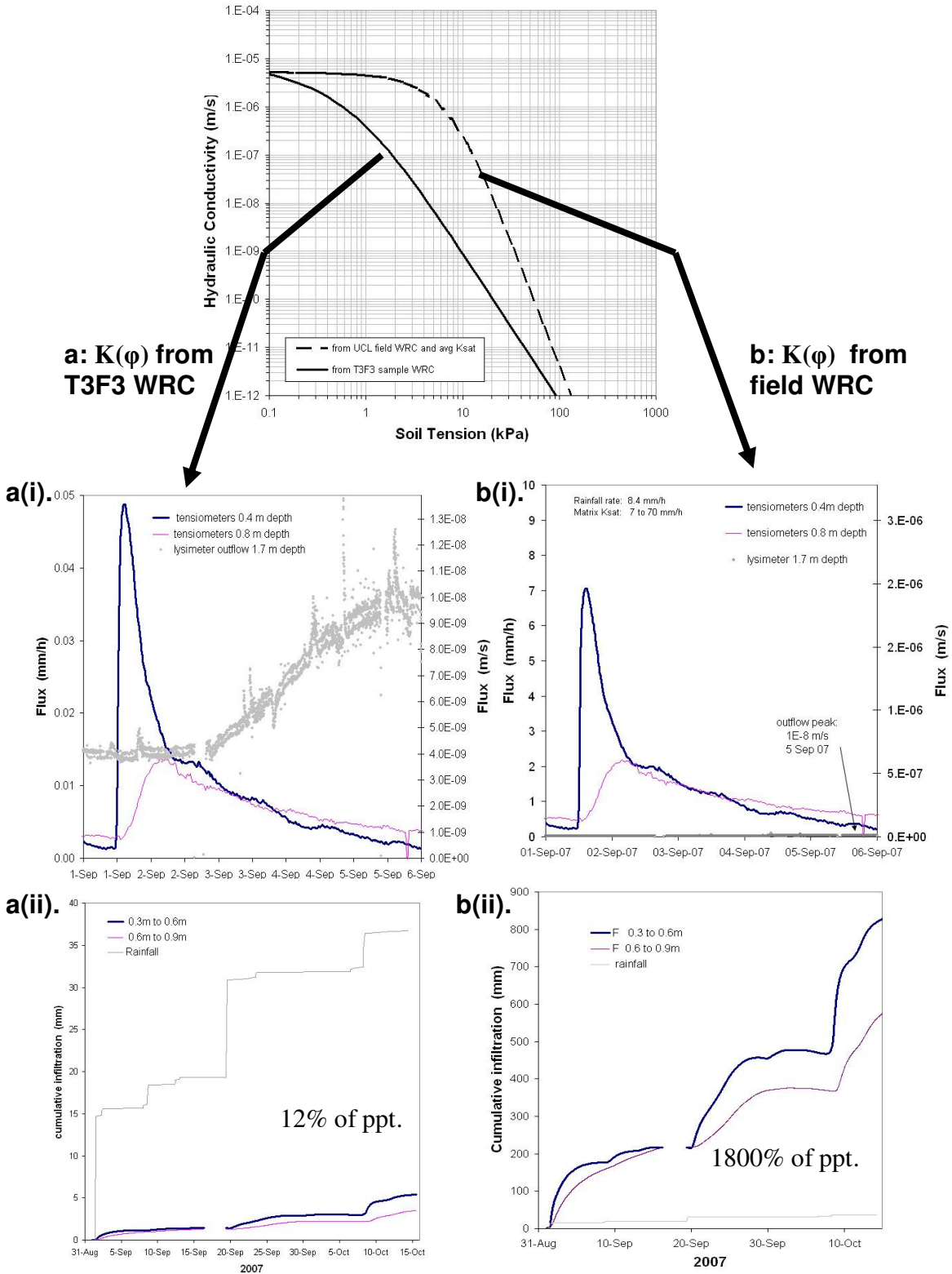


**Figure C.21** Flux calculated at tensiometer profiles at the upper collection lysimeters: underestimation with  $K(\phi)$  curve “a” and overestimation with  $K(\phi)$  curve “b.”

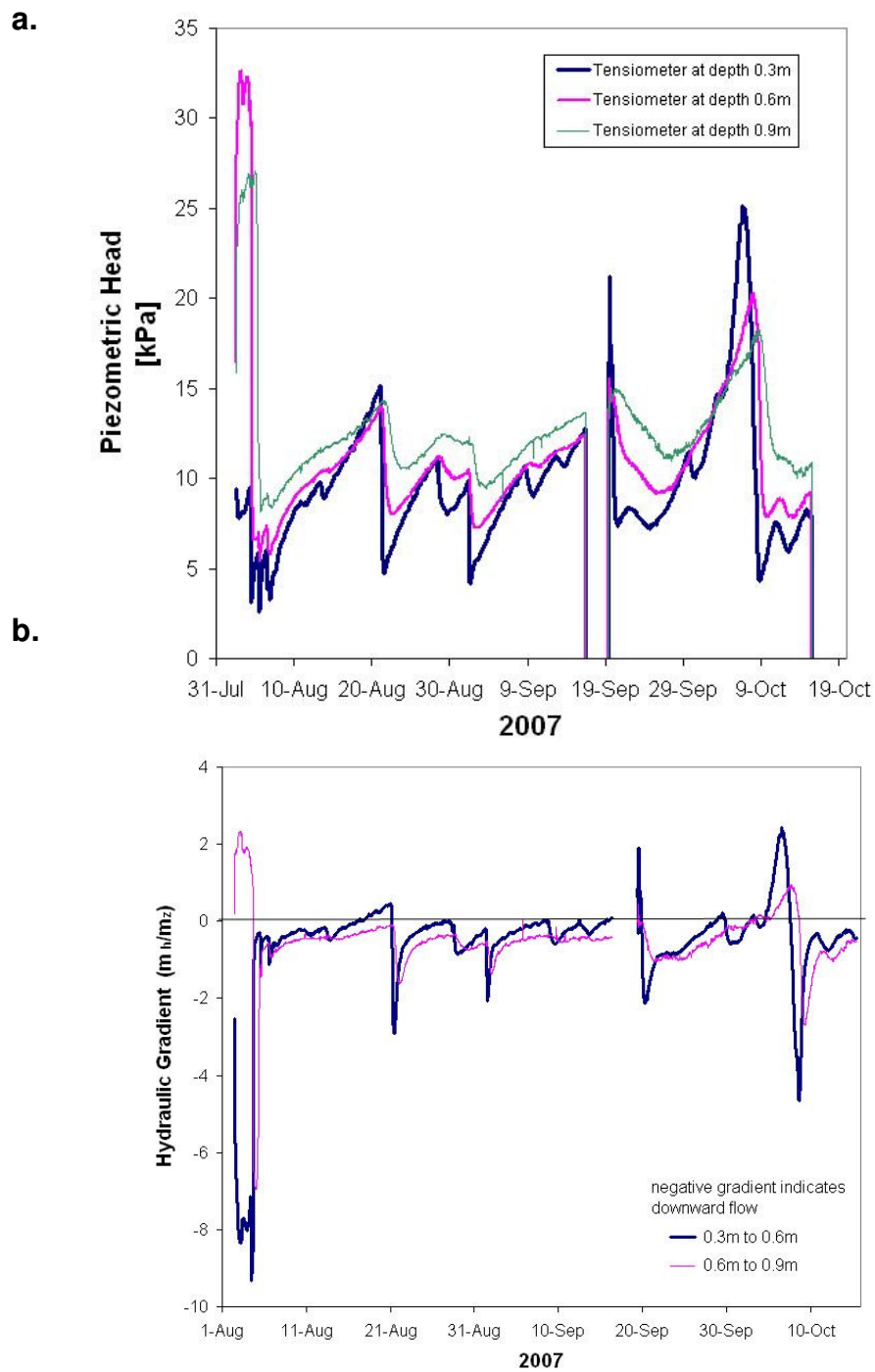


**Figure C.22** (a) Tension head and (b) hydraulic gradient minima at the upper collection lysimeters, which occurred as wetting fronts passed the tensiometers, were used to determine maximum possible hydraulic conductivity points plotted in Figure C.23.

**Table C.8** Values used in the Green-Ampt approach taken in calibration of the  $K(\phi)$  function used at the upper collection lysimeters.

	<b>Rainfall or Evaporation</b>	<b>Max Flux</b>	<b>Gradient</b>	<b>Tension</b>	<b>Max K(h)</b>	
	mm/h	m/s	-	kPa	m/s	
5-Aug-07	12.2	3.40E-06	-9.0	<b>2.6</b>	<b>3.8E-07</b>	
21-Aug-07	1.5	4.2E-07	-2.8	<b>4.9</b>	<b>1.5E-07</b>	
1-Sep-07	8.4	2.3E-06	-2.0	<b>4.2</b>	<b>1.2E-06</b>	
1-Sep-07		1.0E-08	-1.3	<b>9</b>	<b>7.7E-09</b>	*
19-Sep-07	10.8	3.0E-06	-2.0	<b>7.6</b>	<b>1.5E-06</b>	
08-Oct-07	1.6	4.4E-07	-4.6	4.6	9.7E-08	**

\* lysimeter outflow flux

\*\* waste rock likely frozen between a depth of 0.1m and 0.3m

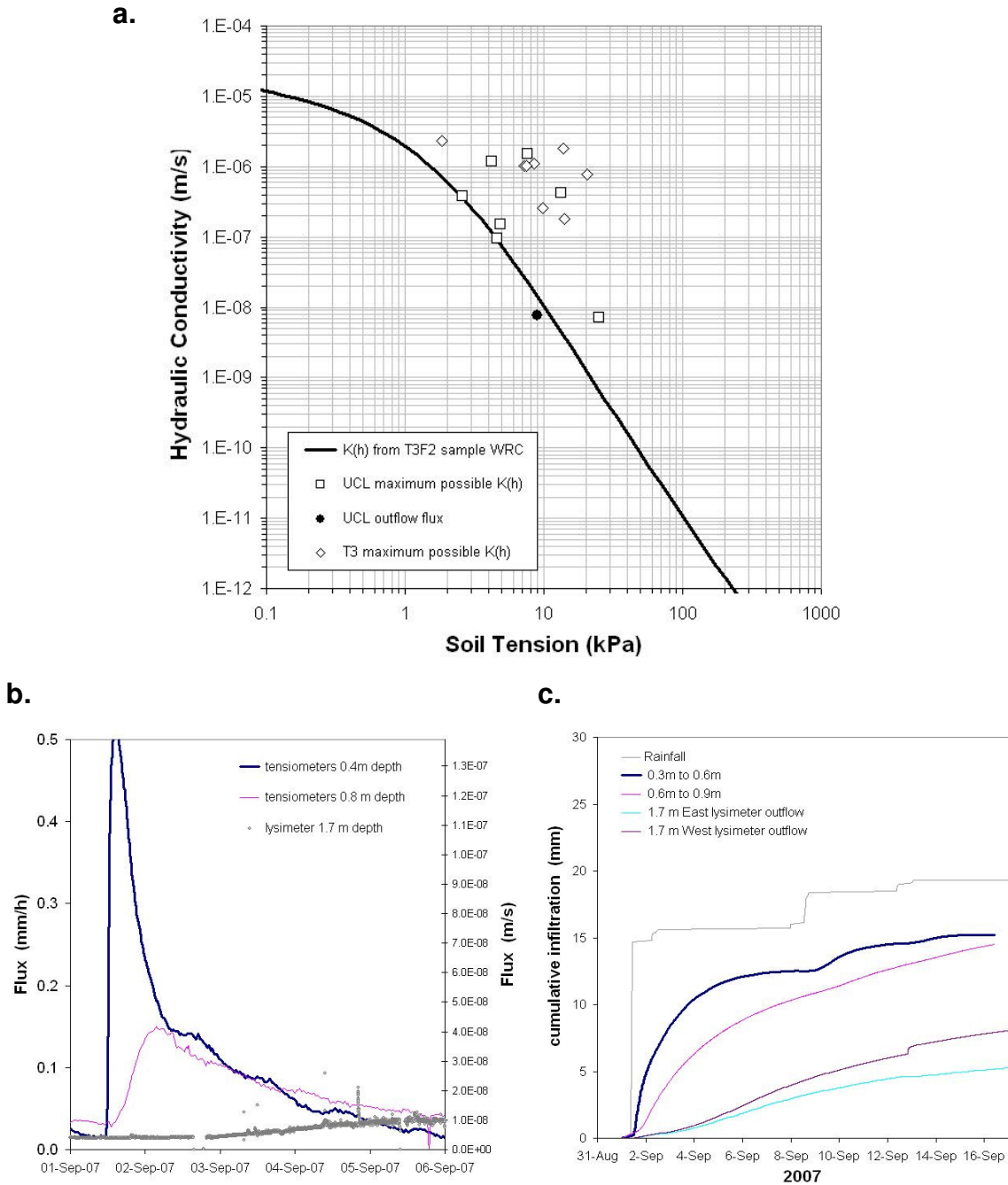
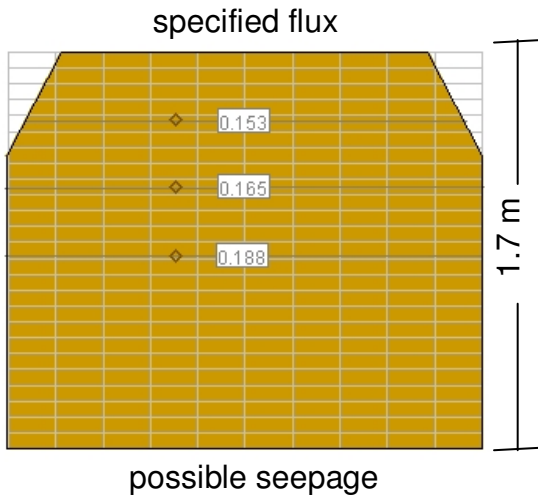


**Figure C.23** (a) Field calibration of the hydraulic conductivity function for the upper collection lysimeters using a Green-Ampt model to determine points in  $\phi - K(\phi)$  space which the  $K(\phi)$  function must be less than. (b) Flux at the 0.4 m and 0.8 m depth, calculated using the gradient measured with tensiometers and the  $K(\phi)$  function in (a), is reasonable relative to measured lysimeter outflow flux. (c) Cumulative infiltration is reasonable relative to cumulative rainfall and cumulative lysimeter outflow flux.

a.



b.

$K_{sat}$	$\theta_s$	$\theta_r$	$\alpha$	$n$
m/s	$m^3/m^3$	$m^3/m^3$	$kPa^{-1}$	-
2.E-05	0.22	0.1	0.45	1.3

c.

$\theta_{0.3(0)}$	$\theta_{0.6(0)}$	$\theta_{0.9(0)}$
$m^3/m^3$	$m^3/m^3$	$m^3/m^3$
0.15	0.17	0.19

d.

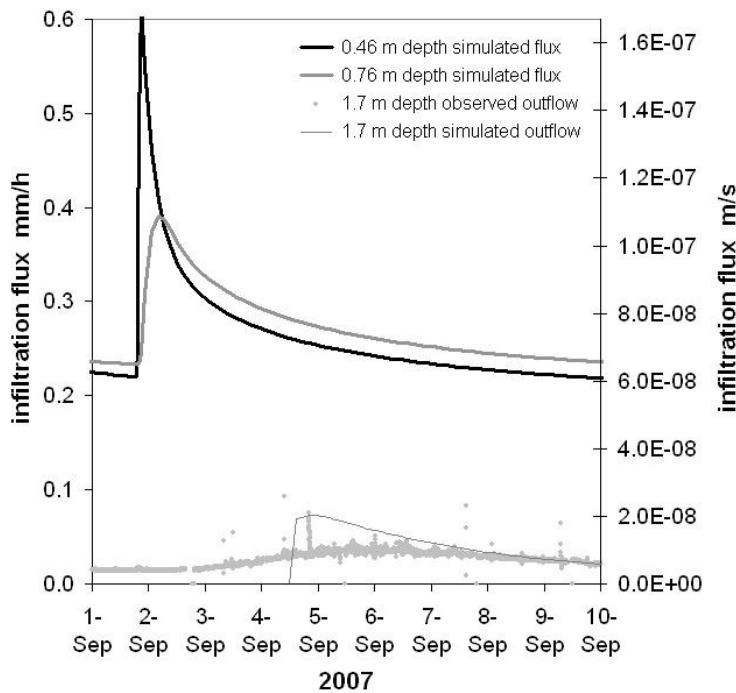


**Figure C.24** VS2D modeling verification of application of the Green-Ampt model condition used in determining the maximum  $K(\phi)$  function, which states that rainfall rate is equal to the maximum flux possible. (a) Model grid, observation points, and boundary conditions, (b) flow equation parameters, (c) initial conditions at the observation points, and (d) results. The model was calibrated to the observed lysimeter outflow flux, and the resulting flux calculated at depths of 0.46 m and 0.76 m were similar to the flux estimates in Figure C.22 using the  $K(\phi)$  function determined with the Green-Ampt approach.

a.



b.

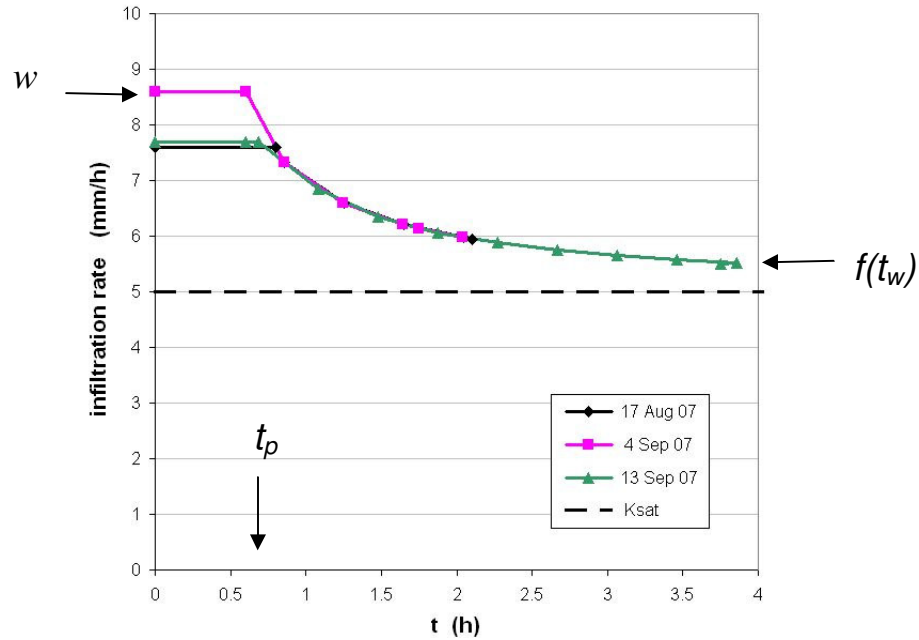


**Figure C.25** (a) Ponding was observed at the surface of the Type 3 test pile during high-intensity rainfall events, for example during this applied rainfall event conducted on September 4, 2007. (b) Infiltration rate into less permeable regions of the surface during applied rainfall events in 2007 that generated ponding.

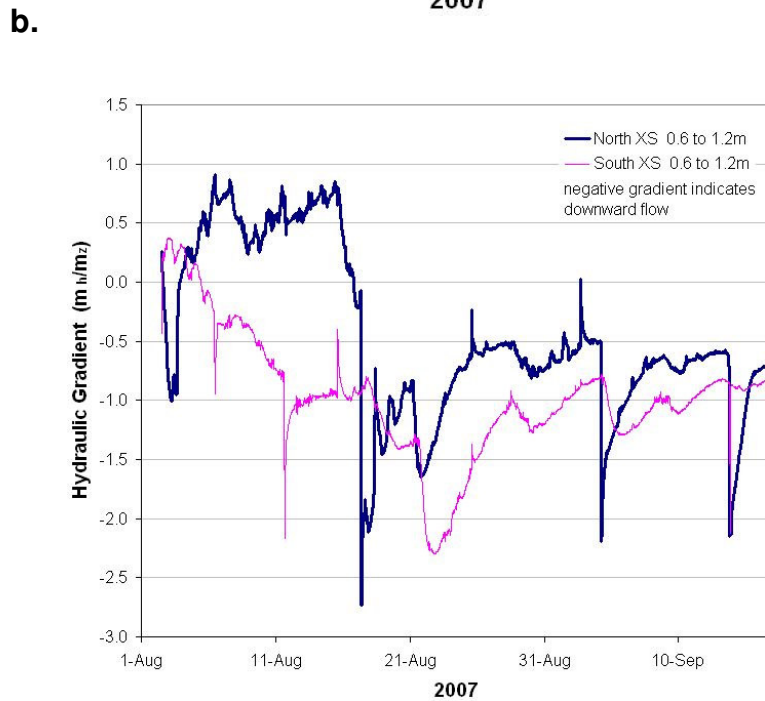
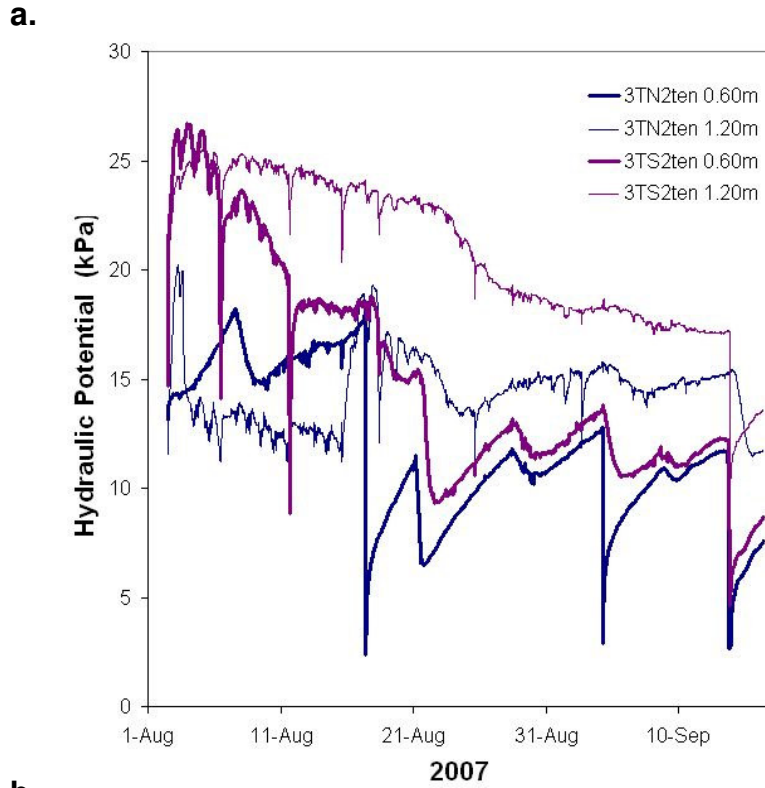


**Figure C.26** (a) Hydraulic potential and (b) hydraulic gradient minima at the Type 3 test pile, which occurred as wetting fronts passed the tensiometers, were used to determine maximum possible hydraulic conductivity points plotted in Figure C.23.

**Table C.9** Values used in the Green-Ampt approach taken in calibration of the  $K(\phi)$  function used at the Type 3 test pile for two scenarios: (a) ponding was not significant in the maximum possible flux analysis of the  $K(\phi)$  function, and (b) ponding was significant significant in the maximum possible flux analysis of the  $K(\phi)$  function.

**a. Ponding was not significant:  $f_M = w$**

	<b>Rainfall</b> mm/h	<b>Max Flux</b> m/s	<b>Gradient</b> -	<b>Tension</b> kPa	<b>Max K(h)</b> m/s
T3 north tensiometer profile					
17-Aug-07	7.6	2.1E-06	-0.9	1.9	<b>2.3E-06</b>
21-Aug-07	1.5	4.2E-07	-1.6	9.8	<b>2.6E-07</b>
4-Sep-07	8.6	2.4E-06	-2.2	8.5	<b>1.1E-06</b>
13-Sep-07	7.7	2.1E-06	-2.1	7.2	<b>1.0E-06</b>
T3 south tensiometer profile					
17-Aug-07	7.6	2.1E-06	-2.7	20.5	<b>7.8E-07</b>
21-Aug-07	1.5	4.2E-07	-2.3	14.2	<b>1.8E-07</b>
4-Sep-07	8.6	2.4E-06	-1.3	13.8	<b>1.8E-06</b>
13-Sep-07	7.7	2.1E-06	-2.1	7.6	<b>1.0E-06</b>

**b. Ponding was significant:  $f_M = f(t_w) = K_{sat} \cdot \left[ 1 + \frac{|\phi| \cdot (\theta_s - \theta_0)}{z_f(t_w)} \right]$**

	<b>Rainfall</b> mm/h	<b>time of ponding</b> h	<b>f(tw)</b> mm/h	<b>Gradient</b> -	<b>Tension</b> kPa	<b>Max K(h)</b> m/s
T3 north tensiometer profile						
17-Aug-07	7.6	0.8	5.9	-8	1.9	<b>2.0E-07</b>
4-Sep-07	8.6	0.6	6.1	-2.2	8.5	<b>7.7E-07</b>
13-Sep-07	7.7	0.7	5.5	-2.1	7.2	<b>7.3E-07</b>
T3 south tensiometer profile						
17-Aug-07	7.6	0.8	5.9	-2.7	20.5	<b>6.1E-07</b>
4-Sep-07	8.6	0.6	6.1	-1.3	13.8	<b>1.3E-06</b>
13-Sep-07	7.7	0.7	5.5	-2.1	7.6	<b>7.3E-07</b>

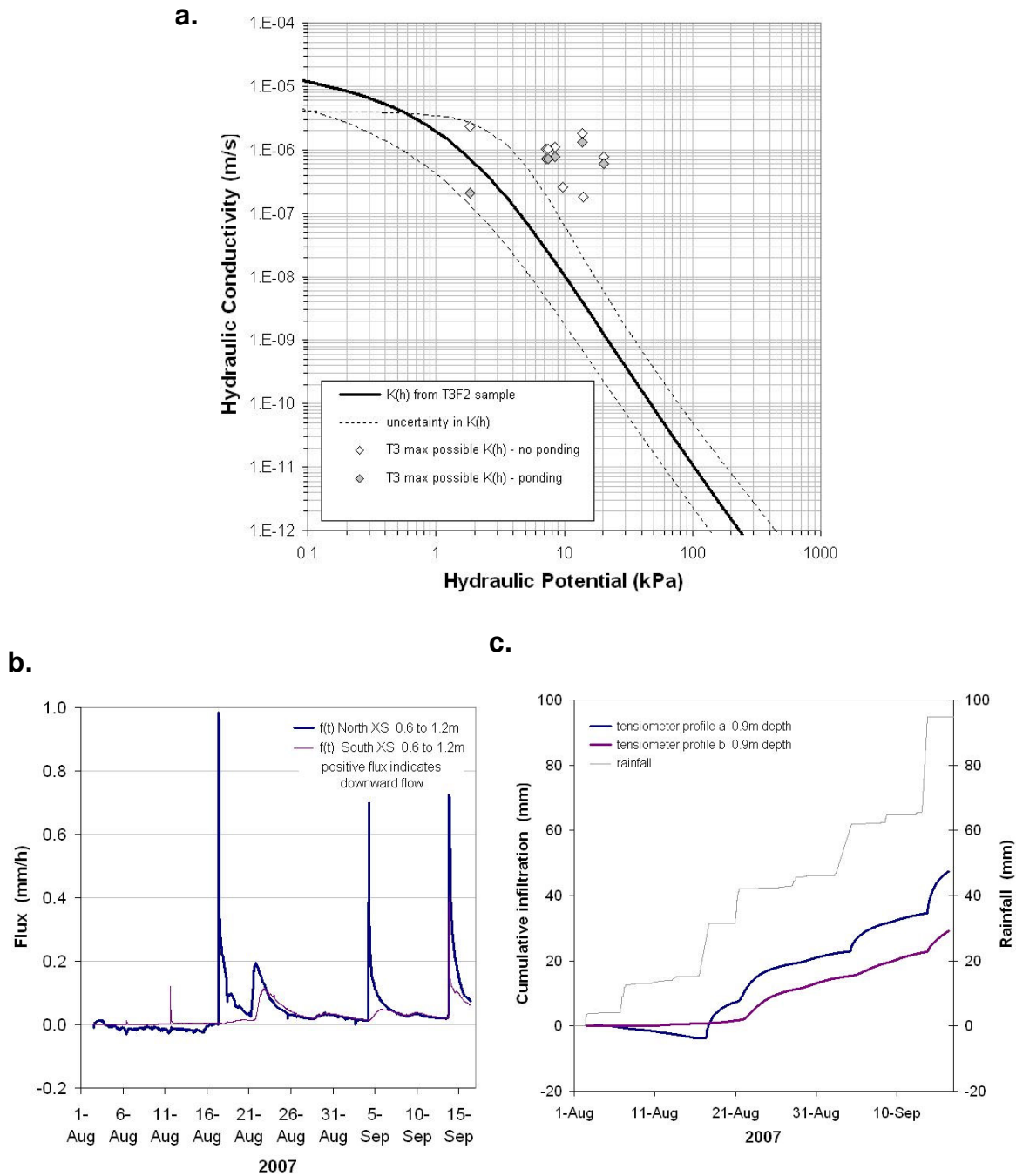


**Figure C.27** (a) Field calibration of the hydraulic conductivity function for the Type 3 test pile using a Green-Ampt model to determine points in  $\phi - K(\phi)$  space which the  $K(\phi)$  function must be less than. (b) Flux at the 0.9 m depth at two tensiometer profiles, calculated using the gradient measured with tensiometers and the  $K(\phi)$  function in (a). (c) Cumulative infiltration, calculated with the  $K(\phi)$  function in (a), is reasonable relative to cumulative rainfall.

APPENDIX D DATA LOGGING DETAILS

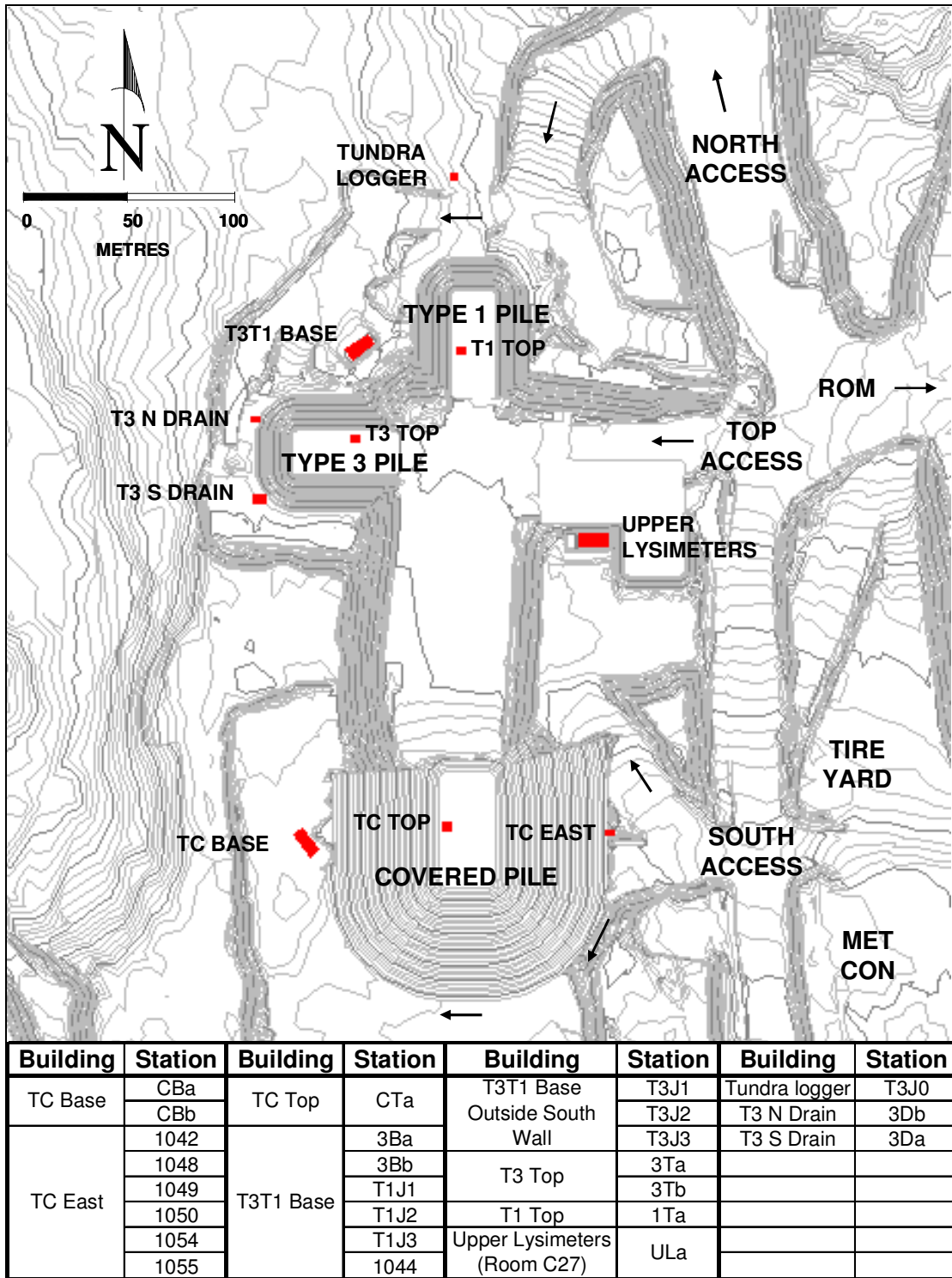


**Figure D.1** A map of the Diavik waste rock test pile research site that includes the instrumentation buildings and data logger stations.



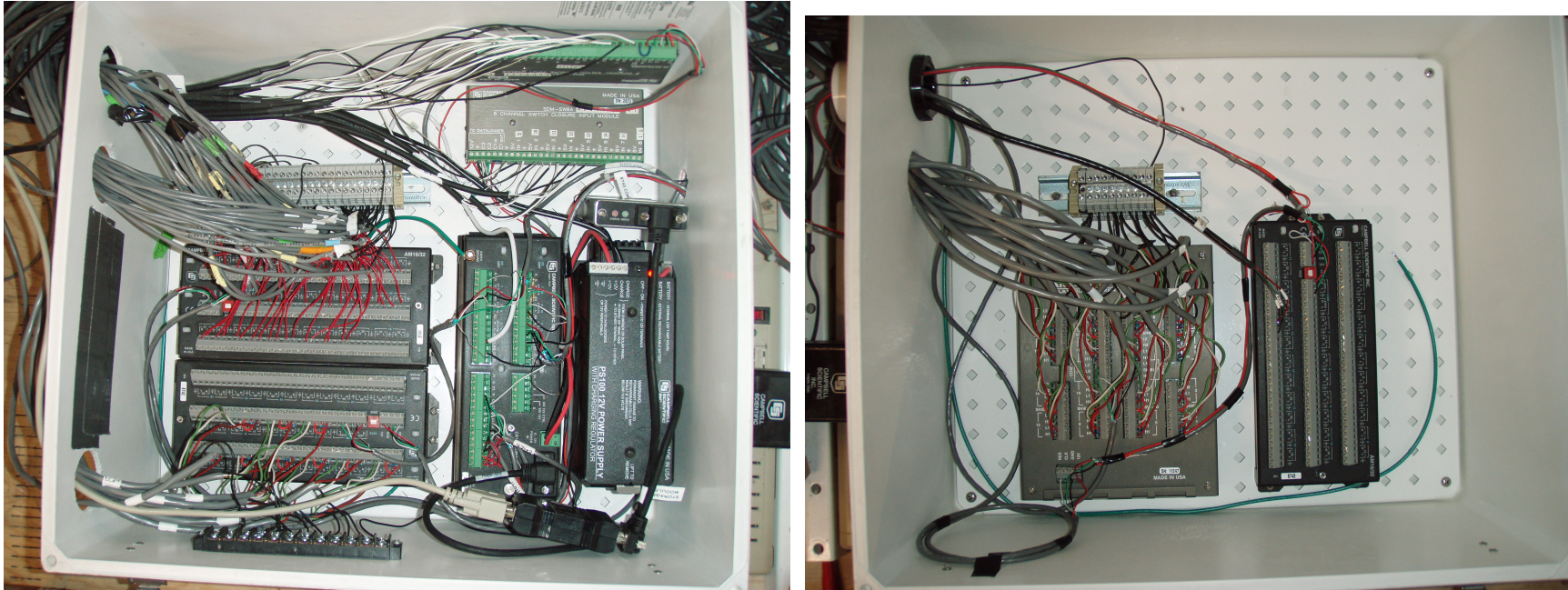
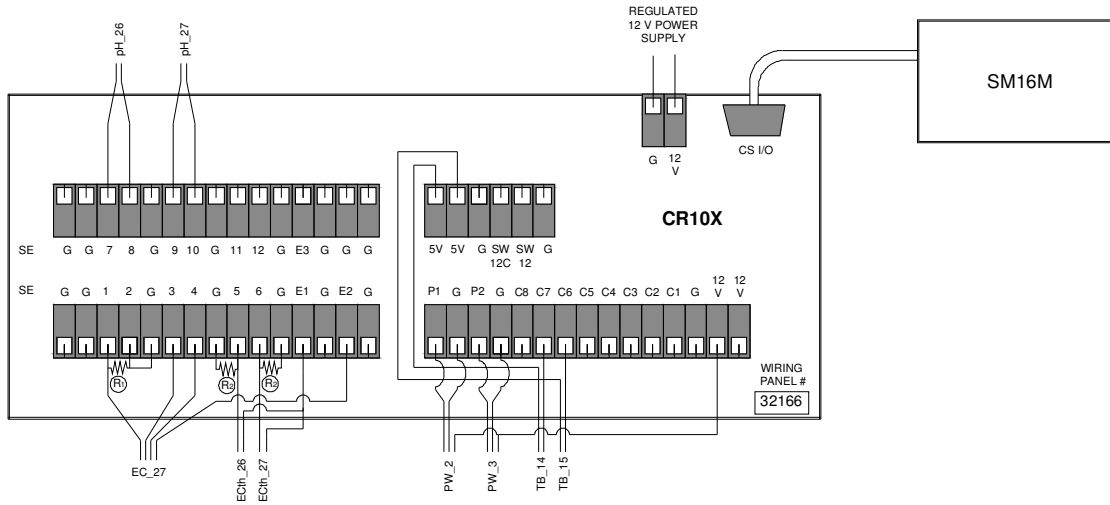


**Figure D.3** Photographs of the 3Ba data logger station.

a.



b.

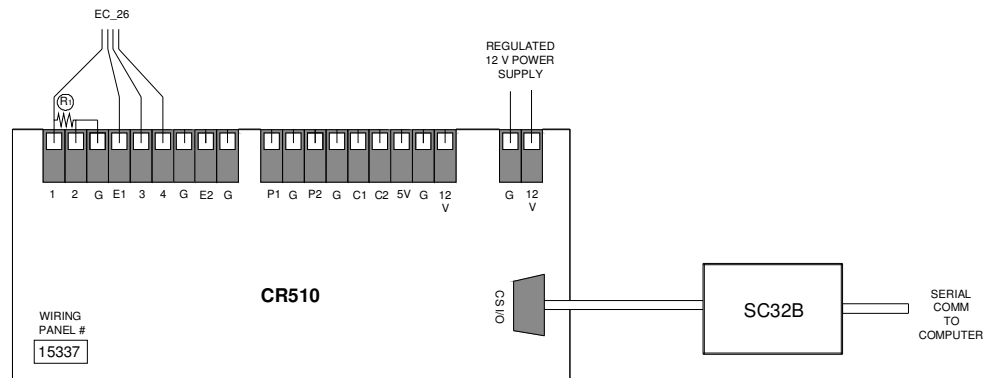
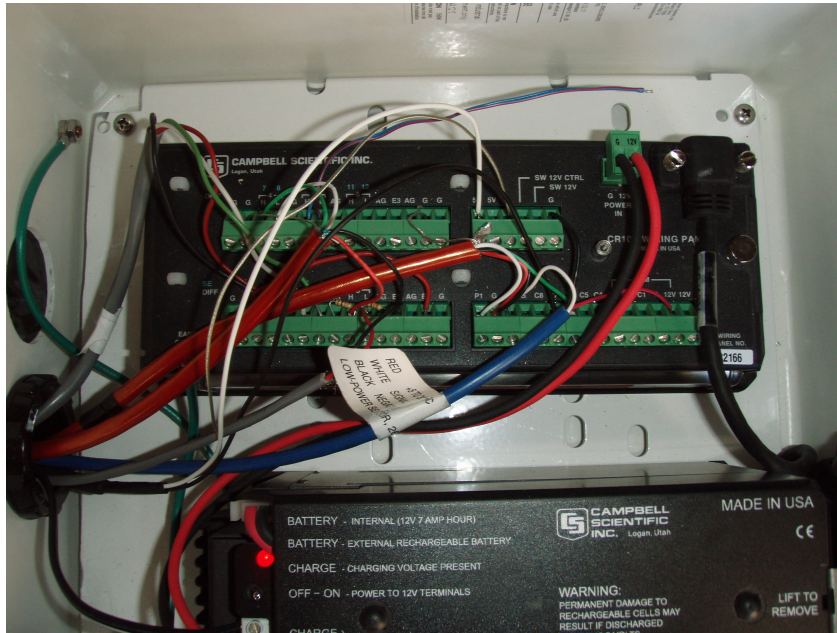


**Figure D.4** Wiring diagrams for the T3 basal drain. (a) Station 3Da measures sensors at both the south drain (TB\_15, PW\_3, EC\_27, ECth\_27, and pH\_27) and the north drain (TB\_14, PW\_2, ECth\_26, and pH\_26). (b) Station 3Db measures only EC\_26.

a.



b.

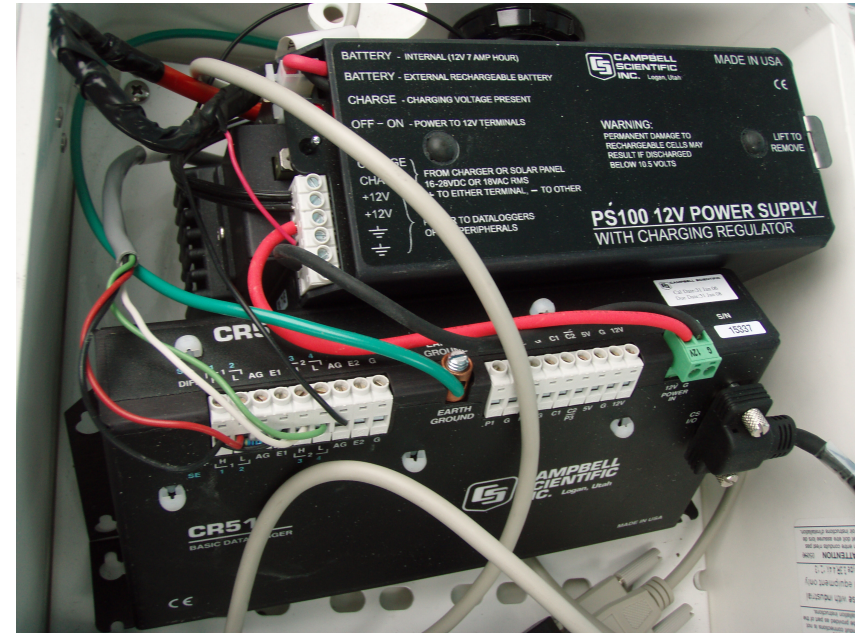


**Figure D.5** (a) The 3Da data logger station is located at the T3 south drain and (b) the 3Db data logger station is located at the T3 north drain.

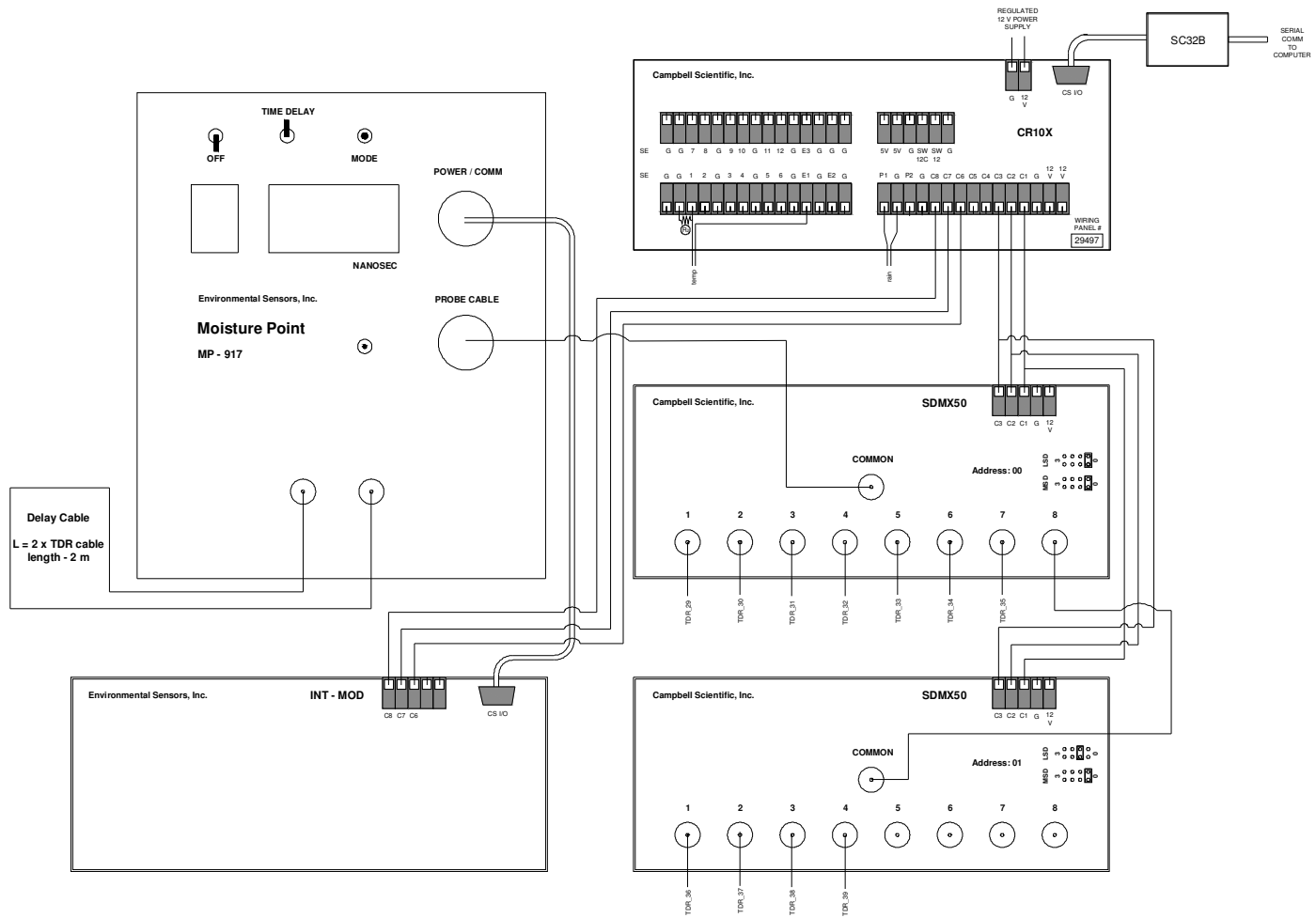
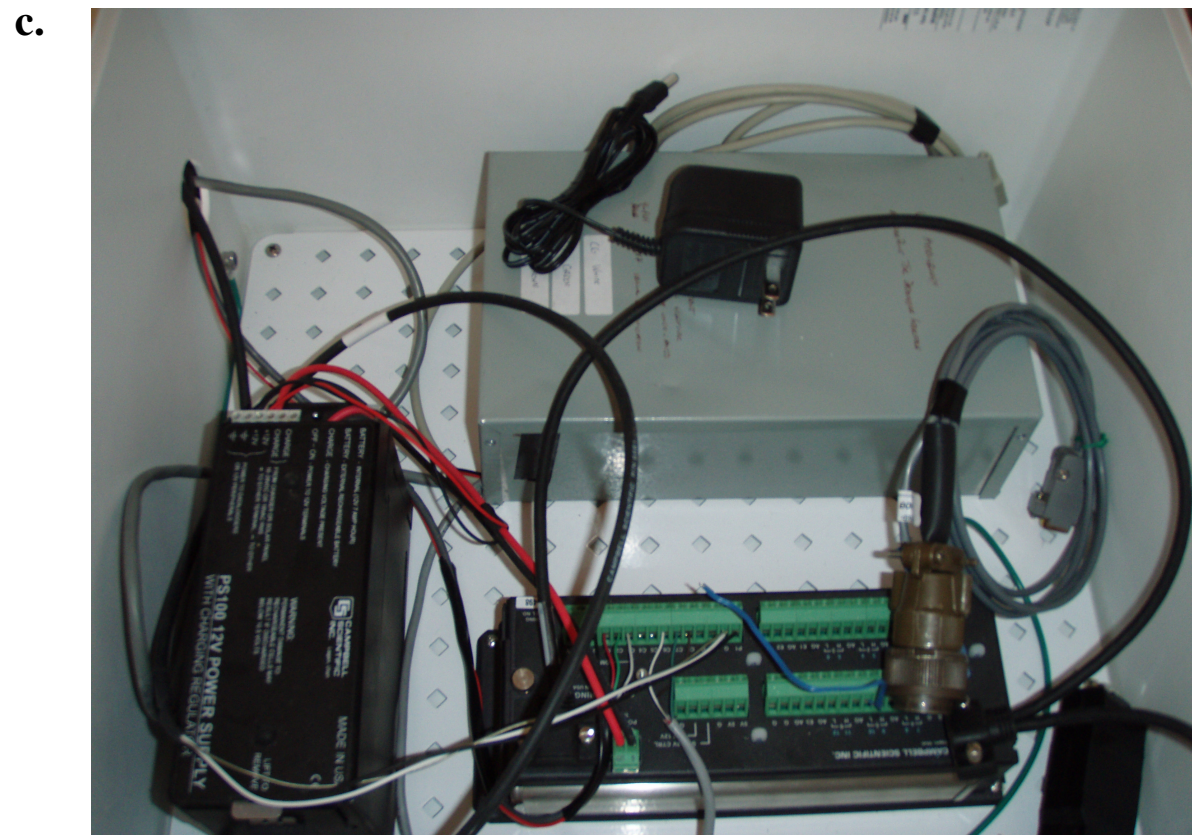
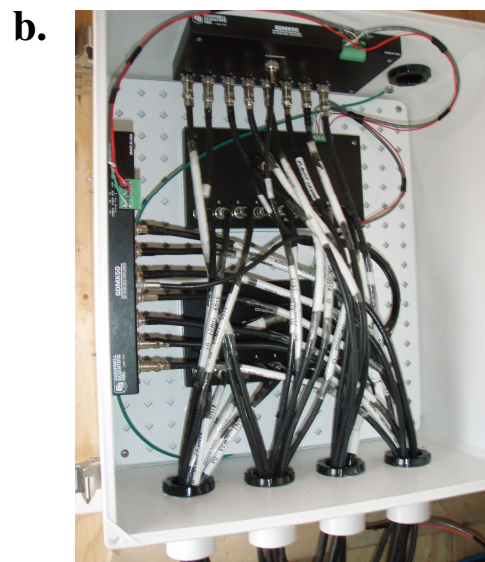
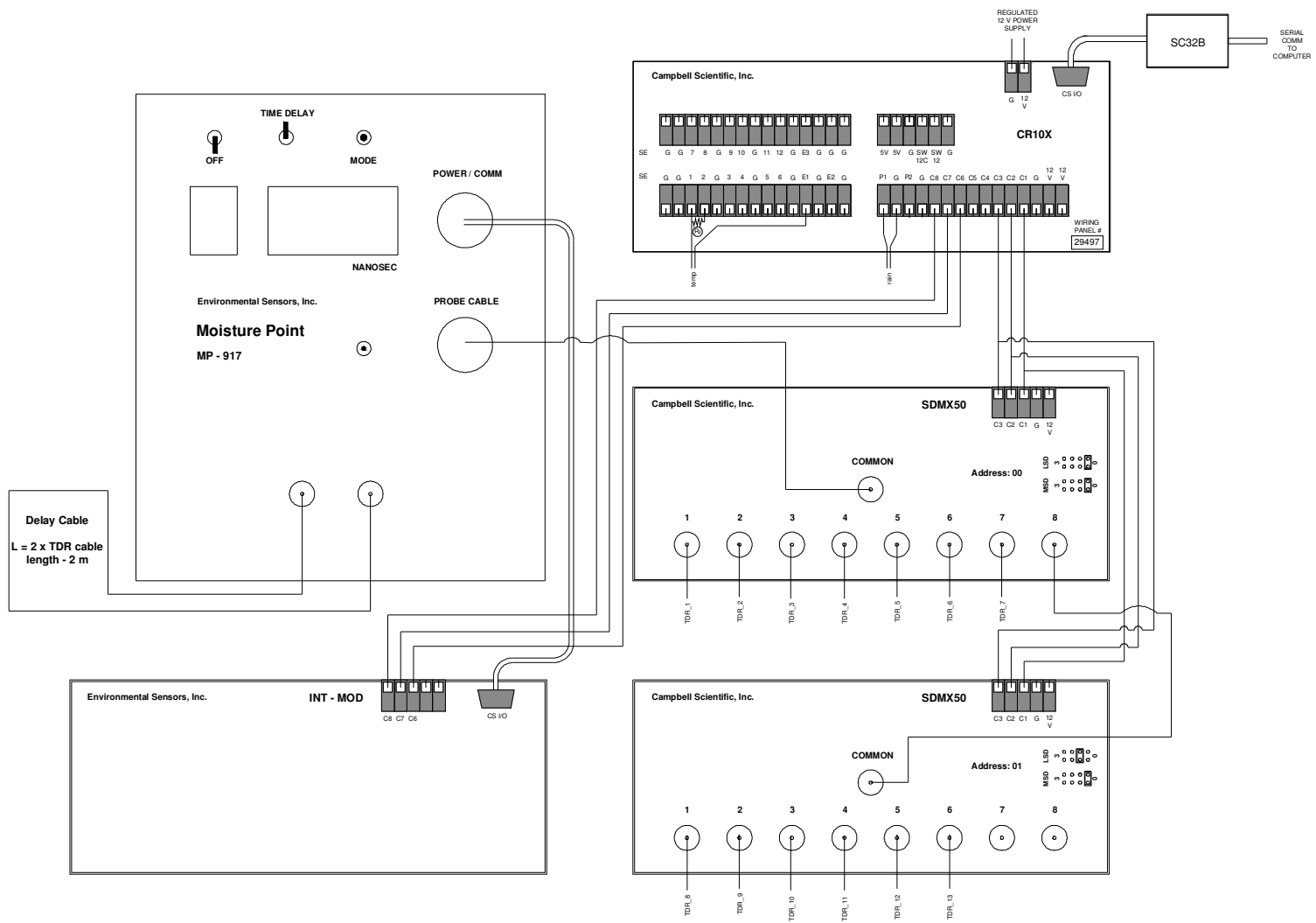


Figure D.6 Wiring diagram for the 1Ta data logger station.



**Figure D.7** (a) The 3Ta data logger station. The 1Ta has the same components as shown in these photographs. (b) Multiplexers for the TDR measurements. (c) The data logger (without the T3 tensiometers installed) and the interconnect module (inside the grey case).



**Figure D.8** Wiring diagram for the 3Ta data logger station.



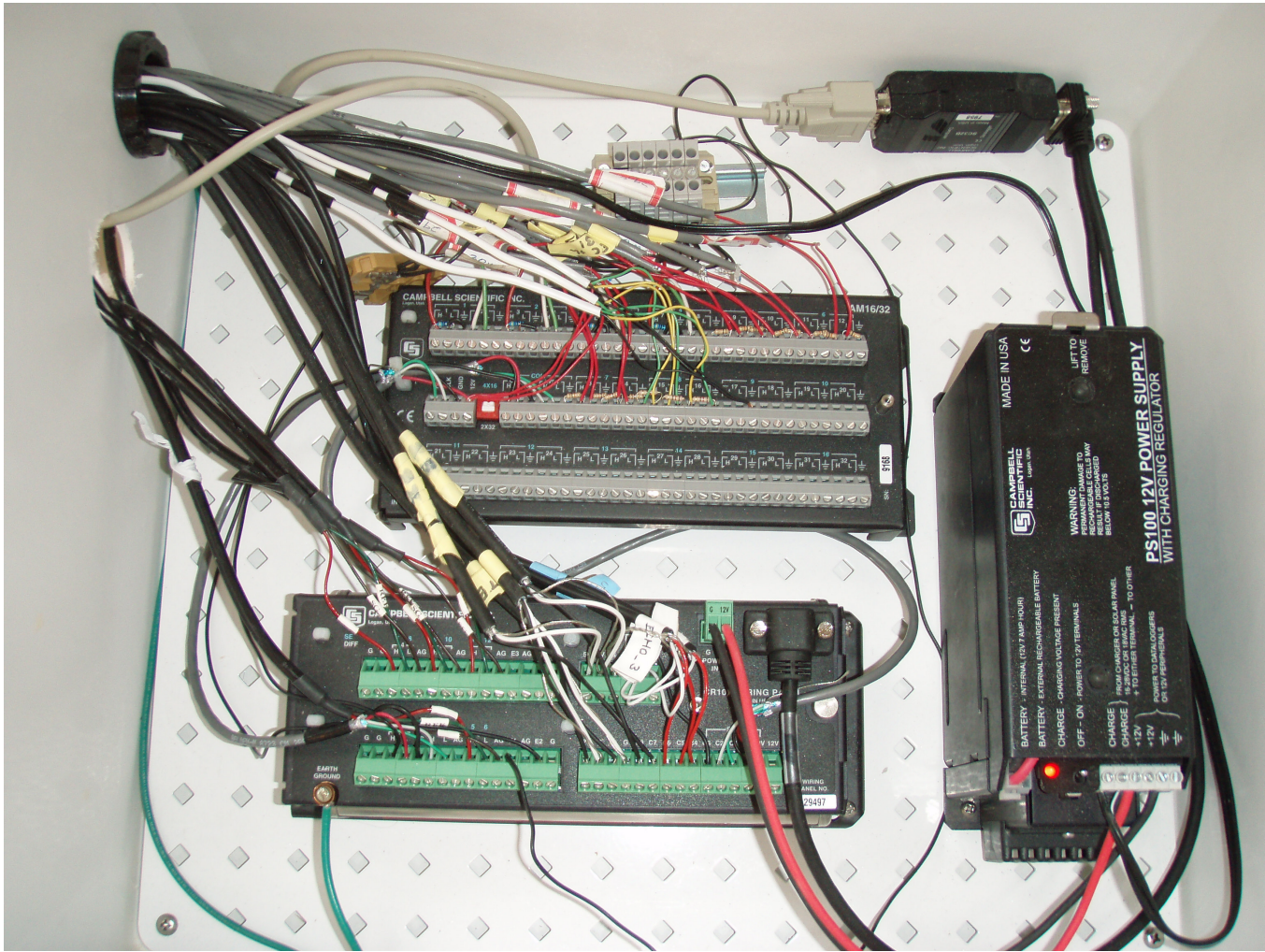


**Figure D.10** The ULa data logger station.

## **D.2 DATA LOGGER PROGRAMS**

All programs were written in the annotated version of the language used by Edlog, the text editor for various Campbell Scientific data loggers, most commonly the CR10X. Newer data loggers like the CR1000 use the programming language CR Basic, which includes many of the same instructions used in Edlog, but on a Visual Basic platform. The manuals for each type of data logger contain thorough explanations of each instruction.

D.2.1 Station 3Ba

```
:{CR10X}
; Data Logger Station: 3Ba
; Data Logger: CR10X S/N46067, Wiring Panel #35265
; T3/T1 Instrument Building

; Measurements:
; - Flow at T1 and T3 basal lysimeters; flow at T1 drain (paddlewheel and tipping bucket)
; - Temperature inside all Electrical Conductivity flow-through cells
; - Temperature inside all T3 lysimeters (at liner) and at the heat trace under the lysimeters
; - Temperature inside 6 of the T1 basal lysimeters
; - Electrical Conductivity of the T3 and T1 basal lysimeter outflow and of the T1 basal drain outflow
; - pH of the T3 and T1 basal lysimeter outflow and of the T1 basal drain outflow
;
; Calculations and Corrections made in this program:
; - Paddlewheel flow is totalized over each second that a pulse is sensed
; - Temperature in degrees Celcius is calculated from single-ended voltage measurement
; - EC in microSiemens/cm is calculated from a half-bridge differential voltage
; - pH is calculated from a differential voltage
; - pH is corrected for the temperature effect
;
; Post-processing Requirements:
; - Flow:
;   1. Array ID 1-12 use the calibration for small tipping buckets
;   2. Array ID 13 uses the calibration for large tipping buckets
;   3. Array ID 41 uses the calibration for paddlewheel gauges
; - Specific Conductance:
;   - Array ID 167: Electrical conductivity must be converted to specific conductance
;     (EC at 25C) using the EC temperature
;   - Note that a further correction may be required to account for the difference between
;     the calibrated data logged probes and a more-frequently calibrated field probe
;
; pH Calibration:
; - In the pH calculations, the offset may be changed from 7.00 to calibrate the probe
; - If necessary to adjust the slope of the calibration curve, this may be done by adding
;   a multiplicative term to the calculations

; Matt Neuner   Version 5, March 2008 edits: EC and pH measured at all ports
```

```
* Table 1 Program
01: 0.125      Execution Interval (seconds)
```

```
; FLOW MEASUREMENTS *****
; *****
```

```
; Tipping Bucket flow gauges monitor the basal lysimeter outflow
; and the low flow of the Type 1 basal drain. An array id and time stamp
; is output only if a tip has occurred.
```

```
; Read the SDM-SWA. The output location (TB_1) is automatically
; incremented.
```

```
1: SDM-SW8A (P102)
1: 13   Reps
2: 00   -- SDM Address
3: 2    Counts function
4: 1    Channel
5: 79   Loc [ TB_1 ]
6: 1.0  Mult
7: 0.0  Offset
```

```
; Check for tip in last 0.125 second
```

```
2: Beginning of Loop (P87)
1: 0000  Delay
2: 13   Loop Count
```

## D.2.1 Station 3Ba data logger program

```
3: If (X<=>F) (P89)
1: 79 -- X Loc [ TB_1 ]
2: 3  >=
3: 1  F
4: 30  Then Do

4: Do (P86)
1: 10  Set Output Flag High (Flag 0)

5: Set Active Storage Area (P80)^21595
1: 1   Final Storage Area 1
2: 1   -- Array ID

6: Real Time (P77)^19187
1: 0100 Day (midnight = 0000)

7: Time (P18)
1: 1   Minutes into current day (maximum 1440)
2: 0000 Mod/By
3: 12  Loc [ Minute ]

8: Sample (P70)^1372
1: 1   Reps
2: 12  Loc [ Minute ]

9: Real Time (P77)^8210
1: 0001 Seconds (midnight = 0000)

; End If tip, then output loop
10: End (P95)

; End loop through the 13 tipping buckets
11: End (P95)

; *****

; Paddlewheel flow meter for the Type 1 basal drain
; Calibration done for pulses per second, but ex int is 0.125s,
; so pulses must be totalized over 1s.

12: Pulse (P3)
1: 1   Reps
2: 1   Pulse Channel 1
3: 2   Switch Closure, All Counts
4: 93  Loc [ PW_1 ]
5: 1.0 Mult
6: 0.0 Offset

PW_1sec=PW_1sec+PW_1

13: If time is (P92)
1: 0 -- Minutes (Seconds --) into a
2: 1 Interval (same units as above)
3: 30 Then Do

14: If (X<=>F) (P89)
1: 2 X Loc [ PW_1sec ]
2: 3 >=
3: 1 F
4: 30 Then Do

15: Do (P86)
1: 10 Set Output Flag High (Flag 0)

16: Set Active Storage Area (P80)^2657
1: 1 Final Storage Area 1
2: 41 Array ID
```

## D.2.1 Station 3Ba data logger program

```
17: Real Time (P77)^244
1: 1100 Year,Day (midnight = 0000)

18: Time (P18)
1: 1 Minutes into current day (maximum 1440)
2: 0000 Mod/By
3: 12 Loc [ Minute ]

19: Sample (P70)^23076
1: 1 Reps
2: 12 Loc [ Minute ]

20: Real Time (P77)^30051
1: 0001 Seconds (midnight = 0000)

21: Sample (P70)^16025
1: 1 Reps
2: 2 Loc [ PW_1sec ]

; Reset second totalizer
PW_1sec=0

22: End (P95)

23: End (P95)

; ***** OUTPUT TO STORAGE MODULE *****

24: Serial Out (P96)
1: 71 Storage Module

* Table 2 Program
02: 1800 Execution Interval (seconds)

; TEMPERATURE MEASUREMENTS *****

; RESET: Activate AM16/32(1)
1: Do (P86)
1: 46 Set Port 6 High

2: Beginning of Loop (P87)
1: 0 Delay
2: 16 Loop Count

; Loop internal to the SET so that oddL, evenH, evenL will not over-write oddH
3: Step Loop Index (P90)
1: 4 Step

; CLOCK:
4: Do (P86)
1: 78 Pulse Port 8

5: Excitation with Delay (P22)
1: 1 Ex Channel
2: 0 Delay W/Ex (0.01 sec units)
3: 1 Delay After Ex (0.01 sec units)
4: 0 mV Excitation

6: Excite-Delay (SE) (P4)
1: 4 Reps
2: 20 Auto 60 Hz Rejection Range (Delay must be zero)(OS>1.9)
3: 7 SE Channel
4: 1 Excite all reps w/Exchan 1
5: 0 Delay (units 0.01 sec)
6: 2500 mV Excitation
7: 13 -- Loc [ Temp_1 ]
```

## D.2.1 Station 3Ba data logger program

8: 1 Mult  
9: 0.0 Offset

; Calculations loop for mux AM16/32(1) \*\*\*\*\*  
; Convert millivolt reading to resistance using  $R(\text{therm}) = ((V(\text{excit}) * R(\text{ref})) / V_{in}) - R(\text{ref})$   
; A 10 kOhm reference resistor is used (9890 multiplier in the second P37 below).

; Rep 1 calc's

7: Z=1/X (P42)

1: 13 -- X Loc [ Temp\_1 ]  
2: 13 -- Z Loc [ Temp\_1 ]

8: Z=X\*F (P37)

1: 13 -- X Loc [ Temp\_1 ]  
2: 2500 F  
3: 13 -- Z Loc [ Temp\_1 ]

9: Z=X+F (P34)

1: 13 -- X Loc [ Temp\_1 ]  
2: -1 F  
3: 13 -- Z Loc [ Temp\_1 ]

10: Z=X\*F (P37)

1: 13 -- X Loc [ Temp\_1 ]  
2: 9890 F  
3: 13 -- Z Loc [ Temp\_1 ]

11: Steinhart-Hart Equation (P200)

1: 1 Repts  
2: 13 -- Source Loc (R)(Ohms) [ Temp\_1 ]  
3: 13 -- Destination Loc (Deg C) [ Temp\_1 ]  
4: 1.28679 A  
5: -3 x 10^n  
6: 2.35938 B  
7: -4 x 10^n  
8: 9.4 C  
9: -8 x 10^n

; Rep 2 calc's

12: Z=1/X (P42)

1: 14 -- X Loc [ Temp\_2 ]  
2: 14 -- Z Loc [ Temp\_2 ]

13: Z=X\*F (P37)

1: 14 -- X Loc [ Temp\_2 ]  
2: 2500 F  
3: 14 -- Z Loc [ Temp\_2 ]

14: Z=X+F (P34)

1: 14 -- X Loc [ Temp\_2 ]  
2: -1 F  
3: 14 -- Z Loc [ Temp\_2 ]

15: Z=X\*F (P37)

1: 14 -- X Loc [ Temp\_2 ]  
2: 9890 F  
3: 14 -- Z Loc [ Temp\_2 ]

16: Steinhart-Hart Equation (P200)

1: 1 Repts  
2: 14 -- Source Loc (R)(Ohms) [ Temp\_2 ]  
3: 14 -- Destination Loc (Deg C) [ Temp\_2 ]  
4: 1.28679 A  
5: -3 x 10^n  
6: 2.35938 B  
7: -4 x 10^n  
8: 9.4 C

## D.2.1 Station 3Ba data logger program

```
9: -8    x 10^n

; Rep 3 calc's

17: Z=1/X (P42)
1: 15 -- X Loc [ Temp_3 ]
2: 15 -- Z Loc [ Temp_3 ]

18: Z=X*F (P37)
1: 15 -- X Loc [ Temp_3 ]
2: 2500 F
3: 15 -- Z Loc [ Temp_3 ]

19: Z=X+F (P34)
1: 15 -- X Loc [ Temp_3 ]
2: -1 F
3: 15 -- Z Loc [ Temp_3 ]

20: Z=X*F (P37)
1: 15 -- X Loc [ Temp_3 ]
2: 9890 F
3: 15 -- Z Loc [ Temp_3 ]

21: Steinhart-Hart Equation (P200)
1: 1 Repts
2: 15 -- Source Loc (R)(Ohms) [ Temp_3 ]
3: 15 -- Destination Loc (Deg C) [ Temp_3 ]
4: 1.28679 A
5: -3 x 10^n
6: 2.35938 B
7: -4 x 10^n
8: 9.4 C
9: -8 x 10^n

; Rep 4 calc's

22: Z=1/X (P42)
1: 16 -- X Loc [ Temp_4 ]
2: 16 -- Z Loc [ Temp_4 ]

23: Z=X*F (P37)
1: 16 -- X Loc [ Temp_4 ]
2: 2500 F
3: 16 -- Z Loc [ Temp_4 ]

24: Z=X+F (P34)
1: 16 -- X Loc [ Temp_4 ]
2: -1 F
3: 16 -- Z Loc [ Temp_4 ]

25: Z=X*F (P37)
1: 16 -- X Loc [ Temp_4 ]
2: 9890 F
3: 16 -- Z Loc [ Temp_4 ]

26: Steinhart-Hart Equation (P200)
1: 1 Repts
2: 16 -- Source Loc (R)(Ohms) [ Temp_4 ]
3: 16 -- Destination Loc (Deg C) [ Temp_4 ]
4: 1.28679 A
5: -3 x 10^n
6: 2.35938 B
7: -4 x 10^n
8: 9.4 C
9: -8 x 10^n

; End measurement and calc's loop for mux AM16/32(1)
27: End (P95)

28: Do (P86)
```

## D.2.1 Station 3Ba data logger program

1: 56 Set Port 6 Low

; ELECTRICAL CONDUCTIVITY \*\*\*\*\*  
; First Mux (11247): T3 EC and the first 4 T1 EC's

; Reset (turn on) mux  
29: Do (P86)  
1: 44 Set Port 4 High

30: Beginning of Loop (P87)  
1: 0000 Delay  
2: 16 Loop Count

; Clock (switch through) the 16 SETs  
31: Do (P86)  
1: 78 Pulse Port 8

32: Excitation with Delay (P22)  
1: 2 Ex Channel  
2: 0 Delay W/Ex (0.01 sec units)  
3: 1 Delay After Ex (0.01 sec units)  
4: 0 mV Excitation

33: Full Bridge w/mv Excit (P9)  
1: 1 Repts  
2: 25 2500 mV 60 Hz Rejection Ex Range  
3: 25 2500 mV 60 Hz Rejection Br Range  
4: 1 DIFF Channel  
5: 2 Excite all reps w/Exchan 2  
6: 2500 mV Excitation  
7: 98 -- Loc [ V2V1\_1 ]  
8: 1.0 Multiplier  
9: 0.0 Offset

; EC Calculations \*\*\*\*\*

; This output is 1000 times the ratio between the potential measured by the central electrodes  
; in the water and the potential measured by the outer electrodes in the solution,  
; in series with the reference resistor. Multiplying by the reference resistance (469.3 Ohms)  
; yields the resistance in the flow-through cell.

34: Z=X\*F (P37)  
1: 98 -- X Loc [ V2V1\_1 ]  
2: 0.001 F  
3: 98 -- Z Loc [ V2V1\_1 ]

35: Z=X\*F (P37)  
1: 98 -- X Loc [ V2V1\_1 ]  
2: 469.3 F  
3: 123 -- Z Loc [ Rs\_1 ]

; Conductance = cell constant (k) / resistance of solution  
; k is determined by Equation \*\* from Won (1987).  
; For the Divaik probes,  $k = 1.884\text{m}^{-1}$

36: Z=1/X (P42)  
1: 123 -- X Loc [ Rs\_1 ]  
2: 123 -- Z Loc [ Rs\_1 ]

37: Z=X\*F (P37)  
1: 123 -- X Loc [ Rs\_1 ]  
2: 1.884 F  
3: 148 -- Z Loc [ EC\_T\_1 ]

; Units conversions to uS/cm  
38: Z=X\*F (P37)  
1: 148 -- X Loc [ EC\_T\_1 ]

## D.2.1 Station 3Ba data logger program

```
2: 10000 F
3: 148 -- Z Loc [ EC_T_1 ]

; Calibration Factor : This factor was derived as the factor necessary to make all EC probes
; output the EC expected when measuring laboratory-prepared KCl solutions.
39: Z=X*F (P37)
1: 148 -- X Loc [ EC_T_1 ]
2: 3.963 F
3: 148 -- Z Loc [ EC_T_1 ]

40: End (P95)

; Deactivate the AM416 multiplexer.
41: Do (P86)
1: 54 Set Port 4 Low

; Second EC Mux (87482): Remaining T1 EC's
; Reset (turn on) the mux
42: Do (P86)
1: 45 Set Port 5 High

43: Beginning of Loop (P87)
1: 0000 Delay
2: 9 Loop Count

; CLOCK: Switches through the 16 SETs
44: Do (P86)
1: 78 Pulse Port 8

45: Excitation with Delay (P22)
1: 3 Ex Channel
2: 0 Delay W/Ex (0.01 sec units)
3: 1 Delay After Ex (0.01 sec units)
4: 0 mV Excitation

46: Full Bridge w/mv Excit (P9)
1: 1 Reps
2: 25 2500 mV 60 Hz Rejection Ex Range
3: 25 2500 mV 60 Hz Rejection Br Range
4: 1 DIFF Channel
5: 3 Excite all reps w/Exchan 3
6: 2500 mV Excitation
7: 114 -- Loc [ V2V1_17 ]
8: 1.0 Mult
9: 0.0 Offset

; EC Calculations *****

; This output is 1000 times the ratio between the potential measured by the central electrodes
; in the water and the potential measured by the outer electrodes in the solution,
; in series with the reference resistor. Multiplying by the reference resistance (469.3 Ohms)
; yields the resistance in the flow-through cell.

47: Z=X*F (P37)
1: 114 -- X Loc [ V2V1_17 ]
2: 0.001 F
3: 114 -- Z Loc [ V2V1_17 ]

48: Z=X*F (P37)
1: 114 -- X Loc [ V2V1_17 ]
2: 469.3 F
3: 139 -- Z Loc [ Rs_17 ]

; Conductance = cell constant (k) / resistance of solution
; k is determined by Equation ** from Won (1987).
; For the Divaik probes, k = 1.884m^-1
49: Z=1/X (P42)
1: 139 -- X Loc [ Rs_17 ]
```

## D.2.1 Station 3Ba data logger program

```
2: 139 -- Z Loc [ Rs_17 ]

50: Z=X*F (P37)
1: 139 -- X Loc [ Rs_17 ]
2: 1.884 F
3: 164 -- Z Loc [ EC_T_17 ]

; Units conversions to uS/cm
51: Z=X*F (P37)
1: 164 -- X Loc [ EC_T_17 ]
2: 10000 F
3: 164 -- Z Loc [ EC_T_17 ]

; Calibration Factor : This factor was derived as the factor necessary to make all EC probes
; output the EC expected when measuring laboratory-prepared KCl solutions.
52: Z=X*F (P37)
1: 164 -- X Loc [ EC_T_17 ]
2: 3.963 F
3: 164 -- Z Loc [ EC_T_17 ]

53: End (P95)

; Deactivate the AM416 multiplexer.
54: Do (P86)
1: 55 Set Port 5 Low

; *****
; pH MEASUREMENTS

; RESET: Activate AM16/32(#8743)
55: Do (P86)
1: 47 Set Port 7 High

; AM16/32 is in the 2X32 mode
56: Beginning of Loop (P87)
1: 0 Delay
2: 25 Loop Count

; Clock (switch through) the first 25 SET's
57: Do (P86)
1: 78 Pulse Port 8

58: Volt (Diff) (P2)
1: 1 Reps
2: 5 2500 mV Slow Range
3: 6 DIFF Channel
4: 223 -- Loc [ pH_mV_1 ]
5: 1 Multiplier
6: 0 Offset

; Calculate the Multiplier for Temperature Correction using
pHMult_1=-1/(((Temp_1+273)/298)*59)
pHMult_2=-1/(((Temp_2+273)/298)*59)
pHMult_3=-1/(((Temp_3+273)/298)*59)
pHMult_4=-1/(((Temp_4+273)/298)*59)
pHMult_5=-1/(((Temp_5+273)/298)*59)
pHMult_6=-1/(((Temp_6+273)/298)*59)
pHMult_7=-1/(((Temp_7+273)/298)*59)
pHMult_8=-1/(((Temp_8+273)/298)*59)
pHMult_9=-1/(((Temp_9+273)/298)*59)
pHMult_10=-1/(((Temp_10+273)/298)*59)
pHMult_11=-1/(((Temp_11+273)/298)*59)
pHMult_12=-1/(((Temp_12+273)/298)*59)
pHMult_13=-1/(((Temp_13+273)/298)*59)
pHMult_14=-1/(((Temp_14+273)/298)*59)
pHMult_15=-1/(((Temp_15+273)/298)*59)
pHMult_16=-1/(((Temp_16+273)/298)*59)
pHMult_17=-1/(((Temp_17+273)/298)*59)
```

## D.2.1 Station 3Ba data logger program

```
pHMult_18=-1/(((Temp_18+273)/298)*59)
pHMult_19=-1/(((Temp_19+273)/298)*59)
pHMult_20=-1/(((Temp_20+273)/298)*59)
pHMult_21=-1/(((Temp_21+273)/298)*59)
pHMult_22=-1/(((Temp_22+273)/298)*59)
pHMult_23=-1/(((Temp_23+273)/298)*59)
pHMult_24=-1/(((Temp_24+273)/298)*59)
pHMult_25=-1/(((Temp_25+273)/298)*59)
```

; Apply the Temperature Correction Multiplier to the Measured pH

```
pH_1=pH_mV_1*pHMult_1
pH_2=pH_mV_2*pHMult_2
pH_3=pH_mV_3*pHMult_3
pH_4=pH_mV_4*pHMult_4
pH_5=pH_mV_5*pHMult_5
pH_6=pH_mV_6*pHMult_6
pH_7=pH_mV_7*pHMult_7
pH_8=pH_mV_8*pHMult_8
pH_9=pH_mV_9*pHMult_9
pH_10=pH_mV_10*pHMult_10
pH_11=pH_mV_11*pHMult_11
pH_12=pH_mV_12*pHMult_12
pH_13=pH_mV_13*pHMult_13
pH_14=pH_mV_14*pHMult_14
pH_15=pH_mV_15*pHMult_15
pH_16=pH_mV_16*pHMult_16
pH_17=pH_mV_17*pHMult_17
pH_18=pH_mV_18*pHMult_18
pH_19=pH_mV_19*pHMult_19
pH_20=pH_mV_20*pHMult_20
pH_21=pH_mV_21*pHMult_21
pH_22=pH_mV_22*pHMult_22
pH_23=pH_mV_23*pHMult_23
pH_24=pH_mV_24*pHMult_24
pH_25=pH_mV_25*pHMult_25
```

; Use an Offset of 7 initially as shown below. Adjust the Offset as necessary during probe calibration.

```
pH_1=pH_1+7.00
pH_2=pH_2+7.00
pH_3=pH_3+7.00
pH_4=pH_4+7.00
pH_5=pH_5+7.00
pH_6=pH_6+7.00
pH_7=pH_7+7.00
pH_8=pH_8+7.00
pH_9=pH_9+7.00
pH_10=pH_10+7.00
pH_11=pH_11+7.00
pH_12=pH_12+7.00
pH_13=pH_13+7.00
pH_14=pH_14+7.00
pH_15=pH_15+7.00
pH_16=pH_16+7.00
pH_17=pH_17+7.00
pH_18=pH_18+7.00
pH_19=pH_19+7.00
pH_20=pH_20+7.00
pH_21=pH_21+7.00
pH_22=pH_22+7.00
pH_23=pH_23+7.00
pH_24=pH_24+7.00
pH_25=pH_25+7.00
```

59: End (P95)

60: Do (P86)

1: 57 Set Port 7 Low

;\*\*\*\*\*

## D.2.1 Station 3Ba data logger program

```
61: Signature (P19)
1: 77   Loc [ ProgSig ]

62: Batt Voltage (P10)
1: 78   Loc [ BatVolt ]

; OUTPUT *****

63: Do (P86)
1: 10   Set Output Flag High (Flag 0)

64: Set Active Storage Area (P80)^9974
1: 1    Final Storage Area 1
2: 167  Array ID

65: Real Time (P77)^13014
1: 1100 Year,Day (midnight = 0000)

66: Time (P18)
1: 1    Minutes into current day (maximum 1440)
2: 0000 Mod/By
3: 12   Loc [ Minute ]

67: Sample (P70)^19131
1: 1    Reps
2: 12   Loc [ Minute ]

68: Sample (P70)^3577
1: 1    Reps
2: 78   Loc [ BatVolt ]

69: Sample (P70)^29072
1: 1    Reps
2: 77   Loc [ ProgSig ]

70: Sample (P70)^4789
1: 64   Reps
2: 13   Loc [ Temp_1 ]

71: Sample (P70)^27532
1: 25   Reps
2: 148  Loc [ EC_T_1 ]

72: Sample (P70)^15665
1: 25   Reps
2: 223  Loc [ pH_mV_1 ]

73: Sample (P70)^7621
1: 25   Reps
2: 198  Loc [ pH_1 ]

74: Do (P86)
1: 20   Set Output Flag Low (Flag 0)

; ***** OUTPUT TO STORAGE MODULE *****
75: Serial Out (P96)
1: 71   Storage Module

* Table 3 Subroutines

End Program
```

D.2.2 Station 3Da

```

;{CR10X}
;
; TYPE 3 SOUTH BASAL DRAIN
; Station: 3Da
; Data Logger: CR10X #32166

; Matt Neuner May 1, 2007

; SUMMARY
; Flow: A tipping bucket flow gauge and paddlewheel flow gauge measure flow at both the north and south drain.
; This program measures every pulse from both flow gauges at each drain, so it will likely become necessary
; to tally pulses over a minute interval if the flow rates become higher.
; Electrical Conductivity: A probe measures EC at each drain.
; Water Temperature: A thermistor in each EC cell measures water temperature.
; pH: South drain only

; Ports -- see wiring diagram

; Version 5 Edits: Paddlewheel pulses totalized per minute

* Table 1 Program
01: 0.125 Execution Interval (seconds)

; Paddlewheel Flow Gauge NORTH DRAIN *****
; Check for pulse in last 0.125sec, output total per minute

1: Pulse (P3)
1: 1 Reps
2: 1 Pulse Channel 1
3: 2 Switch Closure, All Counts
4: 1 Loc [ PW_2 ]
5: 1.0 Mult
6: 0.0 Offset

PW_2sec=PW_2sec+PW_2

2: If time is (P92)
1: 0 Minutes (Seconds --) into a
2: 1 Interval (same units as above)
3: 30 Then Do

3: If (X<=>F) (P89)
1: 18 X Loc [ PW_2sec ]
2: 3 >=
3: 1 F
4: 30 Then Do

4: Do (P86)
1: 10 Set Output Flag High (Flag 0)

5: Set Active Storage Area (P80)^25669
1: 1 Final Storage Area 1
2: 42 Array ID

6: Real Time (P77)^26457
1: 0100 Day (midnight = 0000)

7: Time (P18)
1: 1 Minutes into current day (maximum 1440)
2: 0000 Mod/By
3: 16 Loc [ Minute ]
```

## D.2.2 Station 3Da data logger program

```
8: Sample (P70)^7643
1: 1 Reps
2: 16 Loc [ Minute ]

9: Real Time (P77)^14759
1: 0001 Seconds (midnight = 0000)

10: Sample (P70)^23601
1: 1 Reps
2: 18 Loc [ PW_2sec ]

; Reset second totalizer
PW_2sec=0

11: End (P95)

12: End (P95)

; Tipping Bucket Flow Gauge NORTH DRAIN *****
; Check for pulse in last second

13: Pulse (P3)
1: 1 Reps
2: 6 Control Port 6 (switch closure only)
3: 2 Switch Closure, All Counts
4: 2 Loc [ TB_14 ]
5: 1.0 Mult
6: 0.0 Offset

14: If (X<=>F) (P89)
1: 2 X Loc [ TB_14 ]
2: 3 >=
3: 1 F
4: 30 Then Do

15: Do (P86)
1: 10 Set Output Flag High (Flag 0)

16: Set Active Storage Area (P80)^13899
1: 1 Final Storage Area 1
2: 14 Array ID

17: Real Time (P77)^28327
1: 0100 Day (midnight = 0000)

18: Time (P18)
1: 1 Minutes into current day (maximum 1440)
2: 0000 Mod/By
3: 16 Loc [ Minute ]

19: Sample (P70)^17369
1: 1 Reps
2: 16 Loc [ Minute ]

20: Real Time (P77)^511
1: 0001 Seconds (midnight = 0000)

21: End (P95)

; Paddlewheel Flow Gauge SOUTH DRAIN *****
; Check for pulse in last 0.125 seconds, output total per minute

22: Pulse (P3)
1: 1 Reps
2: 2 Pulse Channel 2
3: 2 Switch Closure, All Counts
4: 3 Loc [ PW_3 ]
5: 1.0 Mult
```

## D.2.2 Station 3Da data logger program

```
6: 0.0   Offset

PW_3sec=PW_3sec+PW_3

23: If time is (P92)
1: 0     Minutes (Seconds --) into a
2: 1     Interval (same units as above)
3: 30    Then Do

24: If (X<=>F) (P89)
1: 19    X Loc [ PW_3sec ]
2: 3     >=
3: 1     F
4: 30    Then Do

25: Do (P86)
1: 10    Set Output Flag High (Flag 0)

26: Set Active Storage Area (P80)^7596
1: 1     Final Storage Area 1
2: 43    Array ID

27: Real Time (P77)^4244
1: 0100  Day (midnight = 0000)

28: Time (P18)
1: 1     Minutes into current day (maximum 1440)
2: 0000  Mod/By
3: 16    Loc [ Minute ]

29: Sample (P70)^27127
1: 1     Reps
2: 16    Loc [ Minute ]

30: Real Time (P77)^4728
1: 0001  Seconds (midnight = 0000)

31: Sample (P70)^11450
1: 1     Reps
2: 19    Loc [ PW_3sec ]

; Reset second totalizer
PW_3sec=0

32: End (P95)

33: End (P95)

; Tipping Bucket Flow Gauge SOUTH DRAIN *****
; Check for pulse in last 0.125 seconds

34: Pulse (P3)
1: 1     Reps
2: 7     Control Port 7 (switch closure only)
3: 2     Switch Closure, All Counts
4: 4     Loc [ TB_15 ]
5: 1.0   Mult
6: 0.0   Offset

35: If (X<=>F) (P89)
1: 4     X Loc [ TB_15 ]
2: 3     >=
3: 1     F
4: 30    Then Do

36: Do (P86)
1: 10    Set Output Flag High (Flag 0)

37: Set Active Storage Area (P80)^20270
```

## D.2.2 Station 3Da data logger program

1: 1 Final Storage Area 1  
2: 15 Array ID

38: Real Time (P77)^21255  
1: 0100 Day (midnight = 0000)

39: Time (P18)  
1: 1 Minutes into current day (maximum 1440)  
2: 0000 Mod/By  
3: 16 Loc [ Minute ]

40: Sample (P70)^22810  
1: 1 Reps  
2: 16 Loc [ Minute ]

41: Real Time (P77)^23033  
1: 0001 Seconds (midnight = 0000)

42: End (P95)

; Output to Storage Module \*\*\*\*\*  
; instr 96, code71 to output to storage mod

43: Serial Out (P96)  
1: 71 Storage Module

\* Table 2 Program

02: 600 Execution Interval (seconds)

; Table 2 executed every 10 minutes.

; Output Timing Flag -- Use this time interval to control the timing of the output.

1: If time is (P92)  
1: 0 Minutes (Seconds --) into a  
2: 30 Interval (same units as above)  
3: 11 Set Flag 1 High

; If Time loop over Table 2 -- Use this instruction to take less measurements during winter.

; Interval must be a number divisible by the execution interval (in minutes).

2: If time is (P92)  
1: 0000 Minutes (Seconds --) into a  
2: 10 Interval (same units as above)  
3: 30 Then Do

; ELECTRICAL CONDUCTIVITY \*\*\*\*\*

3: Full Bridge w/mv Excit (P9)  
1: 1 Reps  
2: 5 2500 mV Slow Ex Range  
3: 5 2500 mV Slow Br Range  
4: 1 DIFF Channel  
5: 2 Excite all reps w/Exchan 2  
6: 2500 mV Excitation  
7: 5 Loc [ V2\_V1 ]  
8: 1 Mult  
9: 0.0 Offset

; The output from the full bridge measurement is 1000 times the ratio of V2/V1.  
; This is the ratio between the potential measured by the central electrodes  
; in the water and the potential measured by the outer electrodes in the solution,  
; in series with the reference resistor. Multiplying by the reference resistance  
; yields the resistance in the flow-through cell.

4: Z=X\*F (P37)

## D.2.2 Station 3Da data logger program

```
1: 5    X Loc [ V2_V1  ]
2: 0.001 F
3: 5    Z Loc [ V2_V1  ]
```

```
5: Z=X*F (P37)
1: 5    X Loc [ V2_V1  ]
2: 469.5 F
3: 6    Z Loc [ Rs     ]
```

```
; Conductance = cell constant (k) / resistance of solution
; k is determined by Equation ** from Won (1987).
; For the Divaik probes, k = 1.884m^-1
```

```
6: Z=1/X (P42)
1: 6    X Loc [ Rs     ]
2: 7    Z Loc [ EC_27  ]
```

```
7: Z=X*F (P37)
1: 7    X Loc [ EC_27  ]
2: 1.884 F
3: 7    Z Loc [ EC_27  ]
```

```
8: Z=X*F (P37)
1: 7    X Loc [ EC_27  ]
2: 10000 F
3: 7    Z Loc [ EC_27  ]
```

```
; Calibration Factor
9: Z=X*F (P37)
1: 7    X Loc [ EC_27  ]
2: 3.9629 F
3: 7    Z Loc [ EC_27  ]
```

```
; NORTH DRAIN EC CELL TEMPERATURE *****
```

```
10: Excite-Delay (SE) (P4)
1: 1    Repts
2: 20   Auto 60 Hz Rejection Range (Delay must be zero)(OS>1.9)
3: 5    SE Channel
4: 1    Excite all reps w/Exchan 1
5: 0    Delay (units 0.01 sec)
6: 2500 mV Excitation
7: 8    Loc [ Vin_1  ]
8: 1    Mult
9: 0.0  Offset
```

```
; Convert millivolt reading to resistance using  $R(\text{therm}) = ((V(\text{excit}) * R(\text{ref})) / V(\text{in})) - R(\text{ref})$ 
; A 10 kOhm reference resistor is used (10000 multiplier in the second P37 below).
```

```
11: Z=1/X (P42)
1: 8    X Loc [ Vin_1  ]
2: 8    Z Loc [ Vin_1  ]
```

```
12: Z=X*F (P37)
1: 8    X Loc [ Vin_1  ]
2: 2500 F
3: 8    Z Loc [ Vin_1  ]
```

```
13: Z=X+F (P34)
1: 8    X Loc [ Vin_1  ]
2: -1   F
3: 8    Z Loc [ Vin_1  ]
```

```
14: Z=X*F (P37)
1: 8    X Loc [ Vin_1  ]
2: 10000 F
```

## D.2.2 Station 3Da data logger program

```
3: 8    Z Loc [ Vin_1  ]

15: Steinhart-Hart Equation (P200)
1: 1    Repts
2: 8    -- Source Loc (R)(Ohms) [ Vin_1  ]
3: 9    -- Destination Loc (Deg C) [ ECth_26 ]
4: 1.28679 A
5: -3    x 10^n
6: 2.35938 B
7: -4    x 10^n
8: 9.4    C
9: -8    x 10^n

; SOUTH DRAIN EC CELL TEMPERATURE *****

16: Excite-Delay (SE) (P4)
1: 1    Repts
2: 20    Auto 60 Hz Rejection Range (Delay must be zero)(OS>1.9)
3: 6    SE Channel
4: 1    Excite all reps w/Exchan 1
5: 0    Delay (units 0.01 sec)
6: 2500    mV Excitation
7: 10    Loc [ Vin_2  ]
8: 1    Mult
9: 0.0    Offset

; Convert millivolt reading to resistance using  $R(\text{therm}) = ((V(\text{excit}) * R(\text{ref})) / V(\text{in})) - R(\text{ref})$ 
; A 10 kOhm reference resistor is used (10000 multiplier in the second P37 below).

17: Z=1/X (P42)
1: 10    X Loc [ Vin_2  ]
2: 10    Z Loc [ Vin_2  ]

18: Z=X*F (P37)
1: 10    X Loc [ Vin_2  ]
2: 2500    F
3: 10    Z Loc [ Vin_2  ]

19: Z=X+F (P34)
1: 10    X Loc [ Vin_2  ]
2: -1    F
3: 10    Z Loc [ Vin_2  ]

20: Z=X*F (P37)
1: 10    X Loc [ Vin_2  ]
2: 10000    F
3: 10    Z Loc [ Vin_2  ]

; Convert resistance to temperature using nonlinear relationship provided by Omega International.

21: Steinhart-Hart Equation (P200)
1: 1    Repts
2: 10    -- Source Loc (R)(Ohms) [ Vin_2  ]
3: 11    -- Destination Loc (Deg C) [ ECth_27 ]
4: 1.28679 A
5: -3    x 10^n
6: 2.35938 B
7: -4    x 10^n
8: 9.4    C
9: -8    x 10^n

; *****
; Temperature Correction for EC -- normalize data to EC at 25C
EC_25C_27=EC_T_27/(0.8703*(1+(0.0213*(ECth_27-18))))

; NORTH DRAIN pH *****
; Temperature correction is for 25C
```

## D.2.2 Station 3Da data logger program

; Calculate the Multiplier for Temperature Correction using

$$\text{pHMult\_26} = -1 / (((\text{ECth\_26} + 273) / 298) * 59)$$

22: Volt (Diff) (P2)

1: 1 Reps  
2: 5 2500 mV Slow Range  
3: 4 DIFF Channel  
4: 12 Loc [ pH\_T\_26 ]  
5: 1.0 Multiplier  
6: 0 Offset

; Apply the Temperature Correction Multiplier to the Measured pH

$$\text{pH\_25C\_26} = \text{pH\_T\_26} * \text{pHMult\_26}$$

; The following instruction applies an Offset to the pH. Use an Offset of 7  
; initially as shown below. Adjust the Offset if necessary during probe calibration.

23: Z=X+F (P34)

1: 12 X Loc [ pH\_T\_26 ]  
2: 7.1 F  
3: 12 Z Loc [ pH\_T\_26 ]

24: Z=X+F (P34)

1: 21 X Loc [ pH\_25C\_26 ]  
2: 7.1 F  
3: 21 Z Loc [ pH\_25C\_26 ]

; SOUTH DRAIN pH \*\*\*\*\*

; Calculate the Multiplier for Temperature Correction using

$$\text{pHMult\_27} = -1 / (((\text{ECth\_27} + 273) / 298) * 59)$$

25: Volt (Diff) (P2)

1: 1 Reps  
2: 5 2500 mV Slow Range  
3: 5 DIFF Channel  
4: 13 Loc [ pH\_T\_27 ]  
5: 1.0 Multiplier  
6: 0 Offset

; Apply the Temperature Correction Multiplier to the Measured pH

$$\text{pH\_25C\_27} = \text{pH\_T\_27} * \text{pHMult\_27}$$

; The following instruction applies an Offset to the pH. Use an Offset of 7  
; initially as shown below. Adjust the Offset if necessary during probe calibration.

26: Z=X+F (P34)

1: 13 X Loc [ pH\_T\_27 ]  
2: 7.1 F  
3: 13 Z Loc [ pH\_T\_27 ]

27: Z=X+F (P34)

1: 22 X Loc [ pH\_25C\_27 ]  
2: 7.1 F  
3: 22 Z Loc [ pH\_25C\_27 ]

; \*\*\*\*\*

28: Signature (P19)

1: 14 Loc [ ProgSig ]

29: Batt Voltage (P10)

1: 15 Loc [ BatVolt ]

30: Time (P18)

## D.2.2 Station 3Da data logger program

```
1: 1    Minutes into current day (maximum 1440)
2: 0000 Mod/By
3: 16   Loc [ Minute  ]

; End loop over table 2 measurements
31: End (P95)

; *****
;
; Table 2 Output
; *****

32: If Flag/Port (P91)
1: 11   Do if Flag 1 is High
2: 10   Set Output Flag High (Flag 0)

33: Set Active Storage Area (P80)^4931
1: 1    Final Storage Area 1
2: 111  Array ID

34: Real Time (P77)^21961
1: 1100 Year,Day (midnight = 0000)

35: Sample (P70)^22136
1: 1    Reps
2: 16   Loc [ Minute  ]

36: Sample (P70)^24323
1: 1    Reps
2: 15   Loc [ BatVolt  ]

37: Sample (P70)^12342
1: 1    Reps
2: 14   Loc [ ProgSig  ]

38: Sample (P70)^18421
1: 1    Reps
2: 7    Loc [ EC_27   ]

39: Sample (P70)^11927
1: 1    Reps
2: 9    Loc [ ECth_26 ]

40: Sample (P70)^601
1: 1    Reps
2: 11   Loc [ ECth_27 ]

41: Sample (P70)^4589
1: 1    Reps
2: 12   Loc [ pH_T_26 ]

42: Sample (P70)^11935
1: 1    Reps
2: 13   Loc [ pH_T_27 ]

43: Do (P86)
1: 20   Set Output Flag Low (Flag 0)

44: Do (P86)
1: 20   Set Output Flag Low (Flag 0)

45: Do (P86)
1: 21   Set Flag 1 Low

; Output to Storage Module *****
```

## *D.2.2 Station 3Da data logger program*

; instr 96, code 71 to output to storage module

46: Serial Out (P96)  
1: 71 Storage Module

\* Table 3 Subroutines

End Program

D.2.3 Station 3Db

```
;(CR510)
;
```

```
* Table 1 Program
01: 1800 Execution Interval (seconds)
```

```
1: Full Bridge w/mv Excit (P9)
```

```
1: 1 Reps
2: 5 2500 mV Slow Ex Range
3: 5 2500 mV Slow Br Range
4: 1 DIFF Channel
5: 1 Excite all reps w/Exchan 1
6: 2500 mV Excitation
7: 1 Loc [ V2_V1 ]
8: 1.0 Mult
9: 0.0 Offset
```

```
2: Z=X*F (P37)
```

```
1: 1 X Loc [ V2_V1 ]
2: 0.001 F
3: 1 Z Loc [ V2_V1 ]
```

```
3: Z=X*F (P37)
```

```
1: 1 X Loc [ V2_V1 ]
2: 470.0 F
3: 2 Z Loc [ Rs ]
```

```
4: Z=1/X (P42)
```

```
1: 2 X Loc [ Rs ]
2: 2 Z Loc [ Rs ]
```

```
5: Z=X*F (P37)
```

```
1: 2 X Loc [ Rs ]
2: 1.884 F
3: 3 Z Loc [ EC_26 ]
```

```
6: Z=X*F (P37)
```

```
1: 3 X Loc [ EC_26 ]
2: 10000 F
3: 3 Z Loc [ EC_26 ]
```

```
7: Z=X*F (P37)
```

```
1: 3 X Loc [ EC_26 ]
2: 3.9629 F
3: 3 Z Loc [ EC_26 ]
```

```
;*****
```

```
8: Batt Voltage (P10)
```

```
1: 5 Loc [ BatVolt ]
```

```
9: Signature (P19)
```

```
1: 6 Loc [ ProgSig ]
```

```
;*****
```

```
10: Do (P86)
```

```
1: 10 Set Output Flag High (Flag 0)
```

```
11: Set Active Storage Area (P80)^21978
```

```
1: 1 Final Storage Area 1
2: 176 Array ID
```

### *D.2.3 Station 3Db data logger program*

```
12: Real Time (P77)^18184
1: 1100 Year,Day (midnight = 0000)

13: Time (P18)
1: 1 Minutes into current day (maximum 1440)
2: 0000 Mod/By
3: 4 Loc [ Minute ]

14: Sample (P70)^18736
1: 1 Reps
2: 4 Loc [ Minute ]

15: Sample (P70)^32646
1: 1 Reps
2: 5 Loc [ BatVolt ]

16: Sample (P70)^2037
1: 1 Reps
2: 6 Loc [ ProgSig ]

17: Sample (P70)^4696
1: 1 Reps
2: 3 Loc [ EC_26 ]

18: Do (P86)
1: 20 Set Output Flag Low (Flag 0)

* Table 2 Program
02: 00 Execution Interval (seconds)

* Table 3 Subroutines

End Program
```

D.2.4 Station 3Ta

```

;{CR10X}

; Diavik Diamond Mines Waste Rock Constructed Pile Expiement
; Matt Neuner's adaptation of Craig Nichol and Joe Marcoline's program UBC1V12W.CSI

; Datalogger: 3Ta = CR10X SN:29498

; This program is written for Time Domain Reflectometry (TDR) measurement of soil moisture content, a rain gauge, and 4
; tensiometers.
; Thirteen TDR probes are controlled by a Moisture-Point 917 instrument (MP-917). The MP-917 is connected to a Campbell
; Scientific
; CR10X datalogger via an interconnect module. The probes are connected to the MP-917 via two SDMX50 multiplexers.
;
;
; Ports:
; C6, C7: serial communication with MP-917
; C8: power control to MP-917
; C1, C2, C3: SDMX50 addressing
; P1: Rain Gauge
; SE1: Thermistor for hut temperature
; SE2 to SE5: Tensiometer input, with a 120 Ohm resistor to G
;
;
; TDR Output:
; Array ID (51 to 63), year, day, minute, diode difference travel time, standard deviation
;
; Note that the calibration data for each probe must be applied individually with the soil calibration function
; to determine the volumetric moisture content.
;
; Rain Gauge Output:
; 24, year, day, minute, cummulative daily rainfall (mm) (output at each 0.1mm)
; 34, year, day, minute, total daily rainfall (mm) (output at end of day)
;
; Datalogger Status Output:
; 131, year, day, hourminute, battery voltage, program signiture, hut temp

* Table 1 Program
01: 1.00 Execution Inerval (seconds)

; RAIN GAUGE *****
; *****

;Reset Daily rainfall total

1: If time is (P92)
1: 0000 Minutes (Seconds --) into a
2: 1440 Interval (same units as above)
3: 30 Then Do
RainLast=Rainfall
Rainfall=0

2: End (P95)

;Check for rainfall tip in last 1 second

3: Pulse (P3)
1: 1 Reps
2: 1 Pulse Channel 1
3: 2 Switch Closure, All Counts
4: 156 Loc [ Rain ]
5: 1.0 Mult
6: 0.0 Offset

4: If (X<=>F) (P89)
1: 156 X Loc [ Rain ]

```

## D.2.4 Station 3Ta data logger program

```
2: 2    <>
3: 0.0  F
4: 30   Then Do
;      Add to daily rainfall total

Rainfall=Rainfall+0.1

;*****
; Output
; 24, year, day, minute, Cumulative daily rain output at each 0.1mm

5: Do (P86)
1: 10   Set Output Flag High (Flag 0)

6: Set Active Storage Area (P80)^23867
1: 1    Final Storage Area 1
2: 24   Array ID

7: Time (P18)
1: 1    Minutes into current day (maximum 1440)
2: 0000 Mod/By
3: 151  Loc [ Minute ]

8: Time (P18)
1: 0    Seconds into current minute (maximum 60)
2: 0000 Mod/By
3: 152  Loc [ Second ]
Minute=Minute+(Second/60)

9: Real Time (P77)^23347
1: 1100 Year,Day (midnight = 0000)

10: Sample (P70)^20516
1: 1    Reps
2: 151  Loc [ Minute ]

11: Sample (P70)^19444
1: 1    Reps
2: 157  Loc [ Rainfall ]

12: End (P95)

;*****
; Output
; 34, year, day, minute, daily rain total

13: If time is (P92)
1: 1439 Minutes (Seconds --) into a
2: 1440 Interval (same units as above)
3: 30   Then Do

14: Do (P86)
1: 10   Set Output Flag High (Flag 0)

15: Set Active Storage Area (P80)^2107
1: 1    Final Storage Area 1
2: 34   Array ID

16: Time (P18)
1: 1    Minutes into current day (maximum 1440)
2: 0000 Mod/By
3: 151  Loc [ Minute ]

17: Time (P18)
1: 0    Seconds into current minute (maximum 60)
2: 0000 Mod/By
```

## D.2.4 Station 3Ta data logger program

```
3: 152   Loc [ Second ]
Minute=Minute+(Second/60)

18: Real Time (P77)^817
1: 1100   Year,Day (midnight = 0000)

19: Sample (P70)^8949
1: 1     Reps
2: 151   Loc [ Minute ]

20: Sample (P70)^18103
1: 1     Reps
2: 157   Loc [ Rainfall ]

21: End (P95)

; DATALOGGER STATUS *****
; *****
; Hut Temperature

22: If time is (P92)
1: 0000   Minutes (Seconds --) into a
2: 480   Interval (same units as above)
3: 30    Then Do

23: Excite-Delay (SE) (P4)
1: 1     Reps
2: 20    Auto 60 Hz Rejection Range (Delay must be zero)(OS>1.9)
3: 1     SE Channel
4: 1     Excite all reps w/Exchan 1
5: 0     Delay (units 0.01 sec)
6: 2500  mV Excitation
7: 162   Loc [ Vin_1 ]
8: 1     Mult
9: 0.0   Offset

; Convert millivolt reading to resistance using  $R(\text{therm}) = ((V(\text{excit}) * R(\text{ref})) / V(\text{in})) - R(\text{ref})$ 
; A 10 kOhm reference resistor is used (10000 multiplier in the second P37 below).

24: Z=1/X (P42)
1: 162   X Loc [ Vin_1 ]
2: 162   Z Loc [ Vin_1 ]

25: Z=X*F (P37)
1: 162   X Loc [ Vin_1 ]
2: 2500  F
3: 162   Z Loc [ Vin_1 ]

26: Z=X+F (P34)
1: 162   X Loc [ Vin_1 ]
2: -1    F
3: 162   Z Loc [ Vin_1 ]

27: Z=X*F (P37)
1: 162   X Loc [ Vin_1 ]
2: 10030 F
3: 162   Z Loc [ Vin_1 ]

28: Steinhart-Hart Equation (P200)
1: 1     Reps
2: 162   Source Loc (R)(Ohms) [ Vin_1 ]
3: 163   Destination Loc (Deg C) [ HutTemp ]
4: 1.28679 A
5: -3    x 10^n
6: 2.35938 B
7: -4    x 10^n
8: 9.4   C
9: -8    x 10^n
```

## D.2.4 Station 3Ta data logger program

```
29: Batt Voltage (P10)
1: 150   Loc [ Batt_Volt ]

30: Signature (P19)
1: 10   Loc [ ProgSig ]

; ***** OUTPUT *****

31: Do (P86)
1: 10   Set Output Flag High (Flag 0)

32: Set Active Storage Area (P80)^24842
1: 1    Final Storage Area 1
2: 131  Array ID

33: Real Time (P77)^12923
1: 1110 Year,Day,Hour/Minute (midnight = 0000)

34: Sample (P70)^20971
1: 1    Reps
2: 150  Loc [ Batt_Volt ]

35: Sample (P70)^22119
1: 1    Reps
2: 10   Loc [ ProgSig ]

36: Sample (P70)^26036
1: 1    Reps
2: 163  Loc [ HutTemp ]

37: Do (P86)
1: 20   Set Output Flag Low (Flag 0)

38: End (P95)

* Table 2 Program
02: 1    Execution Interval (seconds)

; *****
; SOIL MOISTURE CONTENT by Time Domain Reflectometry (TDR)

1: If time is (P92)
1: 0000 Minutes (Seconds --) into a
2: 30   Interval (same units as above)
3: 30   Then Do

; *****
; Machine warm up

2: Beginning of Loop (P87)
1: 0000 Delay
2: 4    Loop Count

;Turn on MP-917
3: Do (P86)
1: 48   Set Port 8 High

;Wait 20 seconds
4: Beginning of Loop (P87)
1: 1    Delay
2: 20   Loop Count
```

## D.2.4 Station 3Ta data logger program

```
;End machine on loop
5: End (P95)

6: Do (P86)
1: 58   Set Port 8 Low

;Wait two seconds
7: Beginning of Loop (P87)
1: 1   Delay
2: 2   Loop Count

;End wait loop
8: End (P95)

;End of the (four measurement discard) loop
9: End (P95)

TDRProbe=0
RawTime=0
SDMChannl=0

;*****
;First Loop for probes 1-7

10: Beginning of Loop (P87)
1: 0000 Delay
2: 7   Loop Count

; The SDMX50 automatically increments to the next channel.

11: SDMX50 Channel Select (P109)
1: 00   SDM Address
2: 1   SDM Channel

;Call the measurement subroutine (Subroutine 91)

12: Do (P86)
1: 91   Call Subroutine 91
;*****

; DATA OUTPUT
; In this example program, the program sets a complete time stamp on
; the data.

13: Time (P18)
1: 1   Minutes into current day (maximum 1440)
2: 0000 Mod/By
3: 151 Loc [ Minute ]

; Set output flag
14: Do (P86)
1: 10   Set Output Flag High (Flag 0)

; Array ID is used to label each probe.
15: Set Active Storage Area (P80)^8112
1: 1   Final Storage Area 1
2: 51  -- Array ID

16: Real Time (P77)^21845
1: 1100 Year.Day (midnight = 0000)

17: Sample (P70)^799
1: 1   Reps
2: 151 Loc [ Minute ]

18: Resolution (P78)
```

## D.2.4 Station 3Ta data logger program

```
1: 1    High Resolution

19: Sample (P70)^26986
1: 1    Reps
2: 167  Loc [ AvgTime ]

20: Sample (P70)^24581
1: 1    Reps
2: 168  Loc [ StdTime ]

;End Probes 1-7 loop
21: End (P95)

;*****

;Select probes connected to second SDMX50
;Second SDMX50 is connected to channel #8 on the first SDMX50 (Address 00)

;Set the first SDMX50 Channel

22: SDMX50 Channel Select (P109)
1: 00    SDM Address
2: 8     SDM Channel

;Loop for probes 8 - 13

23: Beginning of Loop (P87)
1: 0000  Delay
2: 6     Loop Count

24: SDMX50 Channel Select (P109)
1: 01    SDM Address
2: 1    -- SDM Channel

25: Do (P86)
1: 91    Call Subroutine 91

; *****
; DATA OUTPUT

26: Time (P18)
1: 1     Minutes into current day (maximum 1440)
2: 0000  Mod/By
3: 151   Loc [ Minute ] ;

; Set output flag
27: Do (P86)
1: 10    Set Output Flag High (Flag 0)

; Output the moisture from the current probe using label 81.
28: Set Active Storage Area (P80)^24772
1: 1     Final Storage Area 1
2: 58    -- Array ID

29: Real Time (P77)^5111
1: 1100  Year,Day (midnight = 0000)

30: Sample (P70)^11344
1: 1     Reps
2: 151   Loc [ Minute ]

31: Resolution (P78)
1: 1     High Resolution

32: Sample (P70)^13114
1: 1     Reps
2: 167   Loc [ AvgTime ]
```

## D.2.4 Station 3Ta data logger program

```
33: Sample (P70)^22163
1: 1    Reps
2: 168  Loc [ StdTime ]

;End of loop for probes 8-13
34: End (P95)

; ***** SOIL TENSION MEASUREMENTS *****
; Four tensiometers, installed July 2007, at depths of 0.6m and 1.2m.

35: Volt (SE) (P1)
1: 4    Reps
2: 5    2500 mV Slow Range
3: 2    SE Channel
4: 4    -- Loc [ Tension_4 ]
5: 0.0521 Multiplier
6: -25  Offset

; ***** OUTPUT *****

36: Do (P86)
1: 10   Set Output Flag High (Flag 0)

37: Set Active Storage Area (P80)^1813
1: 1    Final Storage Area 1
2: 121  Array ID

38: Real Time (P77)^18212
1: 1110 Year,Day,Hour/Minute (midnight = 0000)

39: Sample (P70)^20996
1: 4    Reps
2: 4    Loc [ Tension_4 ]

; *****

; End if time is 30 min loop.
40: End (P95)

* Table 3 Subroutines

; *****
; SUBROUTINE TDRMEASUREMENT #91
;
; Takes a three measurements of moisture and stores the
; average and standard deviation from a type one probe.

1: Beginning of Subroutine (P85)
1: 91   Subroutine 91

; Zero the moisture content

RawTime_1=0
RawTime_2=0
RawTime_3=0

; *****
; Take Measurements

2: Beginning of Loop (P87)
```

## D.2.4 Station 3Ta data logger program

```
1: 0000 Delay
2: 3 Count(s)

; *****
;
;
; START MEASUREMENT
; Turn the instrument on.
; Port 8 controls power to the MP-917 through the interconnect
; module

3: Do (P86)
1: 48 Set Port 8 High

; Delay Loop. Prevents the datalogger from reading the initial
; instrument identification data. Timed for 15 seconds to skip
; over the 15 second warm-up time.

4: Beginning of Loop (P87)
1: 1 Delay
2: 15 Count(s)

5: End (P95)

; Read serial data from the MP-917

6: Port Serial I/O (P15)
1: 1 Reps
2: 1 ASCII/RS-232, 1200 Baud
3: 0000 CTS/Delay
4: 6 First Control Port
5: 164 -- Output Loc [ RawTime_1 ]
6: 0000 No. of Locs to Send
7: 13 Termination Character
8: 100 Maximum Characters
9: 9500 CTS/Input Wait
10: 164 -- Loc [ RawTime_1 ]
11: 1.0 Mult
12: 0.0 Offset

; Turn the MP-917 off, and wait for the power down. The instrument
; needs time to settle after power off before it starts another
; measurement.

7: Do (P86)
1: 58 Set Port 8 Low

; Power down wait loop, 2 seconds wait
8: Beginning of Loop (P87)
1: 1 Delay
2: 2 Count(s)
; End delay loop
9: End (P95)

; END SINGLE MEASUREMENT
; *****

; End of loop to do three measurements per probe.
10: End (P95)

; *****
; Calculate Average and Standard Deviation
; The lengthy calculation allows the avg. and std.dev. to be calculated correctly while being able to
; discard any unreasonable data that may result from electronic noise.

AvgTime=0
```

## D.2.4 Station 3Ta data logger program

```
StdTime=0
GOOD=0
Sum=0
SUMSQUARE=0
Square=0

11: Beginning of Loop (P87)
1: 0000 Delay
2: 3 Count(s)

12: IF (X<=>F) (P89)
1: 164 -- X Loc [ RawTime_1 ]
2: 3 >=
3: 0.0 F
4: 30 Then Do

13: IF (X<=>F) (P89)
1: 164 -- X Loc [ RawTime_1 ]
2: 4 <
3: 20 F
4: 30 Then Do

14: Z=X+Y (P33)
1: 165 X Loc [ Sum ]
2: 164 --yrLoc [ RawTime_1 ]
3: 165 Z Loc [ Sum ]

15: Z=X*Y (P36)
1: 164 -- X Loc [ RawTime_1 ]
2: 164 --yrLoc [ RawTime_1 ]
3: 166 Z Loc [ Square ]

16: Z=X+Y (P33)
1: 173 X Loc [ SUMSQUARE ]
2: 166 yrLoc [ Square ]
3: 173 Z Loc [ SUMSQUARE ]

17: Z=Z+1 (P32)
1: 172 Z Loc [ GOOD ]

; End if <20 loop
18: End (P95)

; End if > 0 loop

19: End (P95)

; End add three measurements loop
20: End (P95)

21: Z=X/Y (P38)
1: 165 X Loc [ Sum ]
2: 172 yrLoc [ GOOD ]
3: 167 Z Loc [ AvgTime ]

22: Z=X*Y (P36)
1: 167 X Loc [ AvgTime ]
2: 167 yrLoc [ AvgTime ]
3: 174 Z Loc [ SqAvg ]

23: Z=X/Y (P38)
1: 173 X Loc [ SUMSQUARE ]
2: 172 yrLoc [ GOOD ]
3: 175 Z Loc [ SumSqAvg ]

24: Z=X-Y (P35)
1: 175 X Loc [ SumSqAvg ]
```

## D.2.4 Station 3Ta data logger program

```
2: 174  yrLoc [ SqAvg  ]  
3: 176  Z Loc [ Diff  ]  
  
25: Z=SQRT(X) (P39)  
1: 176  X Loc [ Diff  ]  
2: 168  Z Loc [ StdTime ]
```

```
; End of measurement routine
```

```
, *****
```

```
; End Subroutine 91  
26: End (P95)
```

```
End Program
```

## D.2.5 Station 1Ta

```
;(CR10X)

; Diavik Diamond Mines Waste Rock Constructed Pile Expiement
; Matt Neuner's adaptation of Craig Nichol and Joe Marcoline's program UBC1V12W.CSI

; Datalogger: 1Ta = CR10X SN:29497

; This program is written for Time Domain Reflectometry (TDR) measurement of soil moisture content. Ten probes are
; controlled by a Moisture-Point 917 instrument (MP-917). The MP-917 is connected to a Campbell Scientific CR10X datalogger
; via an interconnect module. The probes are connected to the MP-917 via two SDMX50 multiplexers.
; See _____ for diagram.
;
; Table 1 is used only for a time stamp in the winter.
;
; Ports:
; C6, C7: serial communication with MP-917
; C8: power control to MP-917
; C1, C2, C3: SDMX50 addressing
; P1: Rain Gauge
; SE1: Thermistor for hut temperature
;
;
;
; TDR Output:
; Array ID (79 to 88), year, day, minute, diode difference travel time, standard deviation
;
; Note that the calibration data for each probe must be applied individually
; to determine moisture content.
;
; Rain Gauge Output:
; 25, year, day, minute, cummulative daily rainfall (mm) (output at each 0.1mm)
; 35, year, day, minute, total daily rainfall (mm) (output at end of day)
;
; Datalogger Status Output:
; 132. year, day, battery voltage, program signiture, hut temp

* Table 1 Program
01: 1.00 Execution Inerval (seconds)

; RAIN GAUGE *****
; *****

;Reset Daily rainfall total

1: If time is (P92)
1: 0000 Minutes (Seconds --) into a
2: 1440 Interval (same units as above)
3: 30 Then Do
RainLast=Rainfall
Rainfall=0

2: End (P95)

;Check for rainfall tip in last 1 second

3: Pulse (P3)
1: 1 Reps
2: 1 Pulse Channel 1
3: 2 Switch Closure, All Counts
4: 156 Loc [ Rain ]
5: 1.0 Mult
6: 0.0 Offset

4: If (X<=>F) (P89)
```

## D.2.5 Station ITa data logger program

```
1: 156   X Loc [ Rain   ]
2: 2     <>
3: 0.0   F
4: 30    Then Do
;       Add to daily rainfall total

Rainfall=Rainfall+0.1

;*****
; Output
; 25, year, day, minute, cummilative daily rainfall

5: Do (P86)
1: 10    Set Output Flag High (Flag 0)

6: Set Active Storage Area (P80)^10555
1: 1     Final Storage Area 1
2: 25    Array ID

7: Time (P18)
1: 1     Minutes into current day (maximum 1440)
2: 0000  Mod/By
3: 151   Loc [ Minute  ]

8: Time (P18)
1: 0     Seconds into current minute (maximum 60)
2: 0000  Mod/By
3: 152   Loc [ Second  ]
Minute=Minute+(Second/60)

9: Real Time (P77)^23347
1: 1100  Year,Day (midnight = 0000)

10: Sample (P70)^20516
1: 1     Reps
2: 151   Loc [ Minute  ]

11: Sample (P70)^19444
1: 1     Reps
2: 157   Loc [ Rainfall ]

12: End (P95)

;*****
; Output
; 35, year, day, minute, daily rain total

13: If time is (P92)
1: 1439  Minutes (Seconds --) into a
2: 1440  Interval (same units as above)
3: 30    Then Do

14: Do (P86)
1: 10    Set Output Flag High (Flag 0)

15: Set Active Storage Area (P80)^8975
1: 1     Final Storage Area 1
2: 35    Array ID

16: Time (P18)
1: 1     Minutes into current day (maximum 1440)
2: 0000  Mod/By
3: 151   Loc [ Minute  ]

17: Time (P18)
1: 0     Seconds into current minute (maximum 60)
2: 0000  Mod/By
```

## D.2.5 Station 1Ta data logger program

```
3: 152   Loc [ Second ]
Minute=Minute+(Second/60)

18: Real Time (P77)^13760
1: 1100   Year,Day (midnight = 0000)

19: Sample (P70)^30233
1: 1     Reps
2: 151   Loc [ Minute ]

20: Sample (P70)^22826
1: 1     Reps
2: 157   Loc [ Rainfall ]

21: End (P95)

; DATALOGGER STATUS *****
; *****
; Hut Temperature

22: If time is (P92)
1: 0000   Minutes (Seconds --) into a
2: 480   Interval (same units as above)
3: 30    Then Do

23: Excite-Delay (SE) (P4)
1: 1     Reps
2: 20    Auto 60 Hz Rejection Range (Delay must be zero)(OS>1.9)
3: 1     SE Channel
4: 1     Excite all reps w/Exchan 1
5: 0     Delay (units 0.01 sec)
6: 2500  mV Excitation
7: 162   Loc [ Vin_1 ]
8: 1     Mult
9: 0.0   Offset

; Convert millivolt reading to resistance using  $R(\text{therm}) = ((V(\text{excit}) * R(\text{ref})) / V(\text{in})) - R(\text{ref})$ 
; A 10 kOhm reference resistor is used (10000 multiplier in the second P37 below).

24: Z=1/X (P42)
1: 162   X Loc [ Vin_1 ]
2: 162   Z Loc [ Vin_1 ]

25: Z=X*F (P37)
1: 162   X Loc [ Vin_1 ]
2: 2500  F
3: 162   Z Loc [ Vin_1 ]

26: Z=X+F (P34)
1: 162   X Loc [ Vin_1 ]
2: -1    F
3: 162   Z Loc [ Vin_1 ]

27: Z=X*F (P37)
1: 162   X Loc [ Vin_1 ]
2: 10030 F
3: 162   Z Loc [ Vin_1 ]

28: Steinhart-Hart Equation (P200)
1: 1     Reps
2: 162   Source Loc (R)(Ohms) [ Vin_1 ]
3: 163   Destination Loc (Deg C) [ HutTemp ]
4: 1.28679 A
5: -3    x 10^n
6: 2.35938 B
7: -4    x 10^n
8: 9.4   C
9: -8    x 10^n
```

## D.2.5 Station 1Ta data logger program

```
29: End (P95)

; *****
; MAIN TIME STAMP

30: If time is (P92)
1: 1   Minutes (Seconds --) into a
2: 480 Interval (same units as above)
3: 30  Then Do

31: Batt Voltage (P10)
1: 150  Loc [ Batt_Volt ]

32: Signature (P19)
1: 10   Loc [ ProgSig ]

33: Time (P18)
1: 2    Hours into current year { maximum 8784}
2: 0    -- Mod/By
3: 11   Loc [ hour   ]

34: Z=X*F (P37)
1: 11   X Loc [ hour   ]
2: 0.0416 F
3: 12   Z Loc [ JD     ]

35: Do (P86)
1: 10   Set Output Flag High (Flag 0)

36: Set Active Storage Area (P80)^21970
1: 1    Final Storage Area 1
2: 131  Array ID

37: Real Time (P77)^12923
1: 1000 Year (midnight = 0000)

38: Sample (P70)^270
1: 1    Reps
2: 12   Loc [ JD     ]

39: Sample (P70)^20971
1: 1    Reps
2: 150  Loc [ Batt_Volt ]

40: Sample (P70)^22119
1: 1    Reps
2: 10   Loc [ ProgSig ]

41: Sample (P70)^26036
1: 1    Reps
2: 163  Loc [ HutTemp ]

42: Do (P86)
1: 20   Set Output Flag Low (Flag 0)

43: End (P95)

* Table 2 Program
02: 1    Execution Interval (seconds)

; *****
; SOIL MOISTURE CONTENT by Time Domain Reflectometry (TDR)
```

## D.2.5 Station 1Ta data logger program

```
1: If time is (P92)
1: 0000 Minutes (Seconds --) into a
2: 30 Interval (same units as above)
3: 30 Then Do

;*****
; Machine warm up

2: Beginning of Loop (P87)
1: 0000 Delay
2: 4 Loop Count

;Turn on MP-917
3: Do (P86)
1: 48 Set Port 8 High

;Wait 20 seconds
4: Beginning of Loop (P87)
1: 1 Delay
2: 20 Loop Count

;End machine on loop
5: End (P95)

6: Do (P86)
1: 58 Set Port 8 Low

;Wait two seconds
7: Beginning of Loop (P87)
1: 1 Delay
2: 2 Loop Count

;End wait loop
8: End (P95)

;End of the (four measurement discard) loop
9: End (P95)

;*****
;First Loop for probes 1-7

10: Beginning of Loop (P87)
1: 0000 Delay
2: 7 Loop Count

; The SDMX50 automatically increments to the next channel.

11: SDMX50 Channel Select (P109)
1: 00 SDM Address
2: 1 SDM Channel

;Call the measurement subroutine (Subroutine 91)

12: Do (P86)
1: 91 Call Subroutine 91
;*****

; DATA OUTPUT
; In this example program, the program sets a complete time stamp on
; the data.

13: Time (P18)
1: 1 Minutes into current day (maximum 1440)
2: 0000 Mod/By
3: 151 Loc [ Minute ]

; Set output flag
```

## D.2.5 Station 1Ta data logger program

```
14: Do (P86)
1: 10 Set Output Flag High (Flag 0)

; Array ID is used to label each probe.
15: Set Active Storage Area (P80)^90
1: 1 Final Storage Area 1
2: 79 -- Array ID

16: Real Time (P77)^21845
1: 1100 Year,Day (midnight = 0000)

17: Sample (P70)^799
1: 1 Reps
2: 151 Loc [ Minute ]

18: Resolution (P78)
1: 1 High Resolution

19: Sample (P70)^26986
1: 1 Reps
2: 167 Loc [ AvgTime ]

20: Sample (P70)^24581
1: 1 Reps
2: 168 Loc [ StdTime ]

;End Probes 1-7 loop
21: End (P95)

;*****

;Select probes connected to second SDMX50
;Second SDMX50 is connected to channel #8 on the first SDMX50 (Address 00)

;Set the first SDMX50 Channel

22: SDMX50 Channel Select (P109)
1: 00 SDM Address
2: 8 SDM Channel

;Loop for probes 8 - 10

23: Beginning of Loop (P87)
1: 0000 Delay
2: 3 Loop Count

24: SDMX50 Channel Select (P109)
1: 01 SDM Address
2: 1 -- SDM Channel

25: Do (P86)
1: 91 Call Subroutine 91

; *****

; DATA OUTPUT
; In this example program, the program sets a complete time stamp on
; the data.

26: Time (P18)
1: 1 Minutes into current day (maximum 1440)
2: 0000 Mod/By
3: 151 Loc [ Minute ] ;

; Set output flag
27: Do (P86)
1: 10 Set Output Flag High (Flag 0)
```

## D.2.5 Station 1Ta data logger program

```
; Output the moisture from the current probe using label 81.
28: Set Active Storage Area (P80)^13118
   1: 1    Final Storage Area 1
   2: 86   -- Array ID

29: Real Time (P77)^5111
   1: 1100 Year,Day (midnight = 0000)

30: Sample (P70)^11344
   1: 1    Reps
   2: 151  Loc [ Minute  ]

31: Resolution (P78)
   1: 1    High Resolution

32: Sample (P70)^13114
   1: 1    Reps
   2: 167  Loc [ AvgTime  ]

33: Sample (P70)^22163
   1: 1    Reps
   2: 168  Loc [ StdTime  ]

;End of loop for probes 8-13
34: End (P95)

; End if time is 30 min loop.
35: End (P95)

* Table 3 Subroutines

; *****
; SUBROUTINE TDRMEASUREMENT #91
;
; Takes a three measurements of moisture and stores the
; average and standard deviation from a type one probe.

1: Beginning of Subroutine (P85)
1: 91    Subroutine 91

; Zero the moisture content

RawTime_1=0
RawTime_2=0
RawTime_3=0

; *****
; Take Measurements

2: Beginning of Loop (P87)
   1: 0000 Delay
   2: 3    Count(s)

; *****
;
; START MEASUREMENT
; Turn the instrument on.
; Port 8 controls power to the MP-917 through the interconnect
; module

3: Do (P86)
   1: 48    Set Port 8 High
```

## D.2.5 Station 1Ta data logger program

```
; Delay Loop. Prevents the datalogger from reading the initial
; instrument identification data. Timed for 15 seconds to skip
; over the 15 second warm-up time.

4: Beginning of Loop (P87)
1: 1    Delay
2: 15   Count(s)

5: End (P95)

; Read serial data from the MP-917

6: Port Serial I/O (P15)
1: 1    Reps
2: 1    ASCII/RS-232, 1200 Baud
3: 0000 CTS/Delay
4: 6    First Control Port
5: 164  -- Output Loc [ RawTime_1 ]
6: 0000 No. of Locs to Send
7: 13   Termination Character
8: 100  Maximum Characters
9: 9500 CTS/Input Wait
10: 164 -- Loc [ RawTime_1 ]
11: 1.0 Mult
12: 0.0 Offset

; Turn the MP-917 off, and wait for the power down. The instrument
; needs time to settle after power off before it starts another
; measurement.

7: Do (P86)
1: 58    Set Port 8 Low

; Power down wait loop, 2 seconds wait
8: Beginning of Loop (P87)
1: 1    Delay
2: 2    Count(s)
; End delay loop
9: End (P95)

; END SINGLE MEASUREMENT
; *****

; End of loop to do three measurements per probe.
10: End (P95)

; *****
; Calculate Average and Standard Deviation
; The lengthy calculation allows the avg. and std.dev. to be calculated correctly while being able to
; discard any unreasonable data that may result from electronic noise.

AvgTime=0
StdTime=0
GOOD=0
Sum=0
SUMSQUARE=0
Square=0

11: Beginning of Loop (P87)
1: 0000 Delay
2: 3    Count(s)

12: IF (X<=>F) (P89)
1: 164  -- X Loc [ RawTime_1 ]
2: 3    >=
3: 0.0  F
```

## D.2.5 Station 1Ta data logger program

```
4: 30   Then Do

13: IF (X<=>F) (P89)
1: 164 -- X Loc [ RawTime_1 ]
2: 4   <
3: 20  F
4: 30   Then Do

14: Z=X+Y (P33)
1: 165  X Loc [ Sum   ]
2: 164 --yrLoc [ RawTime_1 ]
3: 165  Z Loc [ Sum   ]

15: Z=X*Y (P36)
1: 164 -- X Loc [ RawTime_1 ]
2: 164 --yrLoc [ RawTime_1 ]
3: 166  Z Loc [ Square ]

16: Z=X+Y (P33)
1: 173  X Loc [ SUMSQUARE ]
2: 166  yrLoc [ Square   ]
3: 173  Z Loc [ SUMSQUARE ]

17: Z=Z+1 (P32)
1: 172  Z Loc [ GOOD   ]

;      End if <20 loop
18: End (P95)

;      End if > 0 loop

19: End (P95)

;      End add three measurements loop
20: End (P95)

21: Z=X/Y (P38)
1: 165  X Loc [ Sum   ]
2: 172  yrLoc [ GOOD   ]
3: 167  Z Loc [ AvgTime ]

22: Z=X*Y (P36)
1: 167  X Loc [ AvgTime ]
2: 167  yrLoc [ AvgTime ]
3: 174  Z Loc [ SqAvg   ]

23: Z=X/Y (P38)
1: 173  X Loc [ SUMSQUARE ]
2: 172  yrLoc [ GOOD   ]
3: 175  Z Loc [ SumSqAvg ]

24: Z=X-Y (P35)
1: 175  X Loc [ SumSqAvg ]
2: 174  yrLoc [ SqAvg   ]
3: 176  Z Loc [ Diff    ]

25: Z=SQRT(X) (P39)
1: 176  X Loc [ Diff    ]
2: 168  Z Loc [ StdTime ]

; End of measurement routine

; *****

; End Subroutine 91
26: End (P95)

End Program
```

D.2.6 Station ULa

```
:{CR10X}
;

; UPPER LYSIMETERS
; Station: ULa
; Data Logger: CR10X Wiring Panel #35267

; Matt Neuner July 2007

; Summary
; Four lysimeters buried just below the surface measure net infiltration and geochemistry in the active zone.
; Flow: tipping bucket rain gauges
; Geochemistry: Electrical conductivity and pH probes
; Temperature: EC temperature measured for EC correction
; Temperature measured near the heat trace and in waste rock near the lysimeter
; Moisture Content: 3 ECH2O-TE probes, at depths of 0.3, 0.6, 0.9m
; Soil Tension: 3 Tensiometers, at depths of 0.3, 0.6, 0.9m

; Ports -- see wiring diagram

; Version 5 Edits:
; Note that Version 4 was never an active file.
; 3 Tensiometers installed with Soil Moisture Equip. Model 5301 Tension Transducers; output is matric suction in kPa,
; height of water column, z, must be added to get pressure head in post-processing
; 3 ECHO TE probes installed; output is mV, calibration applied post-process

* Table 1 Program
  01: 0.125      Execution Interval (seconds)

; FLOW MEASUREMENTS *****
; On-demand data output

; UL1 West Type 3 Lysimeter Flow Gauge *****

1: Pulse (P3)
1: 1      Reps
2: 1      Pulse Channel 1
3: 2      Switch Closure, All Counts
4: 29     Loc [ TB_20 ]
5: 1.0    Mult
6: 0.0    Offset

2: If (X<=>F) (P89)
1: 29     X Loc [ TB_20 ]
2: 3      >=
3: 1      F
4: 30     Then Do

3: Do (P86)
1: 10     Set Output Flag High (Flag 0)

4: Set Active Storage Area (P80)^2873
1: 1      Final Storage Area 1
2: 20     Array ID

5: Real Time (P77)^27779
1: 1100   Year,Day (midnight = 0000)

6: Time (P18)
1: 1      Minutes into current day (maximum 1440)
2: 0000   Mod/By
3: 35     Loc [ Minute ]

7: Sample (P70)^13388
1: 1      Reps
2: 35     Loc [ Minute ]
```

## D.2.6 Station ULa data logger program

8: Real Time (P77)^1574  
1: 0001 Seconds (midnight = 0000)

9: End (P95)

; UL2 East Type 3 Lysimeter Flow Gauge \*\*\*\*\*

10: Pulse (P3)

1: 1 Reps  
2: 2 Pulse Channel 2  
3: 2 Switch Closure, All Counts  
4: 30 Loc [ TB\_21 ]  
5: 1.0 Mult  
6: 0.0 Offset

11: If (X<=>F) (P89)

1: 30 X Loc [ TB\_21 ]  
2: 3 >=  
3: 1 F  
4: 30 Then Do

12: Do (P86)

1: 10 Set Output Flag High (Flag 0)

13: Set Active Storage Area (P80)^1320

1: 1 Final Storage Area 1  
2: 21 Array ID

14: Real Time (P77)^28973

1: 1100 Year,Day (midnight = 0000)

15: Time (P18)

1: 1 Minutes into current day (maximum 1440)  
2: 0000 Mod/By  
3: 35 Loc [ Minute ]

16: Sample (P70)^29360

1: 1 Reps  
2: 35 Loc [ Minute ]

17: Real Time (P77)^15631

1: 0001 Seconds (midnight = 0000)

18: End (P95)

; UL3 West Type 1 Lysimeter Flow Gauge \*\*\*\*\*

19: Pulse (P3)

1: 1 Reps  
2: 7 Control Port 7 (switch closure only)  
3: 2 Switch Closure, All Counts  
4: 31 Loc [ TB\_22 ]  
5: 1.0 Mult  
6: 0.0 Offset

20: If (X<=>F) (P89)

1: 31 X Loc [ TB\_22 ]  
2: 3 >=  
3: 1 F  
4: 30 Then Do

21: Do (P86)

1: 10 Set Output Flag High (Flag 0)

22: Set Active Storage Area (P80)^24645

1: 1 Final Storage Area 1

## D.2.6 Station ULa data logger program

```
2: 22   Array ID

23: Real Time (P77)^220
1: 1100   Year,Day (midnight = 0000)

24: Time (P18)
1: 1     Minutes into current day (maximum 1440)
2: 0000   Mod/By
3: 35    Loc [ Minute  ]

25: Sample (P70)^1959
1: 1     Reps
2: 35    Loc [ Minute  ]

26: Real Time (P77)^4908
1: 0001   Seconds (midnight = 0000)

27: End (P95)

; UL4 East Type 1 Lysimeter Flow Gauge *****

28: Pulse (P3)
1: 1     Reps
2: 8     Control Port 8 (switch closure only)
3: 2     Switch Closure, All Counts
4: 32    Loc [ TB_23  ]
5: 1.0   Mult
6: 0.0   Offset

29: If (X<=>F) (P89)
1: 32    X Loc [ TB_23  ]
2: 3     >=
3: 1     F
4: 30    Then Do

30: Do (P86)
1: 10    Set Output Flag High (Flag 0)

31: Set Active Storage Area (P80)^26177
1: 1     Final Storage Area 1
2: 23    Array ID

32: Real Time (P77)^14784
1: 1100   Year,Day (midnight = 0000)

33: Time (P18)
1: 1     Minutes into current day (maximum 1440)
2: 0000   Mod/By
3: 35    Loc [ Minute  ]

34: Sample (P70)^9400
1: 1     Reps
2: 35    Loc [ Minute  ]

35: Real Time (P77)^13828
1: 0001   Seconds (midnight = 0000)

36: End (P95)

* Table 2 Program
  01: 600   Execution Interval (seconds)

; Loop over table 2 measurements
1: If time is (P92)
1: 0000   Minutes (Seconds --) into a
2: 10    Interval (same units as above)
```

## D.2.6 Station ULa data logger program

```
3: 30    Then Do

; Output timing
2: If time is (P92)
1: 0000    Minutes (Seconds --) into a
2: 30     Interval (same units as above)
3: 11     Set Flag 1 High

; \\\\\\\\\\\\\\\\\\\\\\\\\\\\\\\\\\\\\\\\\ Sensors on AM16/32 Multiplexer #9168 \\\\\\\\\\\\\\\\\\\\\\\\\\\\\\\\\\\\\\\\\

; ELECTRICAL CONDUCTIVITY *****

; Zero the input locations prior to measurement.
V2V1_1=0
V2V1_2=0
V2V1_3=0
V2V1_4=0
Rs_1=0
Rs_2=0
Rs_3=0
Rs_4=0
EC_28=0
EC_29=0
EC_30=0
EC_31=0

; RESET: Activates the AM416
3: Do (P86)
1: 41     Set Port 1 High

4: Beginning of Loop (P87)
1: 0000    Delay
2: 4      Loop Count

; CLOCK: Switches through the first 4 SETs
5: Do (P86)
1: 72     Pulse Port 2

6: Full Bridge w/mv Excit (P9)
1: 1      Reps
2: 25     2500 mV 60 Hz Rejection Ex Range
3: 25     2500 mV 60 Hz Rejection Br Range
4: 1      DIFF Channel
5: 2      Excite all reps w/Exchan 2
6: 2500   mV Excitation
7: 1      -- Loc [ V1_V2_1 ]
8: 1.0    Mult
9: 0.0    Offset

; EC Calculations *****

; This output is 1000 times the ratio between the potential measured by the central electrodes
; in the water and the potential measured by the outer electrodes in the solution,
; in series with the reference resistor. Multiplying by the reference resistance (469.3 Ohms)
; yeilds the resistance in the flow-through cell.

7: Z=X*F (P37)
1: 1      -- X Loc [ V1_V2_1 ]
2: 0.001  F
3: 1      -- Z Loc [ V1_V2_1 ]

8: Z=X*F (P37)
1: 1      -- X Loc [ V1_V2_1 ]
2: 469.3  F
3: 5      -- Z Loc [ Rs_1 ]

; Conductance = cell constant (k) / resistance of solution
; k is determined by Equation ** from Won (1987).
; For the Divaik probes, k = 1.884m^-1
```

## D.2.6 Station ULa data logger program

```
9: Z=1/X (P42)
1: 5 -- X Loc [ Rs_1 ]
2: 9 -- Z Loc [ EC_28 ]

10: Z=X*F (P37)
1: 9 -- X Loc [ EC_28 ]
2: 1.884 F
3: 9 -- Z Loc [ EC_28 ]

; Units conversions to uS/cm

11: Z=X*F (P37)
1: 9 -- X Loc [ EC_28 ]
2: 10000 F
3: 9 -- Z Loc [ EC_28 ]

; Calibration Factor : This factor was derived as the factor necessary to make all EC probes
; output the EC expected when measuring laboratory-prepared KCl solutions.

12: Z=X*F (P37)
1: 9 -- X Loc [ EC_28 ]
2: 3.963 F
3: 9 -- Z Loc [ EC_28 ]

; End loop of four EC measurements.
13: End (P95)

;*****
; TEMPERATURE MEASUREMENTS

; RESET: Activate AM16/32(1) by setting Control Port 1 high
14: Do (P86)
1: 41 Set Port 1 High

; Measure the 3 SETs of thermistors
15: Beginning of Loop (P87)
1: 0 Delay
2: 3 Loop Count

16: Step Loop Index (P90)
1: 4 Step

; CLOCK:
17: Do (P86)
1: 72 Pulse Port 2

18: Excitation with Delay (P22)
1: 1 Ex Channel
2: 0 Delay W/Ex (0.01 sec units)
3: 1 Delay After Ex (0.01 sec units)
4: 0 mV Excitation

19: Excite-Delay (SE) (P4)
1: 4 Reps
2: 20 Auto 60 Hz Rejection Range (Delay must be zero)(OS>1.9)
3: 1 SE Channel
4: 1 Excite all reps w/Exchan 1
5: 0 Delay (units 0.01 sec)
6: 2500 mV Excitation
7: 13 -- Loc [ Therm_1 ]
8: 1 Mult
9: 0.0 Offset

; Calculations for ch 1 in each SET *****
; Convert millivolt reading to resistance using  $R(\text{therm}) = ((V(\text{excit}) * R(\text{ref})) / V(\text{in})) - R(\text{ref})$ 
```

## D.2.6 Station ULa data logger program

; A 10 kOhm reference resistor is used (9890 multiplier in the second P37 below).

```
20: Z=1/X (P42)
1: 13 -- X Loc [ Therm_1 ]
2: 13 -- Z Loc [ Therm_1 ]

21: Z=X*F (P37)
1: 13 -- X Loc [ Therm_1 ]
2: 2500 F
3: 13 -- Z Loc [ Therm_1 ]

22: Z=X+F (P34)
1: 13 -- X Loc [ Therm_1 ]
2: -1 F
3: 13 -- Z Loc [ Therm_1 ]

23: Z=X*F (P37)
1: 13 -- X Loc [ Therm_1 ]
2: 9980 F
3: 13 -- Z Loc [ Therm_1 ]
```

; Convert resistance to temperature using nonlinear relationship provided by Omega International.

```
24: Steinhart-Hart Equation (P200)
1: 1 Repts
2: 13 -- Source Loc (R)(Ohms) [ Therm_1 ]
3: 13 -- Destination Loc (Deg C) [ Therm_1 ]
4: 1.28679 A
5: -3 x 10^n
6: 2.35938 B
7: -4 x 10^n
8: 9.4 C
9: -8 x 10^n
```

; Calculations for ch 2 in each SET \*\*\*\*\*

; Convert millivolt reading to resistance using  $R(\text{therm}) = ((V(\text{excit}) * R(\text{ref})) / V_{\text{in}}) - R(\text{ref})$

; A 10 kOhm reference resistor is used (9890 multiplier in the second P37 below).

```
25: Z=1/X (P42)
1: 14 -- X Loc [ Therm_2 ]
2: 14 -- Z Loc [ Therm_2 ]

26: Z=X*F (P37)
1: 14 -- X Loc [ Therm_2 ]
2: 2500 F
3: 14 -- Z Loc [ Therm_2 ]

27: Z=X+F (P34)
1: 14 -- X Loc [ Therm_2 ]
2: -1 F
3: 14 -- Z Loc [ Therm_2 ]

28: Z=X*F (P37)
1: 14 -- X Loc [ Therm_2 ]
2: 9980 F
3: 14 -- Z Loc [ Therm_2 ]
```

; Convert resistance to temperature using nonlinear relationship provided by Omega International.

```
29: Steinhart-Hart Equation (P200)
1: 1 Repts
2: 14 -- Source Loc (R)(Ohms) [ Therm_2 ]
3: 14 -- Destination Loc (Deg C) [ Therm_2 ]
4: 1.28679 A
5: -3 x 10^n
6: 2.35938 B
7: -4 x 10^n
8: 9.4 C
9: -8 x 10^n
```

## D.2.6 Station ULa data logger program

```
; Calculations for ch 3 in each SET *****
; Convert millivolt reading to resistance using  $R(\text{therm}) = ((V(\text{excit}) * R(\text{ref})) / V_{in}) - R(\text{ref})$ 
; A 10 kOhm reference resistor is used (9890 multiplier in the second P37 below).

30: Z=1/X (P42)
   1: 15 -- X Loc [ Therm_3 ]
   2: 15 -- Z Loc [ Therm_3 ]

31: Z=X*F (P37)
   1: 15 -- X Loc [ Therm_3 ]
   2: 2500 F
   3: 15 -- Z Loc [ Therm_3 ]

32: Z=X+F (P34)
   1: 15 -- X Loc [ Therm_3 ]
   2: -1 F
   3: 15 -- Z Loc [ Therm_3 ]

33: Z=X*F (P37)
   1: 15 -- X Loc [ Therm_3 ]
   2: 9980 F
   3: 15 -- Z Loc [ Therm_3 ]

; Convert resistance to temperature using nonlinear relationship provided by Omega International.
34: Steinhart-Hart Equation (P200)
   1: 1 Repts
   2: 15 -- Source Loc (R)(Ohms) [ Therm_3 ]
   3: 15 -- Destination Loc (Deg C) [ Therm_3 ]
   4: 1.28679 A
   5: -3 x 10^n
   6: 2.35938 B
   7: -4 x 10^n
   8: 9.4 C
   9: -8 x 10^n

; Calculations for ch 4 in each SET *****
; Convert millivolt reading to resistance using  $R(\text{therm}) = ((V(\text{excit}) * R(\text{ref})) / V_{in}) - R(\text{ref})$ 
; A 10 kOhm reference resistor is used (9890 multiplier in the second P37 below).

35: Z=1/X (P42)
   1: 16 -- X Loc [ Therm_4 ]
   2: 16 -- Z Loc [ Therm_4 ]

36: Z=X*F (P37)
   1: 16 -- X Loc [ Therm_4 ]
   2: 2500 F
   3: 16 -- Z Loc [ Therm_4 ]

37: Z=X+F (P34)
   1: 16 -- X Loc [ Therm_4 ]
   2: -1 F
   3: 16 -- Z Loc [ Therm_4 ]

38: Z=X*F (P37)
   1: 16 -- X Loc [ Therm_4 ]
   2: 9980 F
   3: 16 -- Z Loc [ Therm_4 ]

; Convert resistance to temperature using nonlinear relationship provided by Omega International.
39: Steinhart-Hart Equation (P200)
   1: 1 Repts
   2: 16 -- Source Loc (R)(Ohms) [ Therm_4 ]
   3: 16 -- Destination Loc (Deg C) [ Therm_4 ]
   4: 1.28679 A
   5: -3 x 10^n
   6: 2.35938 B
   7: -4 x 10^n
   8: 9.4 C
   9: -8 x 10^n
```



## D.2.6 Station ULa data logger program

```
51: Time (P18)
1: 1   Minutes into current day (maximum 1440)
2: 0000 Mod/By
3: 35   Loc [ Minute ]

; *****
; ECH2O TE Probes -- Soil Moisture, Pore Water EC, Temp

52: Do (P86)
1: 43   Set Port 3 High

53: Port Serial I/O (P15)
1: 1   Reps
2: 0   8-Bit, TTL ASCII, 1200 Baud
3: 0   TX after CTS
4: 40   C4 TX/RX, No RTS/DTR (OS>1.14)
5: 45   Start Loc for TX [ ECHO_1 ]
6: 0   Number of Locs to TX
7: 256  Termination Character for RX
8: 50   Max Characters to RX
9: 50   Time Out for CTS (TX) and/or RX (0.01 sec units)
10: 45  Start Loc for RX [ ECHO_1 ]
11: 1.0 Multiplier for RX
12: 0.0 Offset for RX

54: Do (P86)
1: 53   Set Port 3 Low

55: Excitation with Delay (P22)
1: 1   Ex Channel
2: 0   Delay W/Ex (0.01 sec units)
3: 500 Delay After Ex (0.01 sec units)
4: 0   mV Excitation

; ECH2O_2

56: Do (P86)
1: 43   Set Port 3 High

57: Port Serial I/O (P15)
1: 1   Reps
2: 0   8-Bit, TTL ASCII, 1200 Baud
3: 0   TX after CTS
4: 50   C5 TX/RX, No RTS/DTR (OS>1.14)
5: 45   Start Loc for TX [ ECHO_1 ]
6: 0   Number of Locs to TX
7: 256  Termination Character for RX
8: 50   Max Characters to RX
9: 50   Time Out for CTS (TX) and/or RX (0.01 sec units)
10: 46  Start Loc for RX [ ECHO_2 ]
11: 1.0 Multiplier for RX
12: 0.0 Offset for RX

58: Do (P86)
1: 53   Set Port 3 Low

59: Excitation with Delay (P22)
1: 1   Ex Channel
2: 0   Delay W/Ex (0.01 sec units)
3: 500 Delay After Ex (0.01 sec units)
4: 0   mV Excitation

; ECH2O_3

60: Do (P86)
1: 43   Set Port 3 High

61: Port Serial I/O (P15)
```

## D.2.6 Station ULa data logger program

```
1: 1    Reps
2: 0    8-Bit, TTL ASCII, 1200 Baud
3: 0    TX after CTS
4: 60   C6 TX/RX, No RTS/DTR (OS>1.14)
5: 45   Start Loc for TX [ ECHO_1 ]
6: 0    Number of Locs to TX
7: 256  Termination Character for RX
8: 50   Max Characters to RX
9: 50   Time Out for CTS (TX) and/or RX (0.01 sec units)
10: 47  Start Loc for RX [ ECHO_3 ]
11: 1.0 Multiplier for RX
12: 0.0 Offset for RX
```

```
62: Do (P86)
```

```
1: 53   Set Port 3 Low
```

```
; *****
```

```
; End loop over measurements
```

```
63: End (P95)
```

```
; ***** TABLE 2 OUTPUT *****
```

```
64: If Flag/Port (P91)
```

```
1: 11   Do if Flag 1 is High
```

```
2: 10   Set Output Flag High (Flag 0)
```

```
65: Set Active Storage Area (P80)^22991
```

```
1: 1    Final Storage Area 1
```

```
2: 113  Array ID
```

```
; As per DataLogging Scheme.xls Array ID tab
```

```
66: Real Time (P77)^5720
```

```
1: 1100 Year,Day (midnight = 0000)
```

```
67: Sample (P70)^11377
```

```
1: 1    Reps
```

```
2: 35   Loc [ Minute ]
```

```
68: Sample (P70)^18117
```

```
1: 1    Reps
```

```
2: 34   Loc [ BatVolt ]
```

```
69: Sample (P70)^12657
```

```
1: 1    Reps
```

```
2: 33   Loc [ ProgSig ]
```

```
70: Sample (P70)^12037
```

```
1: 4    Reps
```

```
2: 9    Loc [ EC_28 ]
```

```
71: Sample (P70)^17889
```

```
1: 12   Reps
```

```
2: 13   Loc [ Therm_1 ]
```

```
72: Sample (P70)^28789
```

```
1: 4    Reps
```

```
2: 36   Loc [ pH_1 ]
```

```
73: Sample (P70)^23502
```

```
1: 9    Reps
```

```
2: 45   Loc [ ECHO_1 ]
```

```
74: Sample (P70)^30319
```

```
1: 3    Reps
```

```
2: 54   Loc [ Tension_1 ]
```

## *D.2.6 Station ULa data logger program*

75: Do (P86)  
1: 20 Set Output Flag Low (Flag 0)

76: Do (P86)  
1: 21 Set Flag 1 Low

\* Table 3 Subroutines

End Program

## **APPENDIX E DATA SET FOR SEPTEMBER 2006 TO MARCH 2008**

Additional results are included here to provide an overview of the complete data set for the water flow observations made at the study site for the period from September 2006 to March 2008.

### **E.1 Rain**

#### *E.1.1 Natural rainfall*

Figure E.1 shows the locations of the meteorological station, manual rain gauge, and the Waste Rock Test Piles Research Area on the East Island of Lac de Gras: the site of the Diavik Diamond Mines. A rain gauge was installed at the top of the Type 3 test pile September 16, 2006, less than a month after the completion of the construction of the reactive and non-reactive test piles. Another gauge was installed at the top of the Type 1 test pile May 5, 2007. Each gauge was a RM Young tipping bucket rain gauge with a 0.1 mm rain per tip resolution recorded by a Campbell CR10X data logger. No attempt was made to use the gauges to measure the water equivalence of the snowfall. The gauges were not heated and were removed during winter. The data logger measuring the T1 gauge was removed from the station from July 29 to August 12, 2007, at a time when 29.5 mm rain was recorded at the T3 gauge.

Table E.1 summarizes the rainfall and snowfall data on a monthly basis and Figure E.2 is a plot of rainfall on a daily basis at Diavik during the duration of the test piles experiment. During 2007, close agreement was observed between the two gauges at the test piles, but somewhat larger variation was observed when compared to measurements made manually and by a data logging tipping bucket gauge at locations within 1km. Figure E.3 is a histogram showing the variability of daily rainfall at the four gauges at

Diavik mentioned above over a time period of a month. Figure E.4a shows the relationship between daily rainfall measured at the top of the test piles, and Figure E.4b shows the relationship between daily rainfall measured at the top of the Type 3 test pile and at the Diavik meteorological station.

### *E.1.2 Applied Rainfall Events*

Several applied rainfall events were conducted at the Type 3 test pile and upper collection lysimeters (Table E.2). A grid of cups was placed at the ground surface to gauge the applied rainfall (Figure E.5). At the Type 3 test pile three rainfall events were applied in each of 2006 and 2007, each with recurrence intervals of eight to thirty-five years. The rainfall was applied to a 20m x 30m footprint (Figure E.5) at the top of the pile using a calibrated pump-fed oscillating lawn sprinkler system. These events were applied during a time when natural rainfall was about half of the mean annual precipitation and the events amounted to 40% of mean annual precipitation (Gupton 2008). At the Type 3 upper collection lysimeters three high-intensity rainfall events were applied to raise the moisture content in the lysimeters to field capacity before applying an eight-year recurrence interval rainfall event. These events increased the annual precipitation at the Type 3 upper collection lysimeters to 115% of the annual mean or less than half of the total for the rainiest year on record.

## **E.2 Snow**

On a regional scale in the vicinity of Lac de Gras, about 60% of the total precipitation comes as snowfall (Table E.1 and Figure E.6). Due to dry, cold conditions and the long duration of below-freezing temperatures, snow distribution at the ground surface is dominated by transport and deposition by wind. In general, topographic highs

become wind-scoured and slopes become wind-loaded (Figure E.7). Deposition is generally highest at slopes with south and east aspects, as the dominant winds are westerly and northerly. Snow depths were at a maximum at the end of March in 2007. Snowpack ablation (Figure E.8) in April occurred during subzero temperatures (see Figure 3.5) due to sublimation. Photographs of the test piles from April 27, 2007, and March 2008 are shown in Figure E.8. When the spring thaw initiated in 2007 and 2008, snow depths at the tops of the test piles was less than 10 cm. Snow depths on the batters of the test pile (the slopes) are difficult to estimate due to the extreme irregularity in the surface of the boulder-dominated batters.

### **E.3 Evaporation**

In 2006 the Diavik Environment Department maintained an evaporation station that included an evaporation pan, anemometer, and a Kipp and Zonen NR Lite Net Radiometer. A bear, however, destroyed the station in the spring of 2007. The Diavik meteorological station includes an RM Young wind monitor (Campbell Scientific model number 05103-10), a Campbell Scientific HMP35CF relative humidity and temperature sensor, thermistors at 2 m and 10 m height above ground, and a Campbell Scientific LI200s pyranometer for measurement of solar radiation. Evaporation calculated from meteorological observations using the FAO Penman-Monteith method (described in Chapter 2) is shown in Figure E.9. Potential evaporation (PE) plotted in Figure E.9 is the reference evapotranspiration, while evaporation (E) plotted in the figure is the evaporation from a bare soil limited by the estimation of soil moisture available for evaporation (based on the time since rainfall) and the presence of frozen conditions at the surface.

Vapor transport associated with heat transfer during the early winter was observed at localized steam vents (Figure E.10).

#### **E.4 Type 3 Test Pile**

Measurement of volumetric moisture content by TDR commenced on September 19, 2006. Power to the Moisture Point MP-917 TDR instrument was disrupted on October 16, 2006, but the failure was not detected by research personnel until November 2, 2006. Otherwise, the TDR system has provided continuous data with 30 min temporal and 0.5 m<sup>3</sup>/m<sup>3</sup> moisture content resolution (Figures E.11 and E.12).

Measurement of matric suction in the waste rock matrix commenced after installation of tensiometers in shallow (1.3m) boreholes, on August 2, 2007. The use of tensiometers is limited in the early summer by frozen waste rock conditions at the depth of the porous ceramic cup and in the early autumn by freezing ambient temperatures. The distilled water in the body of tensiometers was evacuated soon after the onset of freezing ambient temperatures, on September 17, 2007. The full tension head data set from 2007 at the Type 3 test pile is shown in Figure E.13. Tension measurements at greater depth in the test pile (Figure E.14) were made using the method described in Appendix B, and the data is presented in terms of tension head (accounting for the elevation head). Successful measurements were made on August 7, 2007, but several subsequent attempts yielded measurements with great uncertainty. On these subsequent measurements, the suction was near zero, giving rise to suspicion that the porous cup was not entirely saturated. Suction measurements near zero correspond to atmospheric pressure or saturated conditions. Saturated conditions at depths greater than about 3m

were not expected in August and early September of 2007, based on the TDR measurements.

Outflow from the Type 3 basal drain in 2006 (Figure E.15) was measured manually using a graduated cylinder, bucket, or barrel. Reliable continuous outflow measurements at the basal drain commenced on August 1, 2007. Gauge failure From May to July, 2007, is discussed in Appendix B. Measurements were made during this time with a graduated cylinder and a stopwatch. Each manual measurement recorded was the average of several measurements made over a period of about five minutes. Continuous outflow measurements were made with custom-made high flow tipping bucket gauges. The high flow tipping bucket measures outflow at a resolution of each individual tip, which occurs after about 160 mL of outflow at low flow and after about 220 mL at high flow. Gauge calibration (described in Appendix B) was conducted over at least 15 tips for each flow rate in the calibration in an attempt to average out the difference (about 10mL) in the volume of each half of the tipping bucket. This difference is inherent in the imperfection of the fabrication of the tipping bucket, but the difference becomes greater as the gauge drifts out of level. The inherent imperfection resulted in a gauge precision of about 35 L/d, but the precision was observed to be as poor as 135 L/d at times when the gauge was out of level. The data has been evaluated at 30 min intervals under the assumption that the true flow rate is the average of the record taken by each of the effectively smaller half and effectively larger half of the tipping bucket (Figure E.16). The collection area draining to the gauge at the north basal drain was designed to be equal that of the south basal drain, but the outflow focused at the south basal drain in 2006 and 2007. An interpolation was used (prior to the 30 min evaluation) to sum the flow measured at the

two gauges to find the outflow from the entire basal drain. The interpolation was made by a code written in the Python programming language by Blair Gibson at the University of Waterloo. A plot of the full outflow data set for 2007 is shown in Figure E.17. The cumulative outflow for 2006 to 2007 is plotted in Figure E.18.

### **E.5 Type 1 Test Pile**

Problems with communication between the Environmental Sensors, Inc. MP 917 TDR instrument and the Campbell Scientific CR10X data logger at the Type 1 test pile were not resolved until late August 2007. Prior to that time the data collected was very erratic, and no discernible relationship to moisture content could be made. Measurements made on July 2, 2007, were good, but the waste rock appeared to be frozen at that time at all sensors. The data set for the four functional TDR probes is shown in Figure E.20.

No outflow from the Type 1 test pile reported to the instrument trailer after May 21, 2007. In November 2007 a disconnection in the 6 in. PVC drainpipe for the basal drain was found inside the insulating outer pipe. Thermal expansion of the black insulating pipe in response to solar radiation appears to have forced the drainpipe to become disconnected at a rubber gasket connection. This failure was likely to have occurred in the last week of May 2007. The outflow prior to the failure is shown in Figure E.21.

### **E.6 Upper Collection Lysimeters**

The data set for the moisture content measured by three ECH<sub>2</sub>O probes in a shallow borehole between the lysimeters filled with Type 3 waste rock, during the time until the waste rock froze in 2007, is shown in Figure E.22. Tension head measured with tensiometers in the same borehole, for the full duration of deployment in 2007, is shown in Figure E.23. The distilled water in the tensiometers was evacuated on September 16,

2007, due to the onset of freezing conditions at the surface. The tensiometers were then operated from September 19 to October 15 by heating the portion of the body of the tensiometers that had been exposed to the atmosphere. Temperature measured by the ECH<sub>2</sub>O probes from the time of deployment until March 2008 is shown in Figure E.24. Outflow rate and the specific conductance and pH of the outflow from the west and east Type 3 upper collection lysimeter, from September 1 until flow stopped, is shown in Figures E.25 and E.26, respectively. Less than 10 L of outflow from the west Type 3 upper lysimeter was observed from August 25 to September 1, 2007, but surface tension effects at the spillway to the tipping bucket flow gauge caused the flow to surge and stop repeatedly. On September 1, this problem was alleviated by installing a thin plastic line across the spillway. Outflow from August 27 to September 1 at the east Type 3 upper lysimeter was similarly erratic until September 1.

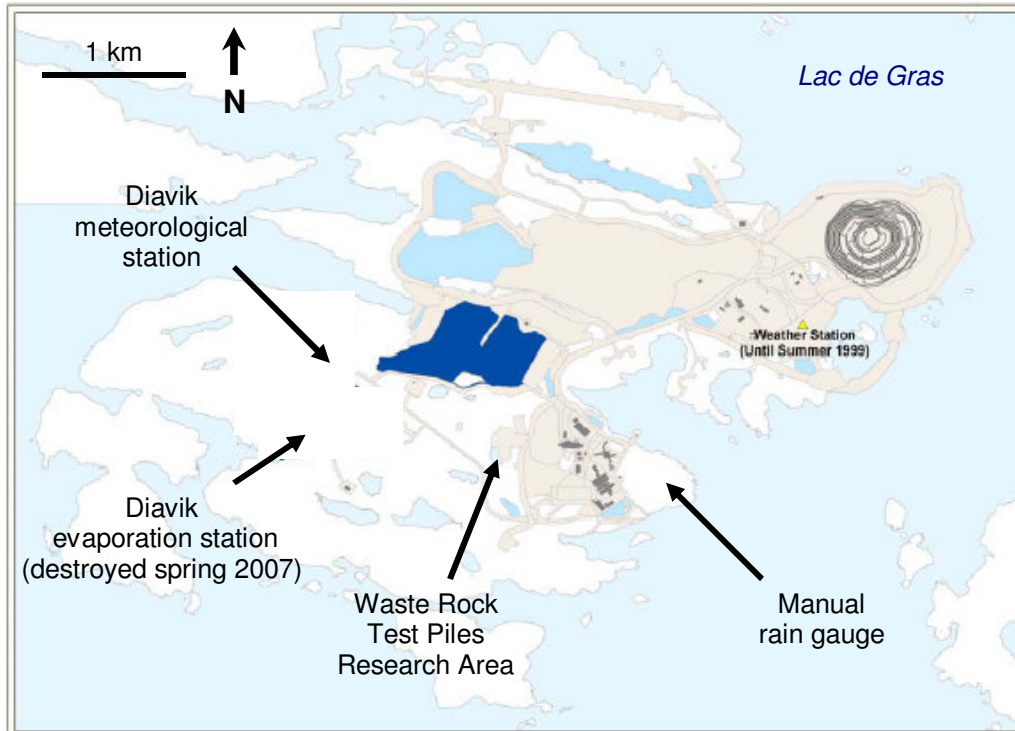


**Figure E.1** Diavik meteorological station locations on the East Island of Lac de Gras.

**Table E.1** A summary of the precipitation data during 2006 and 2007.

<b>Rainfall (mm)</b>	<b>Jan</b>	<b>Feb</b>	<b>Mar</b>	<b>Apr</b>	<b>May</b>	<b>Jun</b>	<b>Jul</b>	<b>Aug</b>	<b>Sep</b>	<b>Oct</b>	<b>Nov</b>	<b>Dec</b>	<b>Annual</b>
Minimum 1959-1995**	0	0	0	0	0	1	13.3	19.1	0.5	0	0	0	34
Maximum 1959-1995**	0	0	0	5.3	30.5	90.2	88.7	152.2	68.7	13.7	0.2	0	450
Mean 1959-1995**	0	0	0	0.3	6.6	24.6	40.6	49.4	24.1	1.9	0	0	148
<b>2006</b>													
T3 Test Pile									5.2*	1.9	0		
Diavik Met. Stn.	0	0	0	0.6	22.5	53.5	24.7	57.9	8.7	7.5	0	0	175
Diavik Manual					1.9	36.8	20.7	35.1	14				109
Ekati Met. Stn.	0	0	0	0.3	39.9	91.3	32.1	72.2	12.7	1.8	0	0	250
Lupin Met. Stn.	0	0	0	0	5	60.5	21.6	35.4	10.4	0.4	0	0	133
<b>2007</b>													
T3 Test Pile					5*	3	28.7	30	5.5	5.1	0		77
T1 Test Pile					5.1*	2.8	13*	25.1*	5.1	6.6	0	0	
Diavik Met. Stn.	0	0	0	2.1	14	4.8	22.8	55.5	6.7	7	0	0	113
Diavik Manual					3.4*	2.4	38.3	61.6	6.9				109
Ekati Met. Stn.	0	0	0	1.4	3.9	6.8	47.6	45.7	11.4		0	0	117
Lupin Met. Stn.	0	0	0	0		0	44.4						
<b>Snowfall (cm)</b>													
Minimum 1959-1995**	0	0	1.2	1.8	0	0	0	0	0	3.5	8.5	2.3	67
Maximum 1959-1995**	43.5	59.2	68.6	53.4	81.3	50.2	6.7	37.8	90.7	157.0	85.4	67.9	365
Mean 1959-1995**	14.3	15.2	20.1	21.8	24.1	7.0	0.4	3.5	25.2	49.4	29.3	22.4	233
<b>2006</b>													
Diavik Manual	20.3	17	24.3	24.4	12.4					25.9	86.8 <sup>+</sup>	13.5	225
Ekati Met. Stn.	15.9	21.8	14.4	17.5	9	0	0	0	4	45.5	7	29.4	165
Lupin Met. Stn.	14.6	6.8	16.8	16.8	4.2	3.2	0	0	0.8	25		8	96
<b>2007</b>													
Diavik Manual	29.2	12	11.1	3.8*	23.4	3.8			9.9	38.6	54.2	13	195
Ekati Met. Stn.	24.2	18.9	14.2	10.9	16.2	0.8	0	2.6	10.8		24.6		123
Lupin Met. Stn.	6.4			14.2		1	0						
<b>Snowpack (cm)</b>													
Ekati Met. Stn. 2006	38	37	43	15	0	0	0	0	0	17	13	24	46
Lupin Met. Stn. 2006	52		78			0	0	0	0	4	4	33	
Ekati Met. Stn. 2007	36	35	35	20	0	0	0	0	3		22		37
Lupin Met. Stn. 2007		54	69	73			0						76

\* incomplete data

\*\* compiled from Contwoyto and Lupin stations by Golder Assoc. 2005

<sup>+</sup> Yelloknife meteorologic station reported 86cm snow in Nov. 2006

**Table E.2** Summary of applied rainfall events conducted at the test piles and collection lysimeters in 2006 and 2007.

**Type 3 Test Pile**

<b>Event</b>	<b>Rainfall</b>	<b>Duration</b>	<b>Rainfall Intensity</b>	<b>Recurrence Interval</b>	<b>Relative Christiansen Uniformity</b>	<b>Tracer Applied</b>
	mm	hr	mm/hr	yrs		
20-Sep-06	24.2	2.37	10.2	30	0.73	-
24-Sep-06	19.0	2.00	9.5	17	0.83	-
26-Sep-06	14.7	1.50	9.8	9	0.90	-
17-Aug-07	16.1	2.12	7.6	9	0.72	D2O
4-Sep-07	15.0	1.75	8.6	8	0.68	-
13-Sep-07	29.2	3.75	7.7	35	0.75	Cl- and Br-

**Type 3 Upper Collection Lysimeters**

<b>Event</b>	<b>Rainfall</b>	<b>Duration</b>	<b>Rainfall Intensity</b>	<b>Recurrence Interval</b>	<b>Relative Christiansen Uniformity</b>	<b>Tracer Applied</b>
	mm	hr	mm/hr	Yrs		
4-Aug-07	23.1	2.83	8.2	20	0.90	-
5-Aug-07	27.7	2.25	12.3	50	0.96	-
6-Aug-07	14.1	1.72	8.2	8	0.92	-
1-Sep-07	14.8	1.75	8.4	8	0.82	-
19-Sep-07	11.6	1.07	10.8	7	0.90	-

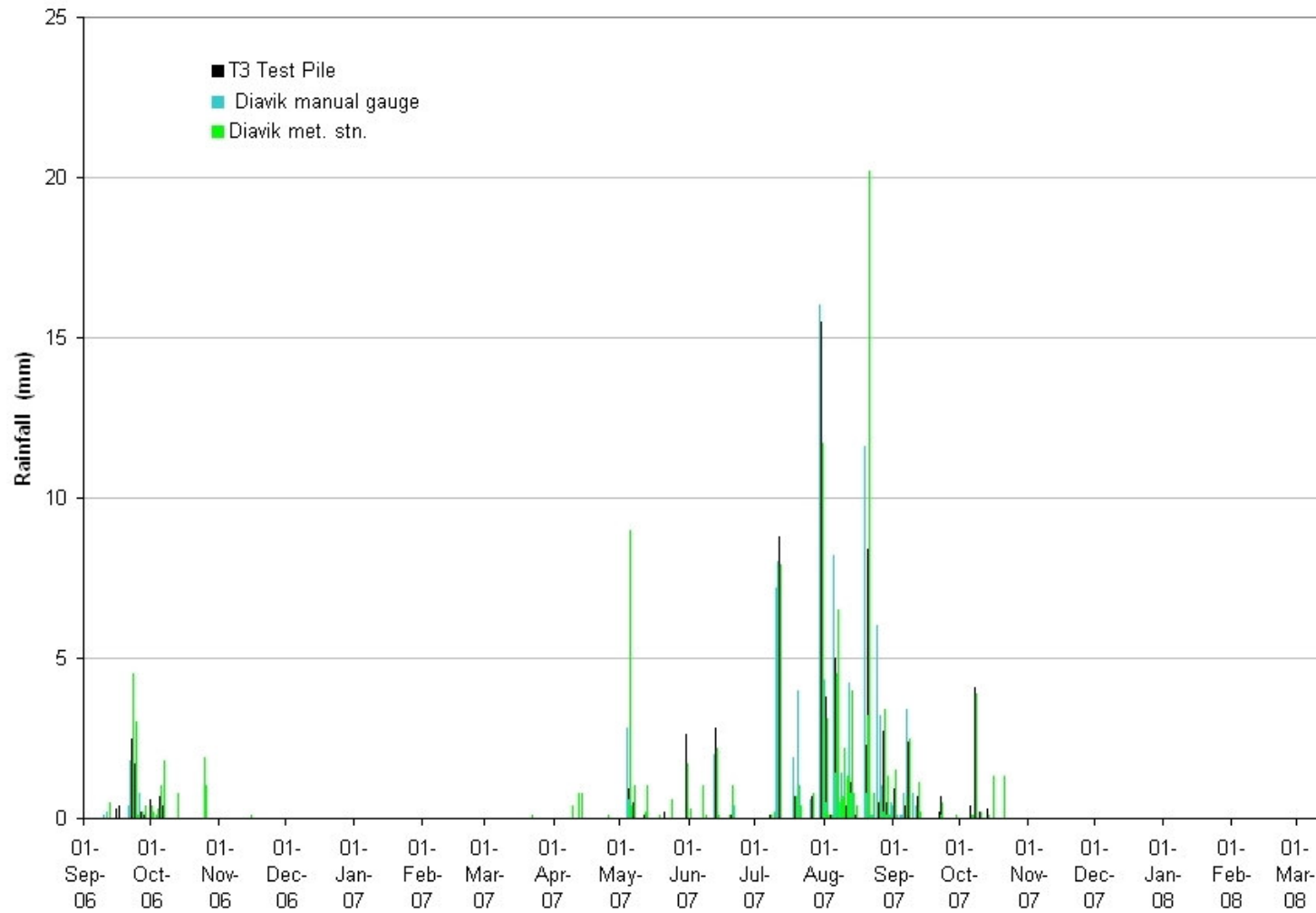


**Figure E.2** Rainfall measured at the top of the Type 3 test pile and at a meteorological station about 1km west of the test piles and a manual gauge about 1km east of the test piles.

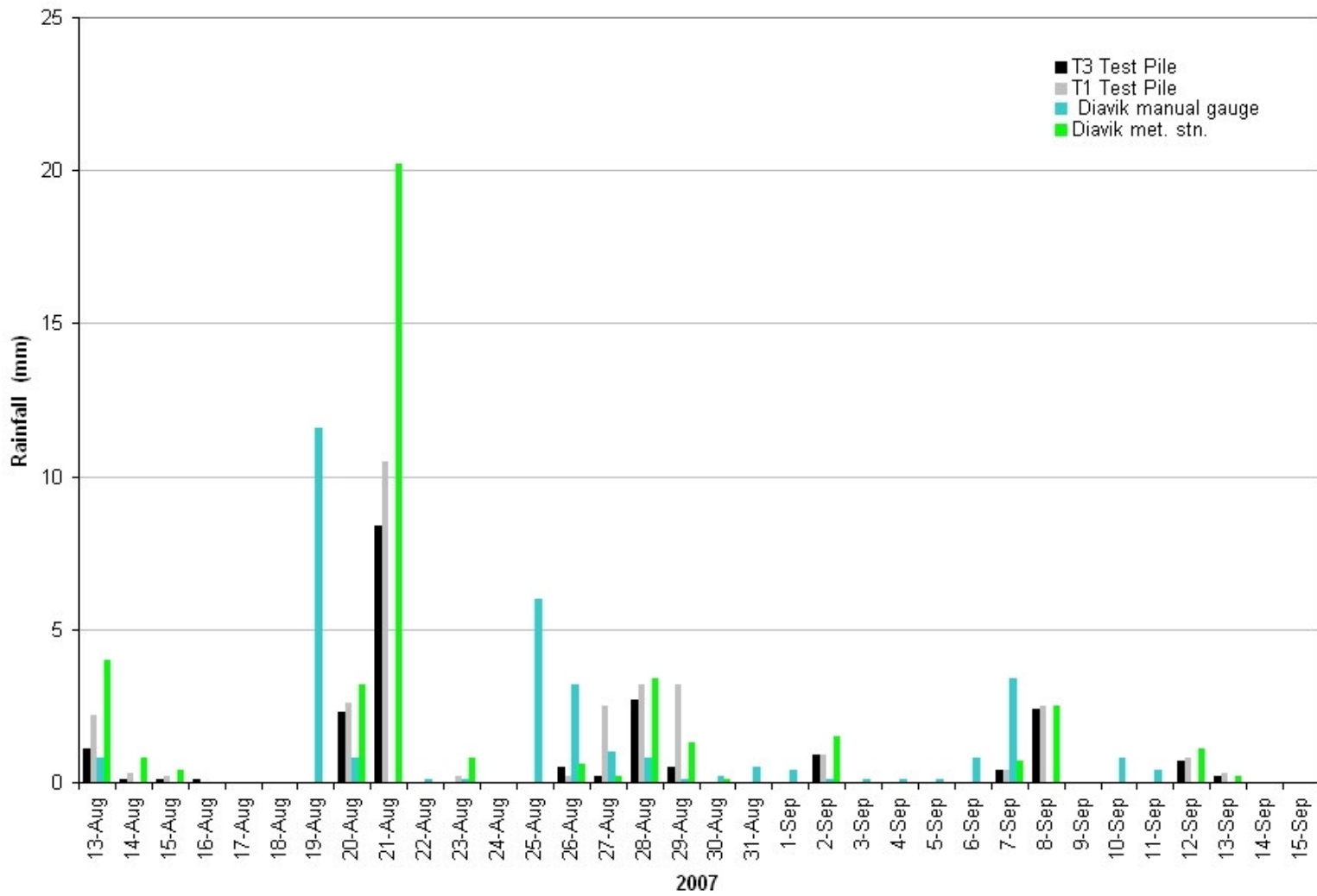
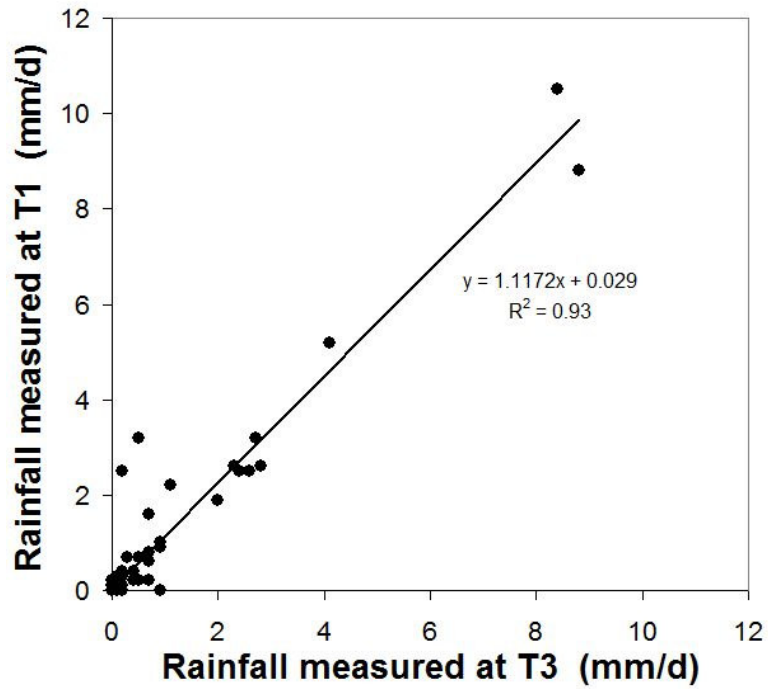


**Figure E.3** A comparison of rainfall measured at the top of the test piles and at the Diavik stations.

a.



b.

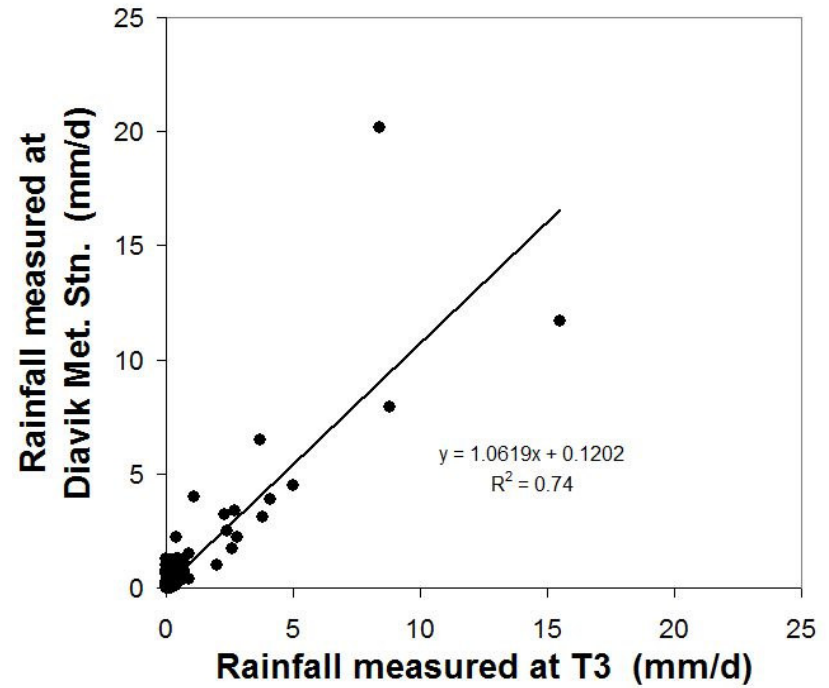


**Figure E.4** Relationships between rainfall measured (a) at the top of the Type 1 and Type 3 test piles and (b) at the top of the Type 3 test pile and at the Diavik meteorological station.



**Figure E.5** An applied rainfall event (a) conducted at the top of the reactive (Type 3) pile. Water from Lac de Gras was pumped from three 1000gal tanks through six sprinklers to wet a 20m x 30m footprint. A grid of cans was used to gauge the applied rainfall (b). Figure continued next page.

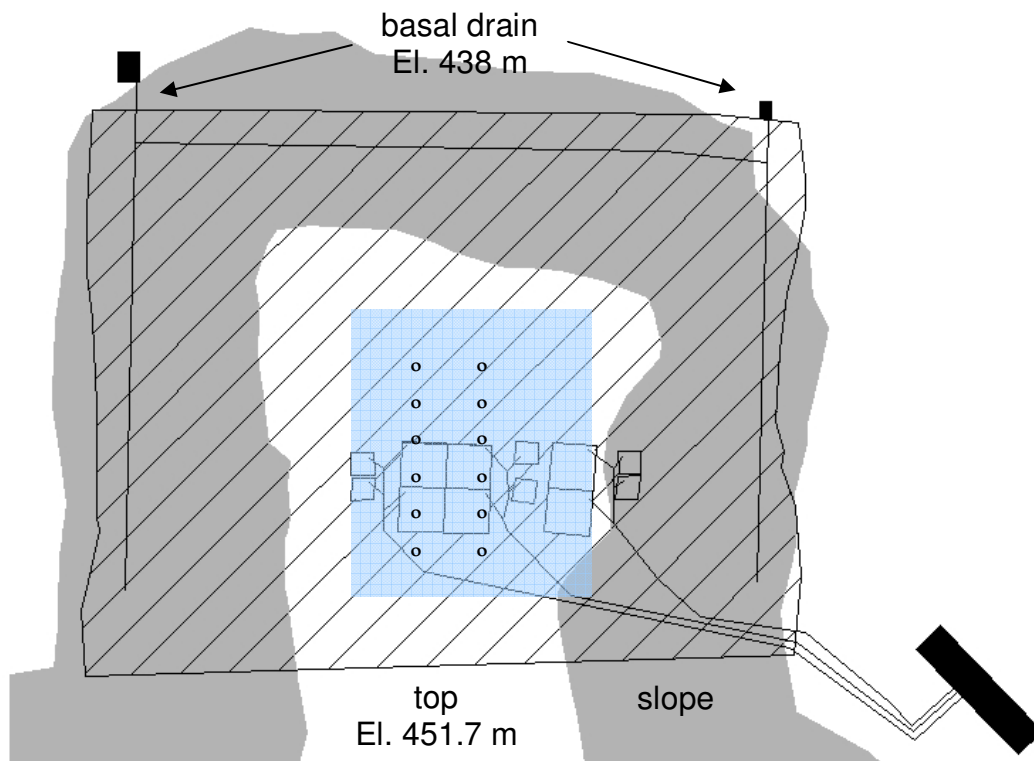


**Figure E.5 continued**

The footprint of a typical applied rainfall event at the Type 3 test pile (left) as seen from a manlift 100 ft. above the surface.

(above) The 20 m by 30 m footprint was above most of the basal lysimeters and all of the TDR probes (° symbols), but only about 20% of the basal drain area.

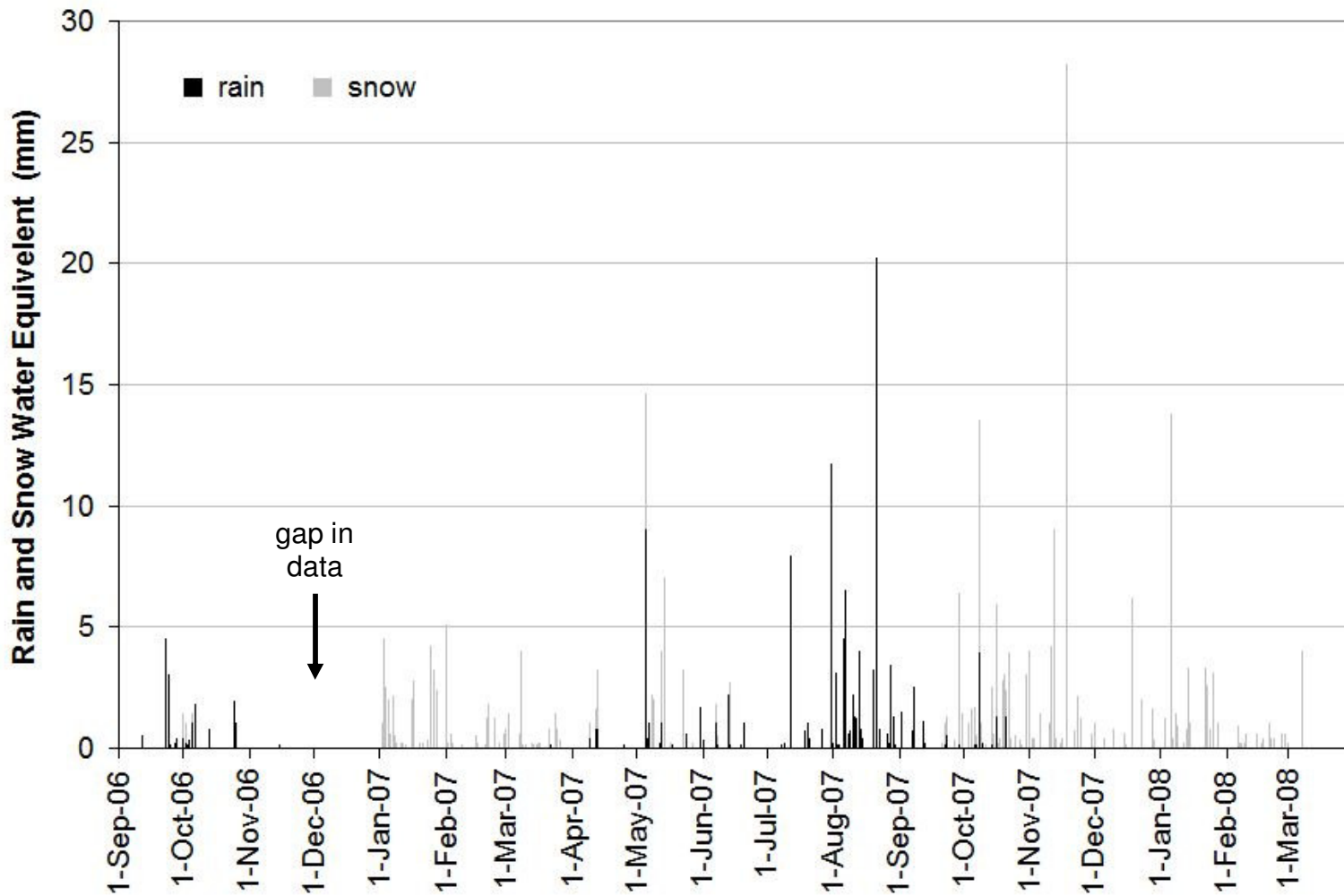


**Figure E.6** Rain and snow at Diavik during the initial 1.5yr of monitoring the waste rock test piles experiment.

a.



b.



**Figure E.7** Wind scouring transports snow from the pile top to the batter at the Type 3 test pile (a, March 16, 2008) and at the Type 1 test pile (b, April 27, 2007).

a.



b.



**Figure E.8** Snowpack on the Type 3 test pile (a) on March 14, 2008, and (b) on April 27, 2007. Maximum wind loading is evident at the tops of the batters. Sublimation gives the pile batter 10cm high snow ridges, giving the fish-scale-appearance in the center of the lower photograph. The south aspect (b, right) appears to show the highest sublimation and snowmelt rate.

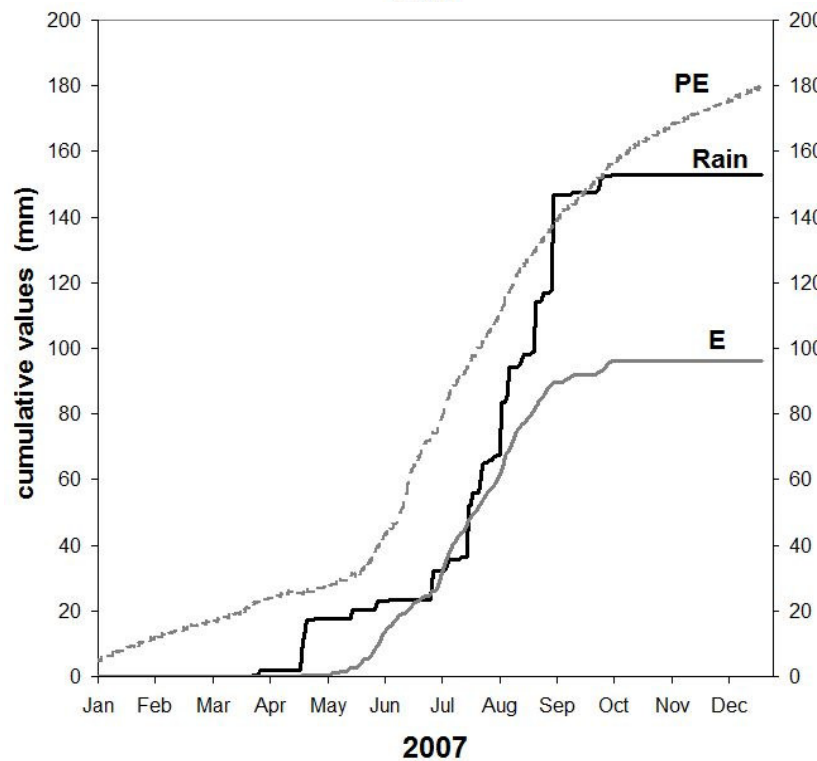
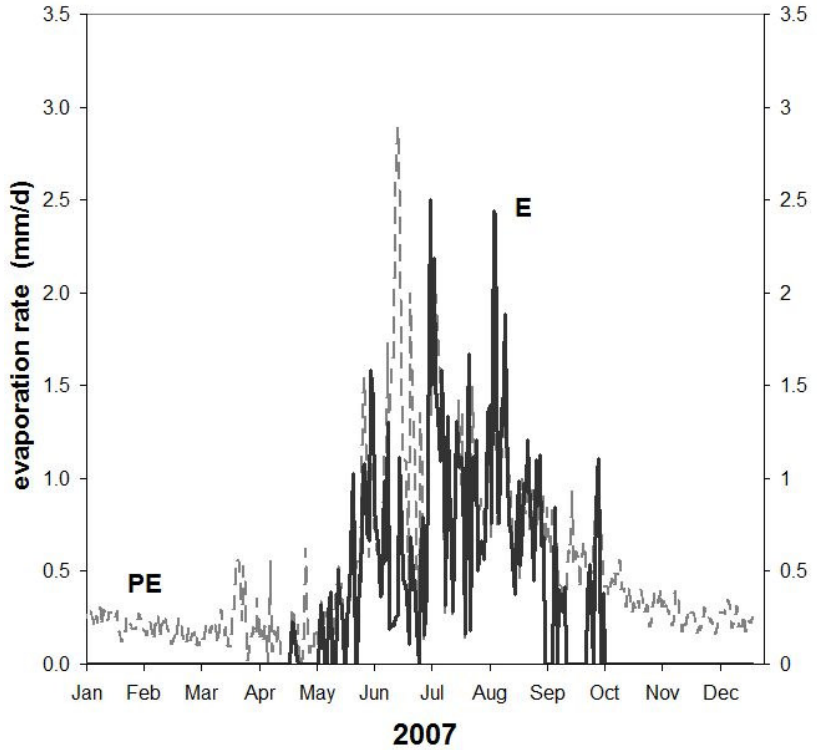


**Figure E.9** (a) Potential evapotranspiration rate (PE) and the estimated evaporation rate (E) from a bare soil subject to the environmental conditions at the top of the Type 3 test pile in 2007: conditions with total rainfall essentially equal to the mean annual. (b) The cumulative values of PE, E, and rainfall at the top of the Type 3 test pile in 2007.

**a.**



*Mike Gupton*

**b.**



*Lianna Smith*

**c.**



**Figure E.10** (a) Vapor transport from (b) discrete vent locations during early winter cooling of a waste rock pile. (c) Large-scale zonation of heat transport appeared evident in early winter as snowfall onto regions of the Type 1 test pile melted upon deposition.

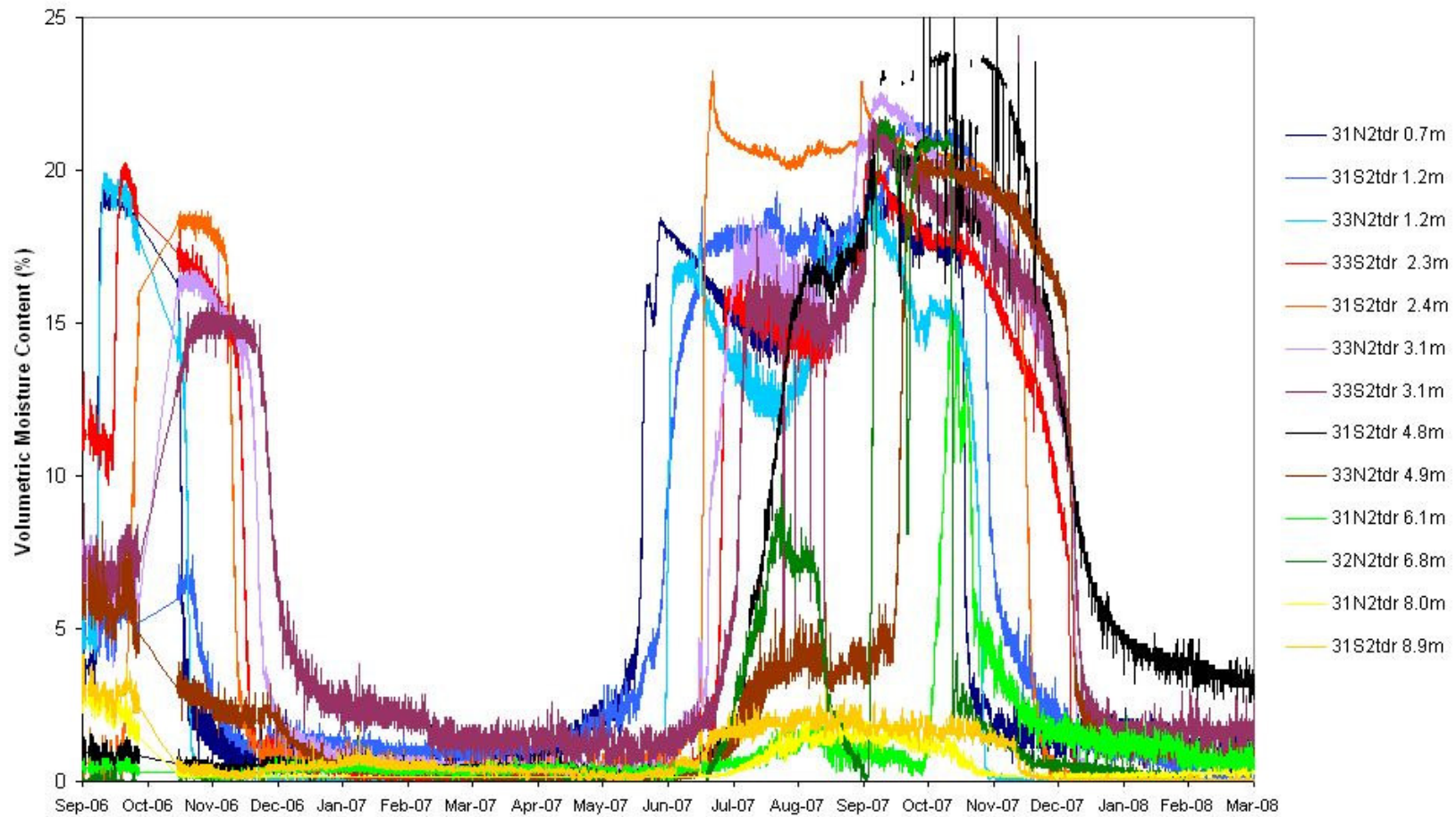


**Figure E.11** Volumetric moisture content measured by TDR at the Type 3 test pile. The depth of each sensor is the last number in the identifier in the legend. Refer to Appendix B for the horizontal positions of the sensors.

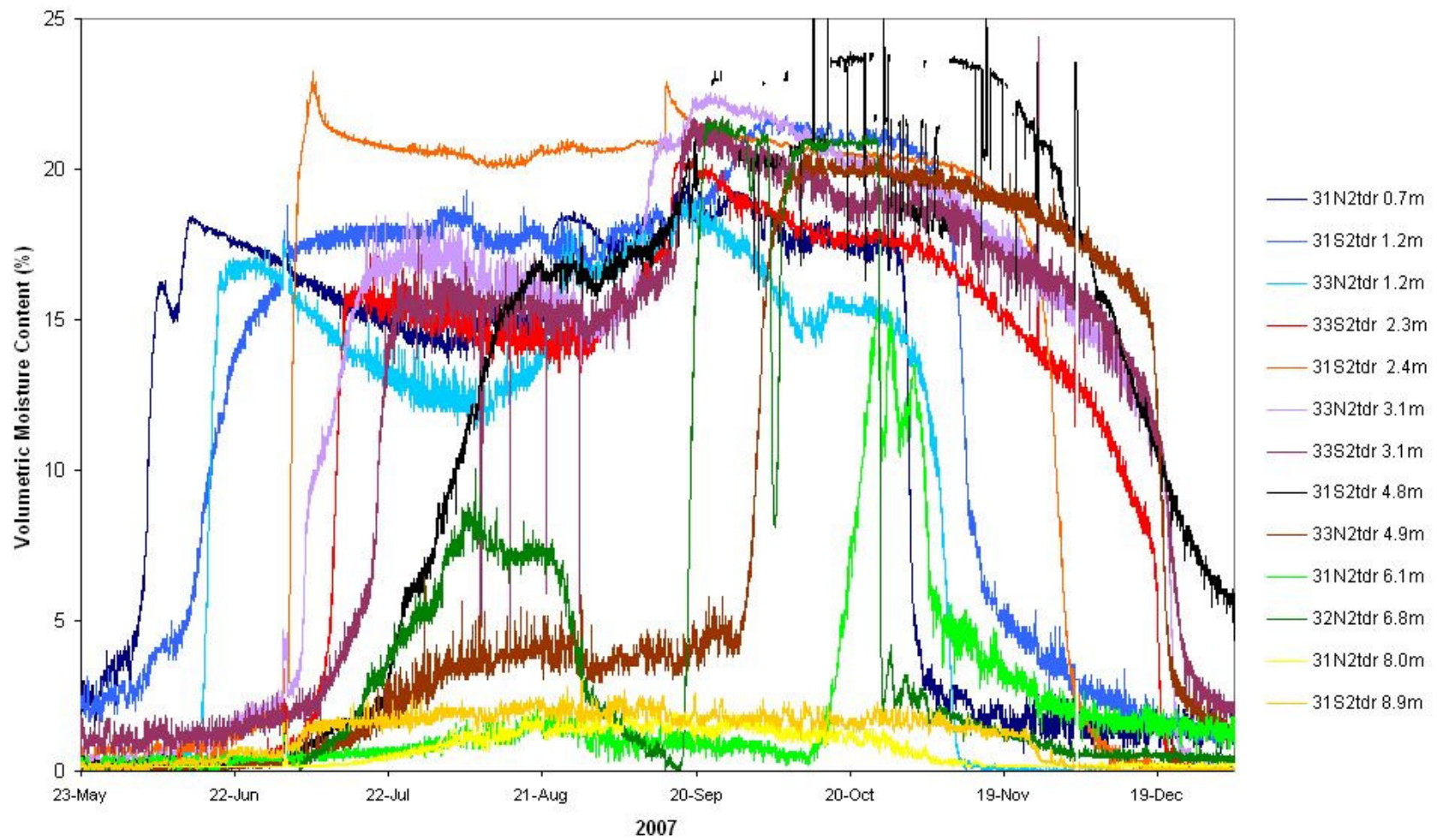


**Figure E.12** Volumetric moisture content measured by TDR in the Type 3 test pile.

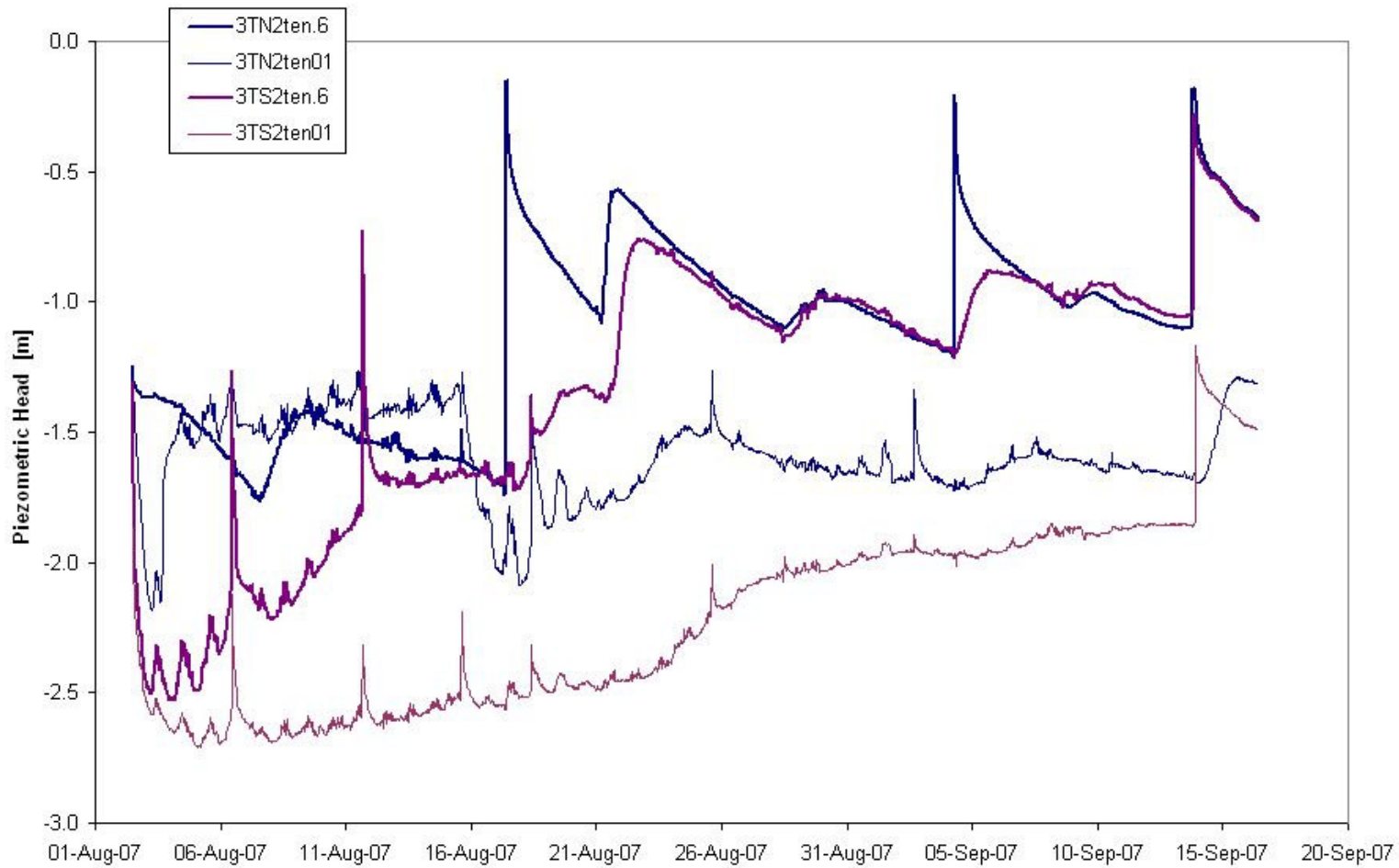


**Figure E.13** Tension head (matric suction plus elevation head) measured at two tensiometer profiles at the top of the Type 3 test pile. Each profile consisted of a ceramic porous cup at a depth of 0.6 m and 1.2 m.

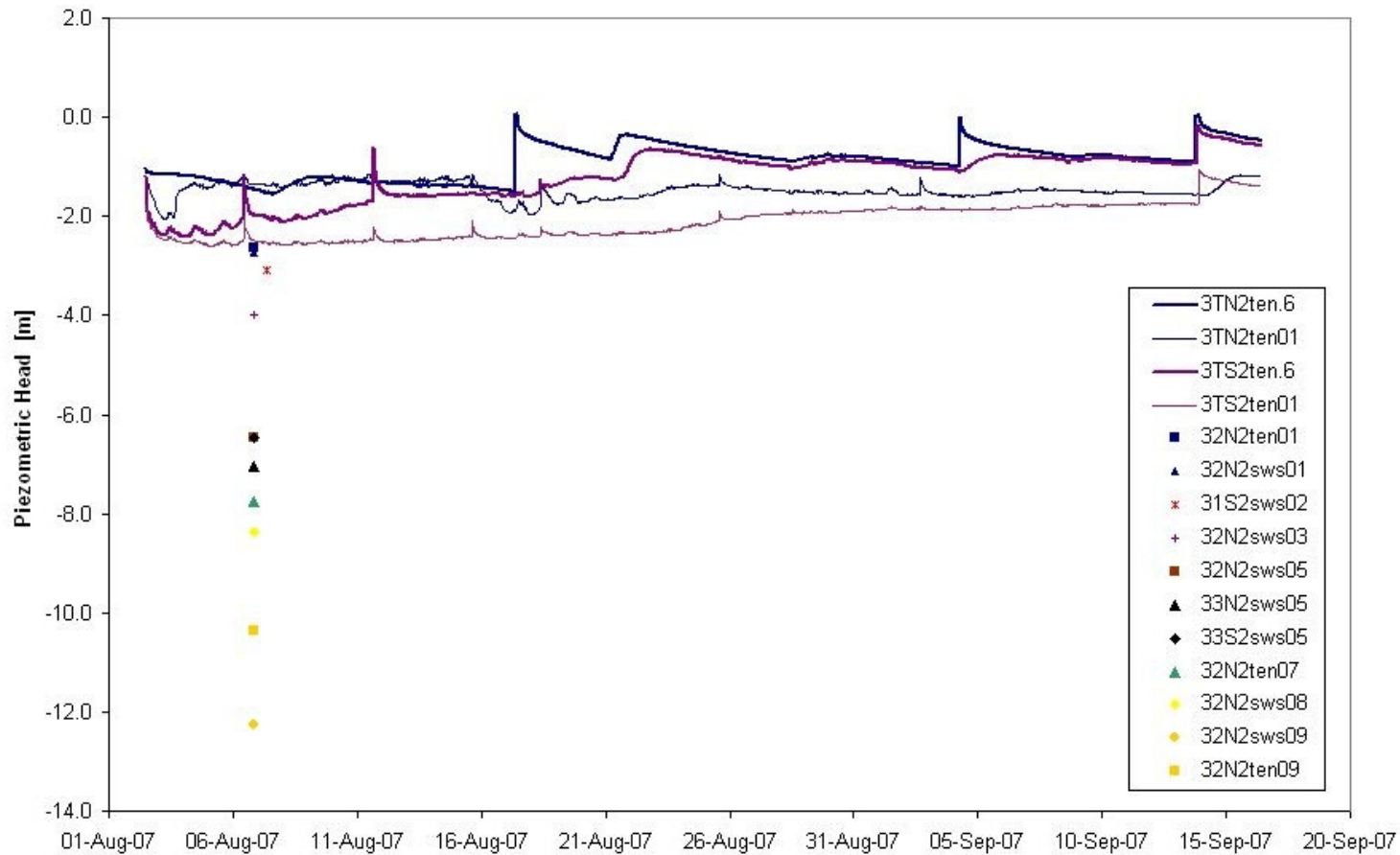


**Figure E.14** Tension head measured continually with tensiometers and pressure transducers and measured at one time with suction samplers at greater depths in the Type 3 test pile. The last character in the labels in the legend indicates approximate depth in meters.

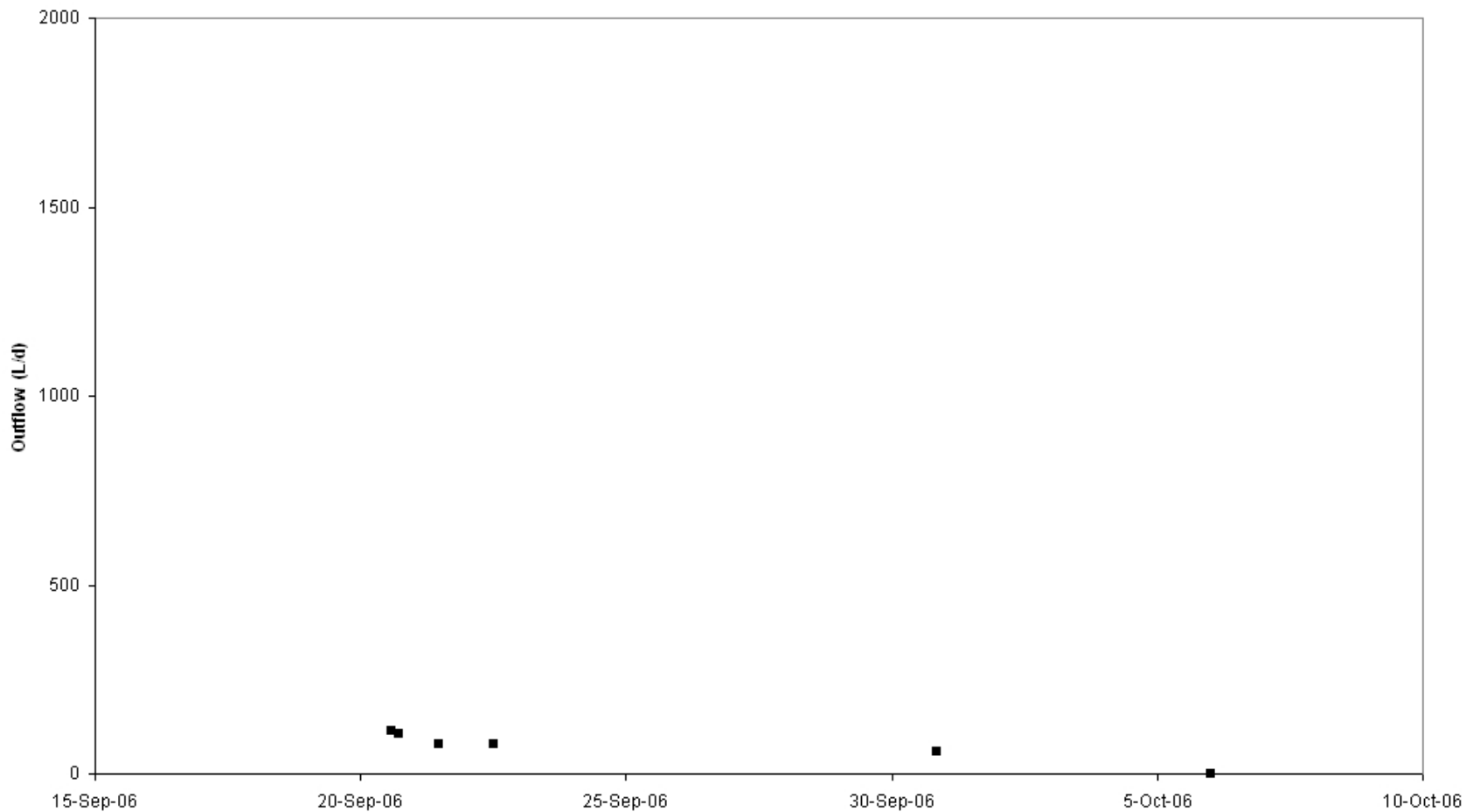


**Figure E.15** The outflow rate at the T3 south basal drain in 2006. No flow was observed at the north basal drain at this time.

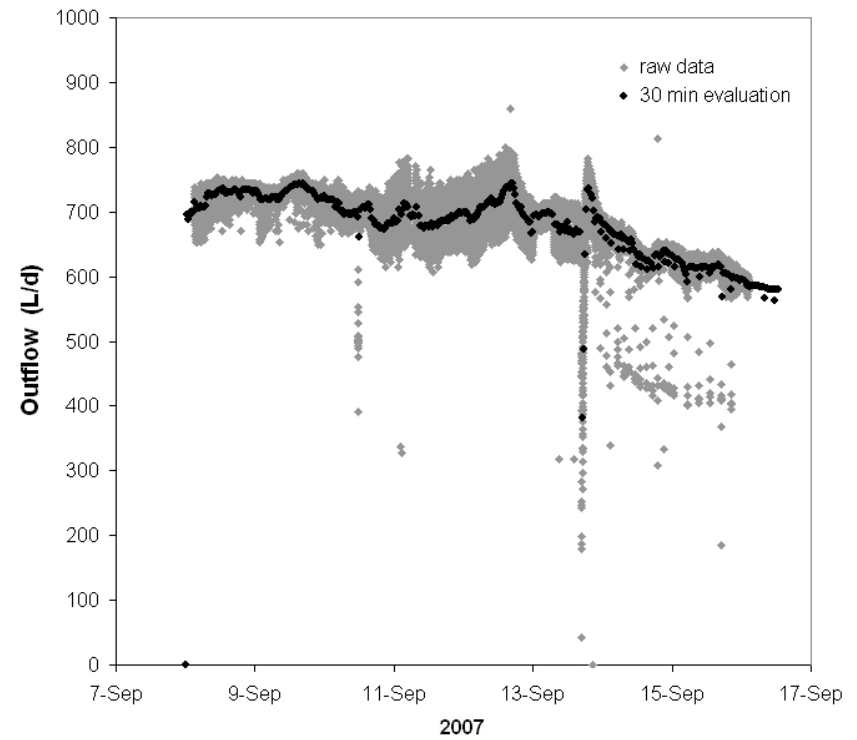
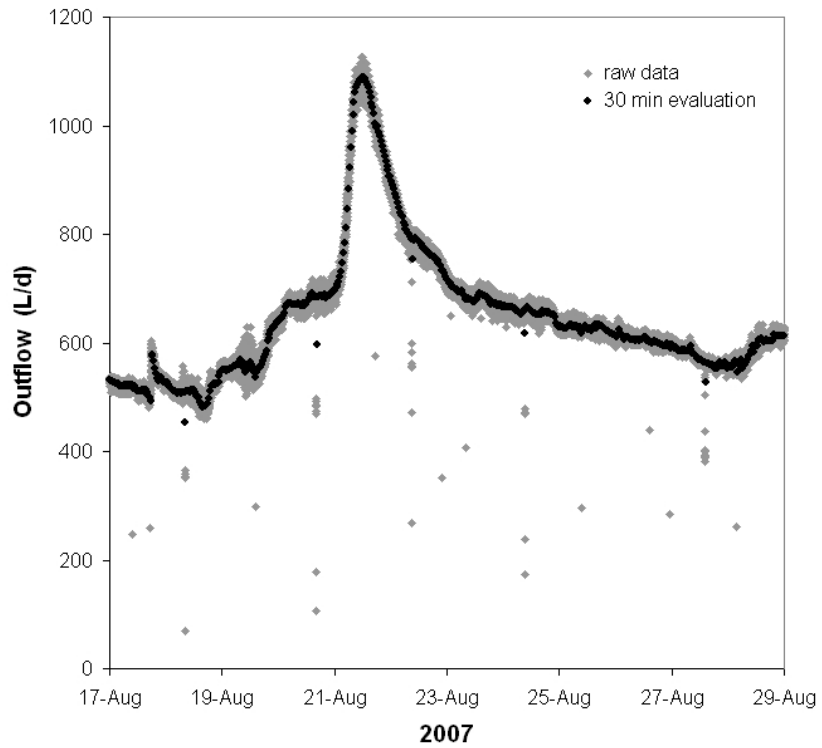


**Figure E.16** Resolution of the basal drain tipping bucket flow gauge. Evaluation of the flow rate every 30 min eliminates variation in the data with the assumption that this variation is noise in the data caused by an imperfectly balanced gauge.

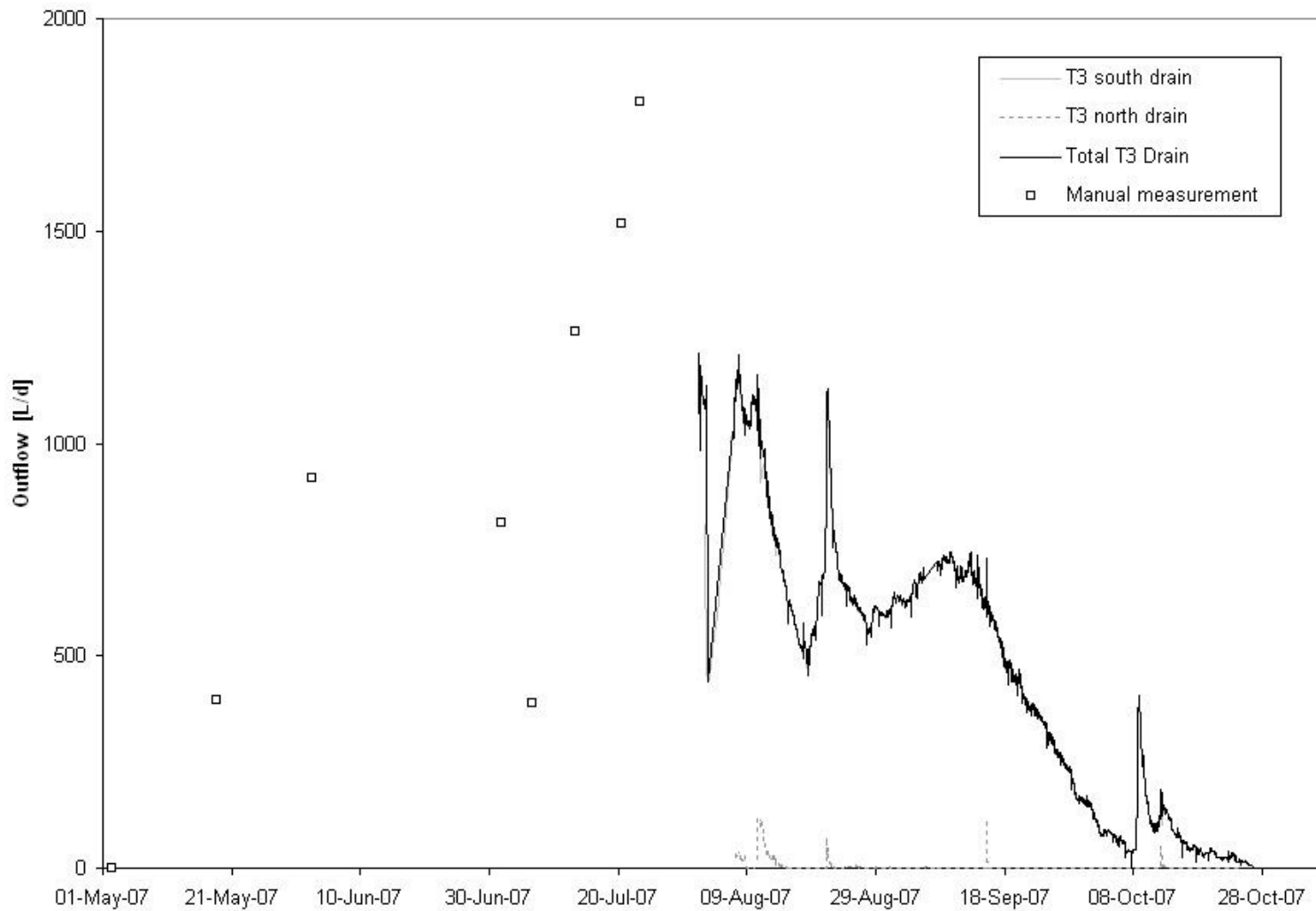


**Figure E.17** The outflow rate at the north and south basal drain in 2007, and the sum of both.

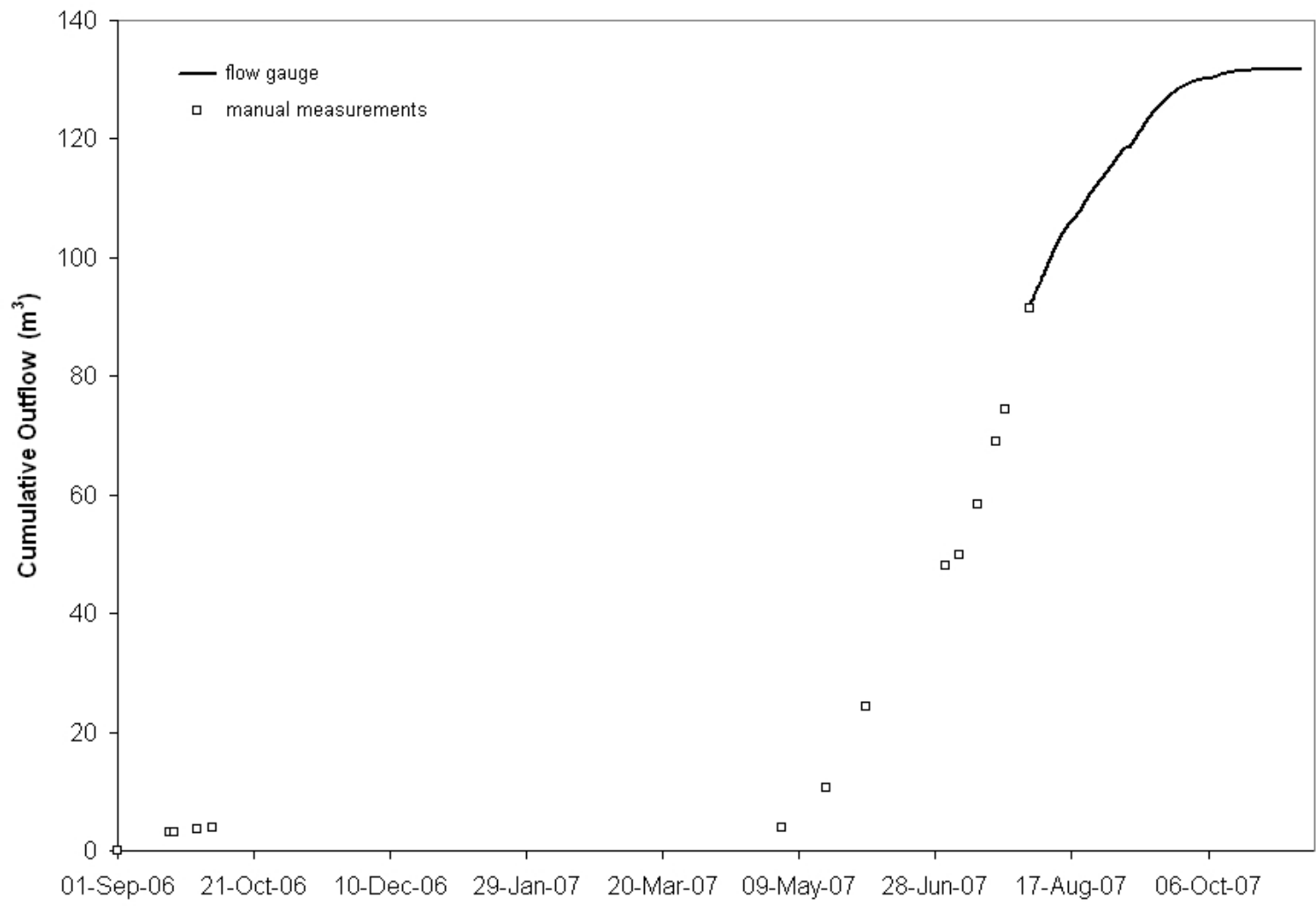


**Figure E.18** The cumulative outflow of the north and south basal drain.

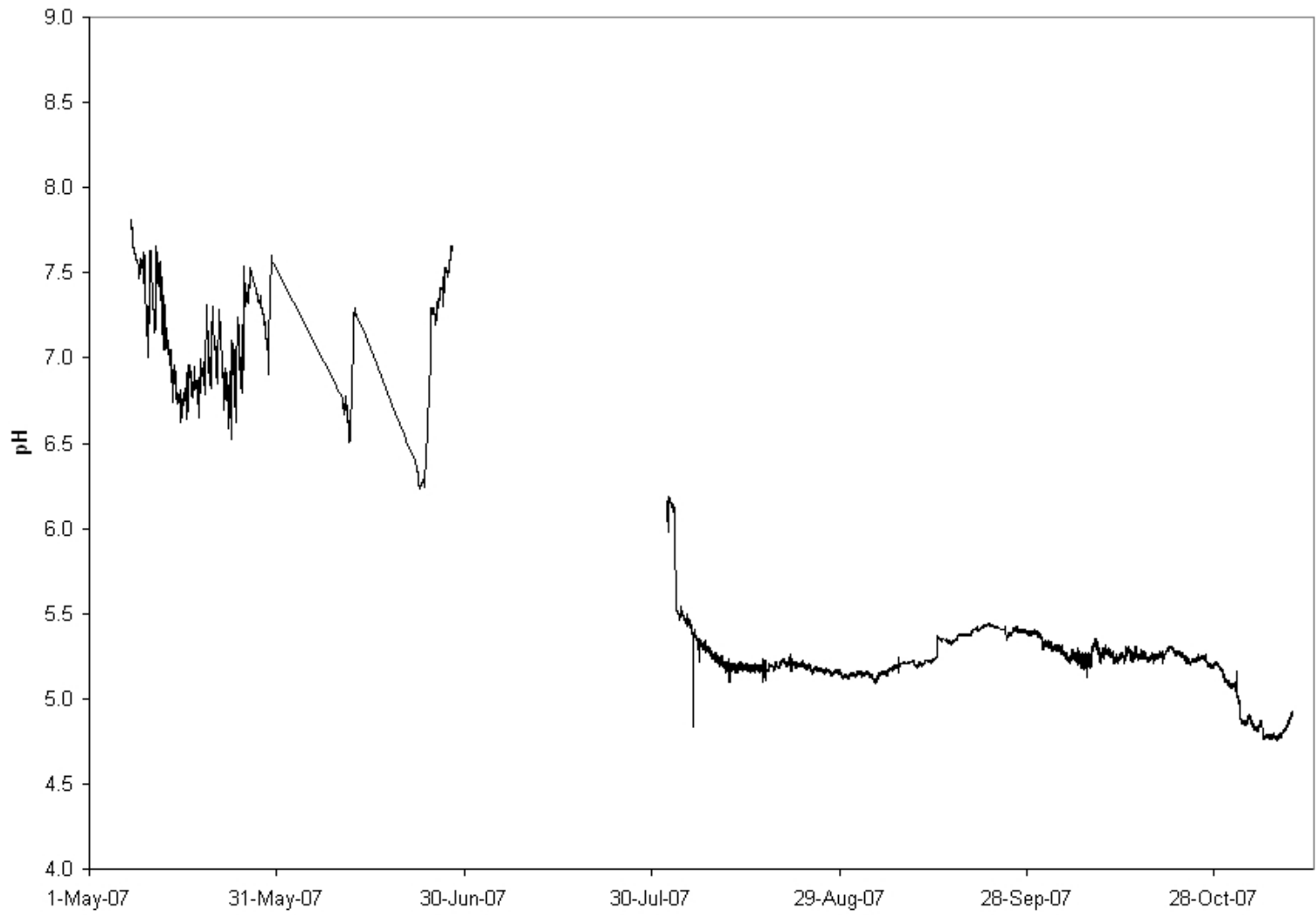


**Figure E.19** The pH of the outflow at the T3 south basal drain, where nearly all of the basal drain outflow reported in 2007.

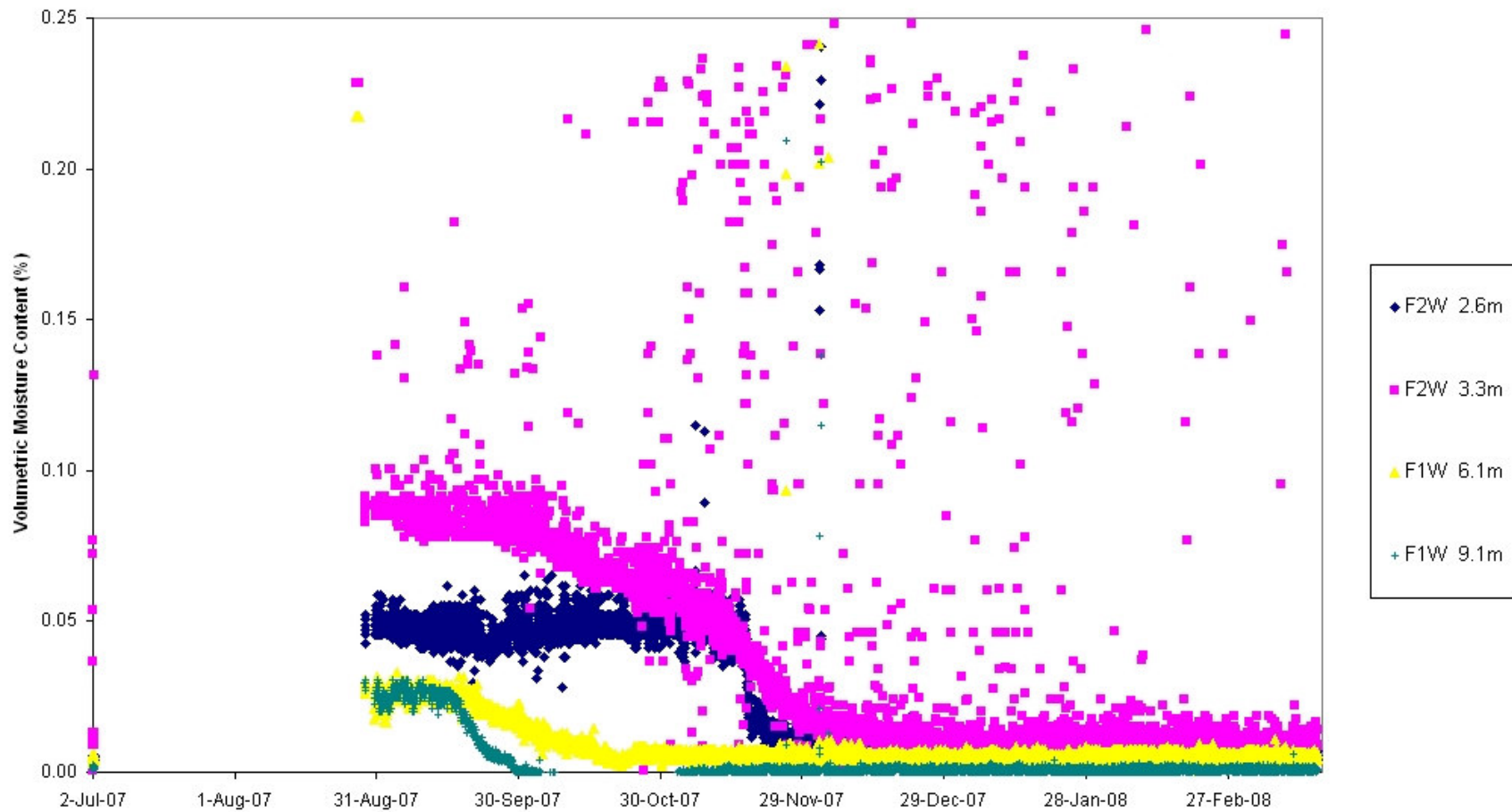


**Figure E.20** Volumetric moisture content measured by TDR at the Type 1 test pile.



**Figure E.21** Outflow at the Type 1 basal drain measured before the drainpipe became disconnected.

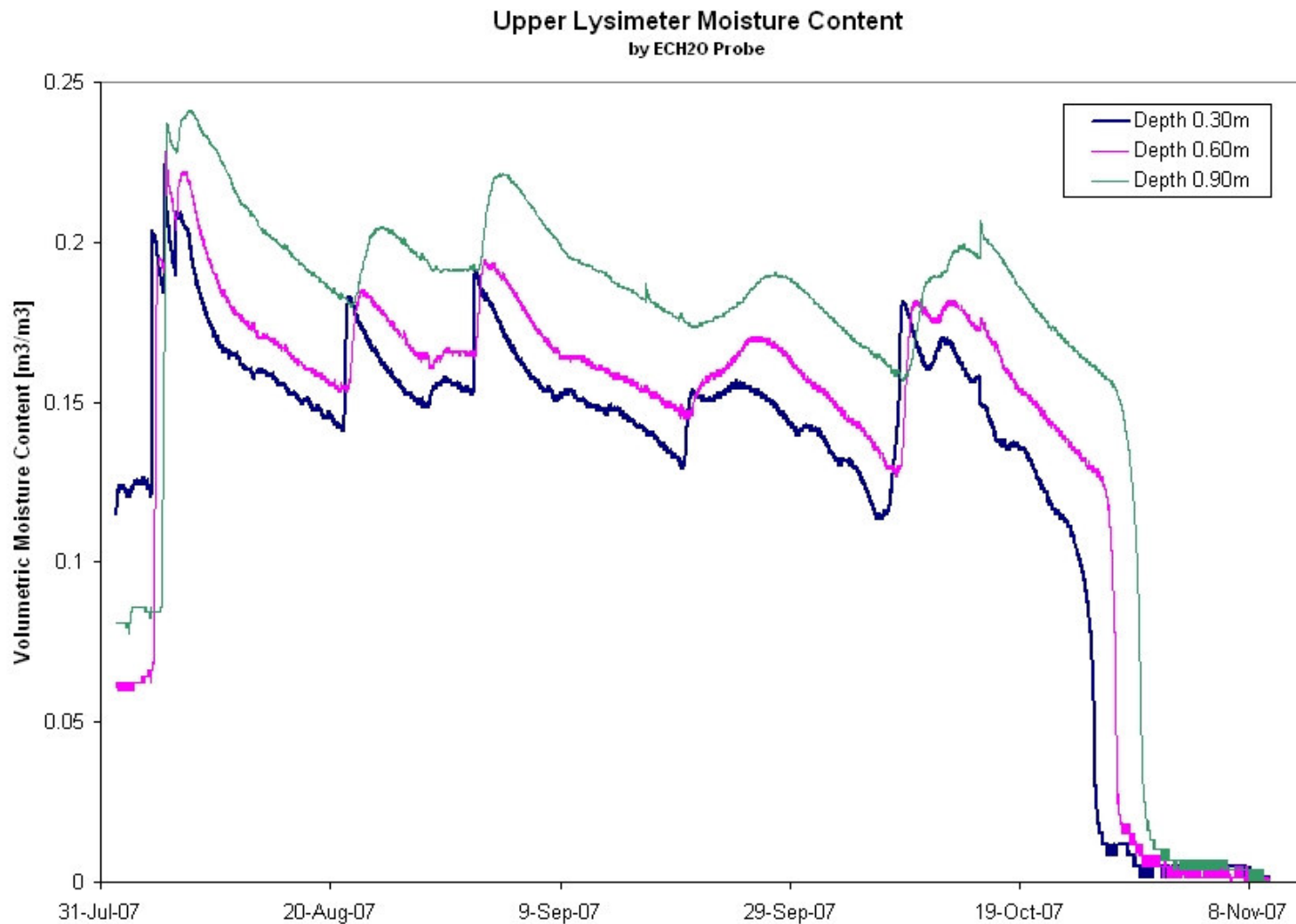


**Figure E.22** Volumetric moisture content measured by ECH<sub>2</sub>O probes between the Type 3 upper collection lysimeters.

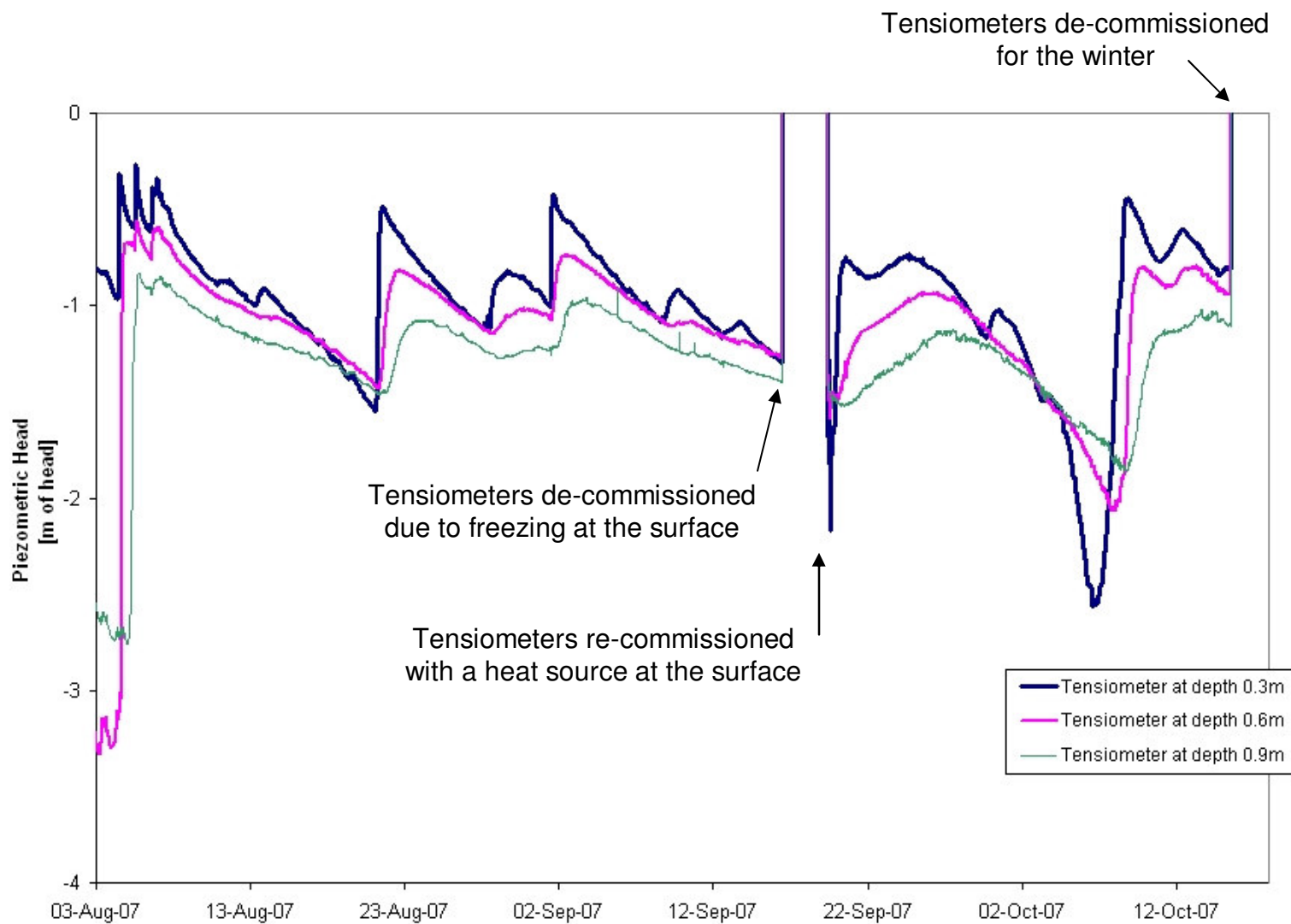


**Figure E.23** Tension head measured at a tensiometer profile between the Type 3 upper collection lysimeters.

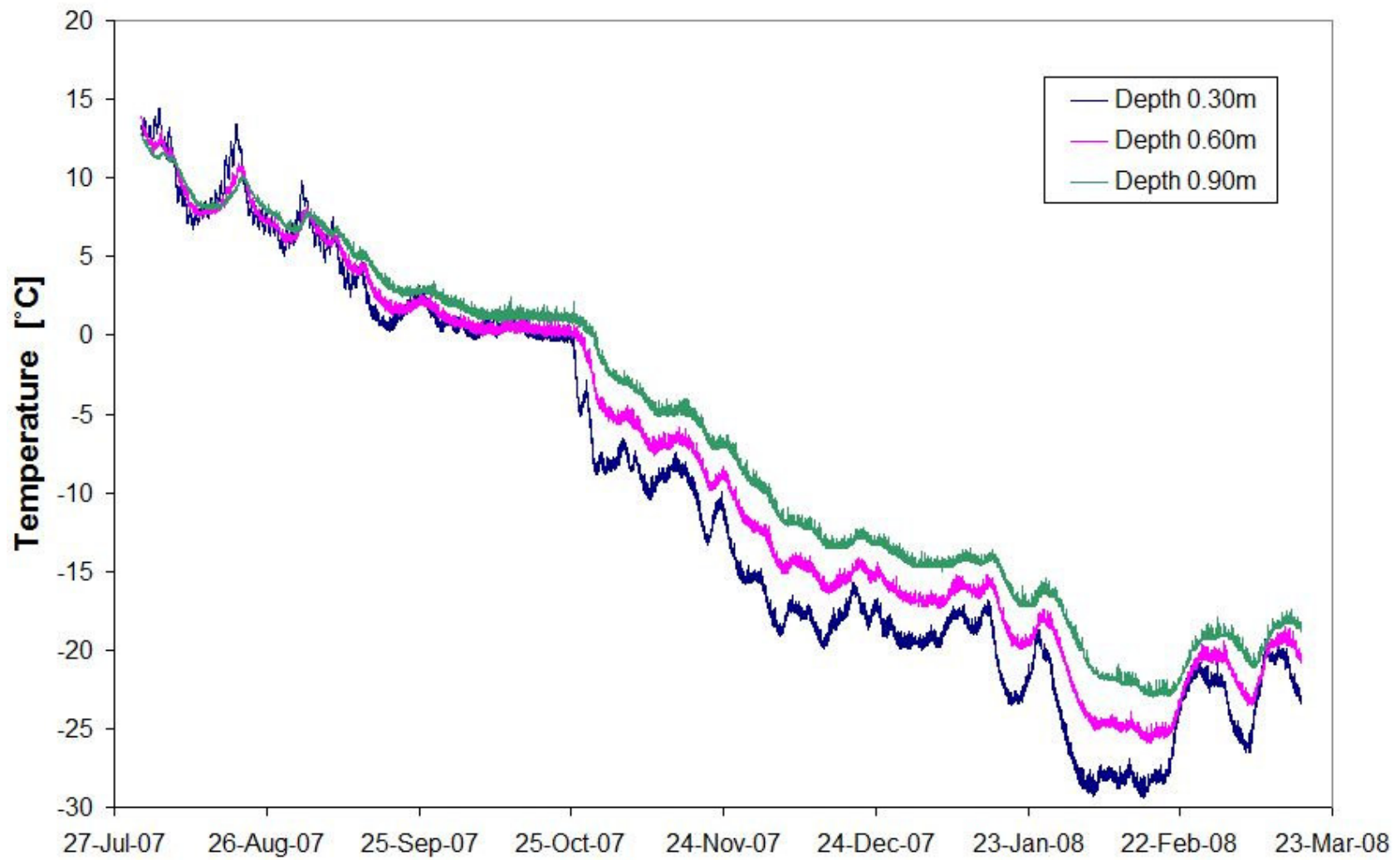


**Figure E.24** Temperature measured by ECH<sub>2</sub>O probes between the Type 3 upper collection lysimeters.

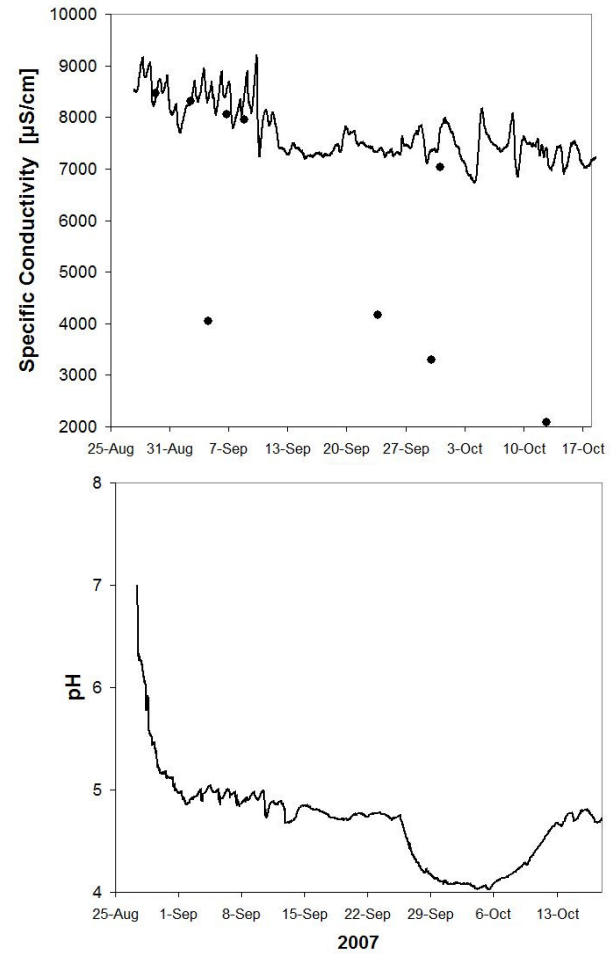
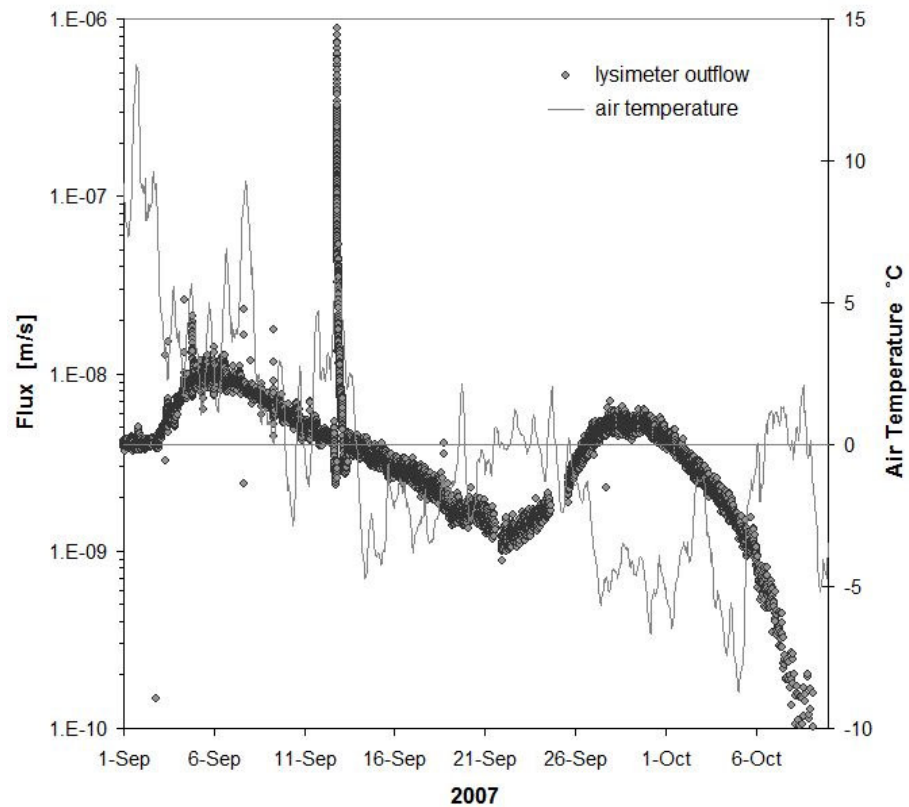


**Figure E.25** Lysimeter outflow response to two applied rainfall events at the West Type 3 upper collection lysimeter.

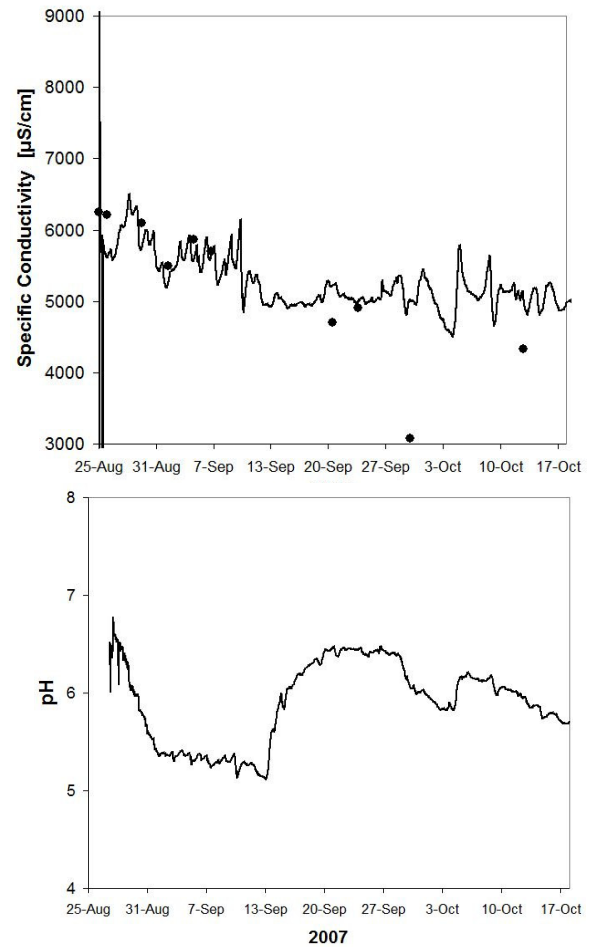
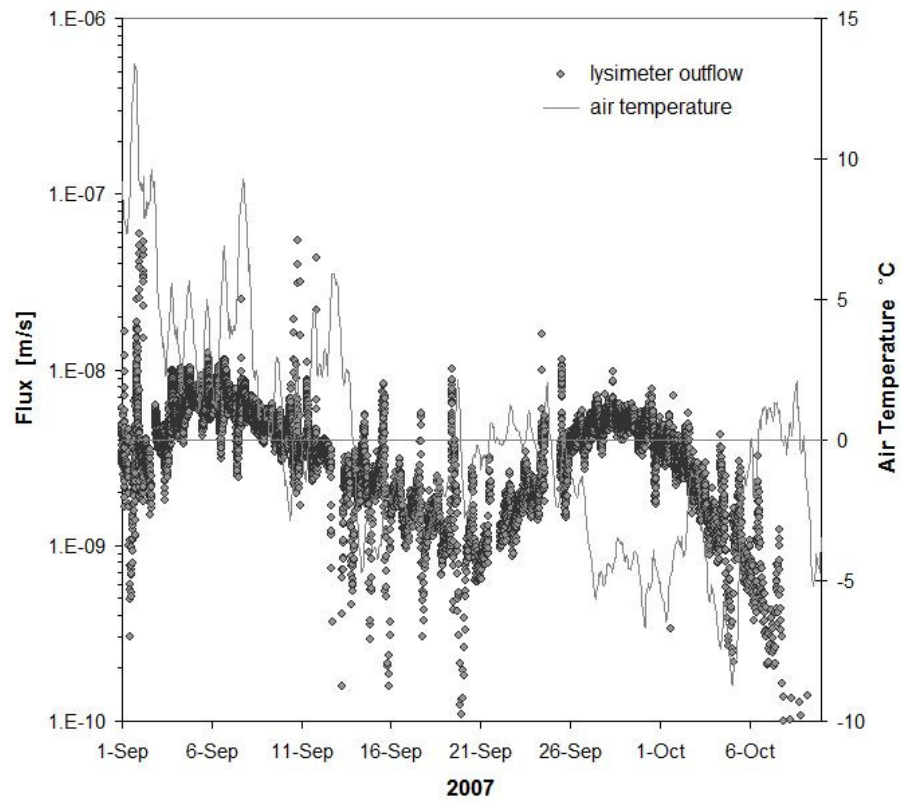


**Figure E.26** Lysimeter outflow response to two applied rainfall events at the East Type 3 upper collection lysimeter.

## REFERENCES CITED IN THE APPENDICES

- Bear, J., 1972. Dynamics of fluids in porous media, Dover Publications, Inc., New York, 764 p.
- Bellehumeur, T., 2001. Mechanisms and spatial variability of rainfall infiltration on the Claude waste rock pile, MSc. dissertation, University of British Columbia, Vancouver.
- Bouwer, H., 1986. Intake Rate: Cylinder Infiltrometer. In: Methods of Soil Analysis. Part 1. Physical and Mineralogical Methods, 2nd Edition, A. Klute (Editor). ASA, Madison, Wisconsin, pp. 825-844.
- Campbell, C.S., 2006. Response of the ECH<sub>2</sub>O EC-10 and EC-20 soil moisture probes to variation in water content, soil type, and solution electrical conductivity, Decagon Devices application note, [www.decagon.com](http://www.decagon.com), Pullman, WA, USA.
- Campbell Scientific, Inc., 2003. CR10X measurement and control system operator's manual, 815 W. 1800 N., Logan, UT 84321, USA, [www.campbellsci.com](http://www.campbellsci.com).
- Campbell Scientific Canada Corp., 2003. Using CSIM11 pH and ORP probes with Campbell Scientific dataloggers instruction manual, 11546 – 149 Street, Edmonton, AB T5M 1W7, [www.campbellsci.ca](http://www.campbellsci.ca).
- Cobos, D.R., 2006. Calibrating ECH<sub>2</sub>O soil moisture sensors, Decagon Devices application note, [www.decagon.com](http://www.decagon.com), Pullman, WA, USA.
- Decagon Devices, Inc., 2007. ECH<sub>2</sub>O-TE / EC-TM probe operator's manual, version 5, [www.decagon.com](http://www.decagon.com), Pullman, WA, USA.
- Decagon Devices, Inc., 2007a. Theory of ECH<sub>2</sub>O probes' operation, [www.decagon.com/Ech2o/theory](http://www.decagon.com/Ech2o/theory), Pullman, WA, USA.
- Diavik Diamond Mines, Inc., 2005. Environmental assessment review and revised effects assessment, internal report, PO Box 2498 5007-50th Avenue, Yellowknife, NT X1A 2P8.
- Dingman, S.L., 2002. Physical Hydrology, 2<sup>nd</sup> Ed., Prentice Hall, Upper Saddle River, NJ, 646p.
- Fredlund, D.G., and H. Rahardjo, 1993. *Soil Mechanics for Unsaturated Soils*, John Wiley and Sons, Inc., New York, 519p.
- Fredlund, M.D., W. S. Sillers, D. G. Fredlund, and G.W. Wilson, 1996. Design of a Knowledge-based system for unsaturated soil properties, *3rd Canadian Conference on Computing in Civil and Building Engineering*, Montreal, Quebec, Aug. 26-28.

- Hook, W. R., N. J. Livingston, Z. J. Sun, and P. B. Hook, 1992. Remote diode shorting improves measurement of soil water by time domain reflectometry, *Soil Sci. Soc. Am. J.*, v. 56, pp. 1384-1391.
- Loague, K., 1990. Simple design for simultaneous steady-state infiltration experiments with ring infiltrometers, *Water Resources Bulletin*, v. 26, n. 6, pp. 935-938.
- Loague, K., and Gander, G.A., 1990. R-5 revisited: spatial variability of infiltration on a small rangeland catchment, *Water Resources Research*, v. 26, n. 5, pp. 957-971, 89WR03131.
- Mackenzie Valley Land and Water Board, 2002. Decision of the McKenzie Valley Land and Water Board Panel Meeting of May 30, 2002; Re: Water License N7L2-1645, pursuant to the Northwest Territories Waters Act.
- Nachabe, M.H., 2002. Analytical expressions for transient specific yield and shallow water table drainage, *Water Resources Research*, v. 38, n. 10, pp. 11-1 to 11-7, doi:10.1029/2001WR001071.
- Nichol, C.F., R. Beckie, and L. Smith, 2002. Evaluation of Uncoated and Coated Time Domain Reflectometry Probes for High Electrical Conductivity Systems, *Soil Science Society of America Journal*, v. 66, pp. 1454–1465.
- O'Kane, M., and Barbour, S. L., 2003. Predicting field performance of lysimeters used to evaluate cover systems for mine waste, from *the Proceedings from the 6th International Conference of Acid Rock Drainage*, pp. 663-669 (The Australasian Institute of Mining and Metallurgy: Melbourne).
- Serway, R., and J. Jewett, 2003. *Physics for Scientists and Engineers* (6 ed.). Brooks Cole.
- Smith, L., 2008. Test piles project 2006 construction summary, report prepared for FDA Engineering, Ltd., 38 Sheep River Cove, Okotoks, AB T1S 2G7, Canada, and submitted to Diavik Diamond Mines, Inc., P.O. Box 2498, 5007 50<sup>th</sup> Ave., Yellowknife, NT, X1A 2P8, Canada.
- Soil Moisture, Corp., 1989. 5301 current transducer operating instructions, P.O. Box 30025, Santa Barbara, CA, 93105, USA; [www.soilmoisture.com](http://www.soilmoisture.com).
- Soil Moisture, Corp., 1995. 1400/1405 Tempe pressure cell operating instructions, P.O. Box 30025, Santa Barbara, CA, 93105, USA; [www.soilmoisture.com](http://www.soilmoisture.com).
- Soil Moisture, Corp., 1997. 2725a jet fill tensiometer operating instructions, P.O. Box 30025, Santa Barbara, CA, 93105, USA; [www.soilmoisture.com](http://www.soilmoisture.com).

- Soil Moisture, Corp., 1997a. 1920F1/K1 pressure-vacuum soil water samplers operating instructions, P.O. Box 30025, Santa Barbara, CA, 93105, USA;  
[www.soilmoisture.com](http://www.soilmoisture.com).
- Steffen Robertson and Kirsten (Canada), Inc., 2003. 2002 waste rock storage area seepage and waste rock survey report, Ekati Diamond Mine, SRK, Inc., Vancouver, BC, [www.srk.com](http://www.srk.com).
- Topp, G.C., J.L. Davis, and A.P. Annan, 1980. Electromagnetic determination of soil water content: Measurements in coaxial transmission lines. *Water Resour. Res.*, v. 16, pp. 574–582.
- Topp, G.C., S. Zegelin, and I. White, 2000. Impacts of the real imaginary components of relative permittivity on time reflectometry measurements in soils. *Soil. Sci. Soc. Am. J.*, v. 64, pp. 1244–1252.
- Williams, D.E., 1981. The well/aquifer model initial results, Roscoe Moss Co., 4360 Worth Street, Los Angeles, CA, 90063, USA,  
[http://www.roscoemoss.com/tech\\_manuals/twam/twam.pdf](http://www.roscoemoss.com/tech_manuals/twam/twam.pdf).
- Won, I.J., 1987. The geometrical factor of a marine resistivity probe with four ring electrodes. *IEEE Journal of Oceanic Engineering*, OE-12: 301-303.
- Yazdani, J., Barbour, L, and Wilson, G.W., 2000. Soil water characteristic curve for mine waste rock containing coarse material, from *Proceedings of the 6<sup>th</sup> Environmental Engineering Specialty Conference of the Canadian Society of Civil Engineers*, London, ON, Canada.
- Young, G. D., 1995. Moisture Point MP-917 technical brief 13: single diode probes. available at [http://www.esica.com/support\\_technical\\_briefs.php](http://www.esica.com/support_technical_briefs.php).
- Zegelin, S., I. White, and D.R. Jenkins, 1989. Improved field probes for soil-water content and electrical conductivity measurement using time domain reflectometry. *Water Resour. Res.*, v. 25, pp. 2367–2376, 89WR01417.